Super-Flexible Sensors and Advanced 3D Morphing Actuators based on Elastic Instability

CONG WANG

PhD

2020

Super-Flexible Sensors and Advanced 3D Morphing Actuators based on Elastic Instability

CONG WANG

A thesis submitted in partial fulfilment of the requirements of the University of Northumbria at Newcastle for the degree of Doctor of Philosophy

Department of Mechanical and Construction Engineering

January 2020

Abstract

Super-flexible devices based on soft materials have the potential to sustain large mechanical deformations, enabling advanced applications such as flexible electronics, soft robots, artificial skin, and biomedical transducers. Subject to a large compression, materials may undergo different types of elastic instabilities such as wrinkles, creases, and folds. Despite recent growing interests in turning this usually unwanted phenomenon into useful engineering applications (e.g. tactile sensing), this topic remains relatively under-researched. Therefore, this thesis focuses on developing the control mechanisms of elastic instabilities, and their applications in sensing and actuation systems.

Elastic instabilities induced strain-gated logic sensing technology is developed by research into micro structured metal-elastomer tri-layer system. The test structures are designed to study the deformation behaviour and to exploit the large strain sensing mechanism. The stepwise electrical signals are achieved (from ~10^{10} to ~120 Ω at first switching stage and then to ~50 Ω at second switching stage) that survived much higher than usual compressive strains of up to 60%.

On the other hand, elastic instabilities induced topo-optical sensing strategy is created by patterning microstructure arrays within the tri-layer system. Two unwanted phenomena (creases/folds and oxygen quenching effect) are turned into a responsive and programmable 'fold to glitter' function through

micro engineering, which can light up areas of an object or material by creating microscopic creases/folds within its surface. The signal-Noise-Ratio (SNR) contrast in optical pattern generation is improved by 6 folds due to the oxygen quenching effect. The numerical analysis by ABAQUS provides the fundamental theory on the mechanism of generating targeted folding through simulating the in-plane and out-of-plane strain energy localization. Different luminescent optical patterns are demonstrated under in-plane uniaxial or equi-biaxial compression.

Apart from the surface deformation, the bulk deformation of heterogeneous layered structures of soft functional hydrogel is also developed to generate the controllable and reconfigurable 3D morphing device. The initial configurations with various shapes (“S”, “W” and “C”) are demonstrated due to the swelling ratio mismatch. The developed sensing and actuation technologies provide opportunities for future applications in flexible electronics, tuneable optics, soft robotics and bio-medical systems.

Acknowledgment

First of all, I wish to express my special gratitude to my principal supervisor Dr. Yifan Li and co-supervisor Dr. Ben Bin Xu for providing me with continuous encouragement and scientific guidance throughout my research time in Northumbria University. Without their fully support and encouraging supervisions, it would be impossible for me to finish this project. I also would like to thank my external advisor, Dr. Jonathan Terry from Edinburgh University for his assistance in clean room in Scottish Microelectronics Centre (SMC).

I would like to express my thanks to the technical staffs, Dr. Alex Laude from Newcastle University, Dr. Pietro Maiello, Rebecca Payne and Gavin Warburton from Northumbria University for their valuable advice and experience. I also acknowledge Prof. Anthony John Walton, Dr. Stewart Smith from Edinburgh University, Dr. Valery Kozhevnikov, Dr. Graeme Turnbull, Dr. Terence Liu, Dr. Sherry Chen, Dr. Gary Wells from Northumbria University.

I thank all the members of staff and academics who I have worked with in Northumbria University. I appreciate to Northumbria University for providing me the PhD studentship and the research facilities.

Finally, I wish to express my deepest gratitude to my families for their endless supporting and the greatest love throughout my life.

Declaration

I declare that the work contained in this thesis has not been submitted for any other degree and that it is all my own work. I also confirm that this work fully acknowledges opinions, ideas and contributions from the work of others. The work was done in collaboration with the University of Edinburgh. The simulation results were performed by Dr. Sherry Chen, Northumbria University. The phosphorescent Iridium-III materials were manufactured by Dr. Valery Kozhevnikov, Northumbria University. The sheet resistance was measured by the Edinburgh University.

Any ethical clearance for the research presented in this thesis has been approved. Approval has been sought and granted by the Faculty Ethics Committee on 27/04/2016.

I declare that the word count of this thesis is currently 30891 words.

Name: Cong Wang

Signature:

Date: 31/01/2020

Contents

List of Figures

List of Tables

Abbreviations

POC – Point-of-care

IC – Integrated circuit

MRL –Mechano-Responsive Luminescence

ML –Mechanoluminescence

MC –Mechanochromism

EL –Electrically-induced Luminescent

PDMS –Polydimethylsiloxane

VPS –Vinylpolysiloxane

SAM – Self-assembly monolayer

SEM – Scanning Electron Microscopy

LSCM –Laser Scanning Confocal Microscopy

OM –Optical Microscopy

FLIM –Fluorescence lifetime imaging

AFM –Atom Force Microscopy

IPA –Isopropyl alcohol

FDTS –Perfluoro-decyl-trichloro-silane

MPTMS –3-Mercaptopropyl-trimethoxysilane

PEB –Post-exposure-bake

FE –Finite Element

SNR –Signal Noise Ratio

NLC –Nominal line contrast

FoA –Fluorescein o-acrylate

Ir-III –Iridium-III

AIE –Aggregation-induced emission

ACQ – Aggregation caused quenching

PBS – Phosphate buffer saline

DI water – Deionized water

3D – Three dimensions

2D – Two dimensions

1D – One dimension

SiO_2 – Silicon dioxide

Nomenclatures

$\boldsymbol{\varepsilon_{comp}}$ – Compression strain

$\boldsymbol{\varepsilon_c}$ – Onset critical strain

$\boldsymbol{\varepsilon_w}$ – Critical wrinkling strain

$\boldsymbol{\bar{E}_f}$ – Young's Modulus of thin film

$\boldsymbol{\bar{E}_s}$ – Young's Modulus of soft substrate

$\boldsymbol{G}$– Shear modulus

$\boldsymbol{\nu}$ – Poisson's ratio

$\boldsymbol{\lambda}$ – Wavelength

$\boldsymbol{\varepsilon_{sub}}$ – Substrate compression strain

$\boldsymbol{\varepsilon_{Au-x}}$ – Au x direction compression strain

$\boldsymbol{\varepsilon_{Au-y}}$ – Au y direction compression strain

$\boldsymbol{\varepsilon_{Gap-x}}$ – PDMS x direction compression strain

$\boldsymbol{\varepsilon_{Gap-y}}$ – PDMS y direction compression strain

$\boldsymbol{L_o}$ – Original length

$\boldsymbol{L}$ –Compressed length

L_{fo} – Finger electrode original length

L_f – Finger electrode compressed length

W_{fo} – Finger electrode original width

W_f – Finger electrode compressed width

L_{go} – Gap original length

L_g – Gap compressed length

W_{go} – Gap original width

W_g – Gap compressed width

R_{finger} – Finger resistance

R_s – Sheet resistance

Φ – Diameter

D – Distance

r – Pitch

h – Thickness

Hc – Self-contact depth

W – Distance between neighbouring lines

Achievements

Publications:

1. **Cong Wang,** Ding Wang, Valery Kozhevnikov, Xingyi Dai, Graeme Turnbull, Xue Chen, Jie Kong, Ben Zhong Tang, Yifan Li, Ben Bin Xu, A Flexible Topo-optical Sensing Technology with Ultra-high Contrast, ***Nature communications****,* 11 (1), 1448. DOI: 10.1038/s41467-020-15288-8.

2. **Cong Wang**, Ben Bin Xu, Jonathan G. Terry, Stewart Smith, Anthony J. Walton, Steven Wang, Haibao Lv, Yifan Li, Flexible, Strain Gated Logic Transducer Arrays Enabled by Initializing Surface Instability on Elastic Bilayers, ***APL Materials***, 7, 031509. DOI: 10.1063/1.5079403.

3. Sreepathy Sridhar*, **Cong Wang***, Jonathan Terry, Xue Chen, Ansu Sun, Zhenghong Li, Haibao Lu, Ben Xu, Yifan Li, Controlled Co-operative Wetting Enabled Heterogenous Structured 3D Morphing Transducers, ***Advanced Materials Interfaces***, Under review.

4. **Cong Wang**, Sreepathy Sridhar, Jonathan Terry, Ansu Sun, Zhenghong Li, Haibao Lu, Ben Xu, Yifan Li, Advanced 3D morphing transducers by smart hydrogel patterning, ***IEEE Transducers* 2019**, DOI: 10.1109/TRANSDUCERS.2019.8808453.

5. **Cong Wang**, Ben Bin Xu, Jonathan G. Terry, Stewart Smith, Anthony J. Walton, Yifan Li, Metal-Elastomer Surface Deformation Control on Super-Compressible Strain Transducer Arrays, ***IEEE IFETC* 2018**. DOI:10.1109/IFETC.2018.8583995.

6. **Cong Wang,** Ding Wang, Valery Kozhevnikov, Ben Bin Xu, Yifan Li, Elastic Instability Induced Mechano-Responsive Luminescence for Super-Flexible Strain Sensing, ***IEEE Sensors* 2017**. DOI: 10.1109. ICSENS. 2017.8234210.

7. **Cong Wang**, Ben Bin Xu, Jonathan G. Terry, Stewart Smith, Anthony J. Walton, Yifan Li, Test Structures for Stepwise Deformation Sensing on Super-flexible Strain Sensors, ***IEEE ICMTS* 2017**. DOI:10.1109/ICMTS.2017.7954281.

8. **Cong Wang**, Sreepathy Sridhar, Jonathan Terry, Zhenghong Li, Haibao Lu, Ben Xu, Yifan Li, Smart surface enabled thin layer heterogeneous responsive soft material patterning, **to be submitted**.

Award and Highlight:

1. **Outstanding Student Paper Award**, 2018 IEEE International Flexible Electronics Technology Conference, Aug 7-9, 2018, Ottawa, Canada.

2. **Research Paper Highlighted** (A Flexible Topo-optical Sensing Technology with Ultra-high Contrast) by EPSRC, PHYS.ORG and IoM3.

Conferences & Seminars & Workshops:

1. *11th World Biomaterials Congress (WBC 2020), 11-16 Dec 2020, Glasgow, UK (***Accepted)**

2. *2019 Yat-sen Forum on Flexible Electronics and Biomedical Devices,* 23-24, November 2019, Guangzhou, China

3. *Droplet 2019 international conference,* 16-18 September 2019, Durham, UK (**Poster**)

4. *20th international conference on Solid-State Sensors, Actuators and Microsystems (IEEE Transducer 2019),* 23-27 June 2019, Berlin, Germany (**Poster**)

5. *5th international soft matter conference, 3-7, June, 2019, Edinburgh (***Oral Presentation)**

6. *The 25th Joint Annual Conference of CSCST-SCI*, 6 - 7 SEP 2018, University of Manchester, UK (**Poster**)

7. *2018 IEEE-IFETC Conference*, 07-09 August 2018, Ottawa, Canada (**Oral Presentation**)

8. *EE PGR Conference 2018 – Research for a Better Tomorrow,* 21 June 2018, Northumbria University, Newcastle upon Tyne (**Oral Presentation**)

9. *UKFN SIG mini-symposium: Structural surfaces and liquid/surface interactions*, 20 April 2018, Heriot-Watt University, Edinburgh (**Video Presentation**)

10. *UK Fluids Networks (UKFN) – Early Career Researcher Event,* 21 March 2018, Northumbria University, Newcastle upon Tyne (**Poster**)

11. IEEE SENSORS 2017, 30 October-01 November, Glasgow, UK (**Poster**)

12. *The 24th Joint Annual Conference of UKFN SIG and CSCST-SCI*, 23 – 24 June 2017, Newcastle upon Tyne (**Oral Presentation**)

13. *EE PGR Conference 2017 – Research Connects,* 15 June 2017, Northumbria University, Newcastle upon Tyne (**Oral Presentation**)

14. *UK Fluid Networks (UKFN) Special Interest Group (SIG) – First Meeting*, 12 April 2017, Newcastle upon Tyne

15. *30th IEEE-ICMTS Conference*, 28-30 March 2017, Grenoble, France (**Oral Presentation**)

16. *The 23rd Joint Annual Conference of CSCST and SCI,* 03 September 2016, Nottingham (**Poster**)

17. *EE PGR Conference 2016,* 20 June 2016, Northumbria University, Newcastle upon Tyne (**Poster**)

Chapter 1

Introduction

Next generation wearable devices and “point-of-care” medical technologies require future sensor and actuator devices to be soft and flexible. This has huge benefits, such as improved end-user comfort, mechanical compatibility with deformable surfaces and structures, skin and other human soft tissues. Super-flexible (e.g. compressive strain above 10%) electronics, sensors and actuators based on soft substrates, where devices are subject to various deformations have grown into one of the more interesting technologies for next generation applications [1]–[11]. Compared to rigid devices, super-flexible sensor and actuator devices are designed to be much softer and more flexible, able to sustain large strain stretching, bending, twisting and compressing [1], [7], [20], [21], [23], [24], [25]–[28], which are not easily achieved by rigid wafer based materials.

When subjected to external stimuli, soft materials can undergo surface and bulk deformations, such as wrinkling, creasing, folding and buckling caused by compressive strains [5], [17], [34], [76], [81], [82], [115], [120], [121], [132], [156], [163], [211], [216]. One of the desirable developments is to make such stimuli-responsive deformation process controllable and programmable, at least for specific configurations [12]–[16].

1.1 Research Problem

Most to-date relevant technologies are focusing on stretching, bending and twisting behaviour of soft devices [20], [21], [23], [24]. One relatively less-developed area is related to compressible device technologies, where interesting scientific phenomena and theories of elastic instabilities induced on the soft surfaces are getting more attention. It is important to notice that the phenomena of elastic instabilities (e.g. wrinkles, creases, folds and cracks) exist widely in nature, and are usually unwanted in engineering applications. Such importance has been recognized by the increasing research carried out to understand the mathematical and physical science behind these changes [17], [34], [76], [81], [82], [120], [121], [132], [156], [163], [216]. To exploit and utilize such otherwise unwanted phenomena for innovative sensing and actuation solutions remain relatively underdeveloped with many unaddressed challenges.

Therefore, this thesis researches into advanced device design, fabrication and characterisation technologies to help furthering the scientific understanding of elastic instabilities in complicated multi-soft-layer structures, and to develop the engineering solutions for controllable and re-configurable sensing and actuation systems.

1.2 Aims and Objectives

This project aims to design, fabricate and exploit new sensing and actuation mechanisms (e.g. flexible strain-gated logic sensing technology, flexible topo-

optical sensing technology and advanced 3D morphing actuation technology) from stimuli-responsive soft materials subject to large strain mechanical deformations by inducing elastic instabilities, at millimetre/micrometre scale, happening on the surface and in the bulk. The micro-structured surfaces of multi-layer elastomer system enabled by various designs (e.g. multiple finger electrodes, single line and square (multi-line) lattice microarrays) and soft lithography based micro-fabrication techniques on flexible substrates have been introduced.

Main objectives of this project include:

1. Investigate the mechanism of targeted elastic instabilities (controllable and reversible) generation on soft surfaces of multi-layer elastomer systems via test structures.
2. Develop design and micro-fabrication techniques for multi-layer sensing structures on different length-scale based on the elastic instability.
3. Develop the understanding of competing surface instability growth induced strain-gated stepwise resistance switching transducers based on micro-structured multi-layer metal-elastomer systems.
4. Research and validate the novel topo-optical sensing mechanism from instability induced Mechano-responsive Luminescence (MRL) on micro-structured multi-layer fluorophore-elastomer systems.
5. Achieve Ultra-high contrast dynamic optical pattern generation by selectively oxygen-quenching of thin phosphorescent Iridium-III

complex optical indicator layer.

6. Print and pattern soft functional hydrogel morphing structure to develop the heterogeneous layered structures of hydrogel to generate reconfigurable 3D morphing device.

The overall objective of this project is shown in **Fig. 1.1**.

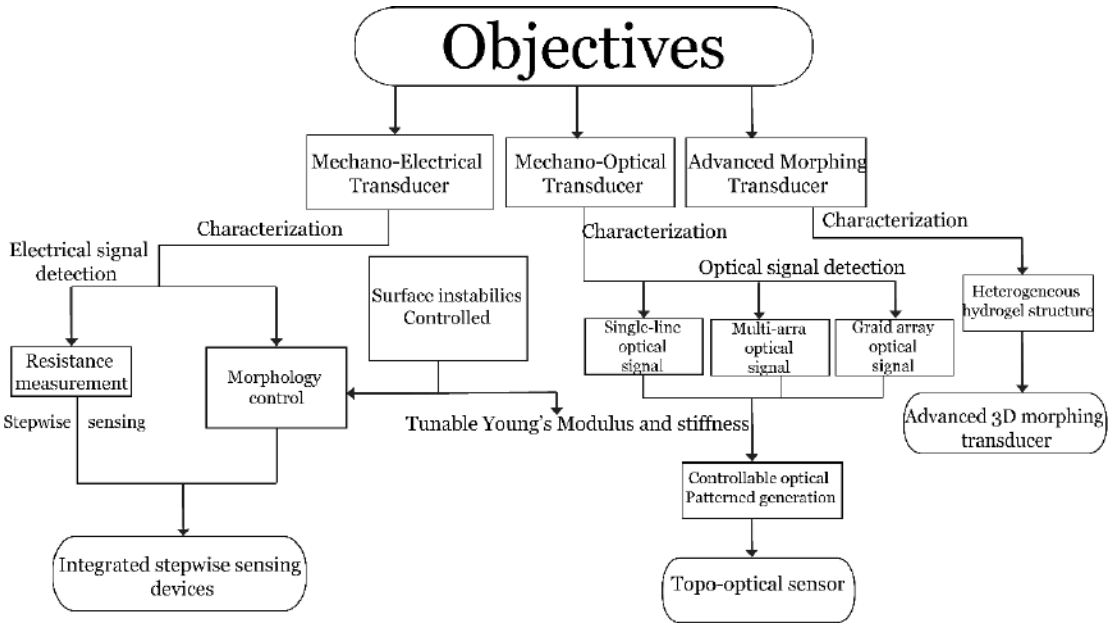

Figure 1.1 Diagram of the proposed research objectives of this project.

1.3 Outline of thesis

This thesis is divided into seven chapters. Chapter 1 is the introduction chapter, which summarizes the main objectives of this project and how the project is inspired with its contributions to novel sensing and actuation mechanism. Following the introduction, Chapter 2 is the literature review chapter that starts with the basic concepts in material science, followed by

the origins and the state of arts of the elastic instabilities phenomenon. The up-to-date flexible sensors and transducers have been discussed as well in this chapter. The experimental skills and technologies used in this work are described in Chapter 3, which briefly summarizes the in-lab techniques for the fabrication methods (e.g. photolithography, soft lithography, self-assembly monolayer (SAM), spin coating, surface casting, micro-pattern transformation, etc.) and related characterization approaches (e.g. Optical Microscopy (OM), Atom Force Microscopy (AFM), Laser Scanning Confocal Microscopy (LSCM), Scanning Electron Microscopy (SEM), etc.). Furthermore, the numerical simulation is provided as well to help understand the specific surface morphology. In Chapter 4, elastic instabilities induced flexible strain gated logic transducers are employed to help achieve a large sensing range with stepwise output signals, by controlling the surface deformation of an array of strain transducers. In Chapter 5, elastic instabilities induced flexible topo-optical transducers are achieved through developing targeted folding and employing the functional luminescence composites on the surface of elastic multi-layer systems in response to high compressive strains. Such strategy is guided by the pre-defined lattice pattern generation, instead of by rearrangement of the molecular compounds. The designed microstructure arrays are used to guide the local energy concentration, controlling the threshold strain and optical pattern morphology. In Chapter 6, a unique way of heterogeneous layered structures of soft functional materials has been established by reconfigurable swelling and de-swelling behaviour to achieve the controllable 3D morphing

transducers. A prototype of controllable 3D morphing transducers by functional different composites of hydrogel is achieved. Chapter 7 presents an overall summary of the project and suggestions for future work.

Chapter 2

Literature Review

The literature review covers the background and theories of this project. It reviews the basic concepts in material science, the theories behind large strain surface deformation induced elastic instabilities within the multi-layer systems, and bulk deformation due to swelling and de-swelling from stimuli-responsive hydrogel materials. It also includes a review of the latest developments in super-flexible electronics and transducers, where the soft substrate can sustain stretching, compressing and twisting, with the deformation strains significantly larger than the typical fracture strains of the metal, semiconductor.

Such surface and bulk deformation responding to stimuli can encourage novel sensing and actuation systems for super flexible transducers which will be extensively developed and discussed in the next few chapters.

2.1 Elasticity

Elasticity is the property of a material in which the material returns back to its original position (i.e. shape and size) under external stimuli such as force or load. Different with plasticity in which the material undergoes permanent deformation under force or load. When the external stimuli are applied on a body within the elastic limit, the body deforms, if it recovers back to its

original status on the removal of the load, the body is called elastic body. Elastic limit is defined as the value of stress within which the material recovers back to its initial stage. If the applied value exceeds the elastic limit, then the material will not completely return to its original form. Substances that display a high degree of elasticity are termed as "elastic." [38], [39].

2.1.1 Stress, Strain and Young's Modulus

Stress (σ) is defined as the ratio of force (F) to the cross-sectional area (A), which given by $\sigma=F/A_o$, with unit of Pa, where A_o is the original cross-sectional area. Strain is the ratio of total deformation to the initial status in which the forces are being applied, given by $\varepsilon=(L-L_o)/L_o$, where L_o means the original status of the sample. Young's Modulus (E) is defined as the ratio of tensile or compressive stress to the corresponding strain within the elastic limit. Young's Modulus is also known as modulus of elastic, with the formula given by $E = \sigma/\varepsilon$, where σ is the tensile or compressive stress and ε is the tensile or compressive strain. The values of Young's Modulus determine the stiffness of materials. The large Young's Modulus indicates that the material deforms less when it is compressed or stretched [38], [39].

2.1.2 Elastic materials

Different with rigid materials such as marble, rock, which do not deform easily due to their tightly bonded molecules that are hard to move past each other. Elastic materials are materials with high elasticity made of long molecules, which able to be bended or stretched several times than their

initial lengths and return back to original shapes and dimensions when releasing the force. In their relaxed states, the structures of elastic materials are disorganised and loosely cross-linked. When applying the force, the structures become distorted and the chains align with each other, allowing the materials to stretch. When releasing the force, the cross-links between chains pull the materials back to their original shapes [38], [39].

The causes of elasticity vary depending on the types of materials. Polymers, including rubber, may display elasticity because that polymer chains are stretched and then subsequently return to their initial status when removing the load. Metals such as copper may exhibit elasticity as atomic lattices change size and shape, once the stimuli are removed, they can return to their original forms [38], [39].

2.1.3 Elastic materials for soft substrate in engineering field

There are many intrinsic elastic materials such as elastomers [56], [57], [58], liquid metals [59], [60], [61], conductive polymers [62], [63], [64], 1D and 2D materials [65], [66], [67], which can achieve the flexibility and stretchability (the capacity for being stretched) corresponding to the external stimuli (e.g. stretching, bending, twisting or compressing),

Elastic materials – Polydimethylsiloxane (PDMS), Ecoflex, hydrogel, Polyethyleneoxide (PEO), and their composites, have been widely used as soft substrates [73], [74]. Among them, PDMS is an optically transparent nontoxic soft silicon elastomer which is the most widely used material in the

microsystem research areas such as microfluidics [32], stretchable electronics [6], [33], [35], tunable lenses and mirrors [36], [37], interferometric sensors [40]. A key feature of PDMS (e.g. Sylgard™ 184) is that the stiffness can be controlled from very soft (e.g. a Young's modulus of 48KPa) to much stiffer (e.g. a Young's modulus of 4MPa) by changing the mixing ratio of PDMS base and curing agent. The softness can help to avoid the problems caused by hard materials such as the formation of sharp shards on breakage that cannot be fabricated in rigid materials (e.g. silicon and glass). Such elastic materials based soft devices have started to make significant impact on emerging applications such as epidermal electronics [1], flexible circuits [20], artificial skins [26], bio-medical electronics [3], [25], [29], presser sensors [30] and soft robotics [31].

(a)

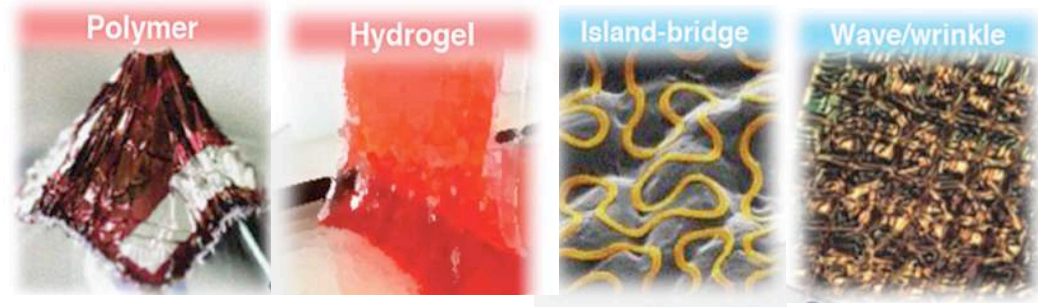

(b)

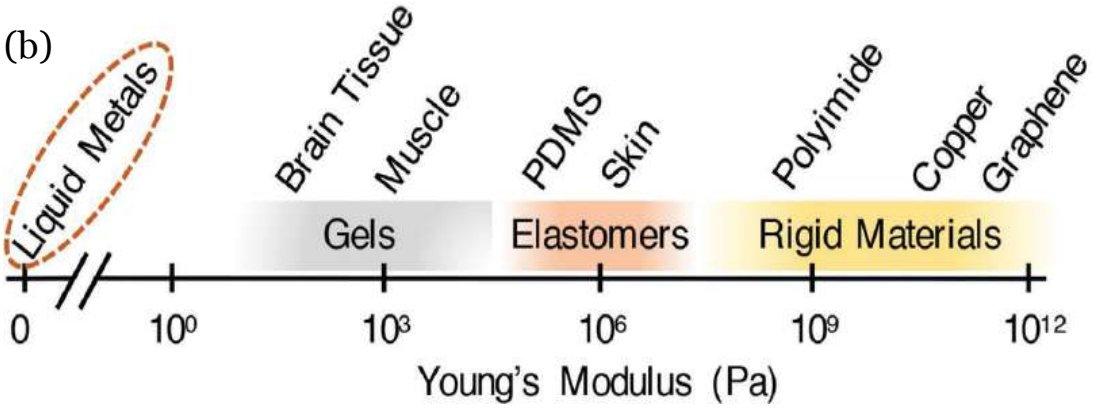

Figure 2.1 (a) Advanced materials including polymers, hydrogels and structural designs commonly used in flexible electronics include waves/wrinkles, islands-bridge [9] (b) Young's Modulus range for different materials [9].

Fig. 2.1 gives the summarization of the state-of-the-art advances in both materials and structures levels which covers a wide range of the flexible electronics topics, with the comparison of Young's Modulus among different materials [9].

2.2 Elastic instabilities

Elastic instabilities have been discovered a long time ago and are commonly observed within nature and our daily life [83]–[85]. Soft materials including polymeric gels, elastomers and biological tissues can easily go through large deformation and generate various morphological stabilities due to their intrinsic features of low elastic moduli and high sensitivity to external stimuli. Because of the capabilities of large and reversible deformations for soft and elastic materials, various types of instabilities can be generated such as wrinkling, creasing, buckling, period-doubling, folding [86]-[91], [162], depending on the elastic and geometric properties of the materials and the loading conditions. There are various ways to induce the instabilities onto the soft materials, such as the thermal variation [111], [112], PH value [95], [113], competing growth and swelling of the films [81], [114]–[117], electrical stimulation [118]–[119], pre-stretched substrates relaxation [33], [120]–[122] and mechanical compression [86], [123], [162].

From the engineering point of view, such elastic instabilities are recognized as undesirable and may pose a limit due to the crack and fracture caused to the constructions, and are often considered to be a nuisance that should be avoided [92]–[95]. However, with the development in engineering field, the controlling and harnessing such morphological elastic instabilities to specific usages have become popular to a number of academic disciplines, which can be potentially used to a broad range of engineering systems as shown in **Fig 2.2**. For example, some significant applications such as biological systems [81], [96], [97], [98], flexible electronics [6], [24], [33], [35], [99], [100], [101], material behaviour measurement [6], [86], [102], [103], [104], sensors and actuators [105], wettability [106], [107], [108] and optical characterization [80], [109], [110].

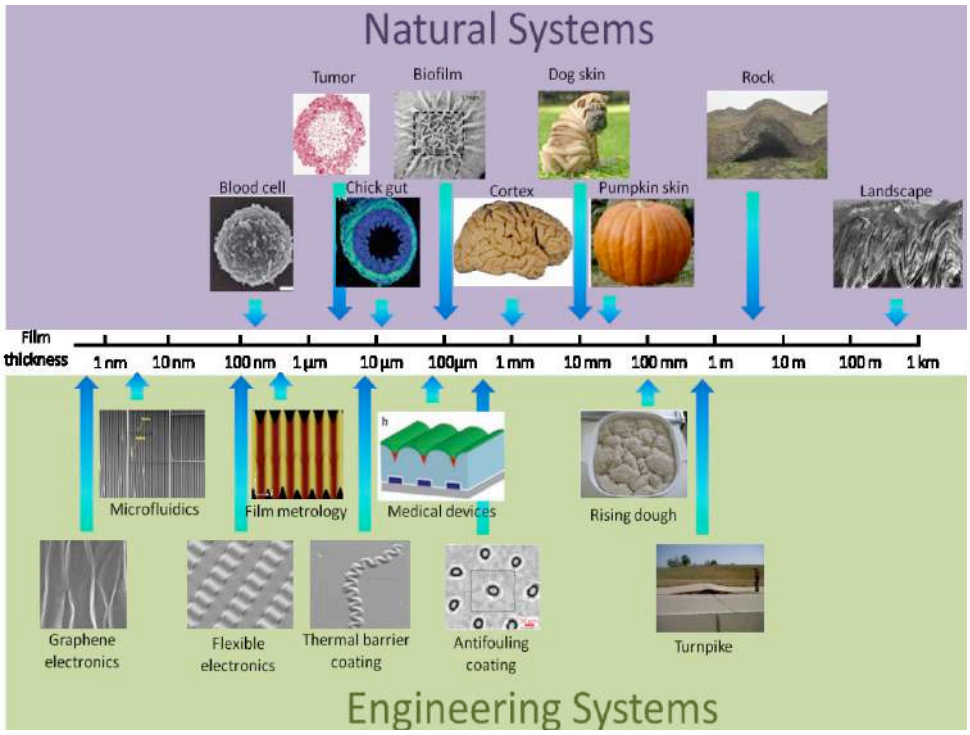

Figure 2.2 The multiscale overview of surface instabilities in natural and engineering systems [251], [252], [253], [254].

This thesis studies the elastic instabilities of wrinkles, creases and folds by mechanical compression of pre-stretched multi-layer elastomer systems (e.g. a bi-layer or a tri-layer system). The following sections introduce the different types of instabilities.

2.2.1 Wrinkle in bilayer systems

When a bilayer system with a stiff thin film on a thick soft substrate is compressed over a critical strain, elastic instabilities of wrinkles are formed [51]. The critical strain of wrinkle indicates the change from initially flat status into unstable deformation [175] for the energy comparison between plane surface and wrinkled status. **Fig. 2.3** shows the schematic view of wrinkle instability formed on a bilayer system. Wrinkles form periodically in a finite space. When under the uniaxial compression, the parallel wrinkles can be generated which perpendicular to the compressive direction [261]. While under the biaxial compression, much more intricate modes of wrinkles can be formed such as herringbone, checkerboard and hexagonal [112], [124], [262], [263].

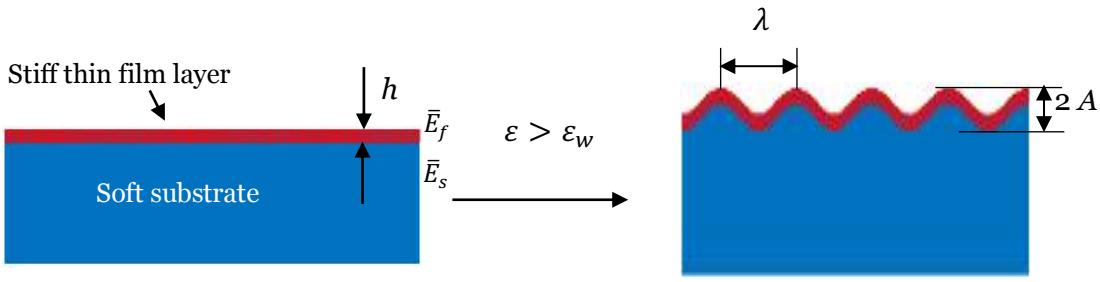

Figure 2.3 The schematic view of wrinkle instability formed on a bilayer system. The stiff film layer (thickness h) attached to a soft substrate over critical compression, with generated wrinkle wavelength of λ and amplitude of A.

The onset of wrinkles can be predicted via the classical linear perturbation analysis [88], [125]–[128], as wrinkles have infinitesimal strain deviating from the smooth state and the cross-sections of wrinkles form smooth undulation. The linear perturbation analysis formulates an incremental boundary value problem with the flat state as a reference, and the onset of wrinkle corresponds to the existence of a non-trivial solution to the incremental boundary value problem, which is an eigenvalue problem [88], [125]–[128]. The wrinkle wavelength is given by $\lambda = 2\pi h\left(\bar{E}_f/3\bar{E}_s\right)^{1/3}$, to balance the energy mismatch between the bending energy of the film and the stretching energy of the substrate, where $\bar{E} = E/(1-v^2)$ is the plane strain modulus [95], with E and v as the young's modulus and poisson's ratio, respectively. The onset critical strain of wrinkle is given via $\varepsilon_w = 0.25\left(3\bar{E}_s/\bar{E}_f\right)^{2/3}$. Although surface wrinkles generate on soft elastic materials with a rigid skin, without such rigid skin layer, soft elastic materials are stable, at small strain to form homogeneous deformations while when applied a large compression strain, the surface is predicted to form a new instability [126] such as crease.

2.2.2 Crease in bilayer systems

Creasing instability is a localized and surface self-contacting phenomenon with a sharp tip, which has been commonly seen in everyday contexts such as baby's arm [130], a bending Liang fen (a starch gel) [255] or on the surface of bread dough rising in a bowl [22] as shown in **Fig. 2.4**. Such creasing instability can be observed on the surface of soft elastomers, hydrogels or gels

under mechanical compression and it plays a crucial role in many natural and engineering systems [5], [75], [79], [81], [163].

Figure 2.4 Creases patterns on (a) baby's arm [130] (b) a bending Liang fen [255] and (c) rising bread dough [22].

Biot [125]–[127] firstly theoretically predicted that the homogenous Neo-Hookean half space would become unstable to the formation of sinusoidal waves under a critical compressive strain of 0.46. For many soft materials, the mechanical behaviour can be captured by linear elastic constitutive models only in a small strain range (<10%), while in the large deformation range, such linear elastic constitutive models cannot fully capture the mechanical behaviour. For the large deformation range, the hyper-elastic constitutive models (e.g. Neo-Hookean material model) can be used for predicting the nonlinear stress-strain behaviours of soft materials. Hyper-elastic material is the special class of material that tends to respond elastically when under large strains. It shows both a nonlinear material behavior as well as large shape changes. The Neo-Hookean material model has been widely used to study the instability behaviours of hyper-elastic materials [17]–[19] similar to PDMS.

While, Biot's prediction was challenged by Gent and Cho [255], where the critical strain for the formation of crease was experimentally found to at the compression strain of 0.35 ± 0.07 in plane surface [255]. Later, Hohlfeld and Mahadevan [130] had numerically simulated and proven that a critical strain for creasing at 0.354, which highly agreed with the experimental observation by Gent and Cho [255].

When a stress-free thin film attached on a pre-stretched substrate under mechanical in-plane compression, at small compressive strain, wrinkles preceded by creases [129]–[130] which form via a linear perturbation. Beyond the critical compression strain, the free surface forms sharp self-contacting characteristic that refers to creases. **Fig. 2.5a** shows the schematic view of creasing instability generated on elastic plain surface under mechanical in-plane compression. The creasing instability is a kind of bifurcation that distinct from wrinkles, formed by nucleation and growth. The compression strain is given by $\varepsilon = 1-(L_o/L)$, Where L_o and L represent original length and released length [81], [117], [120], [121], [131]–[135]. **Fig. 2.5b** shows the experimental observation of creases at strain of 0.51 [120].

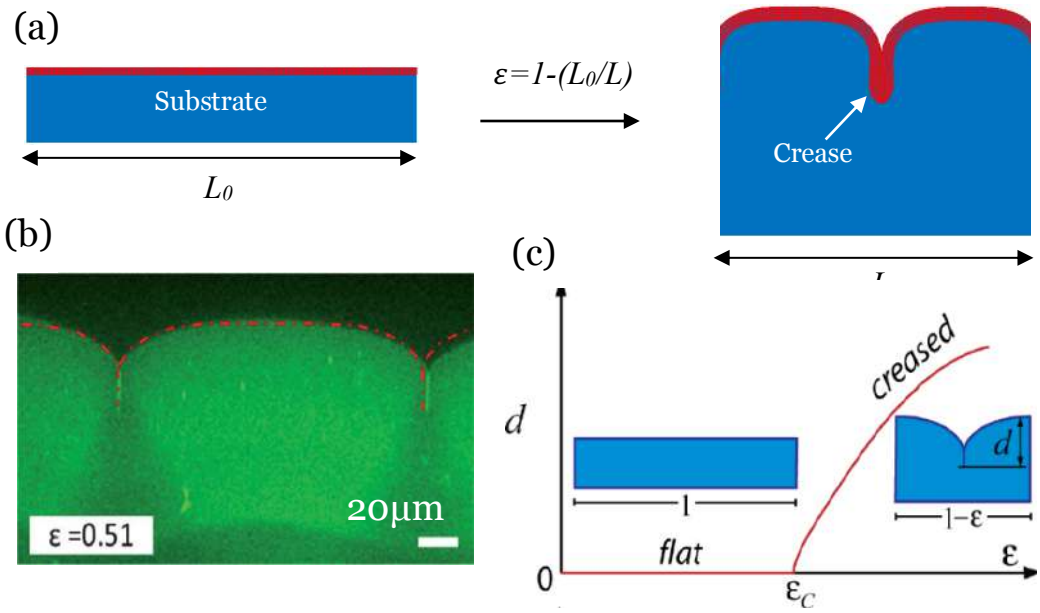

Figure 2.5 (a) The schematic view of creases instability generated on elastic plain surface under mechanical in-plane compression from L_o to L (b) experiment observed as a cross-sectional view of formed creases [120] (c) bifurcation diagram for supercritical crease [216].

Creases might look similar with cracks due to their singular features. While the difference is significant, the fatigue and catastrophic failure will be induced when cycling open and close of cracks. However, because of the elastic property of creases, which makes it promising to cycle and repeat between flat and creased status without being damage. In order to well-defined and control the surface creasing, Ryan C. Hayward and co-workers [216] established a robust way of controlling the hysteretic property of surface creasing by compressing a pre-strain soft bilayer structure, which shading a light in using of such type of instability.

Fig. 2.5c shows a supercritical bifurcation diagram [216] with the applied strain ε and the depth of crease d. At the flat status, the horizontal axis d = 0

while at the creased states with d > 0. When applied strain over a critical value of ε_C, crease was generated. The depth of crease increases gradually as ε increases. When decreased ε, the creases disappeared at the same critical strain ε_C [216]. Based on the ability to form and disappear of creases, the crease-inducing stimuli have been popular in temperature [81], electric fields [118], light [82] and control of chemical patterns [82].

2.2.3 Difference between wrinkle and crease

Wrinkles behave the sinusoidal as the corrugation while creases form the self-contact with a sharp tip. **Fig. 2.6** shows the schematic illustrations of wrinkles and creases. In the simplest context, both of the wrinkles and creases represent a bifurcation from a homogenous compression state. Wrinkles bifurcate by a field of strain infinitesimal in amplitude but finite in space, wherein the surface of the material undulates sinusoidally but remains locally smooth. While creases are localized folds that bifurcate by a field of strain finite in amplitude but infinitesimal in space. The wrinkle state is extremely unstable, it is highly defect sensitive and once formed is dynamically unstable to formation of a crease [120]-[122].

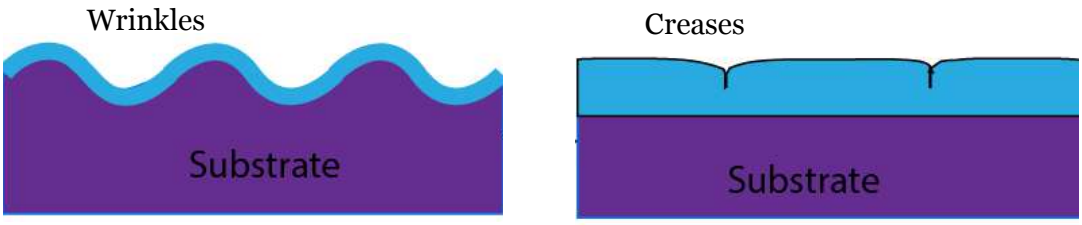

Figure 2.6 The schematic illustration of wrinkles and creases.

2.2.4 Fold in bilayer systems

For the bilayer system with a stiff thin film setting on top of the soft thick substrate, the instability of wrinkles can be formed when compressed to a critical value. If keep on increasing the compression force, the secondary bifurcation will be induced. The secondary bifurcation varies depending on the details of the substrate. The fold can be formed when the amplitude of wrinkle grows large with a high amplitude aspect ratio for self-contact, period multiplication of the wrinkle to set the fold periodicity, and gradually generate fold localization [87], [150], [151], [152], [162]. Here, high amplitude aspect ratio means the amplitude of the wrinkle is much larger compared to its wavelength.

The localized folds can be controlled by the patterns of the substrate and are also observed at different substrates. **Fig. 2.7** shows the progression of the folds with increase of strains from top to bottom for a viscous fluid or an elastic foam [150]. The instability of wrinkle will keep the surface locally smooth while the creases and folds will generate the surface to be self-contact [87], [150], [162].

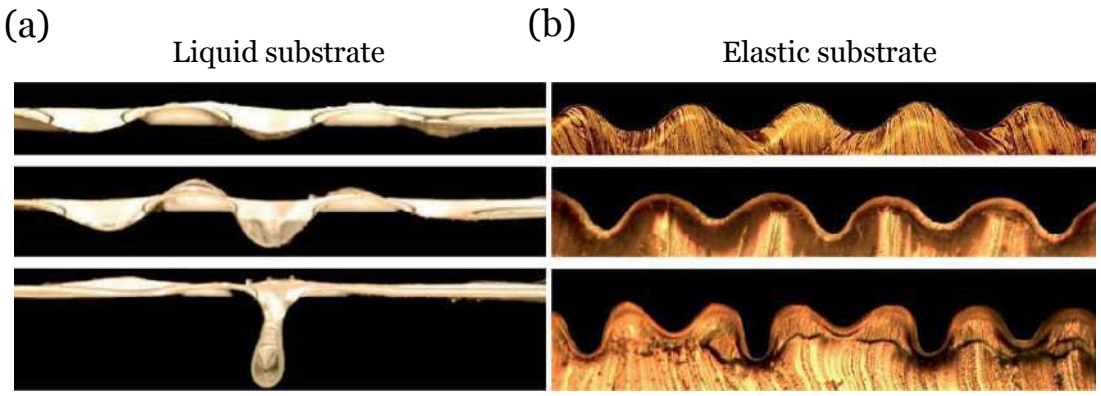

Figure 2.7 Fold instability (a) Progression of the folds with increase of strains from top to bottom when the substrate is a viscous liquid [150] (b) Progression of the folds with increase of strains from top to bottom when the substrate is an elastic solid [150].

2.2.5 Modulus mismatch in multi-layer systems

The surface instabilities growth of bilayer system has been well studied [76], [115], [120], [121], [156], [216]. While in nature and biological fields, many tissues and structures are usually consisted of multilayers with modulus difference among each layer. During deformation or development [153], [154], [155], various layers of structures may undergo different expanding or shrinking ratios, which lead to mismatch strains within different layers. Once apply the mechanical stimuli (e.g. compression) over a critical value to a system, the initially flat surface deforms and bifurcates into different types of instabilities such as wrinkles, creases, folds etc. [128], [159]. Researchers have found that through applying the compressive strain, either creases or wrinkles enable to form firstly due to the ratio of moduli and thickness of an elastic bi-layer system.

As a wrinkled bilayer system, when undergo the further compression, secondary bifurcations generate. Hutchinson et al. [88] found that at a low modulus contrast condition, wrinkles enable to transit into creases. However, for their simulations, there are no further studies beyond the point. Later a numerical simulation studied by Tallinen and co-workers [157] about how the effect of stiffness mismatch between two layers affect the transition status from wrinkles to creases or folds upon the growth of the film relative to the substrate. Further studied by Kim and co-workers [90], [158] via computational simulation regarding with the surface instabilities evolution within the bilayer systems at low modulus ratio conduction. In their study, a phase diagram of three different post-wrinkling bifurcations was made, where wrinkles transited to creases directly, wrinkles formed period doubling before transiting to creases, wrinkles generated period doubling, period quadrupling and then folding. While it only studied by computational simulation without any experimental proof.

Moreover, Wang, et al. [128], [159] have shown the existence of three different post-wrinkle bifurcation modes by both experimentally and numerically, to predict the formation and evolution of different kinds of surface instabilities. In their study shown in **Fig. 2.8**, the incompressible neo-Hookean materials with shear modulus of μ_f and μ_s have been used as film and substrate. The mismatch stain between film and substrate is given by $\varepsilon_M = (L_f - L_s)/L_f$, where L_f and L_s are the original lengths of film and substrate. In **Fig. 2.8b**, as the ε_M is sufficiently low, the flat film-substrate system has much lower potential

energy when compared with any instability. When the ε_M enhance to critical loadings, the flat surface will bifurcate into various instabilities depending on the different modulus ratios [159].

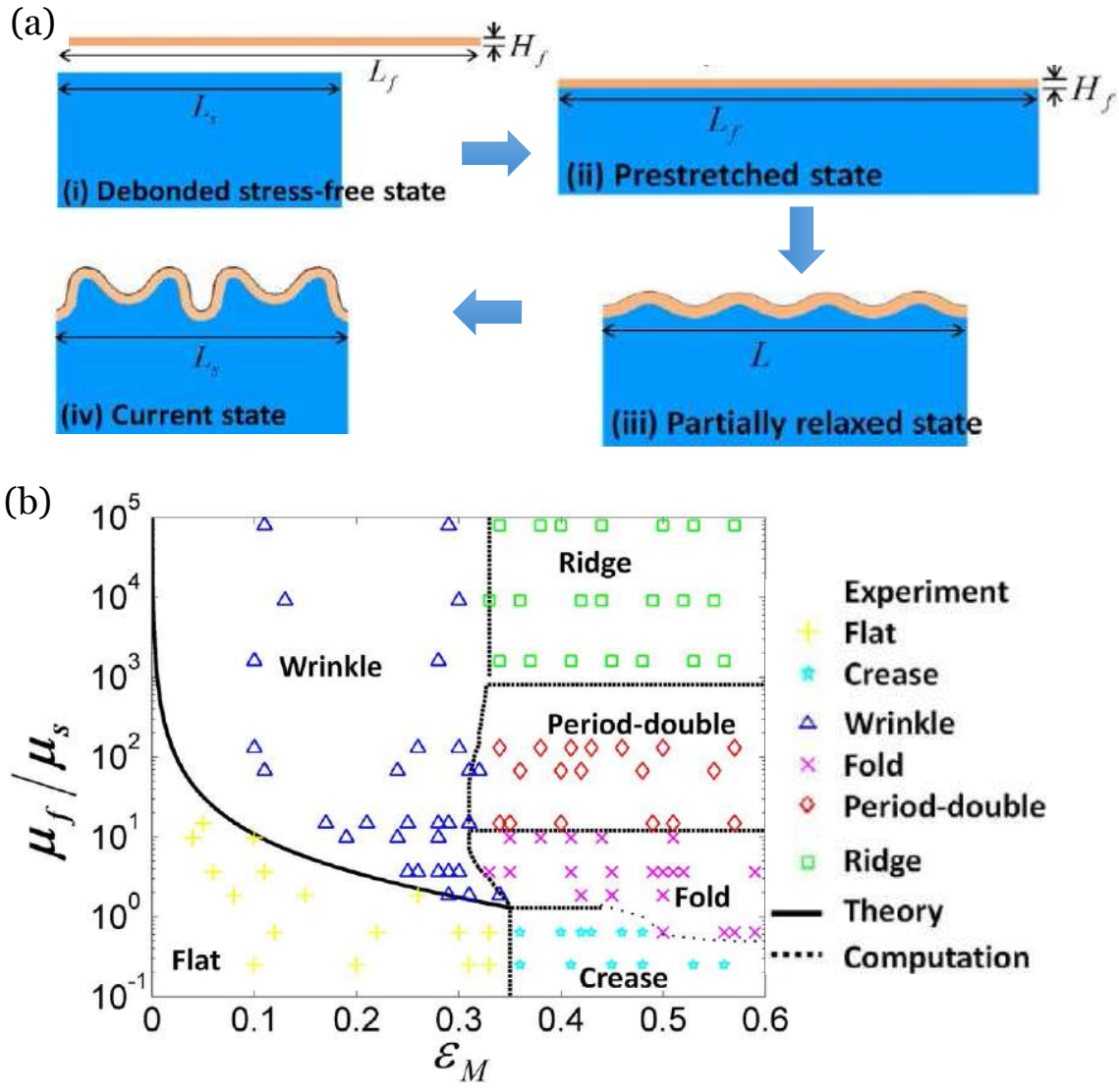

Figure 2.8 (a) The schematic view of inducing the mismatch strain in the film-substrate structure: (i) The film and substrate is first assumed to be detached from each other to form a stress-free state (ii) the detached stress-free substrate is then pre-stretched by a ratio of L_f/L_s and adhered to the film (iii) relaxed to length L, and (iv) eventually relaxed to length L_s at the current state (b) Phase diagram for instability patterns in film-substrate systems [159].

2.2.6 Micro-structured surface for instability engineering

Patterned surfaces that are responsive to mechanical stimuli can be used for designing functional materials with various properties and for controlling the patterns generation [5], [75], [170]. Xu and co-workers [5] demonstrated a patterned single-pair of Au "finger" electrodes as shown in **Fig. 2.9**, with a thin hard Au layer setting on top of PDMS film. Such device relying on the controllable formation of surface creases to bring initially disconnected regions of the metal electrodes into self-contact. By applying compression strain, the Au layer (Young's Modulus 70 GPa) forms wrinkles at lower strain due to its incompressible to help it absorb the deformation energy to protect the Au electrodes. The wrinkle wavelength is given by $\lambda = 2\pi h\left(\bar{E}_f/3\bar{E}_s\right)^{1/3}$ and the onset critical strain of $\varepsilon_w = 0.25\left(3\bar{E}_s/\bar{E}_f\right)^{2/3}$. As increasing the compression strain, the much softer (Young's Modulus 0.4 - 4 MPa) substrate areas can have greater deformation due to the local amplification of strain by the stiff films nearby. Surface creases form in the gap between Au electrodes, generating the desired electrode self-contact switching mode. While for their studies, how the pattern geometry affects the surface instabilities has not been understood yet.

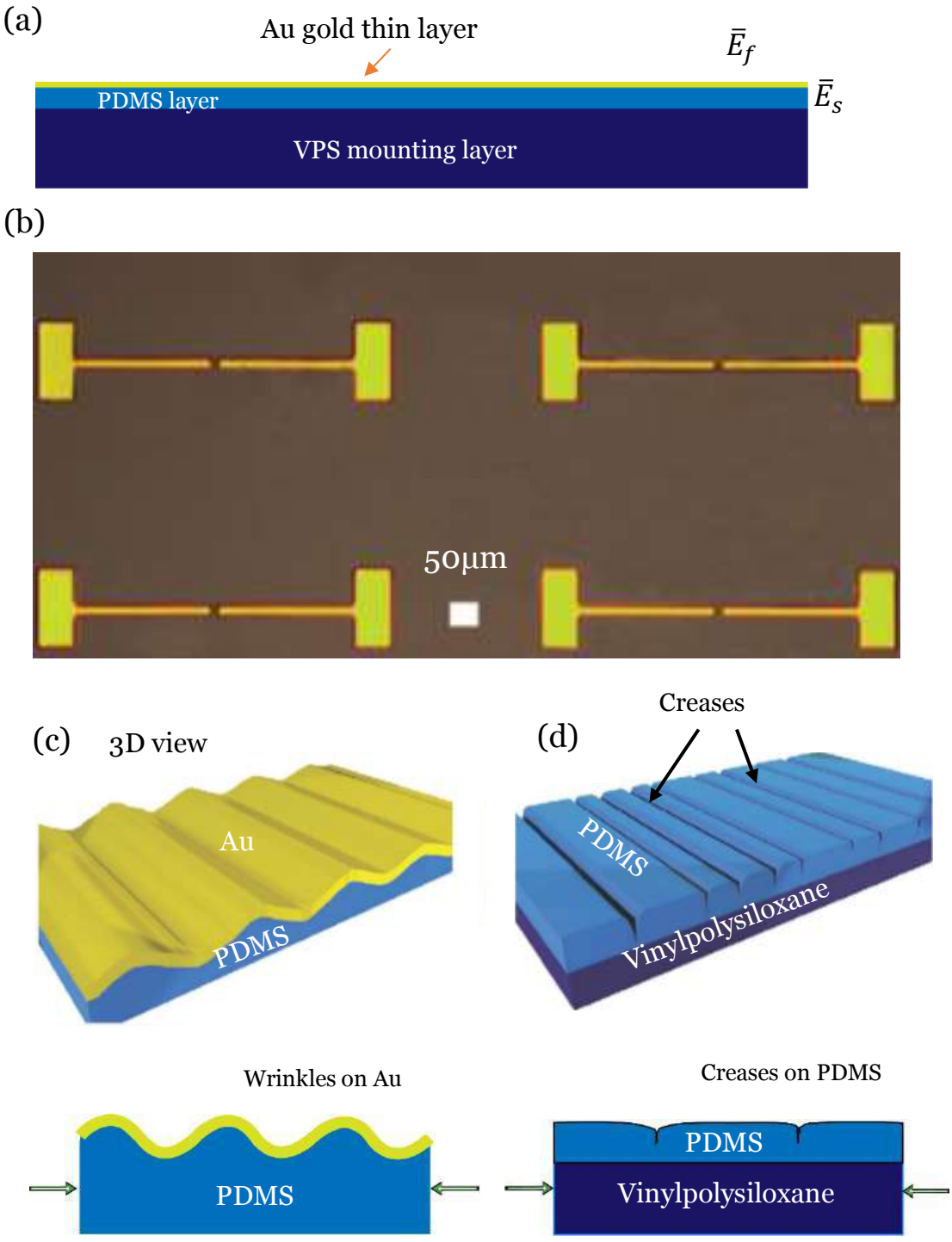

Figure 2.9 (a) Schematic views of Au gold electrode thin layer (b) Optical microscope image of a patterned single-pair of Au "finger" electrodes [5] (c) Schematic illustration of releasing the pre-stretch tri-layer elastomer system (hard Au gold electrodes thin layer-PDMS-VPS), the associated two instabilities are

sketched as the wrinkled Au thin film over the elastic substrate and (d) the generated crease pattern on soft PDMS [5].

Furthermore, to engineer the required controllable elastic instabilities, methods have relied on skin layers mismatch on PDMS substrates [5], [76], [163], [170]. Auguste and co-workers [163] studied how the post-wrinkle bifurcations within an elastic multi-layer system for surface morphologies control. In their studies, they set up a tri-layer system that consists of a mounting layer, substrate layer and film layer (can also be called skin layer), to understand how the ratio effect of an elastic modulus mismatch (e.g. film to substrate modulus ratio, from ~2 to 10) on the pattern formation. Two types of secondary bifurcations have been discovered with (1) direct transition from wrinkles to creases and (2) wrinkles firstly undergo period doubling and then transit to creases. **Fig. 2.10** shows a surface transition of wrinkles to creases. The loading and unloading of the bilayer with modulus mismatch of 5 (0.4 ± 0.05 MPa for substrate and 2.1 ± 0.5 MPa for thin film). The surface stays in the flat state until wrinkles form at a strain of 0.15. Further increasing the compression strain, the amplitude of the self-contacting crease increases, while the amplitudes of the neighbouring wrinkle continue to decrease. Upon subsequently unloading, the self-contacting depth of the crease diminishes while the amplitude of the wrinkle increases. When further releasing of compression, the bilayer system returns to a wrinkled state and then eventually to a flat state [163].

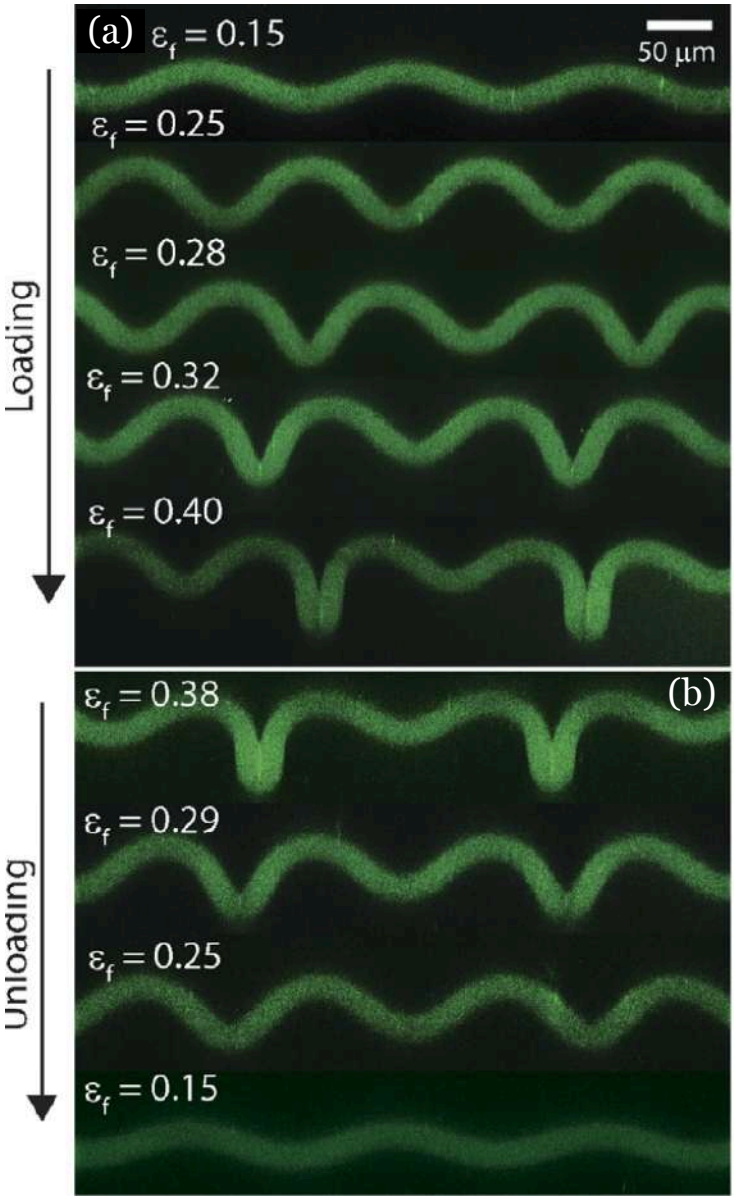

Figure 2.10 Confocal image showing (a) loading and (b) unloading of a bilayer system under compression [163].

Moreover, Ouchi et al [76] has revealed some interesting behaviours in systems with the patterned heterogeneous hard layer within a tri-layer elastomer system to control the surface deformation. They have used the SU8 in **Fig. 2.11** to characterize the instability modes of heterogeneous layers

consisting of regularly patterned hard film stripes supported on a soft substrate, to study how the hard film pattern layer affects the crease formation and how it reacts with the surface instability modes on the hard patterns.

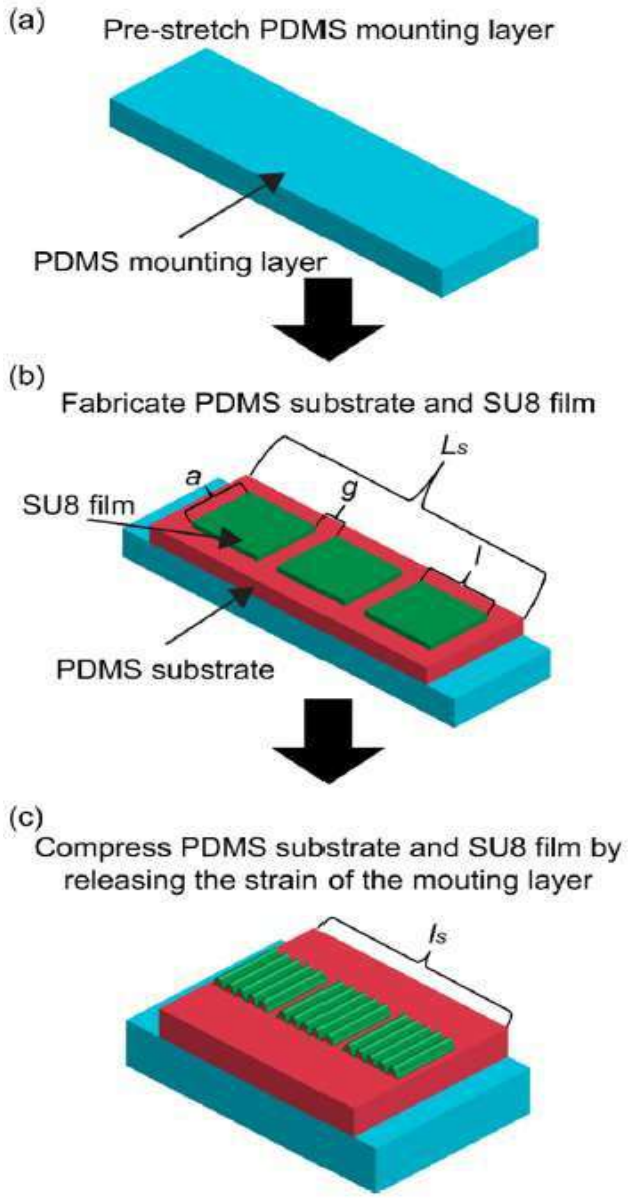

Figure 2.11 Schematic illustration of the experimental system: (a) pre-stretched the PDMS mounting layer (b) fabricated the PDMS substrate layer and the patterned SU8 hard film (c) compressed by releasing the pre-stretched mounting layer [76].

Based on the instability of wrinkle, Bae et al. [164] demonstrated some interesting applications. In their research, an anti-counterfeiting strategy was presented through encrypting microparticles with randomly generated wrinkle patterns [164]. The generated heterogeneously wrinkled patterns enable to function as unique identifiers that similar to human fingerprints. The wrinkling based topographical code could be designed on-demand through tuning wrinkling instability [164].

As shown in **Fig. 2.12**, different decoding scenarios were demonstrated with real world products (passport, ring, watch). Under normal bright field, such wrinkling based topographical codes were invisible, while readable only via Laser Scanning Confocal Microscope (LSCM) [164]. For their research, they provided an experimental platform to study the morphological instabilities of wrinkle patterning on 3D microstructures, the generated patterns were vivid, but the minutiae extraction from these reflective images still need relatively researched and the resulted wrinkling patterns are random and uncontrollable.

Figure 2.12 Demonstration of the authentication process using artificial fingerprints. Decoding using LSCM. Left: Several candidate items requiring the artificial fingerprint for anti-counterfeiting purposes. Taggants were attached on the surface of a passport, a ring, and a watch, respectively. Middle: Magnified image of the taggant region before PDMS coating. Inset represents the same region after PDMS coating for protection. Right: Extracted minutia pattern from LSCM image of the taggant on each item (scale bars: 50 μm) [164].

Latest research by Wang et al. [75] has used the centred lattice array patterned hard layer surface to guide the local strain energy concentration, in which they generated the periodic planar wrinkle 2D patterns and controllable

instability growth by pre-designing the Bravais lattice patterns on a bilayer system [75]. They have used the oxygen plasma to treat the patterned soft PDMS surface to create an additional third thin hardening layer as shown in **Fig. 2.13a**. According to them, by applying the compression to the systems with Young's modulus mismatch of $\bar{E}_f/\bar{E}_s \approx 25$, wrinkles are expected to period doubling then evolve into creases/folds [75]. **Fig. 2.13b** shows the surface modulus measurement obtained by AFM indentation [75], which indicates that when under 10s plasma treatment, the plane-strain elastic modulus mismatch between the thin film and the substrate is around $\bar{E}_f/\bar{E}_s \approx 25$ [75]. Different with the plain surface, where the instabilities of wrinkles, creases/folds occur at random locations when under compressive strain. By introducing the micrometer scale patterns on the substrate, such instabilities are guided by concentrating the local strain energy as shown in **Fig. 2.13c**, which to configure wrinkle pattern at low compression. In **Fig. 2.13d**, a formation of localized wrinkle-to-crease/fold transition was discovered.

While in their study, they mainly investigated the formation and configuration of lateral wrinkle patterns with the dependencies on the geometrical variables of in-plane confinements. The studies were mostly based on the elastic surface patterned with a different type of lattice array. The undertaken experimental observations and simulations in their research mostly focused on relatively low compressive strains (i.e. $\varepsilon < 0.35$), due to the mechanics's nature of wrinkle initiation and relative post-wrinkle development [75]. The transition from wrinkling to creasing at high

compressive strain values (i.e. $\varepsilon > 0.4$) described in their study, provided indicative data with the schematic drawings and the threshold strains captured when the fold occurs, but no systematic studies (experimental or theoretical) on the morphologies and the associated developments. The study on the controllable formation of targeted crease/fold at higher compression (i.e. $\varepsilon > 0.4$) has not studied further and the strain related fold-in depth has not been studied so far.

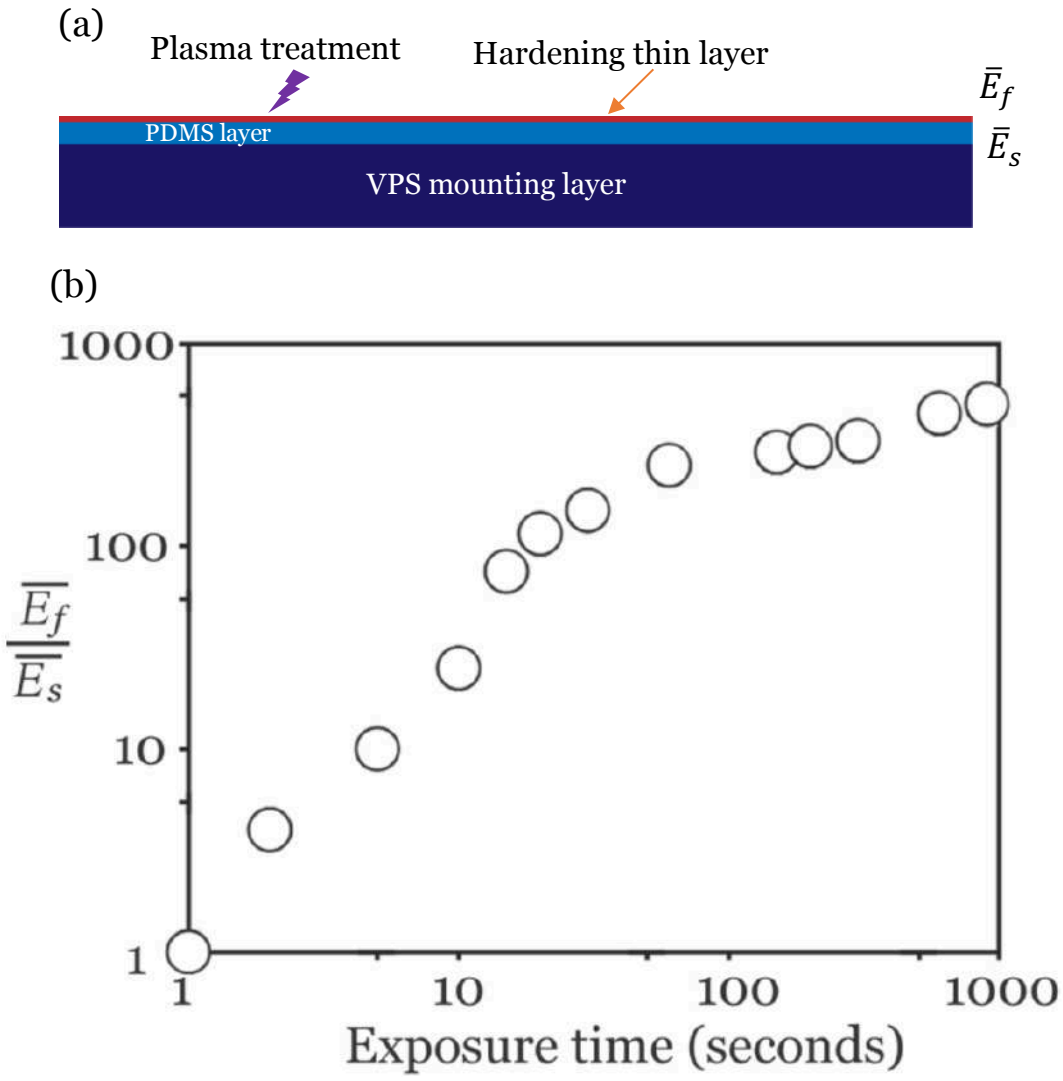

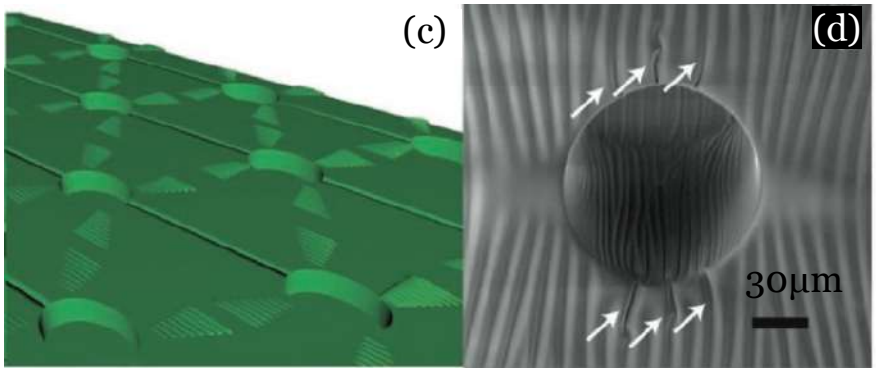

Figure 2.13 (a) Schematic views of PDMS oxygen plasma surface hardening thin layer and (b) The modulus mismatch as function of plasma treating duration [75]. (c) Schematic illustrations of the transition from wrinkling to creasing [75] with (d) SEM image reveals the transition moment from wrinkling to creasing with the captured initialization of creases [75].

2.3 Flexible transducers based on soft substrate

Conventional transducers used in sensors and actuators are typically manufactured by photolithography-based microfabrication technologies on rigid substrates (e.g. silicon and glass). Such processes have also been extensively developed to produce integrated circuit (IC) microprocessors, computer memories since the 1970s [41].

Recently there are growing interests in transducers that based on soft substrates. Unconventional microfabrication techniques have evolved accordingly. For example, the easily accessible soft lithography as shown in **Fig. 2.14**, first introduced by Whitesides et al [42], [43], are now commonly used. Such soft lithography uses an elastomeric stamp, which transfers the pattern to the substrate with flexible organic molecules and materials. It

provides access to 3D structures, forms well defined and controllable surface and tolerate plenty of materials

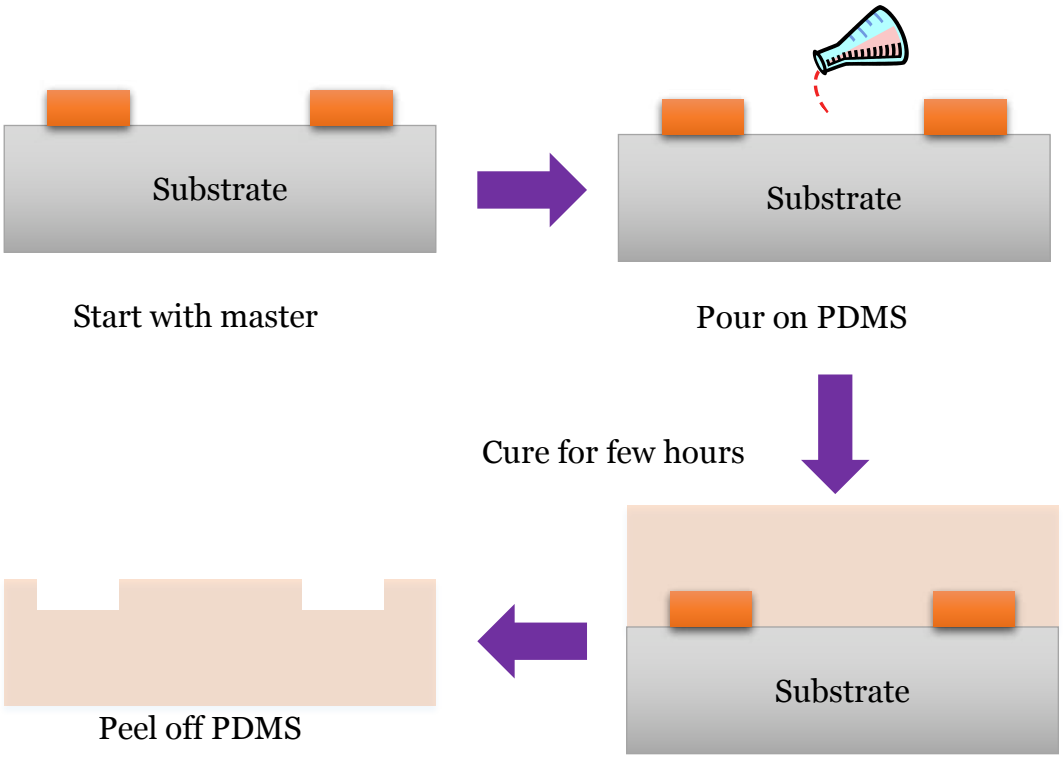

Figure 2.14 Soft lithography process, master pattern (orange colour) can be SU-8, photoresist, silicon and glass.

2.3.1 Flexible strain tolerated interconnects transducers

Wearable electronics devices that monitor various status of human skin can be important in tracking overall health. Conventional electronics are used to mount on skin through mechanical clamps, adhesive tapes, mediated via conductive gels or based from ultrathin-body silicon-on-wafer substrates. These are barely fitted for real practical applications due to their difficulty in building long-lived and robust electrical contacts with skin for reaching reliable signals without feeling uncomfortable [44], [45]. In order to produce the

comfortably wear, scientists have achieved small scaled integrated flexible electronic devices with higher mechanical deformability and structure density skin-like electronics [1], [46], [47], [48]. **Fig. 2.15** shows a flexible electronic device that can attach on human skin, for measuring the skin thermal conductivity at depths up to 6 mm, localized skin heating and cooling [4]. The rapid developing technique has been primarily potentials within applications such as medical treatment [25]–[26], biological signal sensing and biomolecule analysis [27]–[28], health monitoring [1], [3], [46], [47], [49], soft robotics and augmented reality [31], [50].

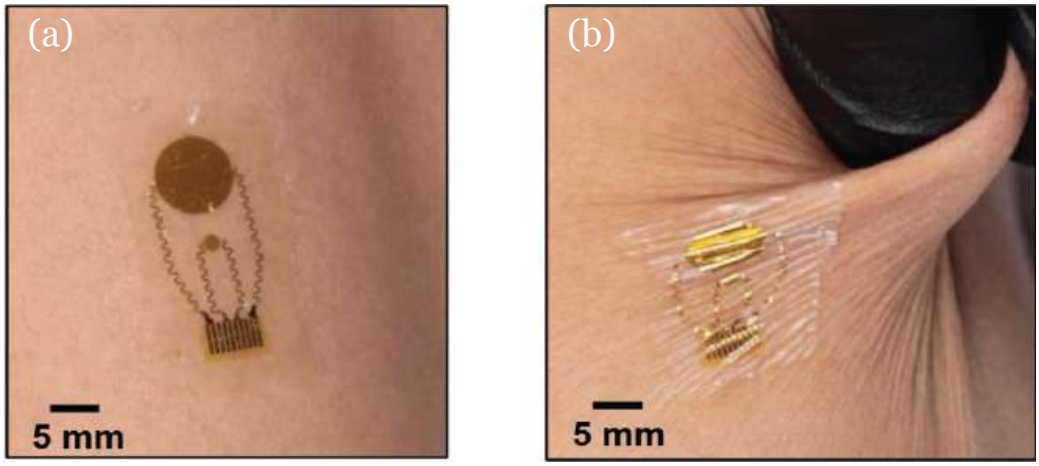

Figure 2.15 Experiment on human skin of a skin-like electronics with (a) relaxed and (b) stretched human skin demonstrating flexibility and conformity [4].

Such flexible electronics are mainly focused on bending, twisting and stretching [21], [24], [33], [52]–[55]. Among the stretchable electronics, the island–bridge [1], [70], [71], [72], [77] with highly mechanical deformable interconnects design has been widely used. By connecting the functional components at the islands via a conductive bridge under given stretching strain, the

interconnects with low effective stiffness deformed to provide the stretchability, which by enhancing the total length of the interconnects. While the rigid devices with high effective stiffness undergo paltry deformation (usually less than 1% strain), to ensure mechanical integrity of the functional materials [77].

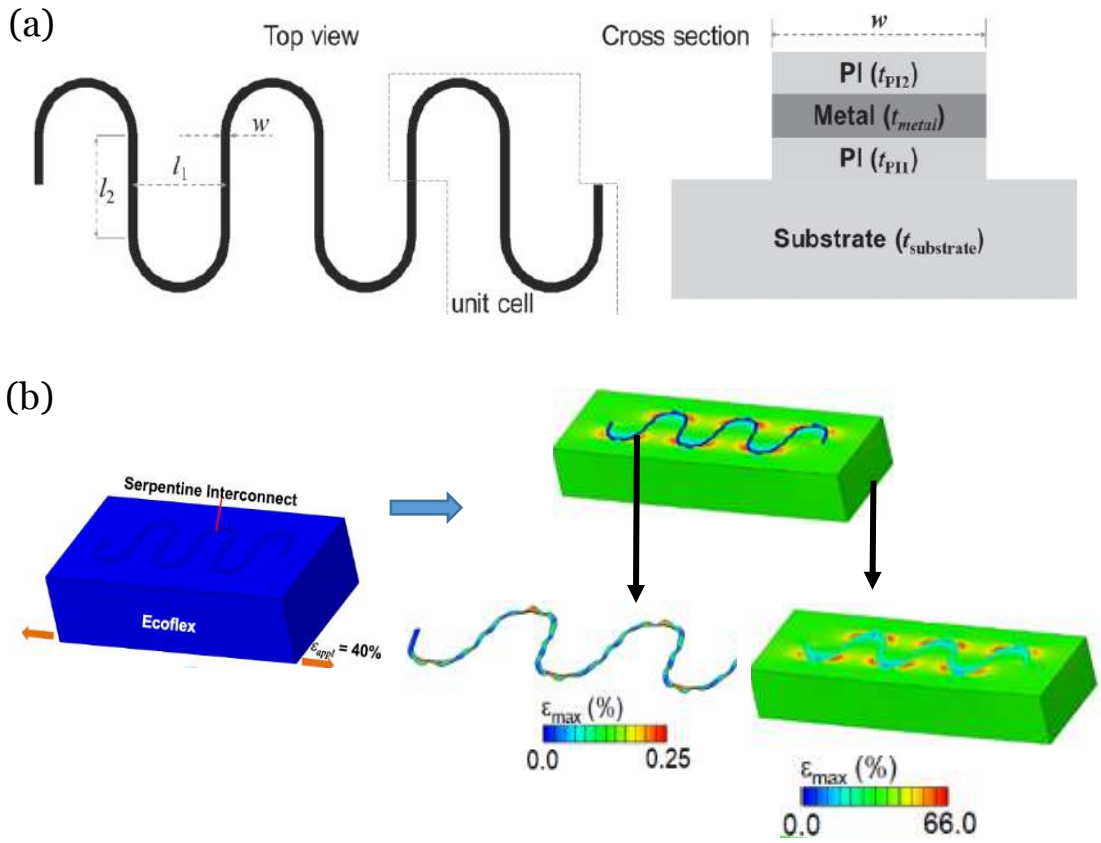

Figure 2.16 (a) Schematic illustrating of geometric parameters for a serpentine interconnect under top and cross section view [77] (b) Distribution of maximum principal strain in the entire system of the metal layer of the interconnect and the substrate, respectively, under 40% stretching [77].

Serpentine interconnections shape as shown in **Fig. 2.16a**, consisting of two half-circles connected through the arcs or straight lines, with the length l_2, spacing l_1, length/spacing ratio α ($\alpha=l_2/l_1$) and the width W [77], enable to

significantly improve the stretchability of the device with more than 100% [1], [77], [165], [167]–[169]. In **Fig. 2.16b**, when applying the stretching strain (e.g. 40%) to the interconnect/substrate system, the local strain at interconnect part is much lower (maximum 0.25%) compared with the stretching strain in the substrate (maximum 66%), which shows an effective strain isolation and high system stretchability. The reason behind is that the interconnect is mostly straight along the vertical direction and is much stiffer than the soft silicone elastomer substrate, the strain transferred to the interconnect is small. Moreover, the strain concentration effect is mainly induced near the interconnect/substrate interface to absorb the strain energy when under the external stimuli, while the strain at other regions is even [77].

Further studied by John A. Rogers and co-workers [77], the mechanical behaviour of interconnect/substrate system can be affected by key materials and geometric parameters. The study of system elastic-stretchability was carried out under two different strategies: prestrain and without prestrain as shown in **Fig. 2.17a-d**. Overall, the prestrain strategy increases the stretchability over the case without the prestrain, by a factor of 2.3 to 3.5 [77]. As shown in **Fig. 2.17a** and **Fig. 2.17b**, for curves with or without the prestrain, the elastic stretchability is less sensitive to the substrate thickness (with the case when the substrate is much thicker than the interconnect) while it is sensitive to the metal thickness, especially when t_{metal} decreases from 4 to 0.3 μm, the stretchability displays a rapid increase. This increase in the elastic stretchability is because of the different buckling modes for thin

and relatively thick metal layers [77]. For curves with or without the prestrain, the elastic stretchability increases as the Young's modulus of substrate decreases which shown in **Fig. 2.17c**. **Fig. 2.17d** indicates that the elastic stretchability is also effected by length/spacing ratio α, when α is smaller than 1, the stretchability increase with α. While when α reaches to 1, the curve seems to be saturated. The reason behind is that as the length l_2 increases from zero, the straight segment bends within the substrate surface to yield additional ability for stretching. However, as l_2/l_1 >1 (l_2 exceeds l_1), the straight segment part will become quite rigid and cannot be bent to provide additional stretchability [77]. This effect is illustrated in **Fig. 2.17e**, showing that the significant bending (in-plane rotation) of the straight segment for α is 0.5, while almost no bending for α is 2 and 3 [77].

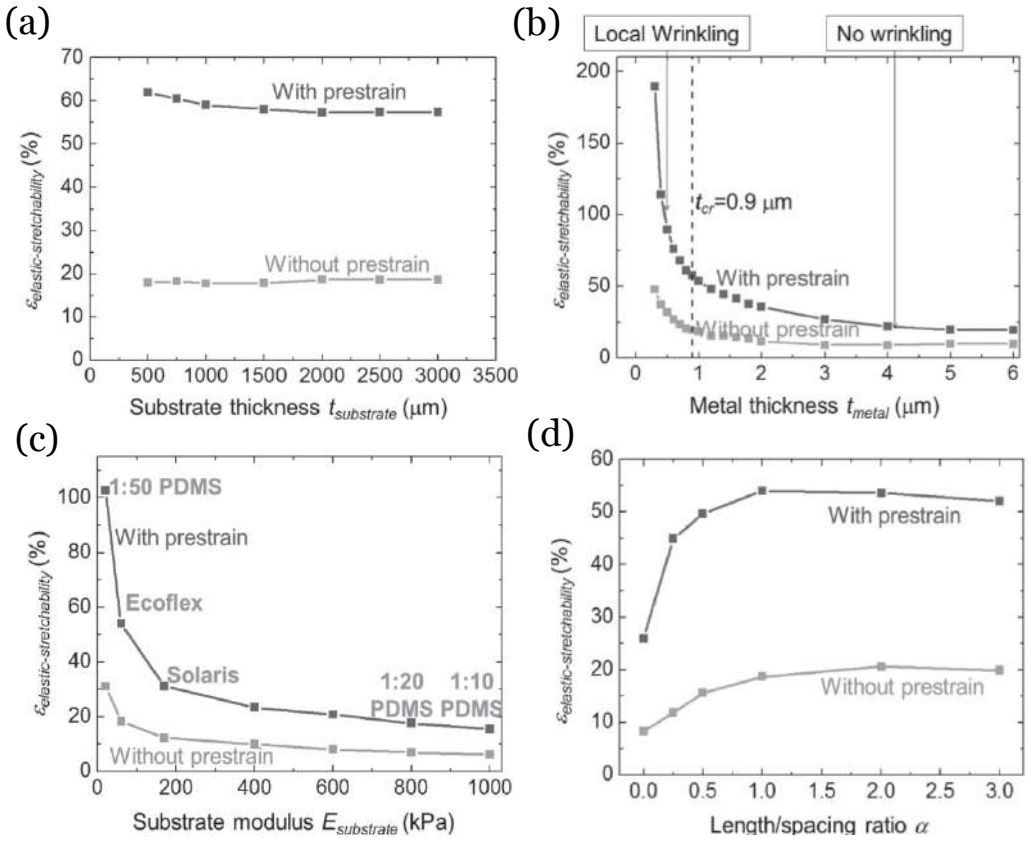

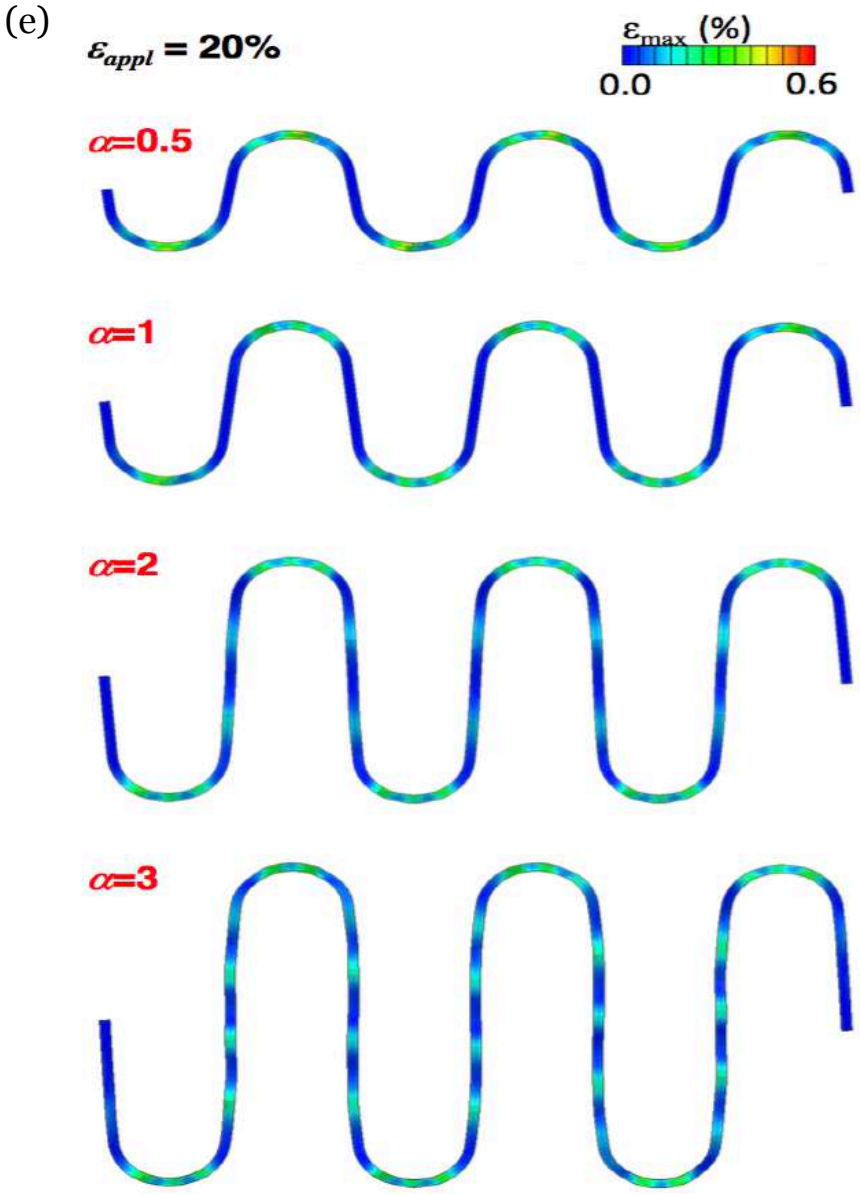

Figure 2.17 (a) Influence of geometric parameters for substrate thickness with and without prestrain [77] (b) Influence of geometric parameters for metal thickness on the elastic stretchability of serpentine interconnects with and without prestrain [77]. (c) Influence of material parameters for substrate modulus on the elastic stretchability of serpentine interconnects with and without prestrain [77] (d) Influence of geometric parameters for the length/spacing ratio with and without prestrain [77] (e) FEA results on deformations of serpentine interconnects under ε_{appl} = 20%, for four different aspect ratios. The colour represents the distribution of the maximum principal strain [77].

In general, the stretchability of the interconnect/substrate system is mainly determined by the layout of the device and the geometric parameters (e.g. width, length, thickness). The controllable deformation can be achieved at this structure level, which can be attributed to the particular designed devices within the limits of the fracture strain for the composite materials, which enable to undergo the certain levels of deformation and can be used for the development of future stretchable devices [77].

2.3.2 Flexible optical transducers

One of the latest trends in developing next generation micro-devices is the flexible optical sensors and transducers, which holds great promises in strain and pressure sensing [2], optical imaging [69], wearable devices [11], [21], [24], [223], [224], electronic skin [225]-[227], anticounterfeiting [228], biological and healthcare applications [220]-[222]. More recent work incorporating them with soft/flexible materials and structures to maximize the light and colour changing effects with greater mechanical deformation [140], [171]. By utilising soft/flexible materials, latest efforts have explored the flexible optical technology with extra controllability and on-demand colour changing such as triboelectric–photonic [229], [230], piezo-electroluminescent [231], piezo-photonics [232]-[234], mechano-responsive-luminescent (MRL) and mechanochromism (MC) [68]-[69], [171], [172], [203], [235], [256], [257].

There are several ways to achieve the optical signal and modulate the luminescent colour or intensity by altering the external stimuli (e.g.

mechanical, electrical). Wavelength-converter materials with mechanically stimulated light switching or colour changing properties such as Mechano-Responsive Luminescent (MRL), Mechanoluminescence (ML), Mechanochromism (MC), or electrically induced luminescent switching (EL), have been researched since the discovery of this phenomenon [79], [136], [137], [138], [139], [171], [182], [191], [260]. Among them, MRL, a tunable and switchable luminescence (or chromism), are used to describe a reversible change in photophysical properties such as luminescence colour, intensity, pattern or lifetime in response to mechanical stimulus, e.g. expansion, compression, bending and twisting [171], [172], [236]. Such terms of MRL have attracted considerable interests for their potentials in sensing/micro-device [69], data storage [237], flexible display [172], [238], [239], [240], etc. Examples can be found, such as using the mechanical force to change the arrangement of luminescent molecular which can lead to the optical switching response used for smart window or flexible display [171], [172], [239]. Such properties could potentially be facilitated for sensing applications integrated with optical detection systems, such as photo-diodes, fluorescence microscopes (e.g. laser scanning confocal microscope (LSCM), fluorescence lifetime imaging (FLIM)), fluorescence scanners and devices with image sensors (e.g. mobile phones, sports smart wristbands).

Fluorescence based flexible optical transducers allow for the effective detection of various analytes with a powerful visualization that can work at a very wide temperature ranges, they do not require electrical cables and are

insensitive to electromagnetic interference when compared with electrical sensors. Fluorescence based flexible optical transducers are mainly benefiting from the intrinsic advantages of fluorescence techniques such as superb sensitivity, rapidity, technical simplicity, real-time and on-site responsiveness [242], which are highly used in biological/physiological fields.

As for many fluorescent compounds (such as crystalline compounds and liquid-crystalline compounds), their photoluminescent properties are significantly influenced by the molecular arrangements, thus, the photophysical properties of such materials can be altered by rearranging of the molecular packing through external stimuli [68], [141], [142], [143], [144], [171]. Majority of the colour conversion work has been utilizing mechano-responsive molecular assembly change in phosphorescent organic and organometallic molecules in the form of liquid crystals [145], [146], [147], dye lasers [148], polymers and nanocrystals [171], [250]. **Fig. 2.18** shows the mechanism for changing the photoluminescence colour of molecular assemblies that respond to mechanical stimuli [68], [166], [171] . Mechanical stimuli of shearing in **Fig. 2.18a** induce the transformation of liquid-crystalline from the metastable cubic phase to a thermodynamically stable columnar phase. The phase transition induces a change in the pyrene moieties arrangement, which leads to interference with excimer formation. The emission spectrum in **Fig. 2.18b** shows a shift from cubic phase (λ_{max}=579 nm) to shear-induced columnar phase (λ_{max}=496 nm). As a result, the photoluminescence colour changes from yellow to blue-green [68], [166], [171], .

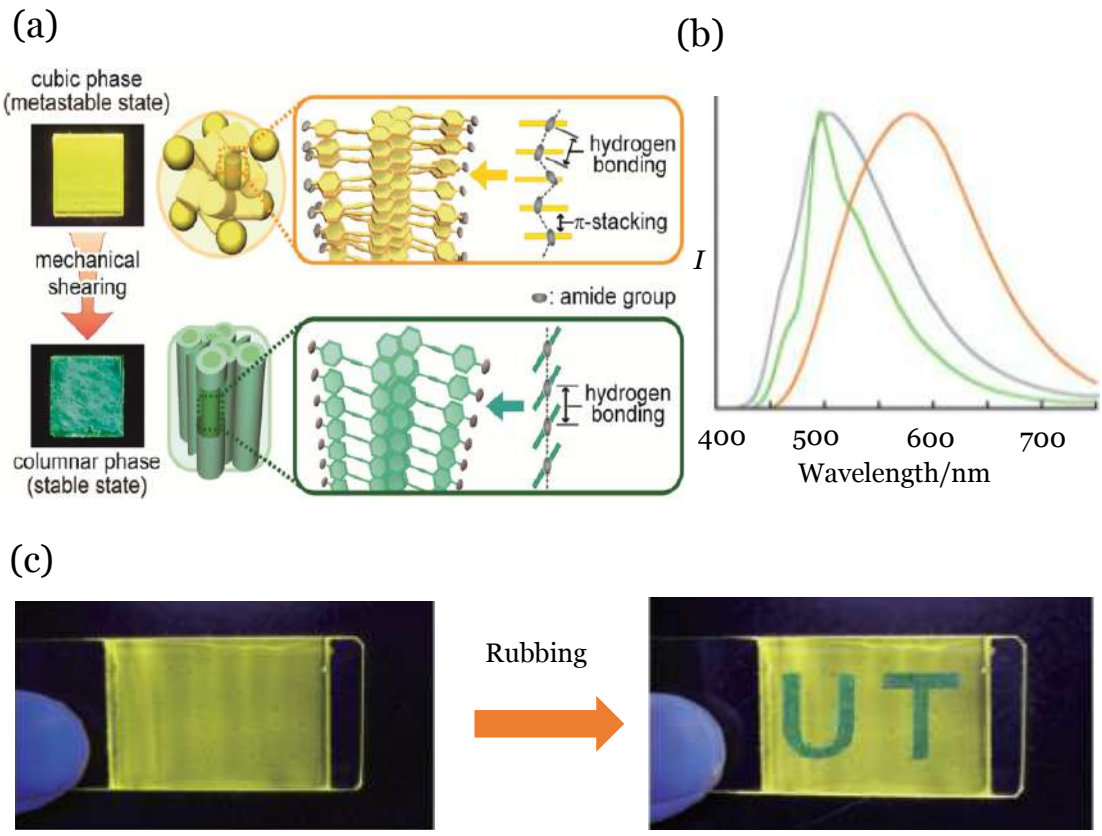

Figure 2.18 (a) Photoluminescence colour change and schematic illustration of molecular assemblies of two phases: cubic phase and shear-induced columnar phase [68], [171] (b) The emission spectra in the cubic phase (orange line), in the shear-induced columnar phase (green line), the gray line is the isotropic phase due to the temperature change [166] (c) The thin film of compound on a glass substrate was obtained by casting from hexane solution (left), and the text 'UT' (right) was formed by rubbing the substrate with a glass rod at room temperature. The yellow emitting part is in the cubic phase and the blue–green emitting part is in the shear-induced columnar phase [68].

Liquid-crystalline material can be easily coated on the surface of a variety of substances (metals, ceramics, plastics and natural macromolecules), while keeping their functional nanostructures [68]. **Fig. 2.18c** shows a thin film of the liquid-crystalline material that easily obtained by solution coating on a glass substrate, also displays a change in luminescence from yellow to blue-

green under rubbing. While alternative ways to achieve the MRL/ML colour-tuning were obtained via mixing the different coloured MRL/ML particles [69], changing the dopant concentration [161], [228] or through combination of fluorescent dyes physically with existing MRL/ML materials [172].

One particular example of MRL is shown in **Fig. 2.19**, which an anticounterfeiting strategy is demonstrated [228]. In their research, a stretchable and transparent excitation-power dependent, color-tunable luminescent PDMS film (LPF) has been presented. The LPF device was fabricated by combining of a PDMS substrate with excitation-power-dependent, color-tunable quantum dots (CdS/ZnS/ZnS:Mn^{2+}/ZnS). Both of the concentration of quantum dots and the power intensity (laser power from weak to strong) can control the photoluminescence tuning. As shown in **Fig. 2.19a**, without irradiation with a laser, the three heart-shaped patterns are almost transparent. While different colours could be observed on the surface of patterns when irradiation with a laser, and the colour changes with the increase of excitation power [228]. The properties of flexibility and stretchability are shown in **Fig. 2.19b** and **Fig. 2.19c**, where the device can be stretched over 50% and twisted 180°.

Fig. 2.19d demonstrates the potential application for anticounterfeiting. The LPF materials with different concentrations of quantum dots were pasted on a banknote and irradiated with daylight or UV flashlight (365 nm). As can be seen on the top of **Fig. 2.19d**, in daylight, the patterns on the banknote are almost transparent. When under the UV flashlight shown in the middle of

Fig. 2.19d, three different colours are observed. Furthermore, a neutral density filter (ND filter) is used to reduce the irradiation power. As shown in the bottom of **Fig. 2.19d**, when under a relatively lower energy, the colour of the pattern has a slight change [228].

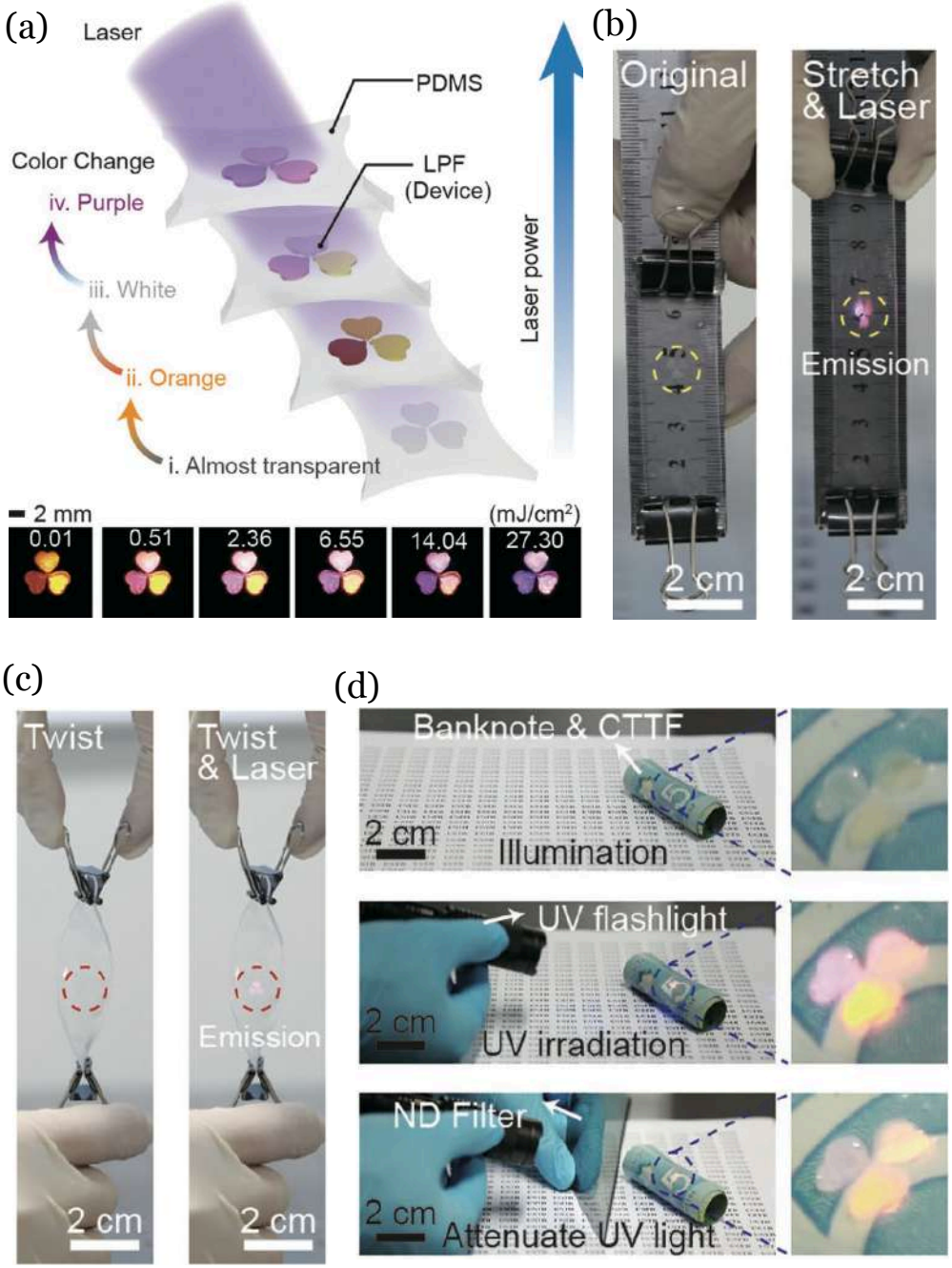

Figure 2.19 Fabrication of luminescent PDMS film grafted CdS/ZnS:Mn^{2+}/ZnS quantum dots and the mechanical and photoluminescence properties as anticounterfeiting materials (a) Schematic illustration and photographs of luminescent PDMS film (LPF) irradiated by a laser with different powers (b) Photographs showing the stretchable and (c) twisting properties of LPF (d) Photographs of LPF material in daylight and under a UV flashlight (365 nm). The LPF material is almost transparent in daylight. The power of UV light was attenuated by an ND filter and the as-observed colour of LPF is changed depending on the different excitation intensities, to provide the anticounterfeiting effect [228].

Furthermore, elastomeric based smart composite materials responding to mechanical stretching can be employed as well, to create tuneable and switchable optical transmittance, angle-independent structural colour, as well as MRL/ML and MC patterns [235], [238], [239], [240]. For example, a series of mechanically induced wrinkles are presented by ShuYang et al [238]-[240], which hold promise for applications of smart window and dynamic display. Angle-independent structural color and reversible transparency can be switched by dynamically and precisely controlling the applied prestrain. For instance, ShuYang et al [239] developed a composite film, the film contains a thin layer of quasi-amorphous array of silica nanoparticles (NPs), which embedded in bulk elastomeric PDMS as shown in **Fig. 2.20**. The structure was highly transparent (>90%, in visible light range) in the initial state (0% strain). When under mechanical stretching, the transmittance was dramatically decreased to 30%. As displayed in **Fig. 2.20a**, by stretching the silica NP/PDMS film device, the transparent property switching from transparency to opacity. The strain-transmittance diagram in **Fig. 2.20b** shows that when the void formation at 20%-80%, the transmittance

decreased significantly, suggesting that the transparency change is mainly based on the void formation. Meanwhile, the size of the silica NPs affects the transparency as well but the overall trends are the similar. Therefore, the void formation has been proposed where the changes in the optical properties could be attributed to the microstructural change. The hidden letters in **Fig. 2.20c-d** can be visualized under large strain stretching due to the change in transmittance, which has seen significant progress in optical applications, such as smart windows with tuneable transparency [239].

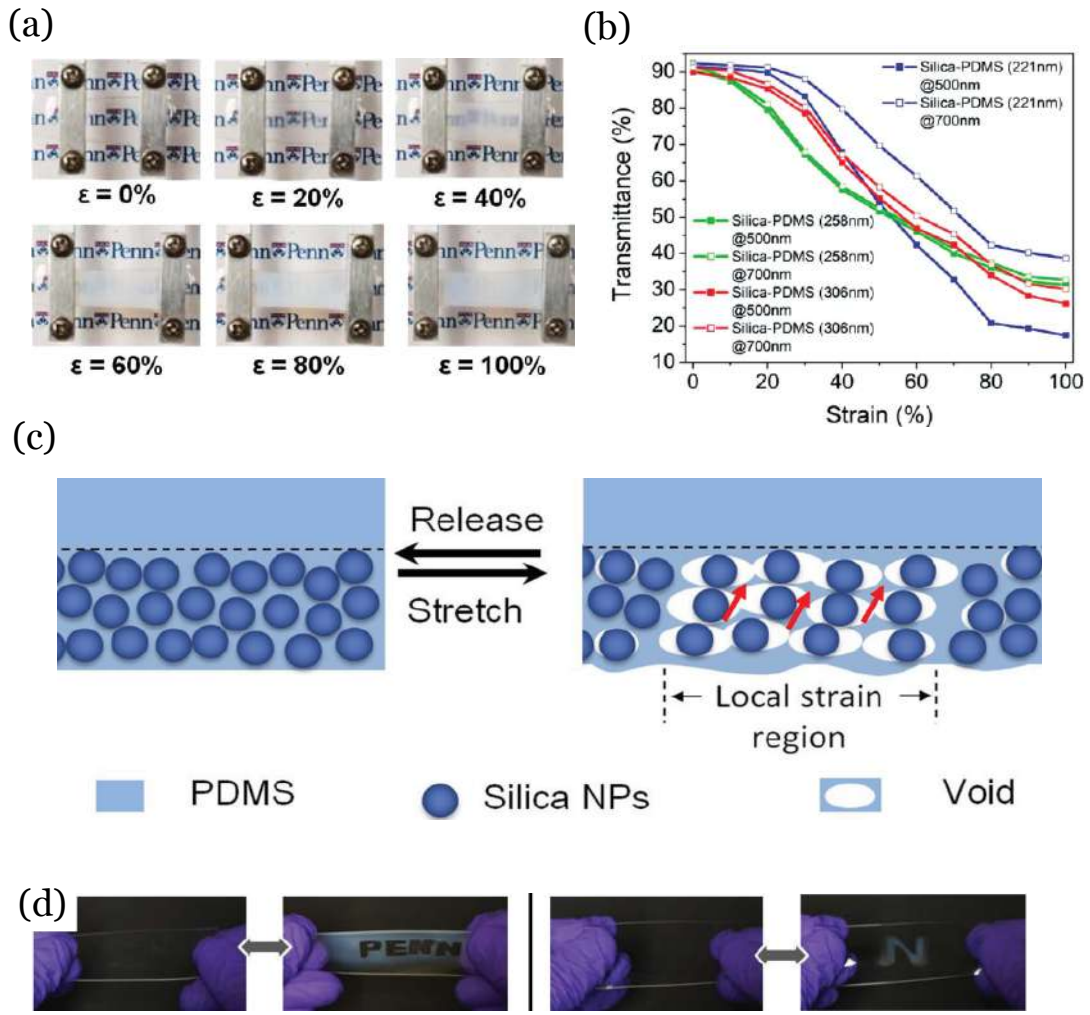

Figure 2.20 (a) Photographs of a silica/PDMS film consists of nanoparticles with diameter of 258 nm at different stretching strains [239] (b) Transmittance and strain

curve at wavelengths of 500 and 700 nm, respectively [239] (c) Schematic illustration of the void formation around the silica particles when stretched. The arrows indicate PDMS ligaments [239] (d) Optical images showing reversible revealing and hiding of the letters patterned within the silica nanoparticle/PDMS film under mechanical stretching and releasing [239].

Moreover, elastomeric materials subject to mechanical stimuli can undergo surface morphological change (e.g. wrinkles and cracks) for creating the optical feature [80], and structural colour with dynamic luminescent patterns [247]. Inspired by skin colour morphing schemes in marine creatures, Zeng et al [79] reported an interesting approach to realize mechanochromic devices by introducing strain-dependent cracks and folds, where light transparent skin cracks were used to produce analogous optical signals. For the luminescent mechanochromism in **Fig. 2.21a**, a stiff ultraviolet shielding film layer is adhered to a soft PDMS substrate that contains a fluorophore layer and a reflector layer. When applying mechanical stretching, distributed cracks generate in the ultraviolet-shielding layer, the crack size is related to the applied tensile strain. These cracks act as 'gates' to adjust the exposure region of the fluorophore and the concomitant ultraviolet-excited fluorescent intensity. The bottom reflector layer can increase the fluorophore luminescence through reflection, leading to a significant improvement of the strain-responsive luminescent performance. Only 5% stretching strain is enough to change the device visibility from a nonluminous state to an apparently eye-detectable luminescent state. As shown in **Fig. 2.21b** and **Fig. 2.21c**, by applying different stretching strains, various luminescence intensity have been achieved via inducing cracks and folds, creating dynamic

optical pattern changes [79]. In their research, the fluorescent intensity depends on the size of cracks, while such cracks are uncontrollable and only the in-plane 2D patterns are achieved.

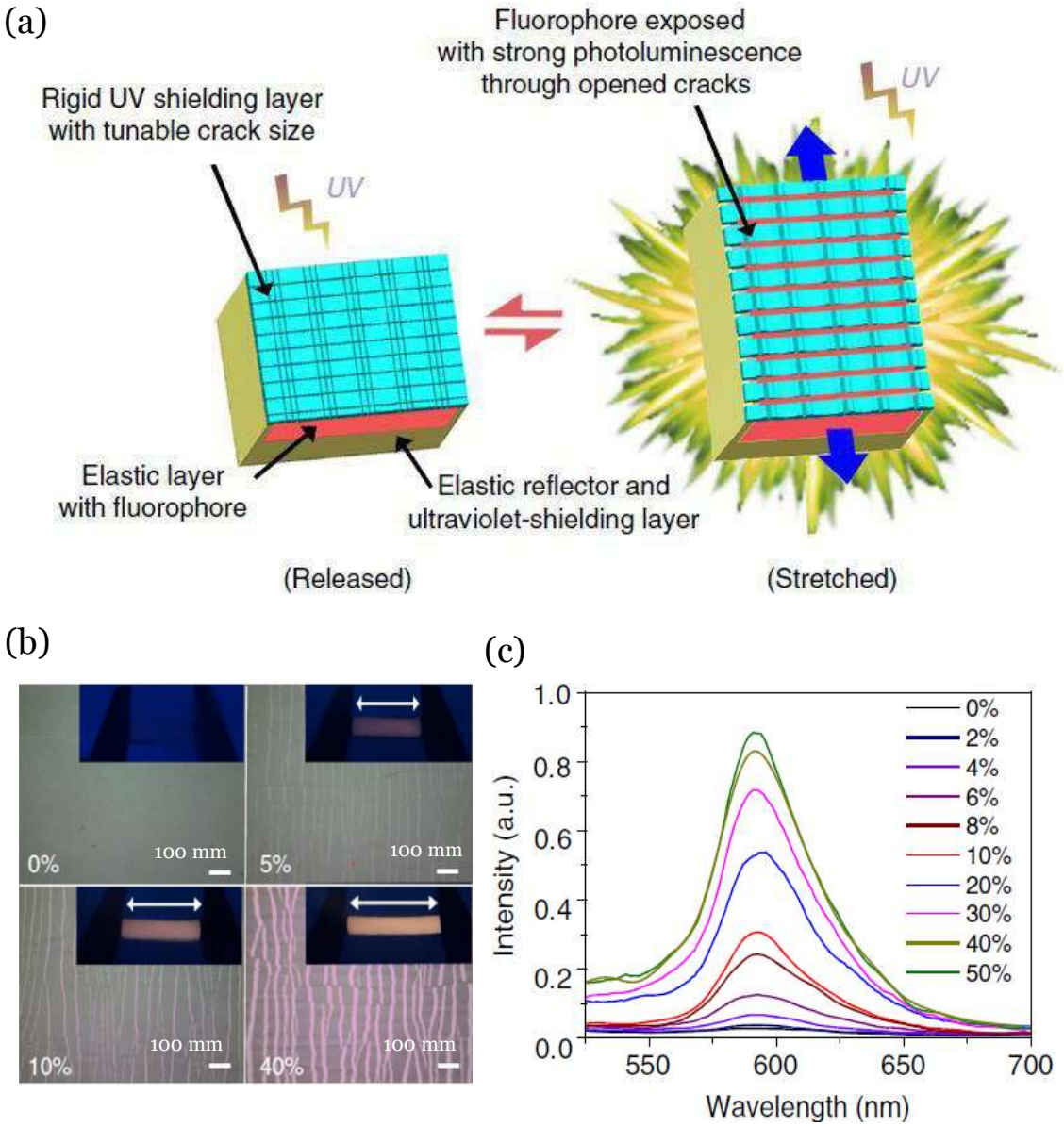

Figure 2.21 (a) Design scheme of the reversible luminescent mechanochromism [79] (b) optical microscope images showing the distribution and size of the longitudinal cracks upon strain in the luminescent mechanochromism. The insets are digital photos of this device experiencing corresponding strains under ultraviolet light (λ=365 nm, white arrow indicating stretch direction) [79] (c) Fluorescent spectra of

the luminescent mechanochromism as a function of strain (excitation wavelength of ultraviolet λ =365 nm) [79].

More recently, the mechanics knowledge on controllably generating elastic instability morphologies and their evolutions e.g. wrinkles, period-doubling, folds and creases, has been extended both theoretically and experimentally [5], [160], [162], [163], [173], [212], even to form 3D structures [202], [248]. Such micro-scale, reversible mechanoresponsive surface morphology change has enabled a range of engineering applications such as tuneable surface wetting [170], flexible electronics [5], [78], tuneable optics [79], [80] and switchable surface chemic patterns [81], [82].

2.3.3 Flexible Shape-morphing transducers

Hydrogel can be synthesized into transparent, elastic solid, stretchable, ionic conductive and shape-morphing soft materials, which has gained increasing attention [11], [174], [182], [185], [188], [190], [258]. Morphing soft materials which exhibit great changes in dimensions responding to different range of external stimulations [74], [114], [192], [193] (e.g. electrical, thermal, mechanical and chemical) have promising applications in various fields, such as biomedical devices [194], biomimetic systems [195], and soft robotics [196]. Hu and co-workers [197] firstly achieved the bilayer bending morphing structure where a responsive hydrogel has been bonded to a nonresponsive gel layer. After that, through bending of hydrogel bilayers, Gracias et al. [198] have demonstrated 3D shapes such as cylinders, spherical capsules, and helices. Yang and co-workers [199] fabricated the snowman like bilayers which forms spherical

capsules. Dickey and Velev [200] achieved reversible patterning of bending via "ionoprinting" of physical cross-links. Furthermore, through using trilayers of responsive hydrogels sandwiched within two patterned stiff layers, researchers [201], [202] have produced the complex and miniature origami structures.

Inspired by the sources of natural, pinecones and bean pods [204], [205] display smart deformations with the releasing of the seeds under desiccation, in which scientists have realized that one of the desirable developments is to make the self-shaping process controllable, programmable and reversible, at least for specific configurations to achieve well-defined complex 3D shapes.

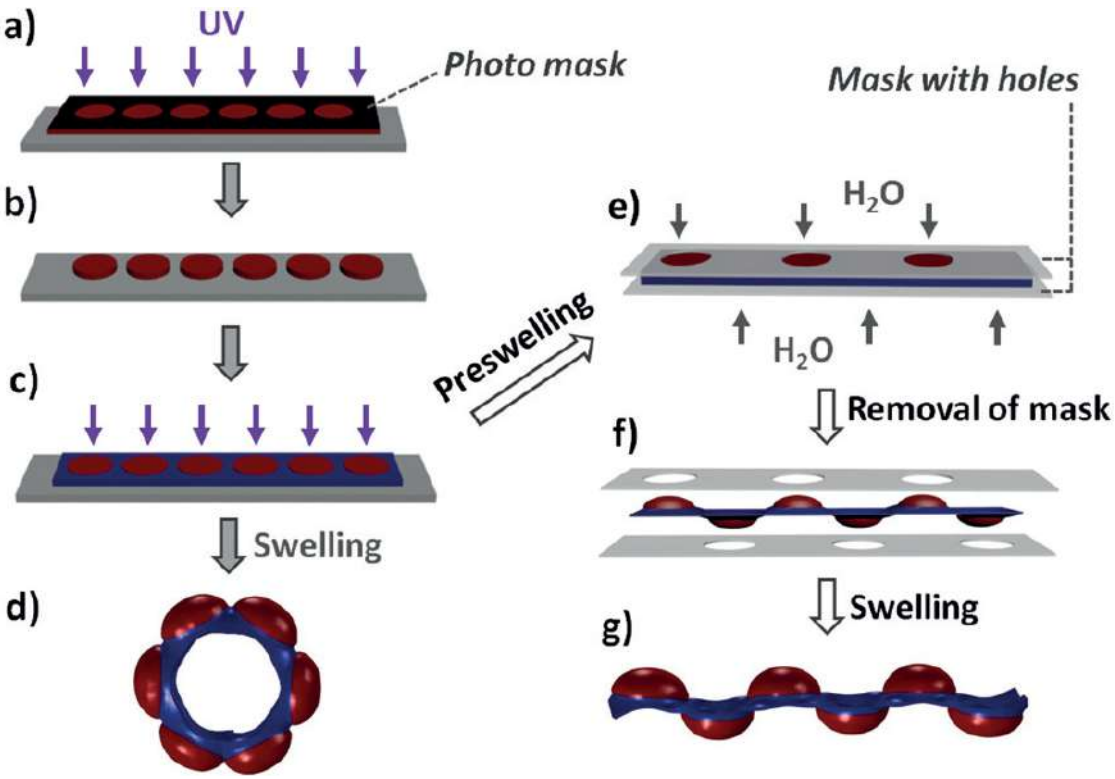

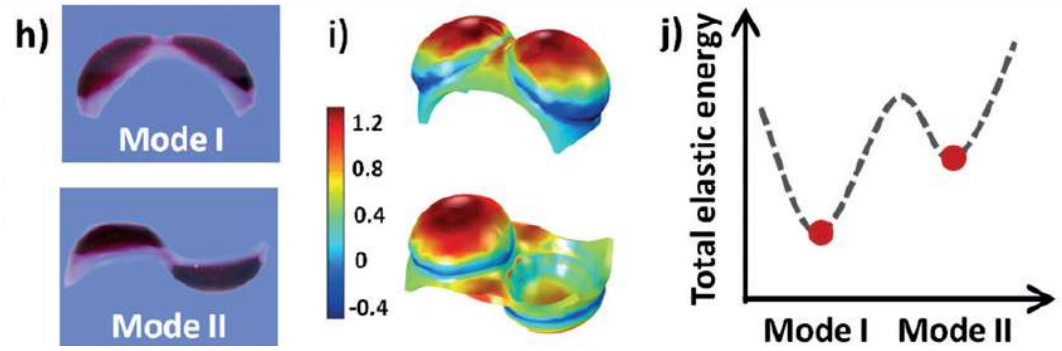

Figure 2.22 a)–g) Preparation of patterned hydrogels and the swelling induced deformations. The composite gel strip was prepared by two-step photo polymerization (a–c). Red: high-swelling gel, blue: non-swelling gel. The as-prepared composite gel strip formed a roll after free swelling in water (d). In contrast, a programmable configuration can be obtained via a pre-swelling step to direct the buckling direction of localized domains (e–g). h)–j) Experimental (h) and computed (i) results of bi-stable configurations of patterned gel with two domes and their relative total elastic energy (j). The colour scale in (i) indicates the in-plane areal strain [12].

Wang et al. [12] have demonstrated programmable, multiple 3D shape control strategythrough planar (flat) patterned, homogeneous swell-able hydrogels. As shown in **Fig. 2.22**, "Pre-designed" complex deformations were demonstrated by the periodically patterned hydrogel blocks made from multi-step lithographically. The pre-swelling step can be applied to guide the shape transformations of identical patterned hydrogel. The shape morphing was generated due to elastic mismatch between non-swelling substrate and swelling gel blocks [12], [13], [206], [207]. Holed "swelling masks" were employed to control the swelling directions to re-configure the deformation patterns [12].

Thin, uniform heterogeneous bio-content deposition was achieved previously by droplet microfluidics utilizing smart surface wettability control (e.g. switchable hydrophobic/philic patterns) [14], [208], [209]. More recently, inspired by natural bio-structures, using droplet microfluidics to control the formation of encoded multifunctional as heterogeneous hydrogel building blocks have been exploited to form complex hydrogel architectures [15], [16], [204], [209].

Relying on such development in smart hydrogel patterning and the morphing technology, in chapter 6 of this thesis, the initial work of design, fabrication and characterization of well-defined controllable morphing technology has been demonstrated by patterning and controlling the variform of hydrogel droplets onto hydrophobically patterned surface, which to achieve the advanced and complex 3D morphing structures.

2.4 Chapter Summary

This chapter introduced the background and theories of basic materials and mechanical properties, elastic instabilities (e.g. wrinkles, creases, folds) within multi-layer elastomer systems and soft materials based super-flexible transducers. The following chapters introduce the design and microfabrication techniques that provide the “smart” soft structures where sensing and actuation transducers will be based on.

Chapter 3

Experimental Methods

Chapter 3 describes the experimental details behind this project, including fabrication process for micro-structured surfaces (e.g. patterned integrated Au electrodes and patterned micro-hole arrays) and related characterization approaches. Also briefly summarizes the key equipment functionality and operational mechanism used in this project such as the Laser Scanning Confocal Microscope (LSCM), Atom force microscopy (AFM).

3.1 Fabrication for Strain-Gated Logic Transducer

3.1.1 Lithography fabrication of patterned Au on silicon

The gold layer was patterned with a lift-off process on the silicon substrates. Firstly, MEGAPOSITTM SPRTM 220-7 positive photoresist was spin coated on silicon wafers. The photoresist then patterned through photolithography process (Karl-Suss™ MA8 mark aligner). An anti-stiction SAM layer Perfluoro-decyl-trichloro-silane (FDTS) was then deposited using a MemsStar AURIX™ system. Au layers with thicknesses ranging between ~16 nm and ~100 nm were then deposited on top of FDTS treated (to reduce Au adhesion to Si) patterned photoresist via sputtering. The lift-off process was performed by soaking the sample in acetone solvent before cleaning with isopropyl alcohol (IPA) and absolute ethanol.

3.1.2 Dual-SAM transfer method

The gold layer was transferred to the bi-layer system through a thiol based dual-SAM (self-assembly monolayer) assisted metal transfer process. Before the SAM treatment, the silicon wafer was cleaned through absolute ethanol for 1 min at glass petri dish followed by drying via N_2. The MPTMS (3-Mercaptopropyl-trimethoxysilane) has been widely used for the transfer of Au films to PDMS [181], [183], [184], [186], [187], [189], [264]. The patterned Au electrodes on FDTS-silicon were then treated with MPTMS as an SAM adhesive to promote adhesion between Au and PDMS, by soaking in 20 mM (9.5 ul MPTMS +2.5 ml absolute ethanol) MPTMS for 3 hours, to help facilitate transfer to the bi-layer elastomer flexible substrate. The samples were then washed in absolute ethanol to remove excessive thiol on Au (only SAM is exposed) before N2 drying and ready for Au transfer process.

3.1.3 Pre-stretched PDMS-VPS bilayer fabrication

The PDMS-VPS bi-layer elastomer is shown in **Fig. 3.1a** that consists of a strip of thick and stiff mounting layer (3 mm thick, 9 mm wide and 30 mm long) made of Vinylpolysiloxane (VPS, Elite Double 22, Zhermack, A-silicone duplicating material, ~0.35 MPa, mixing ratio base with catalyst of 1:1) in **Fig. 3.1b**. The bi-layer structure was prefabricated before being fixed in a mechanical vice and pre-stretched from 5 mm to 30 mm length. The reasons for choosing VPS as the mounting substrate are due to its properties of fast curing at room temperature and easily vary elastic modulus. A softer

unstressed thin polydimethylsiloxane (PDMS, Sylgard™ 184, ~125 μm thick, 30:1 for elastomer base and cross-linker, Young's Modulus of 0.12 ± 0.02 MPa) film layer was then attached on the VPS stiff layer under tensile stress (due to its pre-stretching).

(a)

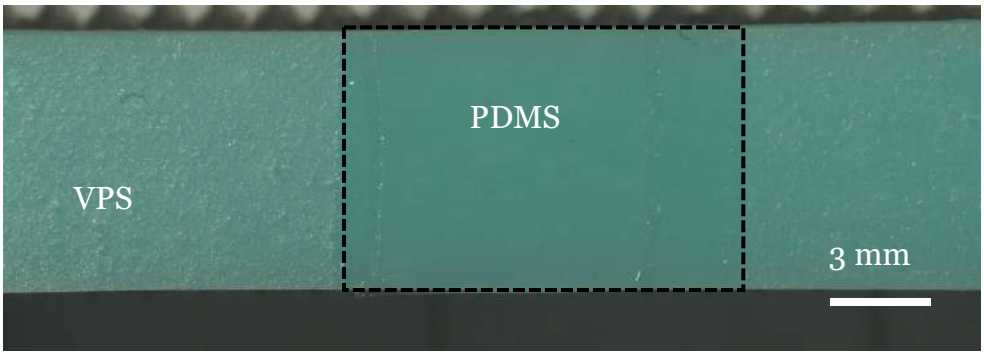

(b)

Figure 3.1 (a) Image of the pre-stretched PDMS-VPS bilayer elastomer structure (b) The bottles of VPS elite double 22 elastomer contains free, uncrosslinked polymer chains.

3.2 Fabrication for Topo-Optical Transducer

3.2.1 Micro-engineering of patterned template

The structural patterned templates of SU-8 pillars were fabricated through photolithographic procedure. Single-line and square (multi-line) lattice arrays of SU-8 pillars were lithographically patterned on silicon substrates to create the stamp template. Silicon wafer was rinsed with Acetone and Isopropyl Alcohol (IPA) about 10 seconds to clean up the surface. Firstly, 1, 1, 1, 3, 3, 3 - Hexamethylsilazane (ACROS ORGANICS) was spin-coated (30 seconds, 1000rpm) onto the silicon wafer to promote adhesion. A thin layer of SU-8 (2025, Micro Chem) was then spin-coated on silicon wafer at desired rotary speed, then wafer was placed on hot plate for soft bake at 95°C for 5 min, before being exposed to UV light under a mask aligner (EVG 620). The exposure energy was linked with the designed SU-8 thickness. Post-exposure-bake (PEB) was then performed (65°C for 1 min, then ramped to 95°C for 5 min). After being developed in an EC (ethylene lactate based) solution for 5 min, the patterned SU-8 templates were cleaned by Isopropyl Alcohol and DI (de-ionized) water. It was baked for another 15 minutes at 200°C before stamp-transfer.

3.2.2 Fabrication of patterned multi-layer elastomeric substrate

The stiff mounting substrate of Vinylpolysiloxane (VPS, Elite Double 22, Zhermack, A-silicone duplicating material, ~0.35 MPa) was cut into rectangular strip (9 mm wide, 30 mm long and 3 mm thick) and mounted on

a mechanical vice, pre-stretched to 300-600% strain under uniaxial tension. The thin soft polydimethylsiloxane (PDMS, Sylgard 184, base-to-crosslinker weight ratio=30:1, Young's modulus of 0.12 ± 0.02 MPa, thickness of ~125 μm) was spin-coated on the fabricated SU-8 pillars, followed by 60 min soft bake at 70°C. An adhesion PDMS layer was then spin-coated (30:1) onto the soft-baked PDMS to bond it to the mounting VPS layer. The structures were cured at 70°C for 8h and then ready for dry peel off. An oxygen plasma treatment (100w, Henniker HPT-100, working power of 100 watt, oxygen/nitrogen ratio ~0.2) of 10 second was applied to create an additional third thin hard skin layer (shear modulus of $G_f \approx 1.8\ MPa$, thickness of 100 nm,) on top of the lattice patterned PDMS surface. **Fig. 3.2** shows the Illustration of fabrication process.

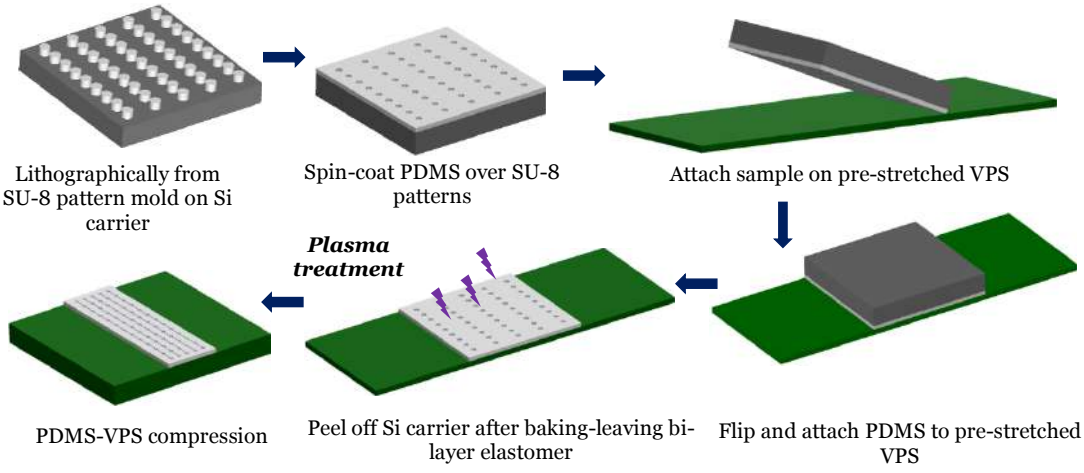

Figure 3.2 The Illustration of fabrication process of structural surface by spin-coating a thin PDMS precursor layer on a lithographically made template.

3.2.3 Solution casting of optical indicator layer

After the plasma treatment, optical indicator solutions (1.3 mM) were prepared by dissolving the fluorophore dye (powder) into the absolute ethanol and chloroform, chloroform is used to avoid the crystallization. Two different fluorescent solutions of Fluorescein O-acrylate (Sigma-Aldrich, FoA) and Iridium-III (Ir-III) have been used.

Table 3.1 Table summarizes two different optical solutions of fluorescein O-acrylate (FoA) and Iridium-III (Ir-III).

Fluorescein O-acrylate (FoA)				**Iridium-III (Ir-III)**			
λ_{ex}	$\lambda_{emission}$	Molecular formula	Molecular weight	λ_{ex}	$\lambda_{emission}$	Molecular formula	Molecular weight
478nm	515nm	$C_{23}H_{14}O_6$	386.4 (g/mol)	407nm	580nm	$C_{72}H_{81}N_6Ir$	1220.6 (g/mol)

Table 3.1 summarizes two different optical solutions. Fluorescein O-acrylate (FoA) is a fluorescent monomer with high quantum efficiency in aqueous media. The excitation and emission wavelength of FoA are within the range of visible light with λ_{ex} = 478 nm, $\lambda_{emission}$= 515 nm. Different monomers (e.g. acrylic acid, styrene and acrylamide) can be copolymerized with FoA, which facilitates the inclusion of the fluorescein with macromolecules. The molecular formula of FoA is $C_{23}H_{14}O_6$ with its molecular weight of 386.4 g/mol. The Iridium-III (Ir-III) complex is a functional material that emits

orange-red coloured light (excitation λ_{ex} = 407 nm, $\lambda_{emission}$= 580 nm) when excited by UV or purple light, either in hypoxia conditioned solutions or polymer matrix. The emission of which is quenched by the presence of oxygen. The molecular formula of Ir-III is $C_{72}H_{81}N_6Ir$ with its molecular weight of 1220.6 g/mol. A droplet (8-10 μl) of fluorescent solution was then casted on the plasma treated surface. The solution droplet then spread and dried at room temperature with around 20s to form an optical indicator layer.

3.3 Numerical Simulation

The commercial simulation package – ABAQUS has been used to simulate surface folding on the multi-layer under uniaxial compression. The incompressible Neo-Hookean material model was used for all elastic materials in this analysis. Both the plasma-treated PDMS film and the un-treated PDMS substrate used in this experiment are hyper-elastic materials. Therefore, Neo-Hookean material model is adopted in the simulations. The input material properties are shown in **Table 3.2**. Where G_1 is defined as Shear modulus of plasma-treated rigid film, G_2 is Shear modulus of soft PDMS substrate, ν_1 is Poisson's ratio of plasma-treated rigid film and ν_2 is Poisson's ratio of soft PDMS substrate. Structural symmetry was assumed when the fold is simulated. The pseudo-dynamic method incorporated in ABAQUS was adopted. The geometrical inputs have been magnified by 1000 times due to the limitation of mesh size in ABAQUS. An element type CAX8H was used for mesh.

Table 3.2 The input material properties for FEA.

G_1	v_1	G_2	v_2
2.5 MPa	0.5	0.1 MPa	0.5

3.4 Characterization Methods

Characterization 1: Strain-Gated Logic Transducer: Mechanical properties were characterized by using a self-designed mechanical vice to measure the strain related physical properties. For capturing and measuring the first visual site of designed structure and how it behaviour with strain change, an upright optical microscope (Nikon LV-100, brightfield reflection mode) and ImageJ 1.50i/Java 1.6.0_24 software were used. Scanning electron microscopy (SEM, MIRA3, TESCAN) was used to observe the surface structures. Atom force microscopy (AFM, D3100, Veeco) and Bruker® GTK interferometer provided a range of in-plane surface morphology change. The AFM is a surface scanning technique that widely used for topography studies. It uses a cantilever with a very sharp tip (made of silicon or silicon nitride) to scan over a sample surface. When the tip is operated to approach the surface, due to the close-range, attractive force between the tip and surface that result the cantilever to deflect towards the surface. The AFM has different operation modes such as non-contact mode, contact mode and tapping mode. Manual probe station was used to measure the electrical signal.

Characterization 2: Topo-Optical Transducer: Upon releasing the pre-stretched VPS mounting substrates, the plasma treated PDMS thin layer experienced uniaxial compression. Incremental deformation in a unit nominal strain of ≈0.004 was applied to the sample during the compression (progressing) or tension (withdrawing/recovery) by a fixed amount at regular intervals in room temperature. An upright optical microscope (Nikon LV-100) was used for observation under reflective white light mode. An atom force microscopy (AFM, D3100, Veeco) was used to profile the surface morphology changes. The surface modulus was measured by AFM indentation [75]. AFM indentation is one of the AFM modes that operate through pushing a tough, sharpened indenter tip with a well-defined shape against the sample surface. It enables to extract sample hardness and elastic modulus via analyzing force-displacement curves. A common limitation is that the penetration depth should not exceed 10% of the coating's thickness to avoid affecting the underlying substrate. For films of 1 μm, this corresponds to a maximum indentation of 100 nm. Furthermore, in order to avoid the surface roughness effect on the measurement, it should be less than 20% of the depth of indentation. The AFM indentation method has been used for elastic modulus characterization of interfaces and thin layers [265].

Fluorescence images were performed by using Nikon A1R Laser Scanning Confocal Microscopy (LSCM) system as shown in **Fig. 3.3**, with the ability to scan samples vertically at different scan steps. For the Fluorescein O-acrylate (FoA) images, the scanner selection was set to be Galvano, with laser

excitation wavelength of 488 nm and emission wavelength of 540 nm. For the Iridium-III images, the scanner selection was set to be Galvano, with laser excitation wavelength of 406.6 nm and emission wavelength of 595 nm.

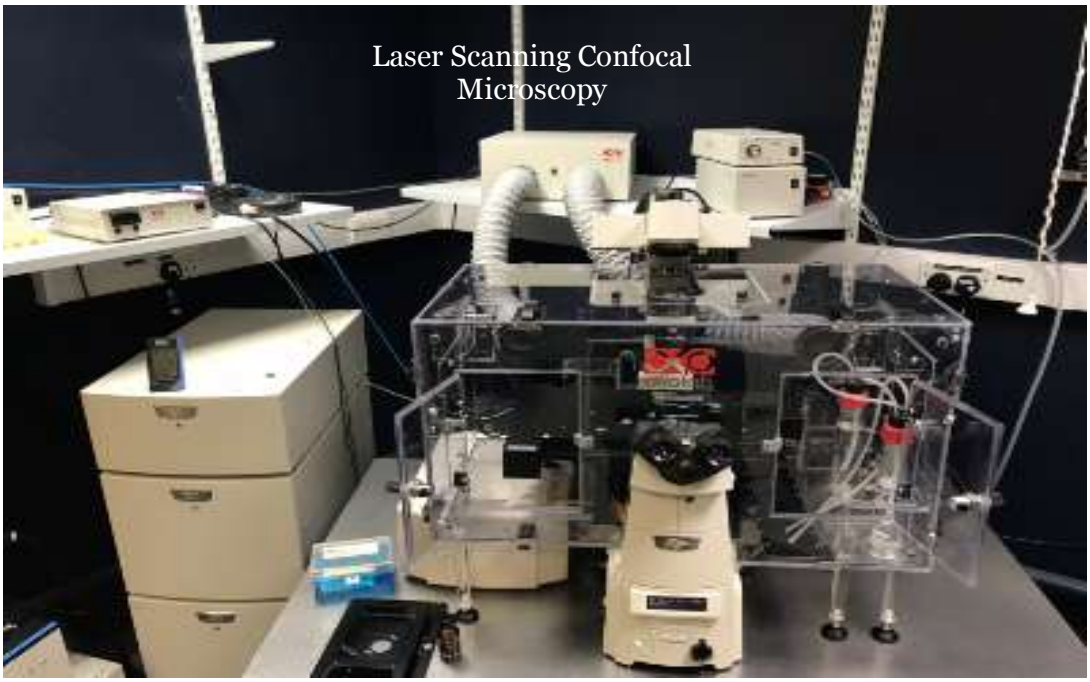

Figure 3.3 Photo of Laser Scanning Confocal Microscopy (LSCM) been used in this project.

Both of the 3D scan and single line scan have been used to characterize the optical signal and the surface morphology change. Before the actual scan, a scan range shown in **Fig. 3.4a** was defined with the top of the scan being the position above the optical layer interface and the bottom being the position over the folding interface. By setting the scan step (such as 0.1 μm) through the entire scan range, all of the scanned layers were combined and a 3D reconstruction was generated.

The 3D scan in **Fig. 3.4b** is the area layer-by-layer scan for a 3D structure view, which gives the top in **Fig. 3.4c**, cross-section in **Fig. 3.4d** and side cross-section view in **Fig. 3.4e**. While single line scan gives a "cross-section" scan. An example of single line scan is shown in **Fig. 3.4f**, single line scan looks similar with the cross-section view of 3D scan, while for line scan, the scan speed is much faster than 3D scan. In this thesis, single line scan has been used for fold-in depth measurement, repeatable and recovery test. The captured fluorophore images were subsequently analyzed by the MATLAB to get its light intensity data and imaging (surf, shading interp).

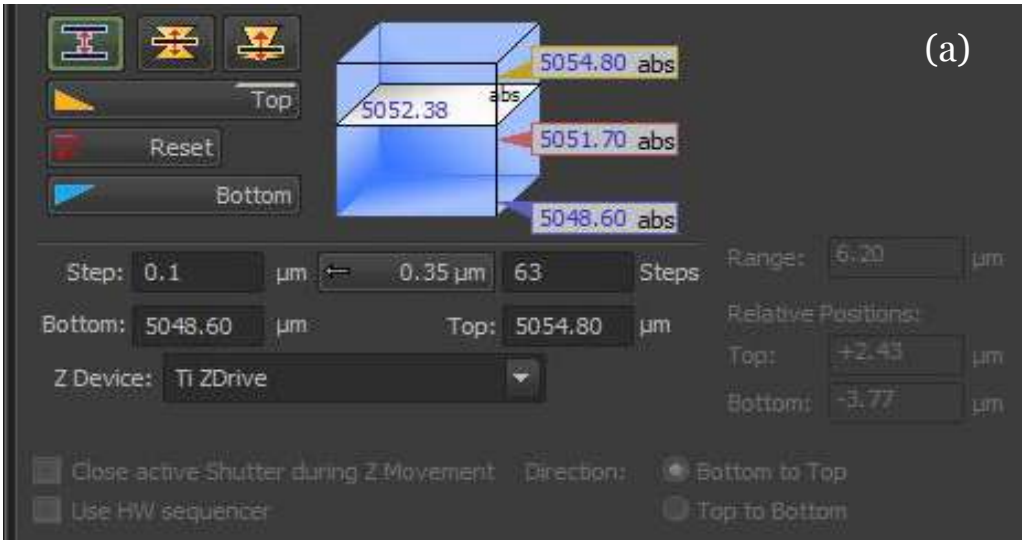

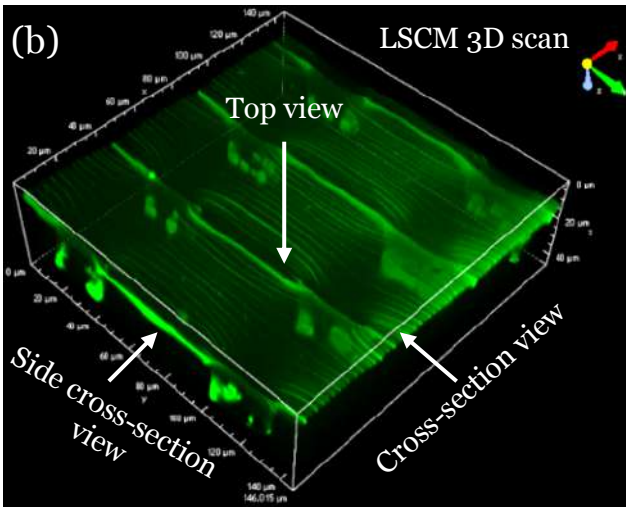

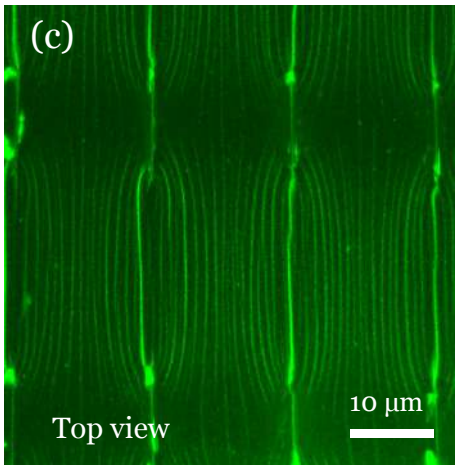

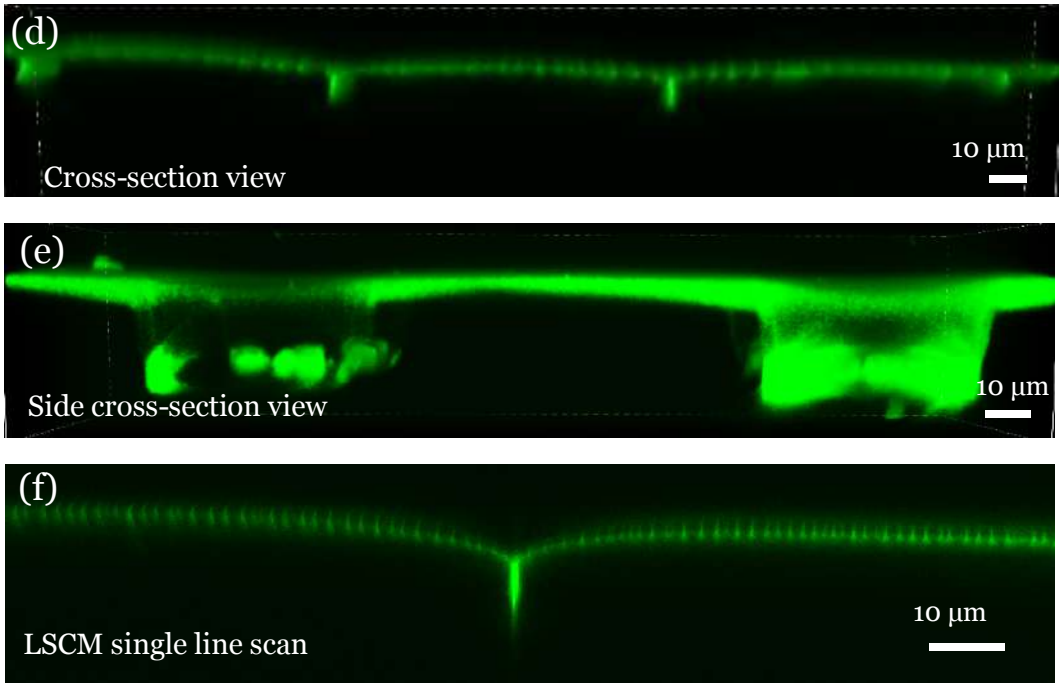

Figure 3.4 (a) Example of the LSCM software interface showing the confocal scan setup (top and bottom) (b) LSCM 3D scan with (c) top view (d) cress-section view and (e) side cross-section view (f) An example of LSCM single line scan.

Chapter 4

Flexible, Strain Gated Logic Transducer Arrays Enabled by Initializing Surface Instability on Elastic Bilayers

Based on the methods introduced in section 3.1 regarding patterned integrated Au thin hard film layer, this chapter describes the detailed research about strain gated logic transducers. Test structures were employed to help achieve a large sensing range with stepwise output signals, by controlling the surface deformation of an array of strain transducers, which has enabled widespread downstream applications.

This chapter discusses arrayed and interconnected multiple finger electrodes switching mechanism with the controllable competing elastic instability growth on super-flexible substrates. By designing and micro-engineering interconnect multi-finger Au test structures on PDMS-VPS elastomer system, which to provide a stepwise resistance-strain response sensing mechanism. This research also experimentally studied instabilities (patterned stiff and soft regions) on heterogeneous surfaces under large compression strains (up to 60%) which could help the development in related theoretical studies.

The characterisation techniques used in this study can be divided into two aspects: surface morphology characterisation and electrical testing. The

common challenge in the study of the compression process is Possion ratio caused effect, which break the electrodes. Therefore, the layout optimizations of a general model and the different test structure designs have been discussed as well.

4.1 Introduction

Among the developed flexible electronics, a versatile set of approaches exploits the sensing and actuation of planar compression strain achieved by triggering the elastic instabilities with placing pre-strain in an elastomer mounting substrate [212]–[214]. Recent research on elastic substrates complying with local features such as metal interconnects and integrated transducers has shown great potential to withstand high strain deformation during bending, compressing and stretching [7], [9], [215]. Such structured elastic surfaces under compressions and stretching can undergo various deformations such as wrinkling, creasing, folding and buckling, which generates interests in engineering applications in sensing and actuation [10], [75]–[76], [121], [163], [170], [214], [216], [217], [218], [259]. Among them, the developed metal-elastomer strain gated transducers have utilized mechanically gated super-flexible electrical switches to provide sensing mechanisms for wearable electronics [5], [78], [218], [219]. Controllably and reversibly generating creasing and other instability patterns on the surfaces of soft materials by temperature [81], mechanical [120], electrical [211] and electrochemical [212] stimulation have attracted considerable interest in developing them into sensing and actuation applications.

Traditional devices are commonly used as “hard” sensors that attached to stiff materials such as metals, concretes and high modulus plastics for monitoring the structure health or quantifying specimen deformational. Compared to single metallic foils, semiconductor devices can exhibit much higher sensitivity due to piezoresistive effects where the resistivity changes rapidly with strain due to the dependence of the bandgap on inter-atomic spacing, but the sensing ranges mostly are within 1 %. Polymer based integrated strain sensor can be readily laminated on and form conformal contact to the human skin, with only modest mechanical constraints on natural motions. Strains measured in this mode on the wrist are up to 10%. Another type - Silicon based integrated sensor can achieve a higher sensing strain up to 20% in **Fig. 4.1**. While in order to achieve a large surface strain sensor, researchers [5], [219] have looked into the sensing range up to 60% with the paired electrode device by inducing the elastic instabilities.

According to Xu and co-workers [5], a flexible large surface strain sensor by using mechanically gated electrical switches onto the Au-elastomer device has been demonstrated. Based on the controllable formation of surface creases to bring initially disconnected regions of the metal electrode into self-contact, which to produce the electrical signal. When the compression strain surpasses threshold values, the measured resistance displayed a significant step change from open (~10^{13} Ω) to close (~10^{2} Ω) after the self-contact of the electrodes. The switching threshold strains can be controlled by geometry design (e.g. Au electrode width W_f, Length L_f, and gap value L_g) as well as

material and structural properties [5], and other research in surface instabilities has shown the deformation mode can also be controlled via such designs [76]. Moreover, the latest study into surface instabilities on such heterogeneous surfaces with patterned regions of different materials (e.g. stiff metal electrodes and soft elastomers) opens the possibilities for research into advanced surface morphing and more complex application devices [76].

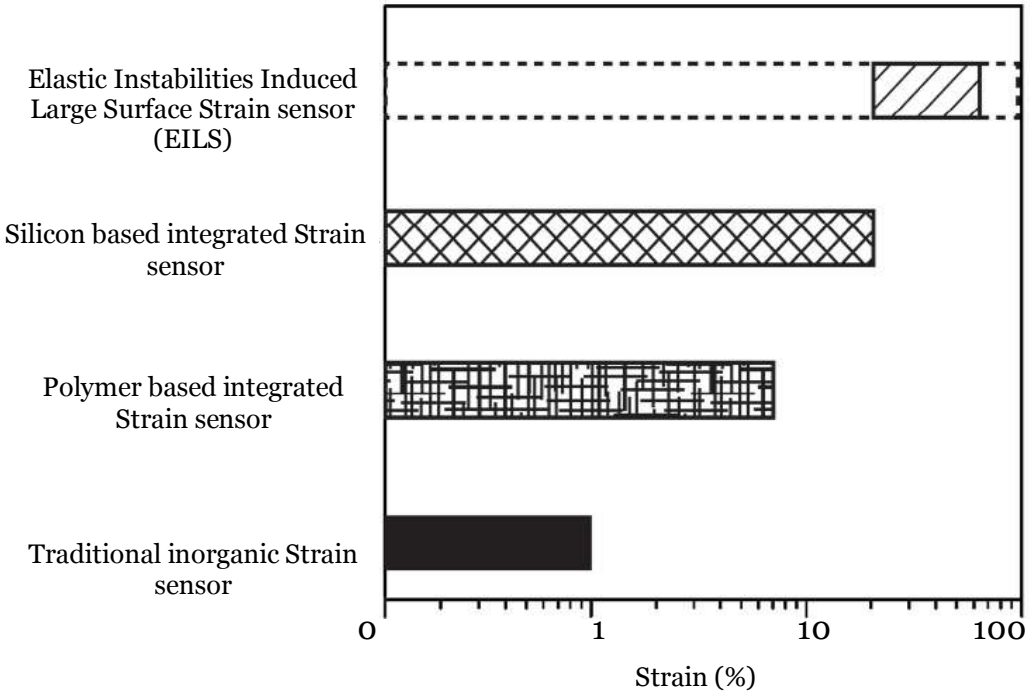

Figure 4.1 Vision map of the sensing range comparing with the existing sensing structures, the provided sensing range (pattern area) for EILS is between 20% to 60%, and it should be possible to extend this to 0-100% through modifying the structural design [219].

4.2 Research development

The single pair of finger electrode (strain-resistance) related structure could be employed for super-flexible substrate strain sensing. While such single

pair of electrode has not studied how the pattern geometries affect the surface instabilities. In addition, each device performs as a digital sensor with "ON/OFF" logic, therefore only measuring a single critical strain value [5].

For future development of transducer arrays applied to a larger area under compression, it is important to develop electrode interconnect technologies that should ultimately enable row-column addressing. And for more complex competing instabilities growth, test structures are needed to study the deformation behaviour and to exploit the sensing mechanism of structural electrodes. In order to increase the number of critical strain values that the transducers can deliver without increasing the pad count, and to understand the relationship between electrode geometries and compression strain ratios. The integrated multi-finger Au geometry test structures have been designed.

The ultimate target is to enable a multi-switching mechanism where the strain value can be determined by measuring the resistance of the test structures. The growing and co-existence of wrinkles and creases on multiple electrodes with different dimensions are observed under lateral strains ranging between 0 and 0.6. In contrast to the previously reported single switching test structures [5], multiple resistance values were generated at different switching strains on an individual device. This has been demonstrated by using the arrayed and interconnected multiple finger electrode test structure with different distances between the electrodes (the gaps are aligned along the compression axis).

Based on the more complex integrated multi-finger Au geometry, its design, characterization, which required for optimization of elastic instability growth and interconnect have become more complex for multi-finger sensors, this will lead to some potential challenges such as possion effect, Au-elastomer bilayer geometry effect (Au width, length, gap etc.) and the comparison of the competing elastic instability growth under theoretical and experimental values.

4.3 Results and discussion

4.3.1 Test structures design and fabrication

The designed and fabricated transducer arrays and interconnects are shown in **Fig. 4.2**. The test structures are designed through "KLayout" software. Each of the paired Au finger electrodes was interconnected by two different configurations. **Fig. 4.2a** shows SEM image (Tescan® Mira3) of the bulk interconnect configuration linking 4 pairs of finger electrode transducers (labelled F1 to F4) with 2 contact electrodes (labelled E). **Fig. 4.2b** shows the serpentine interconnect configuration that helped to protect the Au electrodes from damage caused by perpendicular direction stretching due to Poisson effect. **Fig. 4.2c** shows a SEM cross-sectional view of Au layer with a thickness of 74 nm.

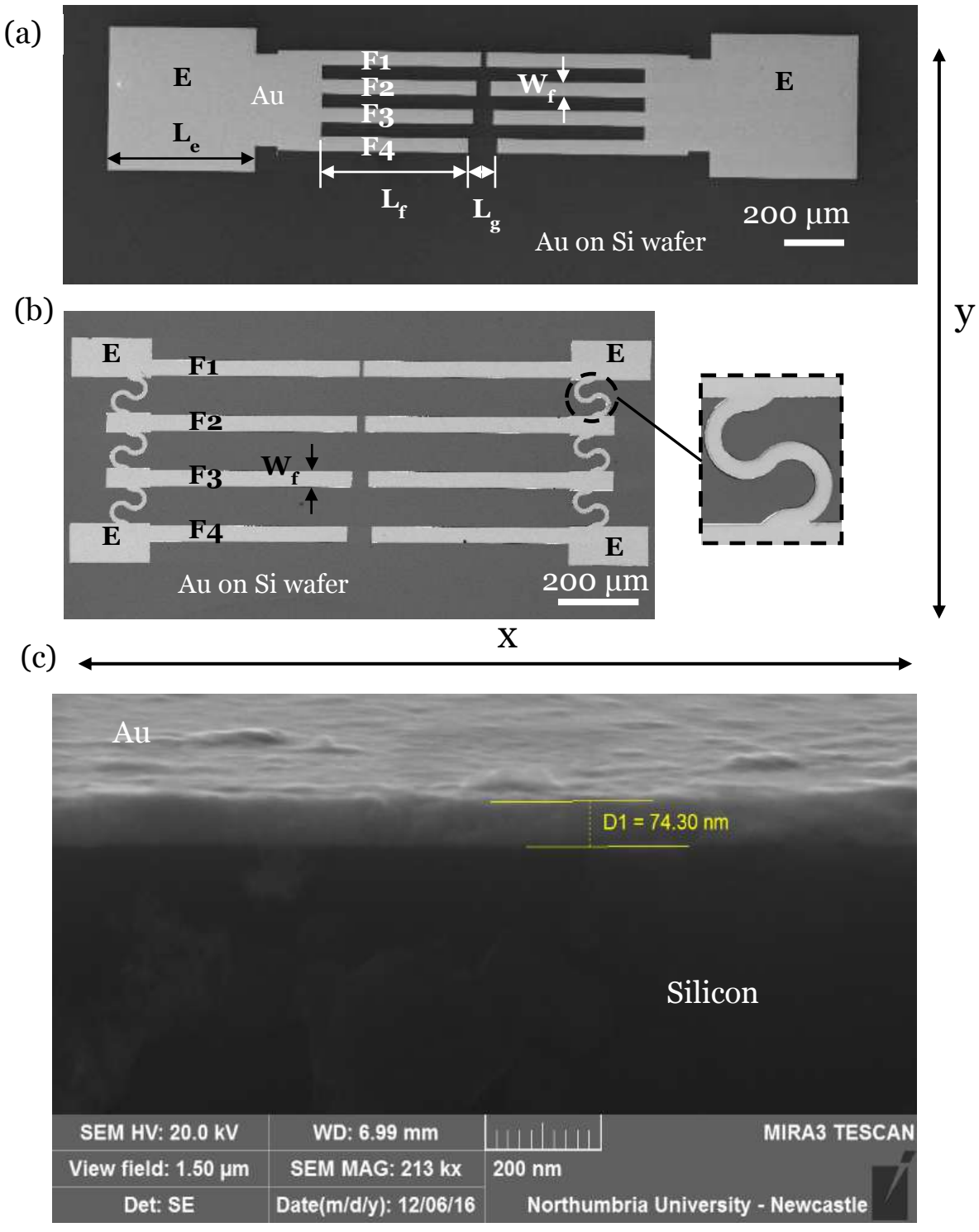

Figure 4.2 SEM scan of layouts showing the multi-switching high-strain sensing transducers with Au on silicon carrier before transferred onto the PDMS-VPS elastomer system with (a) 4 pairs of finger transducers "F" interconnected with two

bulk contact electrodes “E” (b) 4 pairs of finger transducers interconnected with contact electrodes by serpentine structures (c) Cross-section view showing Au thickness.

One main focus is on the relationship between geometry design parameters such as electrode widths W_f, finger electrodes lengths L_f, the gap between the finger electrodes L_g and 2D (top view) deformation for the Au electrodes and gaps in-between at different substrate compression strains ε_{sub}.

Table 4.1 Table of all initial designed values for each parameter.

Au thickness	**Finger length L_f (L_{f1} - L_{f4})**	**Gap value L_g (L_{g1} – L_{g4})**	**Finger width W_f**	**Probe pad length L_e**
16-100 nm	225-265 μm	5-95 μm	20 or 50 μm	500 μm
16-100 nm	500-525 μm	5-95 μm	20 or 50 μm	500 μm

Table. 4.1 summarizes the designed values of each parameter. The original lengths of finger electrodes (L_f = L_{fo} in **Fig. 4.2**) range from 225 μm to 265 μm and 500 μm to 525 μm, with electrode widths W_f either 20 μm or 50 μm (The width of electrode W_f is to protect the Au electrode from bulking delamination). Both of the L_f and W_f are related to the calculated finger resistance (R_{finger}=R_sL_f/W_f, where R_s is the sheet resistance). The gap between the finger electrodes L_g (related to the switching strain) ranged

between 5 μm and 95 μm. The probe pads were all 500 μm × 500 μm (original length $L_e = L_{eo}$ = 500 μm) in size, used for probe station to get the electrical signal. The strains are defined as: $\varepsilon_{Au\text{-}x} = (L_{fo}\text{-}L_f)/L_{fo}$, $\varepsilon_{Au\text{-}y} = (W_{fo}\text{-}W_f)/W_{fo}$, $\varepsilon_{Gap\text{-}x} = (L_{go}\text{-}L_g)/L_{go}$, with the key dimensions such as finger electrode width W_f, Length L_f, and gap value L_g, where the L_{fo}, W_{fo} and L_{go} are the initial values before the mechanical compression.

Since the photolithographically patterned Au electrodes have been deposited onto the pure silicon wafer, the next is to transfer the Au electrodes from silicon wafer to soft PDMS-VPS substrate. The bonding between the metal and the soft substrate is important. If the mettle patterns (such as Au) bond weakly to the substrate such as PDMS, it will be easily damaged or delaminated via external stimuli. Therefore, it is significant to increase the adhesion between the Au and PDMS.

In this thesis, a thiol based dual-SAM (self-assembly monolayer) assisted metal transfer process has been used. As shown in **Fig. 4.3a**, the Au surface is treated by the thiol of MPTMS that acts as a molecular adhesive to promote the adhesion between Au and PDMS. The liquid deposition method is selected because it provides the strongest adhesion between Au and PDMS [181]. **Fig. 4.3b-d** shows the schematic illustrations of dual-SAM (self-assembly monolayer) assisted metal transfer approach.

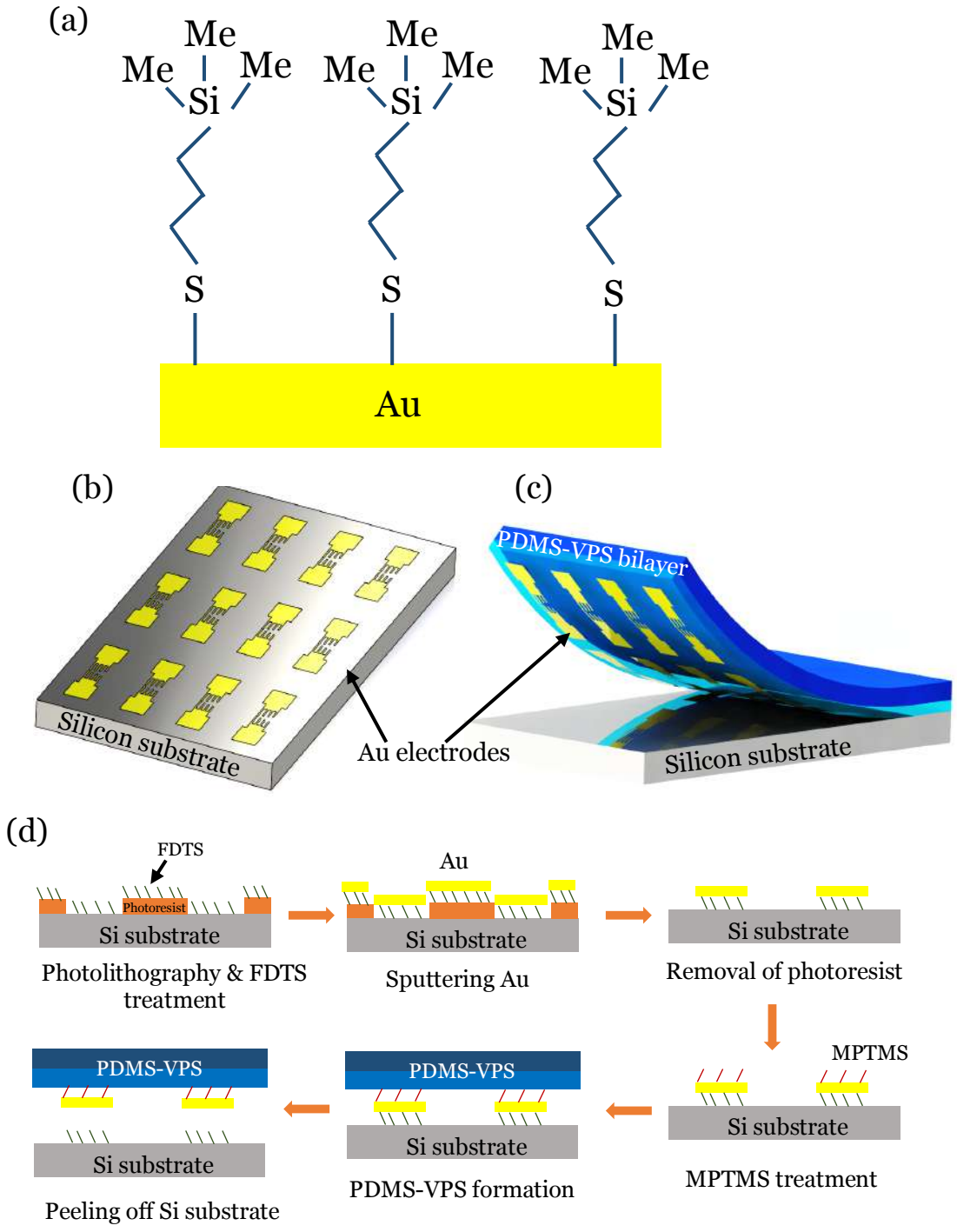

Figure 4.3 (a) Schematic of chemical modification by using MPTMS to promote the adhesion of thin Au film to PDMS (b) Schematic images illustrating the patterned Au and dual SAM Au transfer process: Lift-off + lithographically patterned multi-switching Au strain transducer array on silicon substrate ready for transfer (c) Au

patterns transferred from silicon to PDMS-VPS substrate by dual-SAM (self-assembly monolayer) assisted metal transfer process (d) Illustration of Au fabricated and transferred to PDMS-VPS bilayer through a dry peel-off method.

The Au-on-Silicon samples with MPTMS-SAM adhesive were then flipped and pressed (load of 5 g/cm^2) against PDMS surface of the pre-stretched PDMS-VPS substrate for 5 minutes, before being peeled off to complete the Au PDMS-VPS transducer device fabrication as shown in **Fig. 4.4a** and **4.4b**. **Fig. 4.4c** displays the SEM cross-sectional view, showing transferred Au sitting on the bilayer structures (total thickness around 110 µm) and **Fig. 4.4d** shows a demonstration of flexibility by bending the device.

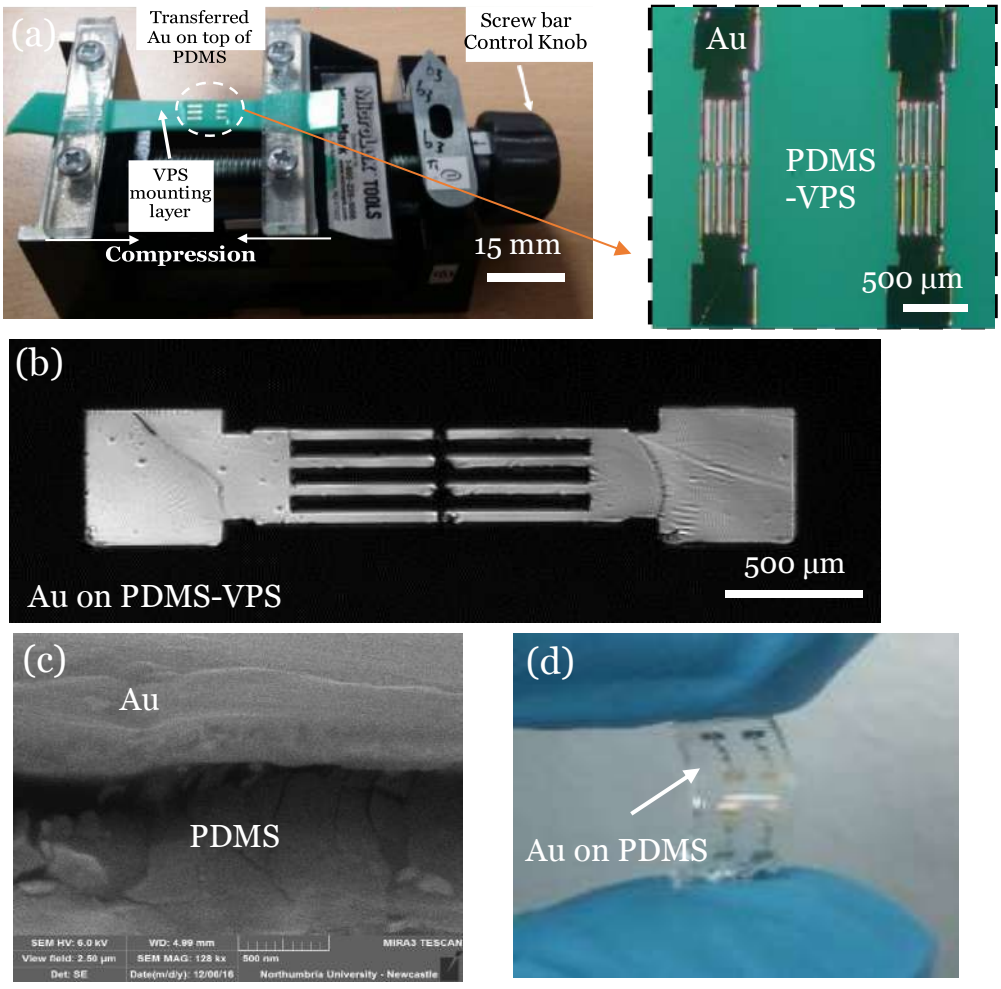

Figure 4.4 (a) Photo of the entire device (left) tensioned in the mechanical vice with a microscopic top view (right) of patterned multi-switching Au strain transducer array on PDMS-VPS bilayer substrate and (b) Nikon optical microscope view (c) SEM cross-sectional view of Au siting onto PDMS (d) Finger bending shows the flexibility.

While this SAM transfer process is not successful at initial stage, with some failing examples as shown in **Fig. 4.5a** and **Fig. 4.5b**, reasons behind are that the concentration of MPTMS (5-25 mM), thiol treatment time (20-540 min), methods of deposition (e.g. liquid deposition, vapour deposition, spin deposition), thiol types (e.g. MPTMS, 11-mercaptoundecanoic acid, bis (2-methacryloyl) oxyethyl) and different loads and loading times can all affect the Au transfer rate [5], [181], [219]. The adhesion was examined by using a tape adhesion test [181].

The yield of the transfer technology is investigated for different loads and various loading times. It can be observed in **Fig. 4.5c**, with a low load below 5 g/cm^2, the metal film cannot be transferred at all, but a successful transfer can be made with a load of 5 g/cm^2 and loading times longer than 5 min. With a higher load (>5 g/cm^2), the results suggest that it is more likely to lead to a passive pattern, where undesired patterns are transferred with mechanical fracture. It is thought that this might due to the total load energy applied on the metal thin film, which destroys the homogeneity of film and the patterned part stays on the silicon wafer as a result of a local surface energy concentration due to the feature sizes [5], [219].

(a)

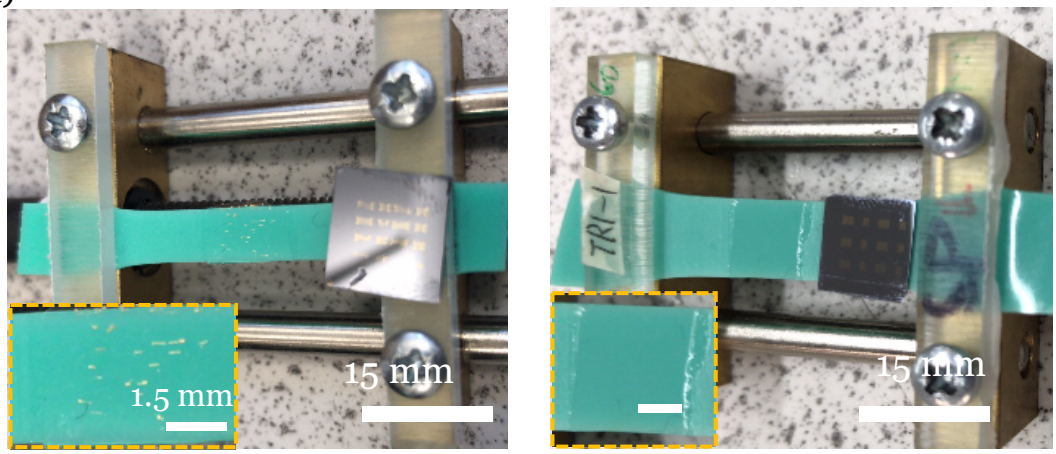
1.5 mm
15 mm
TRI-1
15 mm

(b)

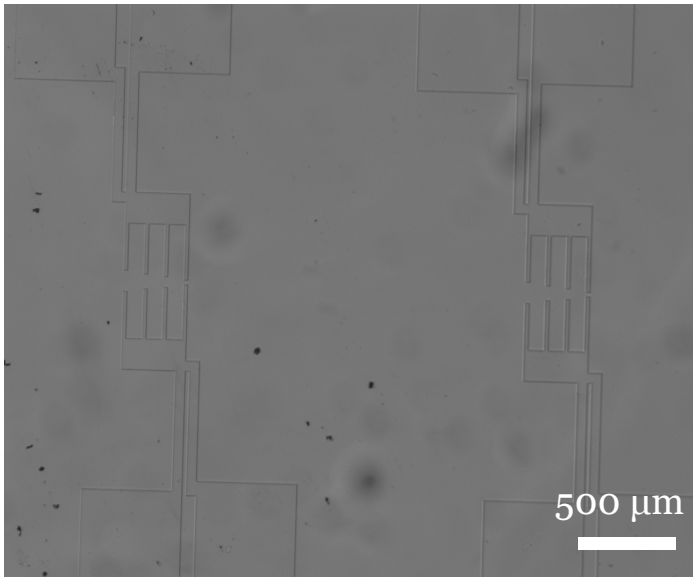
500 µm

(c)

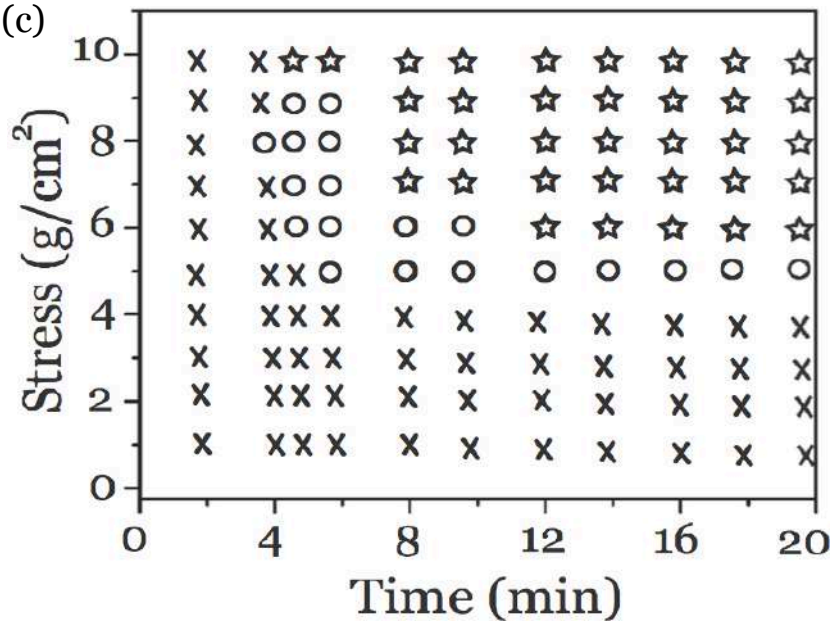
Stress (g/cm²)
0
2
4
6
8
10
0
4
8
12
16
20
Time (min)

Figure 4.5 (a) Photos showing the unsuccessful transfer samples (b) optical microscope observation of unsuccessful transfer samples (c) the transfer technique optimization diagram for the loads and loading time, three type of results are show as Type I (X),Type III (☆) and Type II - desired pattern transferred (o) [219].

4.3.2 Surface morphology characterization

The uniaxial (x-direction) substrate compression was provided by releasing the pre-stretched PDMS-VPS mounting layer through slowly turning the screw thread (~1.25 mm/turn, 5s) of the mechanical vice from L_o to L as shown in **Fig. 4.6**. Different releasing rates (5s, 100s, 1000s) have been studied with increasing average strain rates over the range of $1.7 \times 10^{-5} - 3.4 \times 10^{-3}$ s^{-1}, a decrease in ε_{sub} by 0.1 is observed. The observation suggests that the viscoelastic relaxation of the soft PDMS layer used here is important, at least at the faster loading/unloading rates studied.

When releasing the pre-stretched PDMS-VPS mounting layer by a fixed amount at regular intervals, the differences have been observed for both Au finger electrode and PDMS along the x and y direction. As illustrated in **Fig. 4.6a**, wrinkles on Au finger electrodes started to develop at low strain, and eventually both wrinkles on Au and creases on PDMS after substrate strain $\varepsilon_{sub} = (L_o\text{-}L)/L_o$ went beyond threshold. **Fig. 4.6a and 4.6b** show that the reversible wrinkling process on Au has reduced finger length from L_{fo} to L_f, resulting a local strain change $\varepsilon_{Au\text{-}x} = (L_{fo}\text{-}L_f)/L_{fo}$. Meanwhile as discussed, the gap area in-between (softer PDMS surface) will have its local strain amplified due to surrounding stiffer film patterns with $\varepsilon_{Gap\text{-}x} = (L_{go}\text{-}L_g)/L_{go}$.

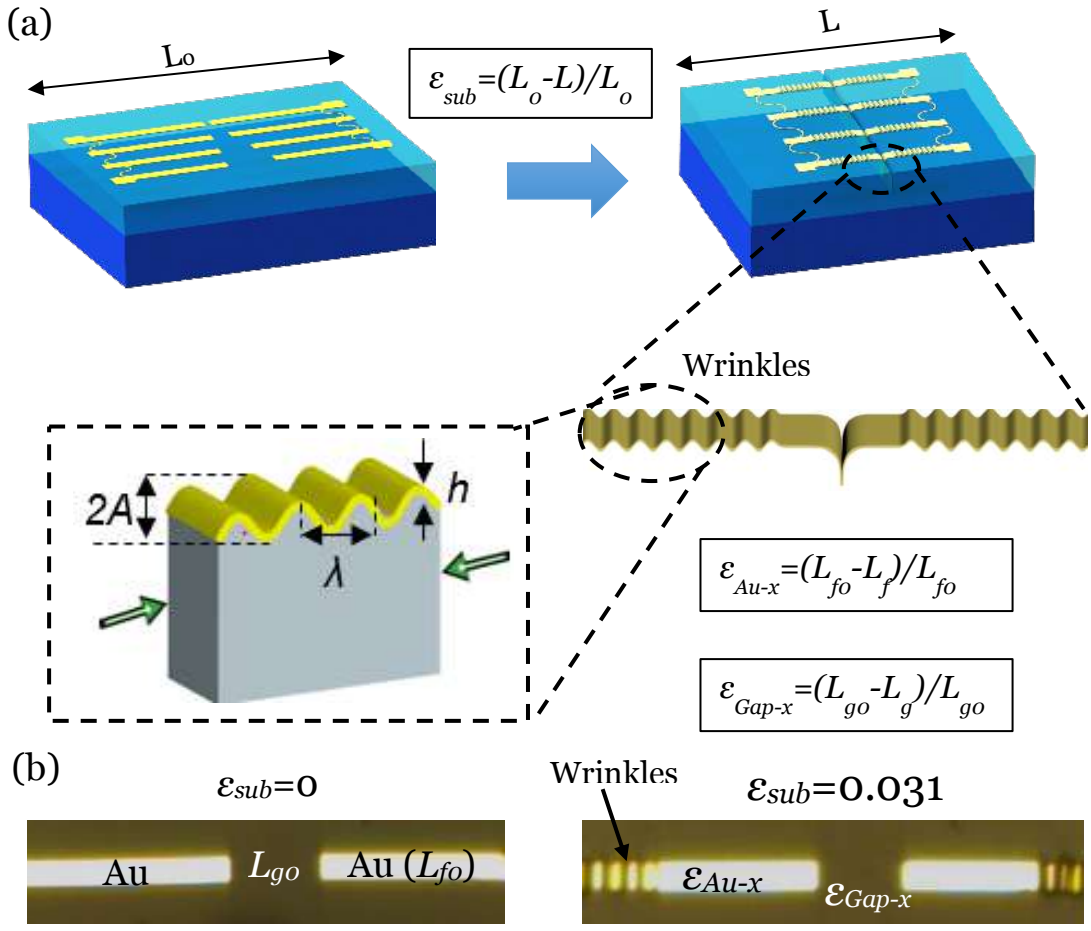

Figure 4.6 (a) 3D Schematics showing the Au wrinkling and PDMS creasing deformation process under uniaxial substrate compression, pair finger electrodes were brought into self-contacted due to PDMS creasing, with wrinkling set on Au finger electrodes (b) Top view optical microscopic image showing local strain changes on Au due to wrinkling, and PDMS gap area due to creasing.

Fig. 4.7a shows the Au wrinkling 3D profiles obtained by Atomic Force Microscopy (AFM Bruker™ 3100) scan with which progressively grew under different substrate strains to ascertain the surface morphology profiler change during the x-direction compression. Based on the critical wrinkling

strain of $\varepsilon_w = 0.25\left(\frac{3\bar{E}_s}{\bar{E}_f}\right)^{2/3}$ from linear stability analysis. The expected theoretical $\varepsilon_w = 6.7\times10^{-4}$ calculated based on the elastic plane-strain moduli of $E_f = 7\times10^{10}$ Pa and 74 nm gold film of $E_s = 4\times10^{5}$ Pa.

In reality, the wrinkles started to form at a substrate strain $\varepsilon_{sub} = 9\times10^{-3}$. This indicates and confirms that the local strains on stiff Au electrodes significantly lagged behind those of the substrate and soft PDMS gap areas, which is welcomed as a helpful technique to protect metal films under large compression strains. The wrinkles on Au continuously grew under further x-direction compression, covering the majority of the Au electrodes at the substrate strain of 0.12. The wrinkle wavelength at substrate strain $\varepsilon_{sub} = 0.12$ was theoretically calculated to be 17 μm according to $\lambda = 2\pi h\left(\bar{E}_f/3\bar{E}_s\right)^{1/3}$, which closely agreed with the actual measured value of 18 μm. **Table. 4.2** summarizes the corresponding values between theoretical and experimental.

Table 4.2 Comparison of theoretical and measured values for the critical wrinkling strain and its amplitude.

Critical wrinkling strain (ε_w)		**Amplitude of wrinkling (λ_0)**	
Measured value	Calculated value	Measured value	Calculated value
9×10^{-3}	6.7×10^{-4}	18 μm	17 μm

Further compression leads to a reduction in wavelength which in agreement with previous findings in [5], [219]. The progressive wrinkling over this range of

strain presumably reflects the influence of the gold film boundaries, as the in-plane dimensions of the electrodes are only several times larger than the wrinkle wavelength. **Fig. 4.7b** shows the cross-section wrinkling profile of the Au finger electrodes sustaining various substrate strains (e.g. 0.009, 0.031, 0.12, 0.34). The cross-section lines were taken from the 3D profile shown in **Fig 4.7a**.

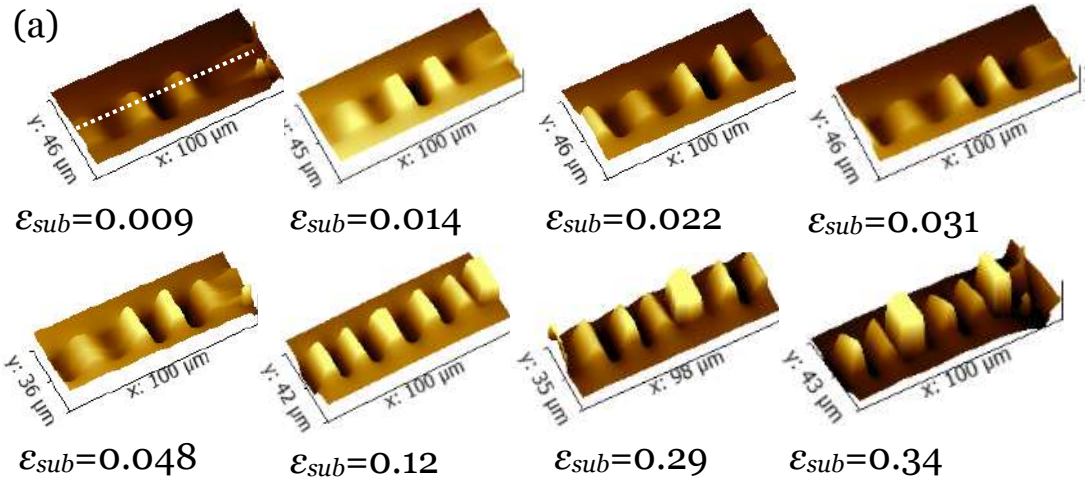

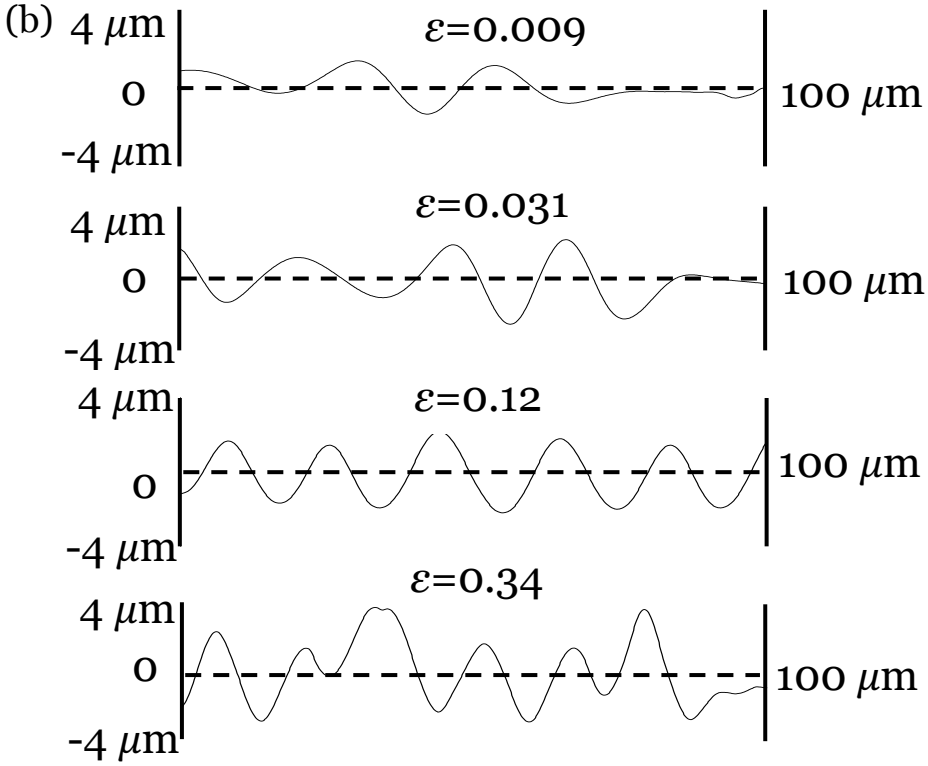

Figure 4.7 (a) Bruker™ AFM scan 3D surface profile view of the wrinkle development on Au electrodes at various substrate strains for a device with W_f = 25 μm, L_g = 50 μm and L_f = 225 μm (b) Cross-section wrinkling profiles for the Au finger electrodes sustaining various substrate strains. These cross-section lines were taken from (a).

To further understand this local strain difference between Au and PDMS areas against the substrate strain, characterization experiments were designed and conducted by using Nikon® LV-100 optical microscope. Study focused on local strains of each Au finger electrodes of $\varepsilon_{Au\text{-}x} = (L_{fo}\text{-}L_f)/L_{fo}$, as well as PDMS gap area of $\varepsilon_{Gap\text{-}x} = (L_{go}\text{-}L_g)/L_{go}$ between the paired finger electrodes. The lengths data L_{fo}, L_f, L_{go} and L_g were all measured by the Nikon system from top view. The relationships between $\varepsilon_{Au\text{-}x}$, $\varepsilon_{Gap\text{-}x}$ and ε_{sub} were comparatively studied against other key geometry design parameters of the Au electrodes such as L_f, L_g, finger width W_f and locations in the transducer array (E, F1 to F4).

For measuring the 2D electrode geometry deformation, ImageJ 1.50i/Java 1.6.0_24 software was used on photos taken by an upright optical microscope (Nikon® Eclipse LV100, with a brightfield reflection mode). To quantitatively study the Au electrode deformation, compression strains were calculated before and during the formation of crease between electrodes by measuring the length change. **Fig. 4.8a** shows the relationship between the Au local strains against the substrate strains. The $\varepsilon_{Au\text{-}x}$ always lagged behind the ε_{sub}, which is indicated by the dash line. The reason behind is that the greater stiffness of the Au electrode induces the disproportion concentrated of the

compression compared with the soft PDMS layer (Young's Modulus of Au is far large that the PDMS). Therefore, when under the same in-plain substrate compression strain ε_{sub}, the deformation for Au and PDMS is not uniform which display a strain lag. The strain gap was observed to be constantly ~0.03, until ε_{sub} = 0.45 where this gap increased to around 0.05 when large creases started to appear on PDMS surfaces which absorbed more strain energy. This has confirmed previous assumption that the local strains on stiff Au electrodes significantly lagged behind those of the substrate. Together with the reversible wrinkling mechanism, most Au electrodes remain intact where no degradation or delamination of the electrodes is observed after > 10 cycles of repeated compression. Essential to determine the switching strain values that brings Au finger pair electrodes into self-contact. A slight hysteresis of around 0.025 in ε_{sub} is observed between loading and unloading cycles. This may because of the viscoelastic nature of the substrate, or the influence of surface adhesion. **Fig. 4.8b** to **4.8d** show detailed comparative study results of the PDMS gap strain $\varepsilon_{Gap\text{-}x}$ versus the substrate strain ε_{sub}. When $\varepsilon_{Gap\text{-}x}$ = 1 at L_g = 0, it was an indication that the PDMS area in the gap was completely folded into the crease from the top view, as illustrated in **Fig. 4.6a**. The corresponding value of ε_{sub} at this point is close to the switching strain.

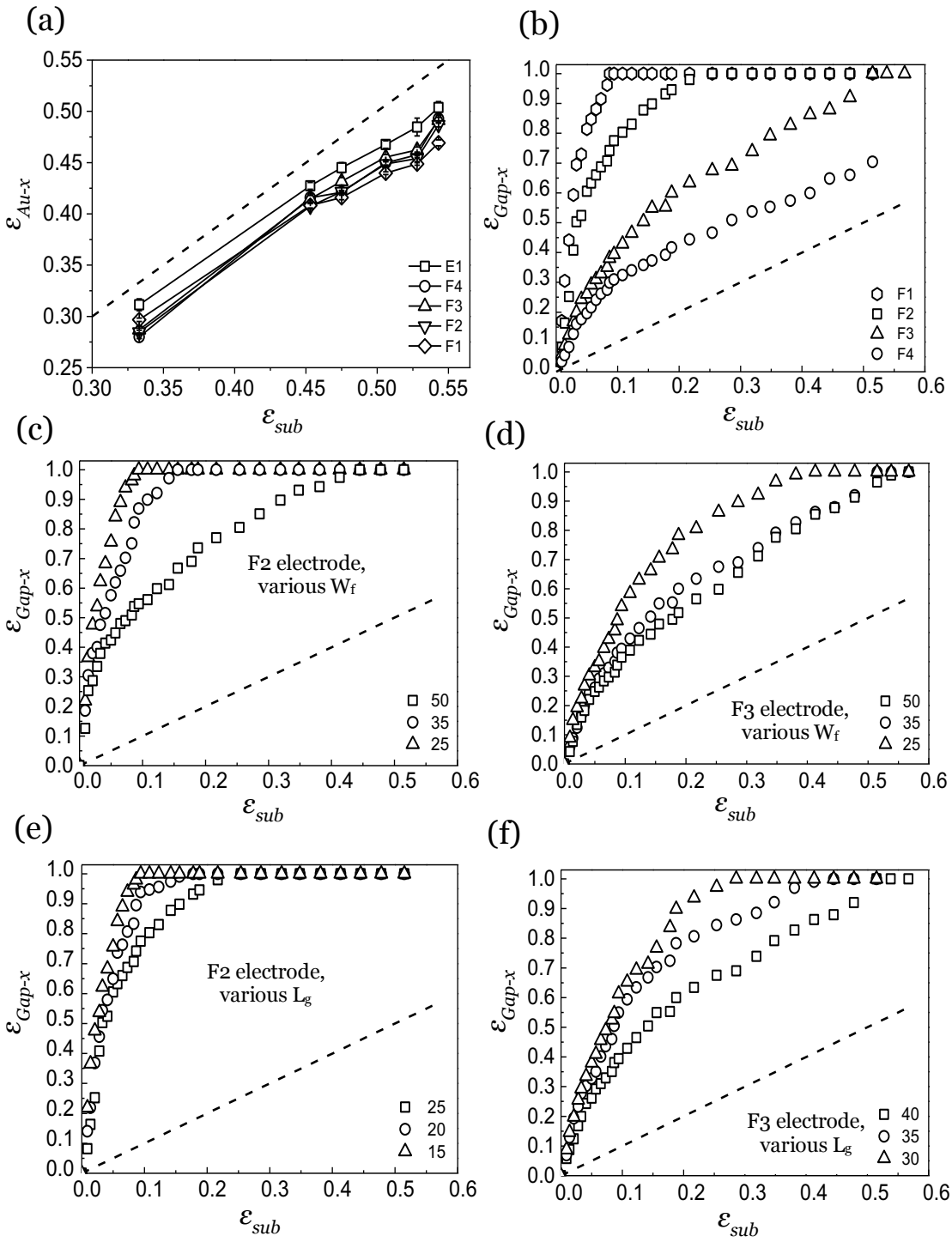

Figure 4.8 Local strain change comparisons: (a) Au electrodes strain vs. substrate strain comparing F1 to F4, and contact pads E1 (b) The PDMS gap strain vs. substrate strain comparing between electrodes with varied L_{go} and L_{fo} (c-d) Finger electrode widths W_f effect on the PDMS gap strain vs. substrate strain for F2 and F3 electrodes (e-f) Finger electrode gap L_g effect on the PDMS gap strain vs. substrate

strain for F2 and F3 electrodes, all dashed lines in figures indicate substrate strain value as a reference.

Fig. 4.8b shows the results comparison between different finger electrodes (F1 to F4) on the same transducer array where W_f = 35 μm, initial L_{fo} ranges from 225 μm to 250 μm, and L_{go} from 10 μm to 55 μm respectively. All $\varepsilon_{Gap\text{-}x}$ are far greater than the ε_{sub} (indicated by dash line) due to the expected strain amplification effect. It can be observed for pair electrode F1 with smallest L_{go}, the self-contact strain is around ε_{sub} = 0.08, significantly lower than typical creasing strains of around 50% on plain PDMS surfaces [5], [121]. As L_g gradually increased, it required much higher substrate strains to bring F2 and F3 pair electrodes into self-contact, at ε_{sub} = 0.2 and ε_{sub} = 0.5 respectively. For F4 electrodes, it is understandable that the large L_{go} made it impossible for the pair of electrodes to reach each other before the 0.6 substrate strain limit in **Fig. 4.8b**, due to insufficient self-contact depth (estimated to around 19 μm) before reaching the limit. Since the natural wavelength of crease is ~3.5 times of substrate thickness of 110 μm in this case, multiple creases may occur at larger distances, which prevents the electrodes from achieving contacts even at higher strains.

Furthermore, finger electrode width W_f (25 μm, 35 μm and 50 μm) effect on gap strain $\varepsilon_{Gap\text{-}x}$ has been compared as well, which shows in **Fig. 4.8c** and **4.8d**. The initial gap distance L_{go} for F2 electrodes in **Fig. 4.8c** was kept at 15 μm while L_{go} for F3 was kept at 25 μm. The electrode lengths L_{fo} are 250 μm and 245 μm, respectively. It was clearly observed in both cases that

electrodes with narrow W_f (25 μm) had much lower ε_{sub} of 0.1 and 0.4, respectively, when electrode pair made self-contact. This suggests a wider Au electrode may require more energy to be pulled into the creasing created in the PDMS gap area, since the electrode prefers small wrinkling. **Fig. 4.8e** and **4.8f** show the finger electrode gap L_g effect on gap strain $\varepsilon_{Gap\text{-}x}$. The finger electrode width W_f for F2 and F3 electrodes were kept at 35 μm. The gap values for F2 electrode various from 15 μm to 25 μm, and 30 μm to 40 μm for F3 electrode. It is understandable that in both cases, the shorter L_g could have lower ε_{sub} for the self-contact of paired electrode.

To have a better understanding of how the finger electrodes been contacted due to the elastic instability of creasing, **Fig 4.9** shows the Au finger electrodes (sequential microscopic images, bright area) and the PDMS gap, before and after the contact caused by instability of creasing. The substrate strains change from 0.38 (**Fig. 4.9** - image 1) to 0.52 (contact point, **Fig. 4.9** - image 5), 0.55 (**Fig. 4.9** - image 6).

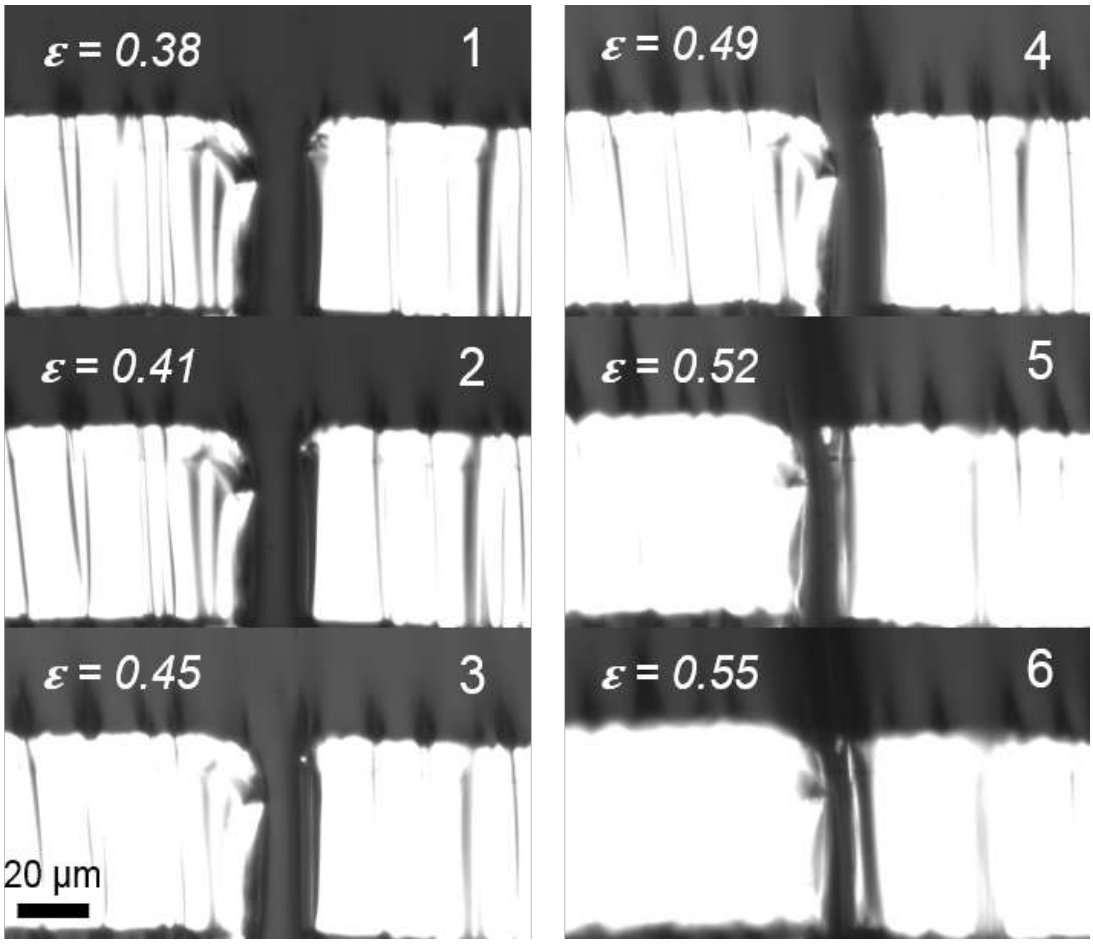

Figure 4.9 Sequential microscopic images showing the Au finger electrodes (bright area) and the PDMS gap, before and after the contact caused by creasing. The substrate strains change from 0.38 (image 1) to 0.52 (contact point, image 5), 0.55 (image 6).

4.3.3 Electrical characterization

Based on the above deformation study, multi-step or "stepwise" electrical resistance change corresponding to different levels of ε_{sub} has been demonstrated. Generally, 2-point electrical measurements are normally used for resistance measurements and I-V curve generation. While when the resistance being measured is relatively low, or the contact resistance or the

resistance of probes is relatively high, 4-point measurement is more accurate because it avoids the errors caused by wire resistance which reduces the effect of test lead resistance. In this thesis, the resistance was currently measured by 2-point measurement, the reasons behind are that in our case, the wire resistance can be ignore due to our large measured resistance. Meanwhile, currently the probes are too sharp and because of the very thin film layer (74 nm thick for Au layer and 110 μm thick for PDMS layer), it is easily to damage the Au electrodes by contacting with four probes.

The Everbeing EB8 manual probe station (with EB-05 probes) connected to a Keithley® 4200 analyzer (I-V mode, -1V to +1V sweep, with 0.2V/step) was used to characterize the resistance value change as shown in **Fig. 4.10a** and **Fig. 4.10b**.

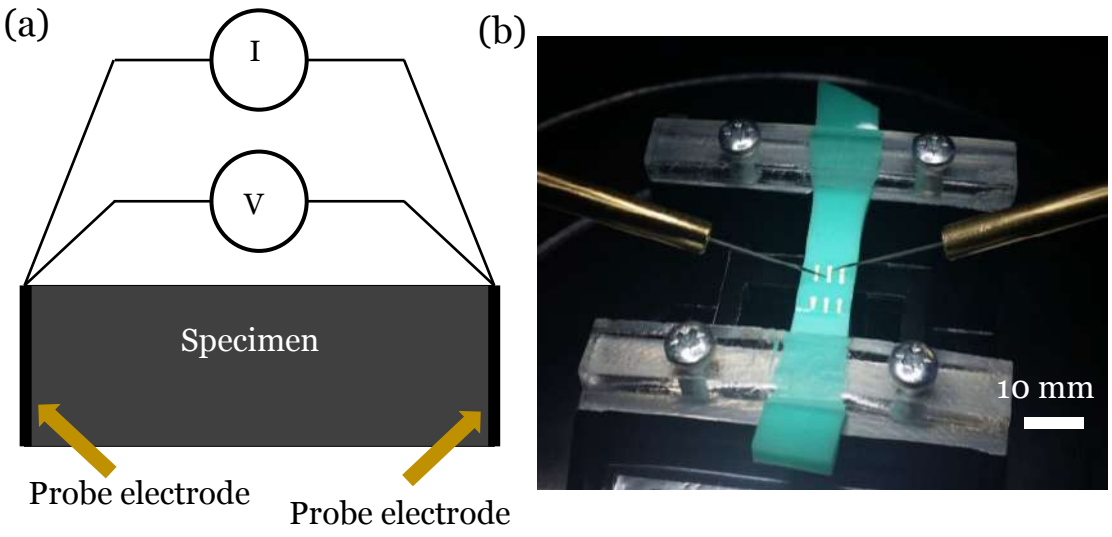

Figure 4.10 (a) schematic illustration of 2-point resistance measurement with (b) photo shows resistance measurement performed using an Everbeing EB8 manual probe station.

For the designed L_g values (L_f = 510 μm and 520 μm, respectively), according to $R_{finger}=R_sL_f/W_f$, where R_s is the sheet resistance (related to the Au thickness), the estimated finger electrode resistance R_{finger} would be in the region of 50 Ω. The relation between sheet resistance and Au thickness is measured by Edinburgh University [266]. It should be noted that due to the conductivity of Si substrate, the sheet resistance of Au on Si could not be detected properly. Hence, the patterned Au finger electrodes had their resistance measured on the PDMS-VPS substrate

Edinburgh University developed a test structure of suspended Greek cross measurement platform to determine the sheet resistance [266]. The arms of the test structures are made of polysilicon/silicon nitride (Si_3N_4). Different thicknesses of Au were blanket evaporated onto the platform. The electrical isolation between the test structure and the surrounding silicon (Si) substrate was ensured by the suspension of the platform. Electrical measurement on Au sample was achieved by using a HP4062B semiconductor parametric test system, a Solartron 7065 voltmeter and a semiautomatic probe station. The extracted average effective resistivity for Au is 5.1×10^{-8} Ω·m [266], which is more than 100% higher than the bulk value of 2.44×10^{-8} Ω·m [267]. Despite the spread in effective resistivity values and the error from the thickness measurements, the extracted effective resistivity agrees with values found in the literature for thin Au films being $3.0\text{-}5.0\times10^{-8}$ Ω·m [268].

The calculated resistance at contacted of each finger electrode from F1 to F4 will be 100 ohm, 50 ohm, 33.3 ohm and 25 ohm respectively when R_{finger} = 50 ohm. **Fig. 4.11** shows the 3D schematic illustrations of Au-PDMS-VPS elastomer system under mechanical compression with the corresponding Au contacted for each pair of finger electrode. Such integrated structures enable a multi-switching sensing mechanism where the strain value can be determined by measuring the resistance of the strain sensors.

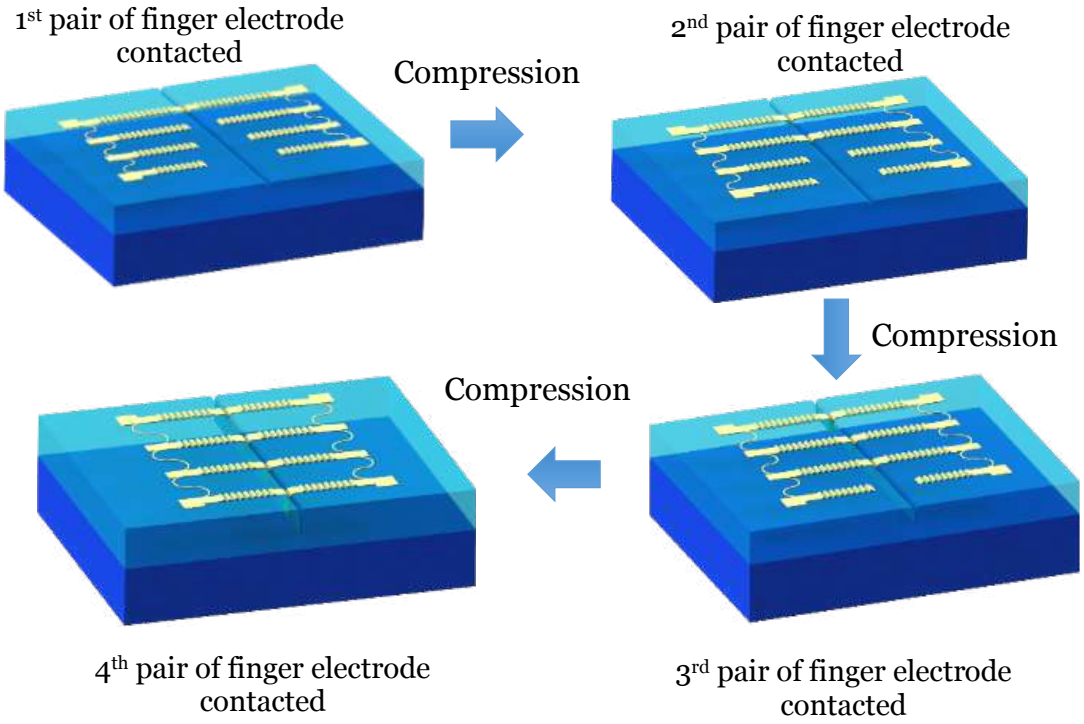

Figure 4.11 3D schematic illustrations of Au-PDMS-VPS elastomer system under mechanical compression with the corresponding Au contacted sequently for each pair of finger electrode.

According to *I=U/R*, in order to avoid the overheating of the Au electrode caused by the large current, the sweep voltage was set -1V to +1V with

0.2V/step. As shown in **Fig. 4.12**, the stepwise strain-resistance sensing has been achieved by surface elastic instability induced multifinger electrodes with different distances between the electrodes. When the first pair electrodes were in contact, the original open circuit changes to be a closed series circuit, the calculated resistance of would be expected to be ~100 Ω, assuming the contact resistance is zero. This will be reduced to 50 Ω when the second switching being achieved (The serious circuit becomes a parallel circuit).

Fig 4.12b shows that between 0.45 and 0.52, the first step switching stage was achieved, with an average resistance of ~120 Ω which is slightly higher than the calculated value (100 Ω), this may due to contact resistance between the microelectrodes in the gap or between the large electrode pads and probes. The average current at first step switching stage is 4.56 mA. Before the second step switching stage, subsequent compression leads to a slight decrease in resistance consistent with the reduction in effective electrode length as more of the gold surface is pressed into contact. Under further compression, the second step switching stage has happened at the substrate strain range of $0.54 < \varepsilon_{sub} < 0.58$ by measuring the average resistance to be ~ 50 Ω with an average current of 14.27 mA. Note that the error bars indicate multiple measurements at different current levels that in most cases indicate that Joule heating is not influencing the measurement. The probe-Au electrode contact resistance was characterized to be ~7.9 Ω with a standard deviation of 1.17. The variation of the experimental resistance values may

mainly be caused by the contact resistance between the touching Au finger electrodes. The corresponding substrate strains at switching were also in good agreement with the electrode deformation observations.

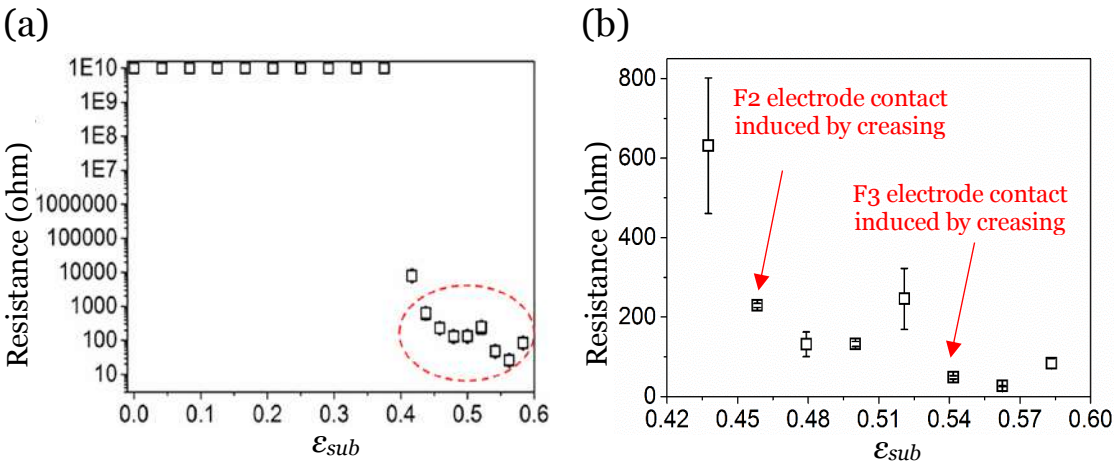

Figure 4.12 (a) Resistance of the structure as a function of strain. The resistance change during the two-stage switching are highlighted in a red ring and detailed in (b) Two-stage resistance switching strain sensing: Resistance of the transducer array as a function of strain during the two-stage switching period (0.45< ε_{sub} <0.52, and 0.54< ε_{sub} <0.6).

4.3.4 Poisson's effect caused damage and improved interconnects design

Poisson's effect is used to describe the expansion of a material in directions perpendicular to the loading direction, where Poisson's effect is measured by Poisson's ratio *v*. During the substrate compression process where there is a large strain change from 0 to 0.6, it is inevitable that tensile transverse strains (y-direction) perpendicular to the compression direction (x-direction) with $G=E/2(1+v)$, which generated by the uniaxial compressive strain change

due to the Poisson's effect (where *G* is shear modulus, *E* represents Young's modulus and *v* is the Poisson's ratio).

In order to understand how x-direction compression affects the y-direction tension, the length changes between x and y-axis have been experimentally measured as shown in **Fig 4.13a**. The Poisson's effect is defined as $\nu_p = |\Delta Y/\Delta X|$, where $\Delta Y = YY - YY_o$ and $\Delta X = XX - XX_o$, YY_o and XX_o are the original length. **Fig 4.13b** shows the relation between substrate compression strain (0-0.6) and Poisson's effect.

(a)

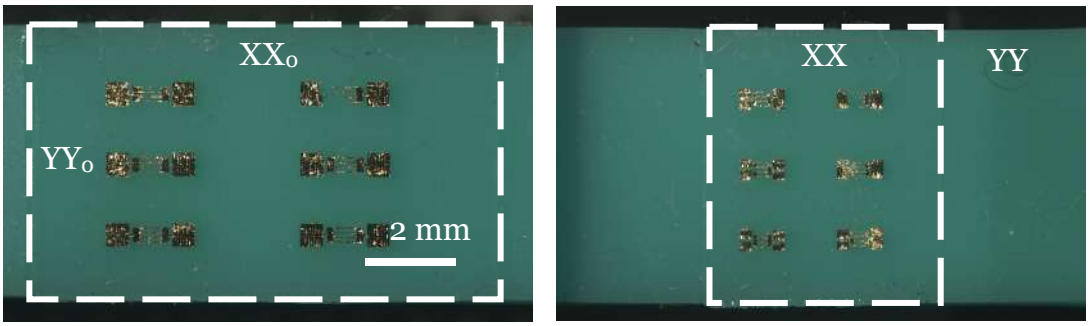

(b)

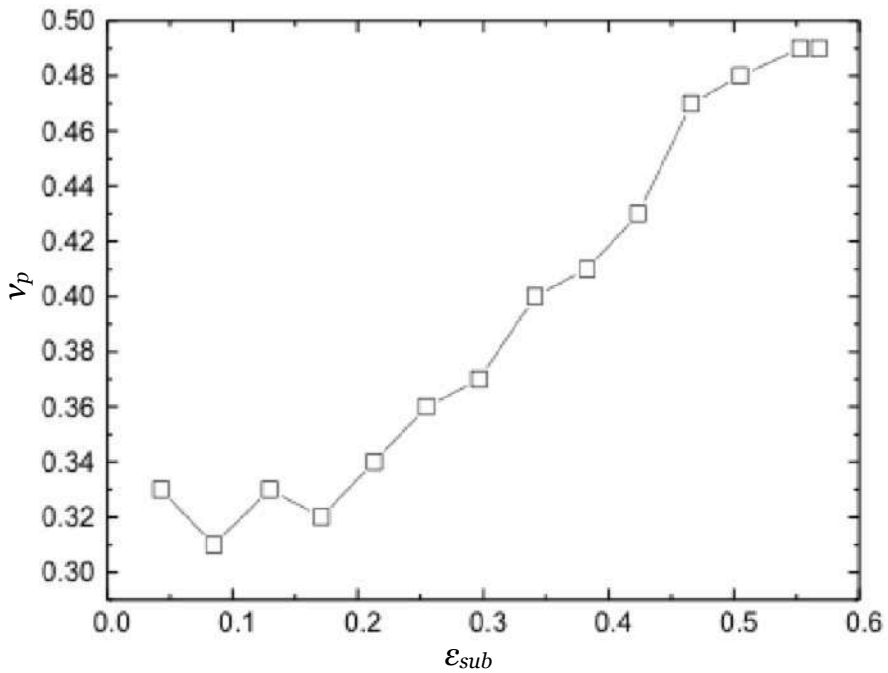

Figure 4.13 (a) Photos show the experimental measurement of length change at x and y-axis during x direction compression (b) relation between the substrate compression strain and Poisson's effect.

As shown in **Fig. 4.14a**, this non-uniform strain distribution causes the unwanted damage (cracks) to some bulk interconnection part of (typical fracture strain >> 1%) the transducers when substrate strain went above 0.25. In order to prevent such damage, serpentine shaped Au interconnects have been designed to "bridge" connect finger electrodes "islands" across the serpentine spacing W_g in some devices.

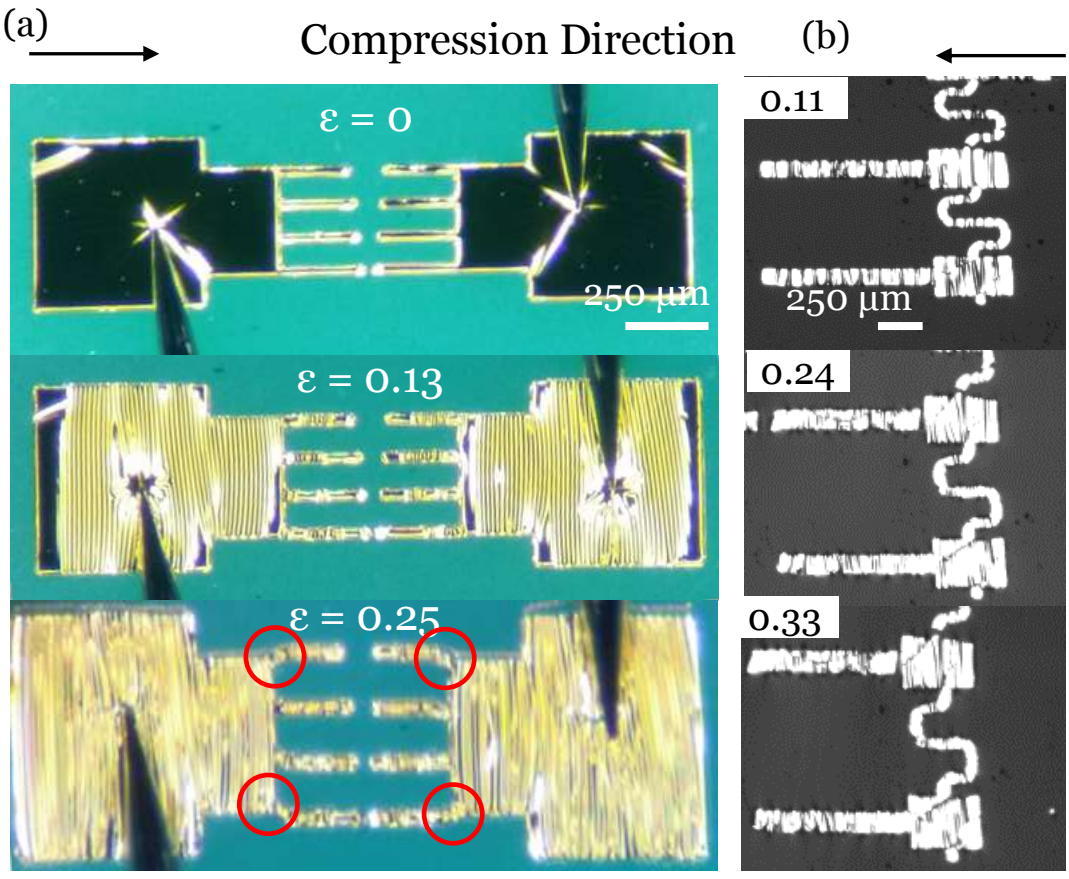

Figure 4.14 (a) Consecutive microscopic images at various substrate strains on bulk interconnect electrode devices with probing needles (dark coloured) in the view.

Circled areas started showing interconnecting areas of F1 and F4 finger electrodes being stretched due to Poisson effect (b) Consecutive microscopic images showing serpentine shaped structure significantly reduced interconnects stretching from Poisson effect up to 33% substrate compression.

Fig 4.14b shows the effect of y stretching onto the gap serpentine as substrate strain increases. It successfully prevented cracking damage for substrate strains up until 0.33. The interconnecting areas of finger electrodes F1 and F4 started to sustain certain degrees of damage beyond 0.35, while F2 and F3 remained intact up to 0.6 substrate strain. Future work will focus on optimizing the interconnect designs for better protection.

4.4 Chapter Summary

In summary, a new strategy has been established to detect the multiple strain values on a soft elastic substrate to study the metal-elastomer deformation behaviour of a super-compressible strain transducer array. The concept has been presented in which elastomeric substrates with engineered distributions of a set of materials and structural characteristics yield stepwise strain sensing of in-plane deformations. The relationships between electrode geometries and compression strain ratios have been studied, together with the growth and co-existence of wrinkles and creases on multi-switching electrodes. Multi-steps of electrical resistances were generated at different switching strains on an individual device. This has been demonstrated by using the arrayed and interconnected “multiple finger” electrode soft electronics with different distances between the electrodes, the related

technologies and newly developed sensing mechanism could shed a light on the future stretchable/epidermal electronics, flexible sensors, health monitoring, and wearable device applications.

Chapter 5

A Flexible Topo-Optical Sensing Technology with Ultra-high Contrast

Targeted folding of elastic surface at a pre-defined location controlled by patterned micro-hole arrays thin hard layer can be harnessed to develop novel sensing mechanism. Switchable high contrast luminescent patterns responding to mechanical compression (up to 60%) of the super flexible elastomer substrate have been created under photoexcitation and studied in this chapter.

Inspired by the way the outer layer of plants and animals can change colour in nature, and the phenomenon of Mechano-Responsive Luminescence (MRL) (described in section 2.3.2), this topo-optical strain sensing strategy has been demonstrated by employing PDMS based functional luminescence composites multi-thin layer structure, where fluorescent pattern signal was generated at designed strain values. Line-shaped fluorescent patterns were switched ON and OFF by elastic instabilities (e.g. creasing, folding) on micro-structural soft surfaces during compressive deformation. Furthermore, optical pattern contrast can be highly improved by inducing specific fluorophore material (Iridium-III complex) to diminish the background fluorescent signal. The unique self-contract geometry of folding area preserves intensity by mechanically creating a hypoxia zone, whereas the

intensity reduces significantly for the rest area of surface due to the oxygen quenching of a certain Iridium-III fluorophore material at the open air. This study bridges the gap in current mechano-responsive luminescence mechanism by utilizing the unwanted oxygen quenching effect of Iridium-III (Ir-III) fluorophores to enable a high contrast optical signal on surface. The key objectives in this part of my work is to investigate:

- Controllable formation of targeted creases/folds.
- Translate this topographical transition into a dedicated sensing signal (e.g. optical patterns) in responding to certain compressive strain.
- The optimisation of contrast by selectively oxygen-quenching of the coated Iridium-III complexes fluorophore layer.

5.1 Introduction

Developing flexible optical sensors and actuators have hold promises in many applications areas, especially mechano-responsive luminescence (MRL) based flexible optical sensors as described in section 2.3.2. However, the optical performance has been discounted by aggregation caused quenching (ACQ) [242], [243], thus limit the further applications for MRL materials. Whereas the current advances in Aggregation-induced emission (AIE) have achieved emergence characteristics at molecular level to overcome the drawbacks of ACQ [244]-[246], novel optical sensing mechanisms remain yet to be exploited to enable wider scale-up perspectives.

Inspired by epidermal colour changing scheme from nature, researchers have been able to amplify signal contrast by generating luminescent molecular dominos [171] thus realize multi state optical switching by engineering micro/nano-structures on surface [235]. By far, all practiced strategies rely on molecular/particle arrangements under mechanical stimuli, which will easily result into a noisy and low-resolution signal, which poses challenges in triggering controllable signals for scalable applications.

5.2 Research development

Different to the majority of current MRL material development as described in section 2.3.2, which is mainly focused on liquid crystal for colour-tuning [171], mixing the different coloured MRL/ML particles [69], combination of fluorescent dyes physically with existing MRL/ML materials [172], or swelling based fold-in induced to selectively form some surrounding chemical patterns [81]. The surface topology enabled optical sensing in response to large compressive strain has not been reported elsewhere.

Therefore, a different strategy of controllable mechanoluminescent pattern generation has been demonstrated, by triggering hypoxia induced photoluminescent inside surface-folding elastic instability (creasing) generated on multilayer elastomeric substrates under large compressive strain (up to 60%).

5.3 Results and discussion

5.3.1 Surface instability growth in multi-layer elastomer systems

Discussed in section 2.2, a classical bi-layer elastomer system typically consists of a soft layer on a stiff mounting layer. For example, PDMS thin film (Young's modulus 48 KPa) and PDMS stiff mounting substrate (Young's modulus 800 KPa) (similar to [103], [120]). While in this project, a tri-layer system with Young's modulus mismatch across different layers has been created, with an additional third thin hard-skin layer on top of PDMS film. When releasing the plasma treated (10s) pre-stretched tri-layer elastomer system (hardskin-PDMS-VPS layers) over a critical value as shown in **Fig. 5.1a**, in-plane uniaxial compressive strain $\varepsilon_{comp} = \frac{L_0}{L} - 1$ can be generated. The plain elastic surface deforms and undergoes a complex morphology change under various compressive strains, yielding an elastic morphological development (e.g. instabilities transition from wrinkles to creases/folds) on the surface. The formation of surface wrinkles releases in-plane compression of the hard layer to release stress. After applying further compression, the wrinkles develop bifurcations to randomly generate the creases/deep folds as shown in **Fig. 5.1b** and **Fig. 5.1c**. The sizes of these creases, e.g. depth and width are in the micrometre scale, with lengths varied from micrometres to millimetres when substrate strain goes above 52%.

The stress-strain curve of the multi-layer system largely follows the mounting substrate layer with dominant thickness over PDMS (3 mm VPS and 125 μm

PDMS). The typical depth of the surface instabilities is very shallow (1 to 18 μm) when compared with the much thicker and stiffer VPS mounting substrate (3 mm thick). Therefore, the generation of surface instabilities does not affect the overall stress-strain curve of the whole system. And the stress-strain curve of standalone PDMS with various mixture ratios has already been well researched [269], [270], [271], [272], [273].

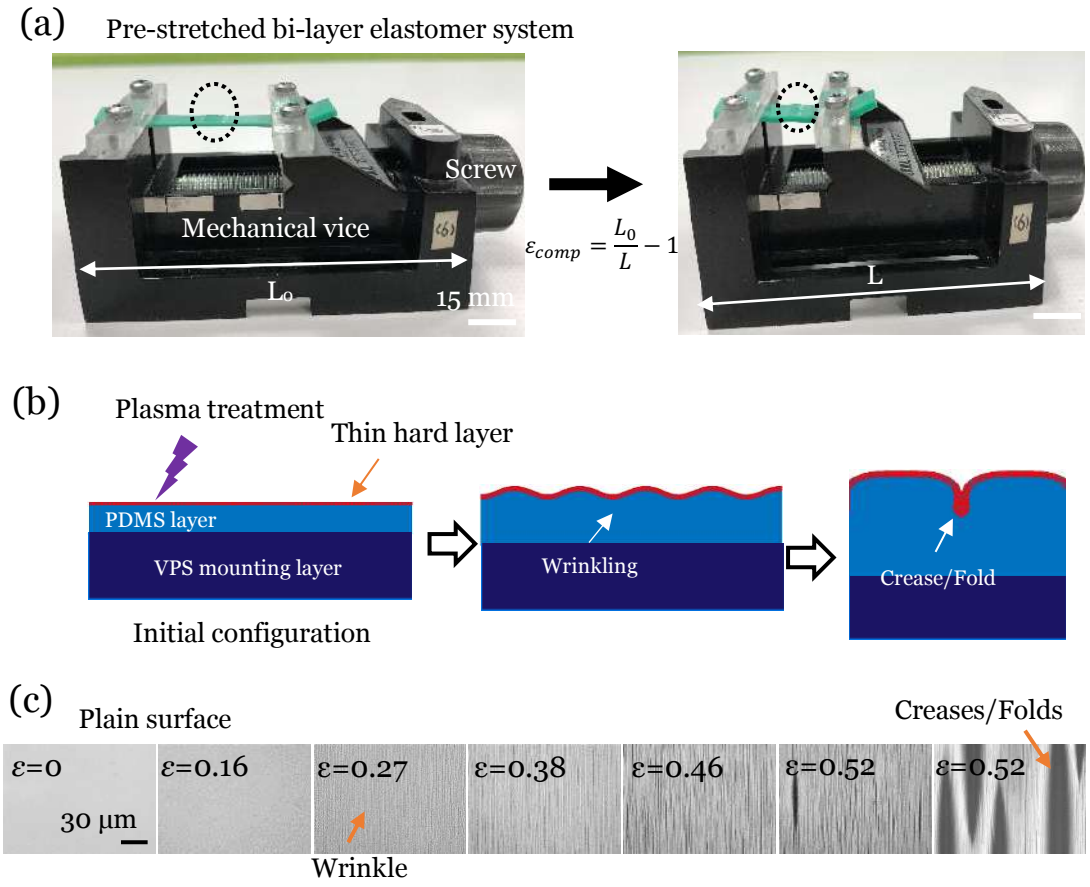

Figure 5.1 (a) Pre-stretched tri-layer elastomer system (left) with under mechanical compression process (right) (b) Schematic illustration of the instability pattern evolution transition on a tri-layer elastomer system (hardlayer-PDMS-VPS) under mechanical compression with (c) Nikon optical microscope view.

5.3.2 Configuration of targeted folding on elastic multilayer

For the plain surface shown in **Fig. 5.1c**, creasing/folding morphology evolves at random location when applying a uniaxial compression strain $\varepsilon_{comp} = \frac{L_0}{L} - 1$. In order to guide a more regular pattern generation for controlling the local energy concentration and spatial location of the required deep creasing patterns, e.g. parallel lines of deep creases/folds. Lattice single and multi-line array patterns have been designed.

Fig. 5.2a shows the illustration of designed patterns that consist of arrays of circular holes with different diameters Φ, distance of D, thickness h and width distance W. **Fig. 5.2b** shows the schematic illustrations of the morphological changes on plain and patterned surface. With the designed structures, the arrays of circular holes (aligned in y-direction) on PDMS surface helps to control surface creasing patterns during uniaxial compression, by concentrating the local energy to promote local strain concentration. Therefore, the regular surface creases/folds are expected to form along the column of holes perpendicular to the compression axis in **Fig. 5.2c**, when compared with the plain surface in **Fig. 5.2d**.

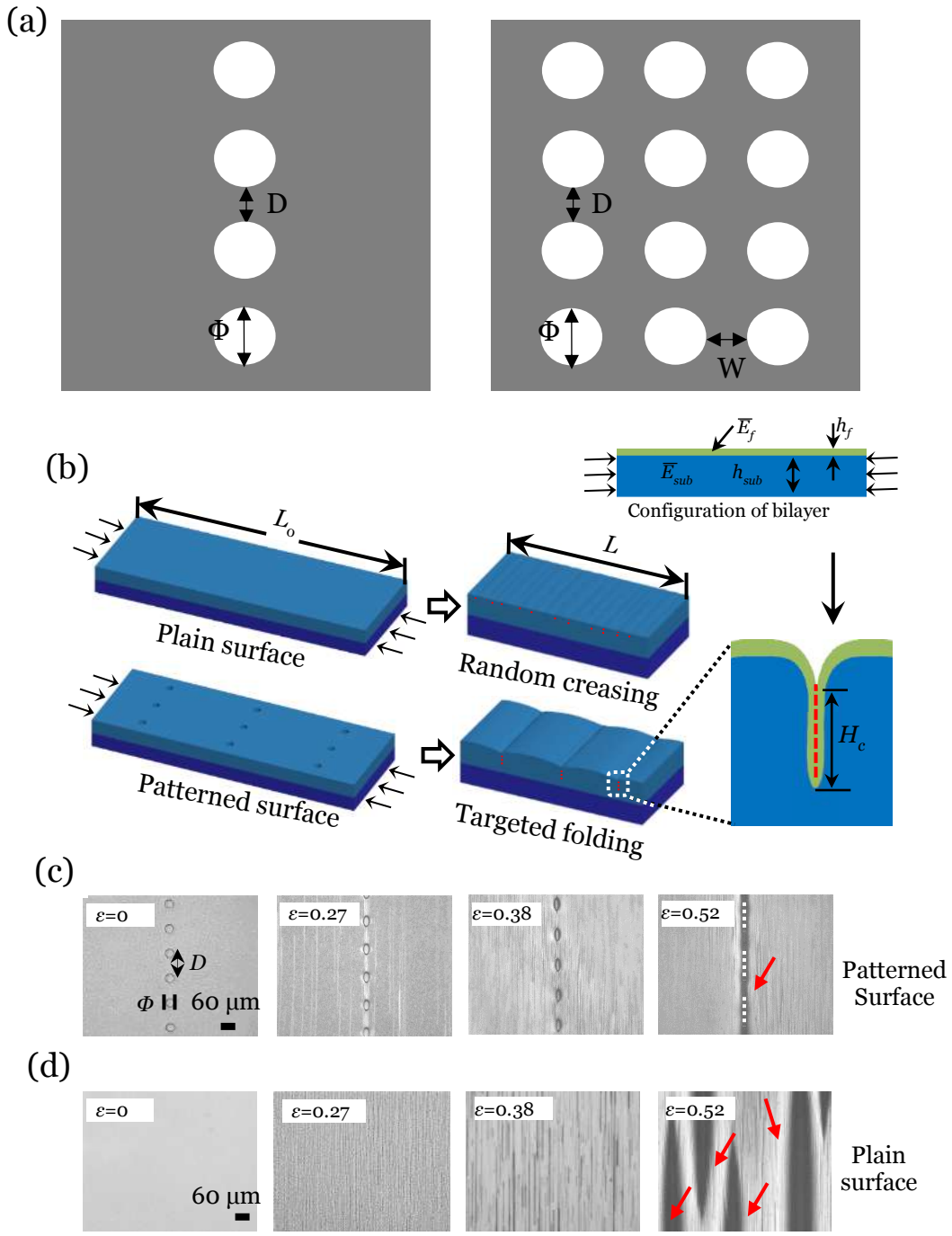

Figure 5.2 (a) Illustration of patterned micro single and multi hole array structures with different parameters (b) Illustration of a 3D schematic drawings for plain and patterned surface (c-d) optical microscopic images showing organized and random surface crease/fold patterns induced by mechanical compression on patterned and

plain surfaces with designed hole-array (Φ=60μm, D=120 μm, h=12 μm) respectively, at different compression strains of 0, 0.27, 0.38 and 0.52.

Fig. 5.2c and **5.2d** show the comparison of morphology evolution between plasma treated plain and patterned surface (single array of circular micro-holes, diameter $\Phi = 60\ \mu m$, gap ratio $r = \frac{D}{\Phi} = 2$, hole depth $h = 12\ \mu m$) observed by Nikon Eclipse™ LV100 optical microscope. Wrinkle patterns are developed globally for both plain and centre lattice hole patterned surfaces at low compressive strains and evolved into visible textures when strain increases to ε = 0.27. A strain energy localization guided by the pre-placed pattern can be clearly identified along the micro-holes array. The surface presents a post-wrinkling development with mixed morphologies at middle compressive strains (i.e. ε = 0.38). According to Kim and co-workers, surface wrinkles will first undergo period doubling, followed by the formation of creases under a modulus ratio (G_f/G_{sub}) between 5.86 and 13.89 [158], [163]. A threshold strain (ε_{th}) is the compressive strain when the first fold occurs on surface, which is experimentally defined at when a large crease connects the adjacent holes during in-plane (x-y) pattern development with the fold in depth above 2 μm. Here, a compressive strain of ε = 0.52, which is slightly higher than ε_{th}, is chosen to compare folding conditions at same energy level. A few random folds have been observed (pointed by red arrows) in **Fig. 5.2d** on the plain surface, while a single big fold locates at the area that is defined by the pre-placed holes on surface (dotted line) in **Fig. 5.2c**.

The in-plane strain energy localization that triggers crease generation is guided by the curved geometrical boundary from the hole patterns. To investigate such morphological pattern generation with various hole array designs, the in-plane (x-y plane) and out-of-plane morphology development has been studied at different substrate compressive strains under reflected light Nikon optical microscopy (Nikon Eclipse™ LV100) shown in **Fig. 5.3a**. To have a more detailed understanding of the surface morphology changes when gradually increasing the in-plane uniaxial compressive stain, Bruker Atomic Force Microscope (AFM) has also been used. Two regions of stress concentration areas have been focused which indicated as region 1 and 2 in **Fig. 5.3b**. The morphology evolution on a surface with a single-line circular hole array ($h = 12\,\mu m, \Phi = 80\,\mu m, r = D/\Phi = 2$) at various compressive strains of 0, 0.04, 0.14, 0.16, 0.27, 0.38, 0.50, 0.52, 0.55 have been characterized. For hole patterned surface (Φ=80 μm and D=160 μm), the wrinkling has been found to start at a small compression strain of ε=0.04 at region 1. When increasing the compression strain, the small crease firstly start to nucleate at ε=0.14 between holes, and continue to growth at ε=0.38, until two large creases evolved from apexes of the two adjacent holes and connected each other in the midway at a threshold strain ε_{th}=0.52. The self-fold surface keep growth with the increasing of the compressive strain to ε=0.55 as shown in **Fig. 5.3b** and **5.3c**.

The normalized wrinkle amplitude of A/λ_o at region 1 of **Fig. 5.3a** has been plotted as a function of the compression strain shown in **Fig. 5.3d**, which the

bifurcation of wrinkle to crease transition is observed. The critical wrinkling strain is found to start at ε_{sub}≈0.04. When keep increasing the compression strain, the critical strain for wrinkle-crease transition is ε_{sub}≈0.14. It can be seen that these values are considerably lower in the hole patterned system, which highly agreed with the comparison results for nonpatterned and Bravais lattice patterned surface [75]. In their research, the critical strain of wrinkling and the wrinkle bifurcations for patterned surface were found to be smaller when compared with nonpatterned system [75]. The reason behind this threshold reduction effect is due to the stress concentration at the edge of the hole relative to the nonpatterned system, the compressive stress is strongly enhanced at the edge of hole and therefore causes reduction in the various thresholds.

(a)

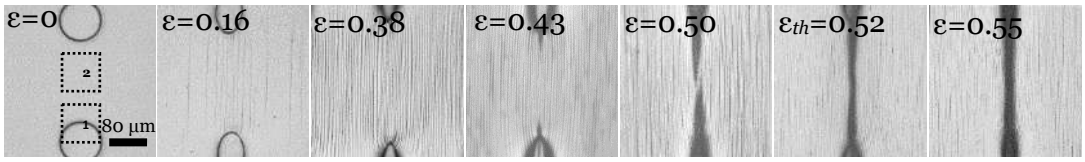

(b)

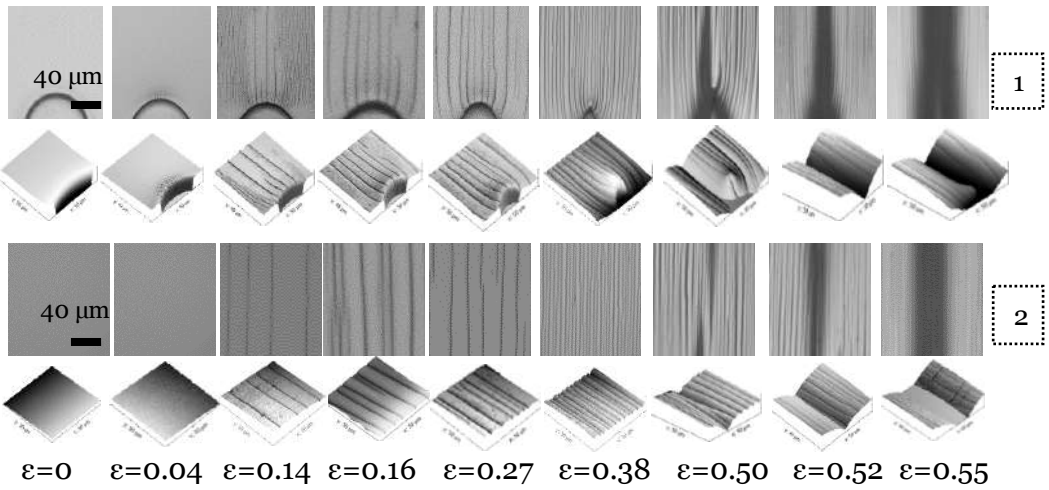

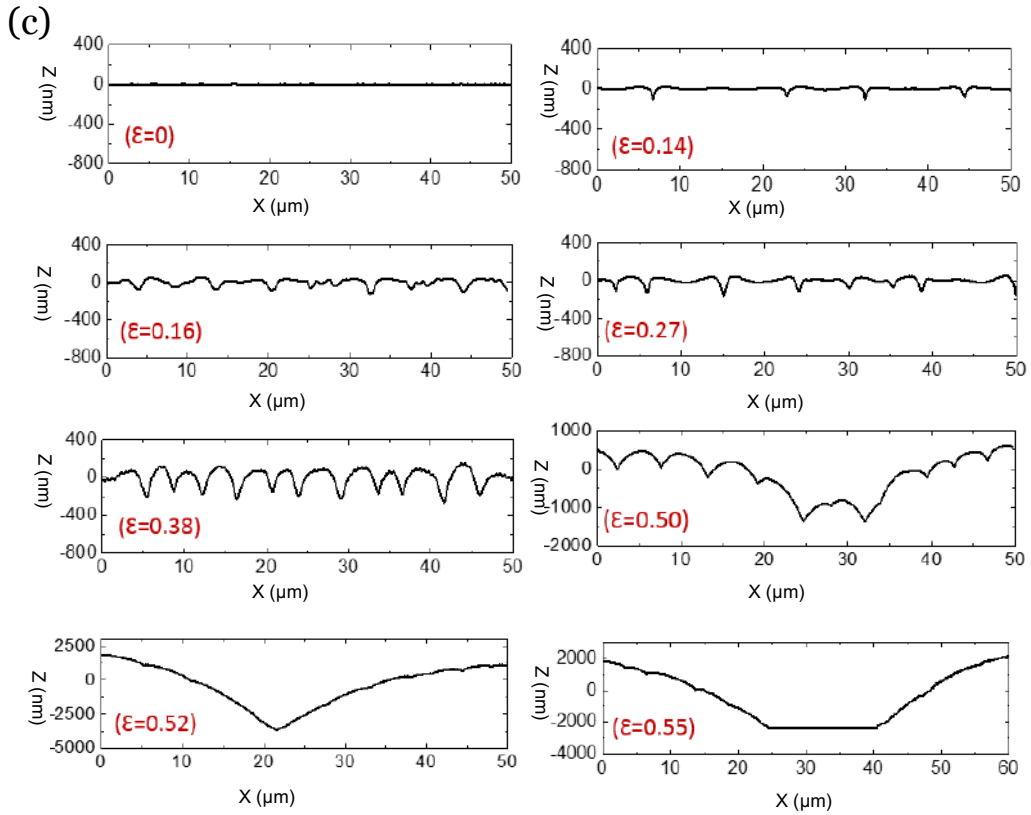

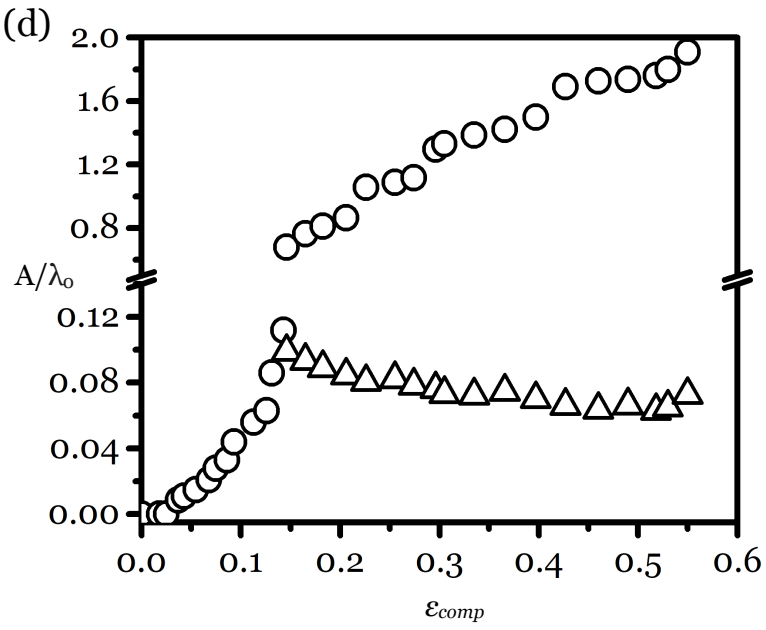

Figure 5.3 (a) The observation of surface morphology evolution on patterned surface at different compression strains by Nikon optical microscopic and (b) AFM and Nikon optical microscopic view of hole-patterned (*Φ=80 μm* and *D=160 μm*)

surface showing the surface evolution growth during uniaxial compression at different strains of 0, 0.04, 0.14, 0.16, 0.27, 0.38, 0.50, 0.52 and 0.55 with two regions of 1 (near the hole) and region 2 (middle area) (c) the surface morphology development plotted which depended on the compression strain at region 2 (d) normalized amplitudes changes along with wrinkle to crease transition, represented with first order (o) and second order (Δ).

Apart from the micro-hole patterned surface, in order to investigate the tuneable strain-related response, i.e. characterize the threshold strains ε_{th} for pattern generation, the hole array designs have been varied with different shapes (circle, diamond, triangle and hexagon) and array geometry parameters displayed in **Fig. 5.4a**.

Fig. 5.4b demonstrated the relationships of pattern generation threshold strain vs. surface structure geometry with varied gap ratio D/Φ from 1 to 5, the size of the pattern Φ is 40 μm. As expected, in a 1D circular hole array, holes closer (smaller D/Φ ratio) to each other were connected by large crease at significantly lower compression strains. In **Fig. 5.4b**, the experimental results seem larger than the simulation results for $\Phi = 40\ \mu m$, but good agreements on the overall trend are obtained for the surface, even for those surfaces patterned with different D/Φ. It should be noted that the surface has been slightly over-compressed to determine the closure stage for each hole under reflective optical microscope, due to the visco-elastic nature of surface and the out of plane deformation when the hole closes. Therefore, the experimental ε_{th} values are likely to be slightly larger than the simulated ones.

This trend appears in regardless of patterned shapes after testing varied shapes (circles, diamonds, triangles and hexagons) and different D/Φ as shown in **Fig. 5.4d, Fig 5.4e, Fig 5.4f and Fig 5.4g**. It can be observed that with a fixed depth h of 12 μm, where a range of ε_{th} from 0.38 (diamond angle 60, Φ = 20 μm, $\frac{D}{\Phi} = 1$) to 0.6 (diamond angle 90, Φ = 80 μm, $\frac{D}{\Phi} = 5$) can be achieved by designing the varied shapes and different D/Φ. The relationship of pattern generation threshold strain vs. depth of lattice pattern has been studied as well with varied Φ from 20 to 80 μm. However, as indicated in **Fig. 5.4c**, the ε_{th} shows less sensitivity on the depth of lattice pattern, which agrees with the formal reported results on configuring the wrinkle patterns using Bravais lattice [121].

(a)

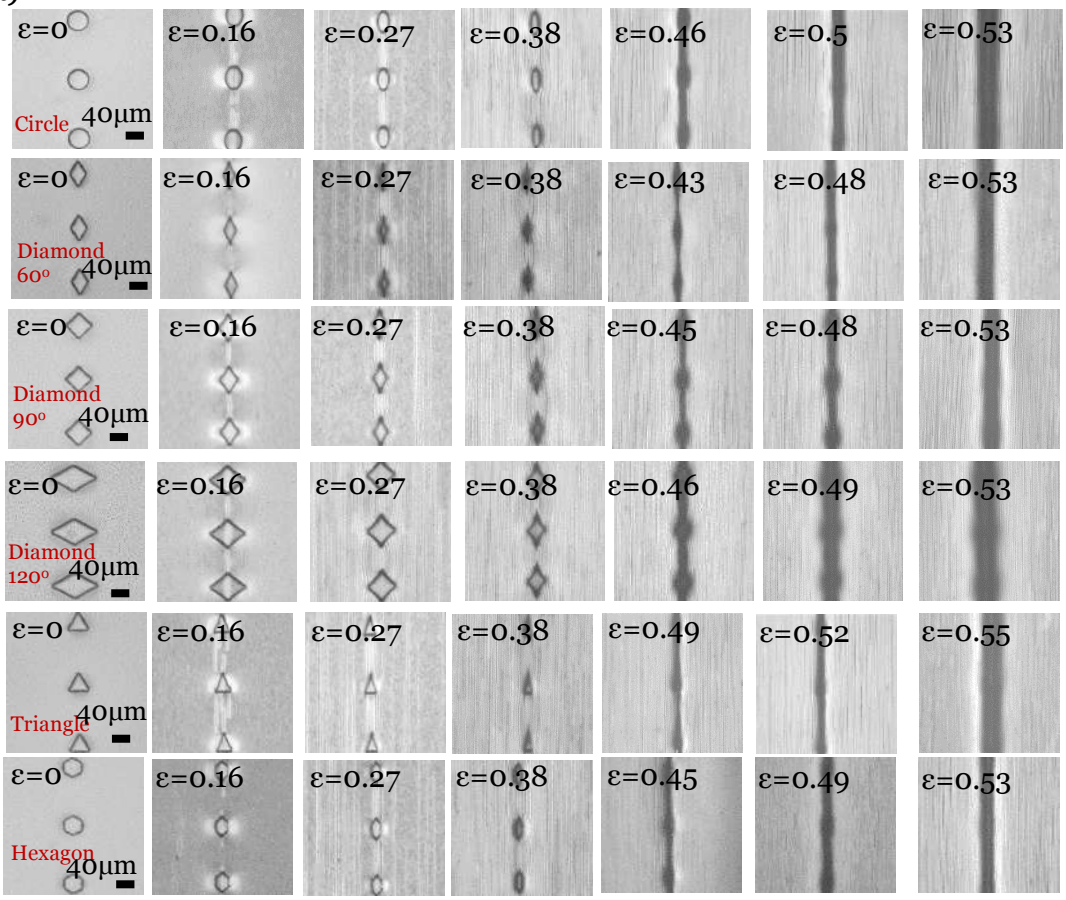

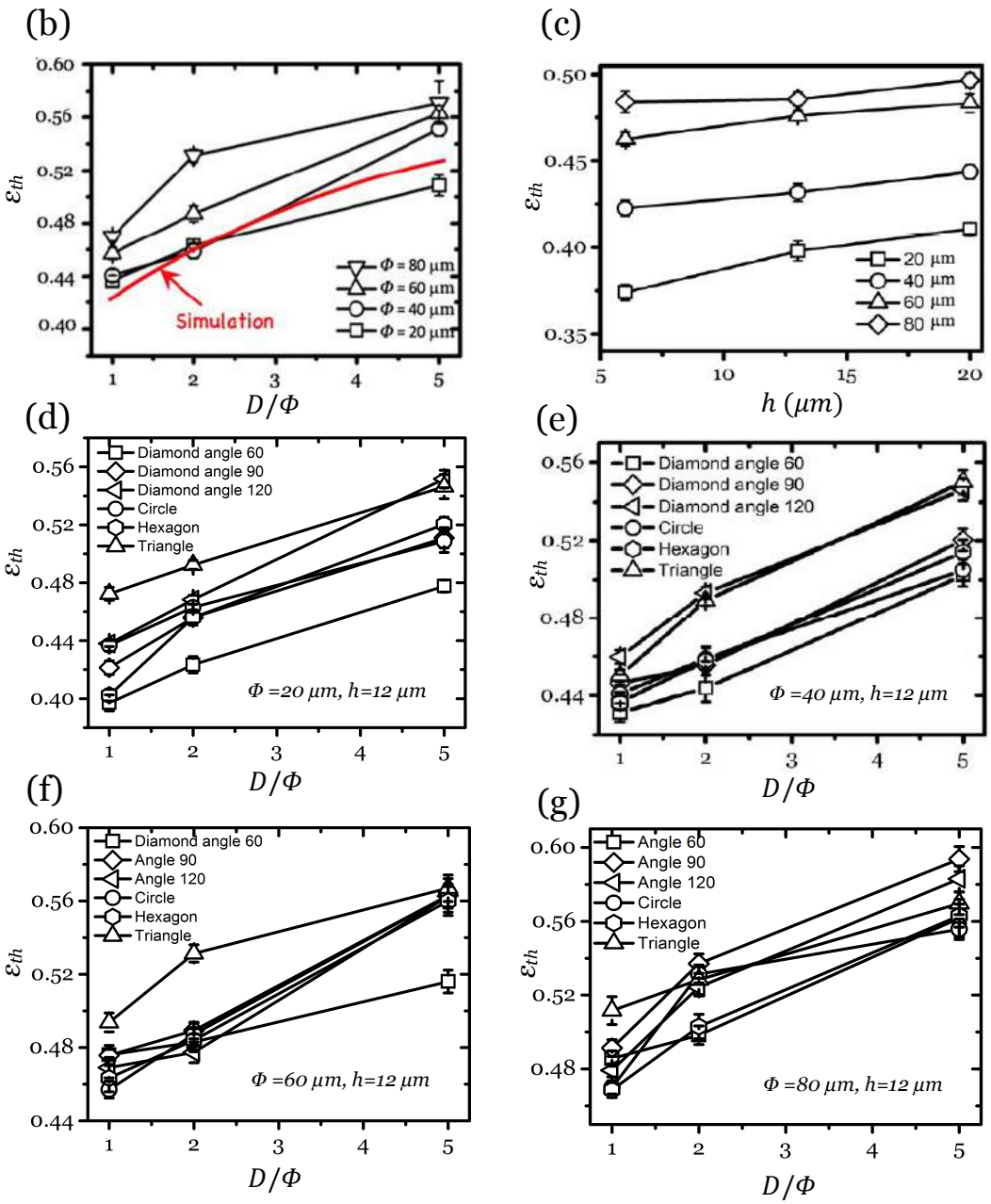

Figure 5.4 (a) Nikon optical microscopic view of designed and fabricated single micro-patterned arrays with different shapes (circle, diamond, triangle and hexagon), showing the surface evolution growth during uniaxial compression at various compression strains (b) Comparison of the simulated ε_{th} (threshold strain of hole closure) with experimental ones at different D/Φ for the surface with a single hole array. (c) Summary of threshold strains to achieve targeted folding with dependence on the hole depth. (d-g) Large creasing/folding generation threshold

strain vs. D/Φ for circular, diamond, hexagon and triangle shapeed holes with Φ = 20 μm, 40 μm, 60 μm and 80 μm.

5.3.3 Simulation of self-contact depth guided by surface lattice pattern

Following the surface morphology evolution, numerical analysis was performed with commercial finite element simulation software–ABAQUS, to understand the mechanism of generating targeted folding. **Fig. 5.5a** shows the material properties in ABAQUS FEA. Neo-Hookean material model is chosen. The parameter C10 in the table is equal to half of the shear modulus, and D1 is set to 0, which corresponds to incompressible materials, i.e. Poisson's ratio = 0.5.

The single arrays of holes with varied geometrical inputs are considered to simulate the in-plane and out-of-plane strain energy localization. By comparing the simulation results for D/Φ=1 and D/Φ =5 as indicated in **Fig. 5.5b** and **Fig. 5.5c**, which showing that a concentrated in-plane strain localisation for D/Φ=1 is stronger than that for D/Φ=5. The out-of-plane (cross-section) simulation results suggest a progressing deformation with the closure of hole (initiation of H_c), development of H_c as a folded contact with non-contact at the bottom, then finally reaching a fully self-contact stage (creasing type).

(a)

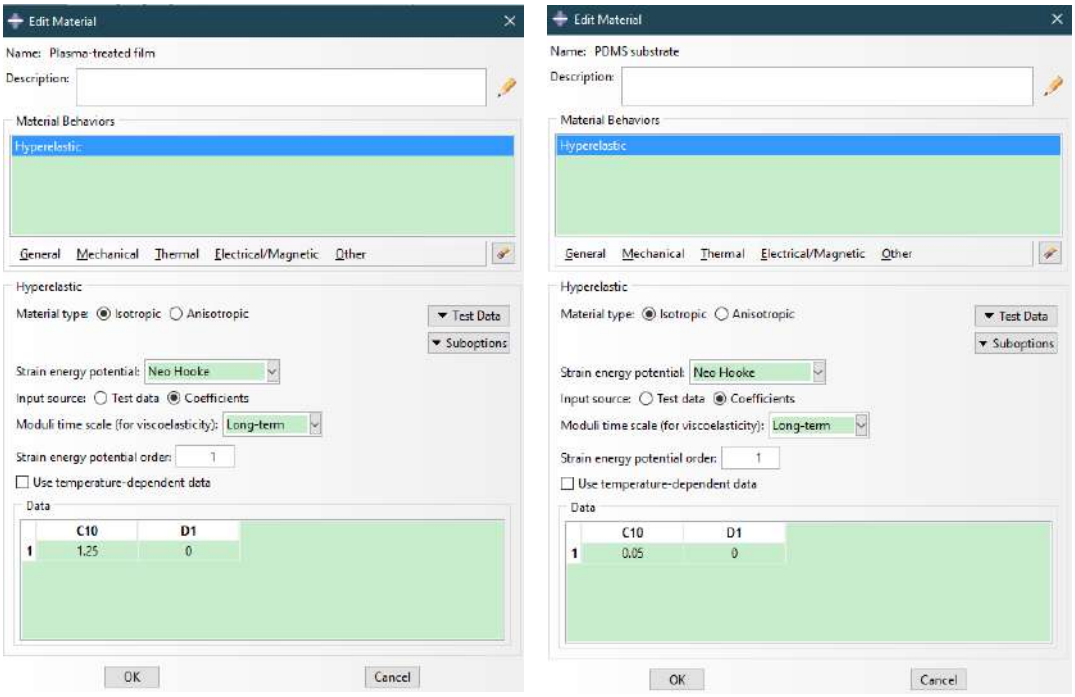

(b)

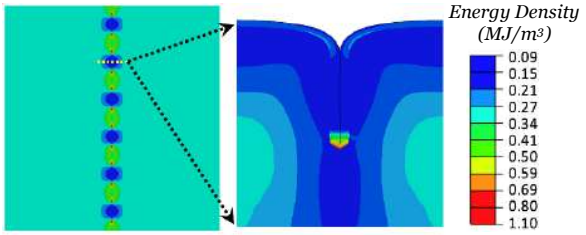

D/Φ =1

(c)

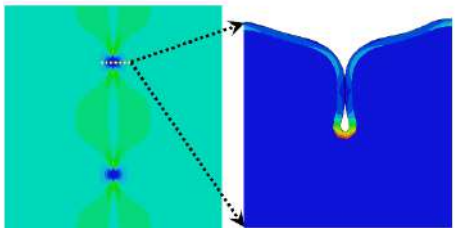

D/Φ =5

Figure 5.5 (a) Table of key input material properties for FEA parameters (b) Finite element (FE) simulation of guided formation of fold on lattice patterned surface and assessment of robustness. In-plane and out of plane (i.e. cross-section) strain energy analyses for the surfaces with a single micro-hole array (Φ = 40 μm) of D/Φ =1 and (c) D/Φ =5, at a nominal compressive strain ε_{comp} of 0.5.

As described above, the development of self-contact is rapid from an onsite H_c at ε_{th}, to the H_c that can provide enough contrast. Therefore, the ε_{th} as a function of D/Φ (Φ = 40 μm) has then been numerically analysed to study the threshold of generating optical signal guided by hole pattern. The simulations

for surface patterned with sharp corners (diamonds, squares, triangles and hexagons) are less successful at the moment as the current simulation programme doesn't allow the mesh process to progress over the sharp corner.

Following to the onsite of folding, further transient development of H_c is critical in determining the intensity of optical signal. **Fig. 5.6a** shows the nominal self-contact depths (H_c/h) for different D/Φ (Φ =40 μm) as a function of compressive strain, to understand this geometrical development. Excellent alignments are found between the numerical outcomes and experimental results for D/Φ=1 and D/Φ=5, meanwhile a slight mismatch is presented for D/Φ=2. A region (grey zone) with H_c/h values between 0.15 to 1.2 located on a strain range of 0.39 – 0.59, is outlined by analysing the experimental results where the ideal optical signals can be expected. The results from cyclic testing in **Fig. 5.6b** indicate a good resilience on generating target folding with a desired self-contact H_c (H_c of 10 μm for Φ =40 μm and H_c of 18 μm for Φ=80 μm, D/Φ=2).

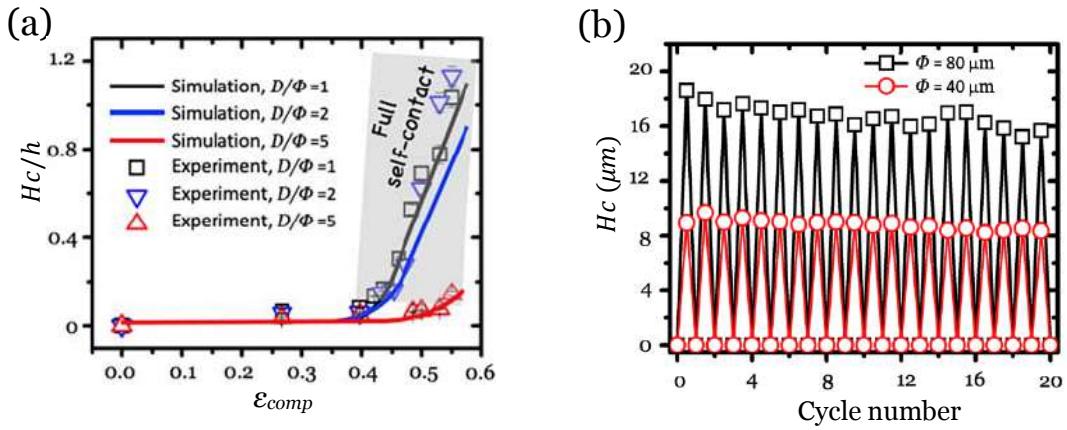

Figure 5.6 (a) Comparison of FE simulation results of H_c with experimental ones under a progressive ε_{comp} for the surface with a single micro-hole array (Φ = 40 μm)

(b) The cyclic testing results with $\Phi = 80\ \mu m$ and $\Phi = 40\ \mu m$ (D/Φ =2), to assess the robustness of generating self-contact H_c.

Fig. 5.6b shows the saturation process of this reversible self-contacting which represented the self-adaption of the multi-layer system to reach the desired H_c for sufficient contrast, as well as the durability for the initial 20 cycles. While in order to validate the durability of system under high compressive strains for more cycles, and to understand how it might sustain many repeated load cycles. The testing has been further to 100 cycles, the reversible result in **Fig. 5.7** reveals a reliable reproducibility of H_c even after 100 cycles, due to the elastic nature of multi-layer.

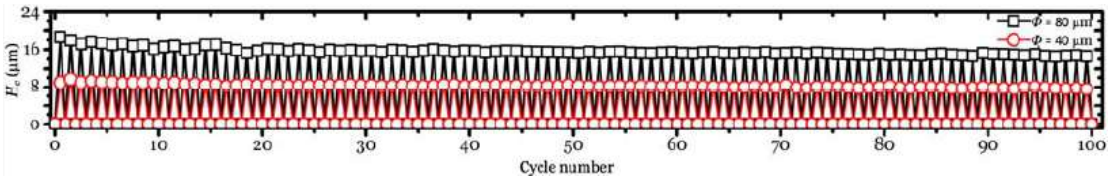

Figure 5.7 The cyclic testing results (up to 100 cycles) for samples with Φ = 80 μm and Φ =40 μm (D/Φ=2).

While the studies on nucleation and growth of creases/folds in the PDMS based elastic multi-layer usually took it as a pure elastic system, there have been questions on the possible relaxation/hysteresis on the generation of creases/folds during cyclic testing and/or compression-recovery curve, and the dependencies on the system settings. Further study on the relaxation of folding by tracing H_c over a long time duration, to compare with the simulation results in **Fig. 5.8a** at a nominal compressive strain (ε_{comp}) of 0.5, indicates a limited relaxation in H_c, which is in the same trend with the

theoretical approximation. **Fig. 5.8b** indicates that during compression/recovery cycle, low hysteresis on is observed. The reason could be the elastic nature of the multi-layer system and low surface tension [121], [241] after being coated by fluorophore compound.

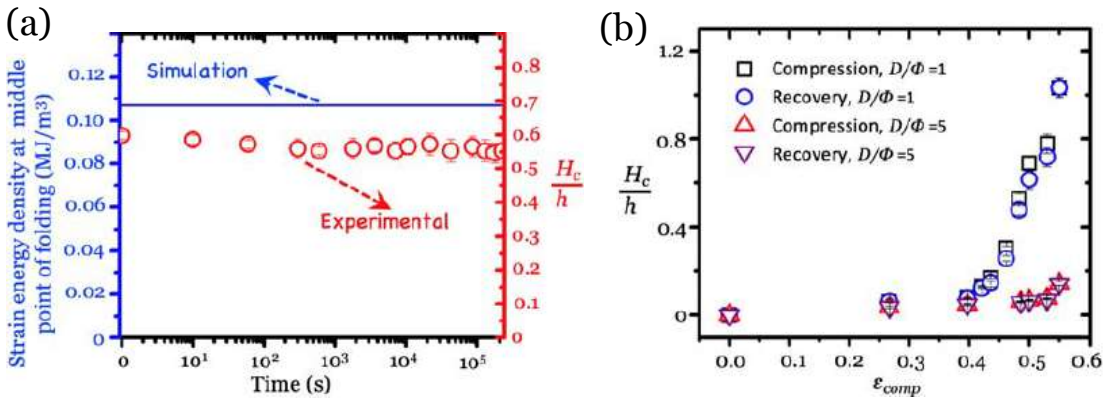

Figure 5.8 (a) Comparison the simulation and experimental results for relaxation behaviour under a progressive ε_{comp} =0.5 for the surface with a single micro-hole array (Φ=40 μm, D/Φ=5). (b) The hysteresis results for targeted folding depth on the surface with a single micro-hole array (Φ=40 μm, D/Φ=1 and D/Φ=5).

While the self-contacting depth of *Hc* was normally in micro-scale (a few micron metres to tens micro metres), human naked eye and mobile phone camera based morphology observation was still possible when the length exceeds ~ 10 mm as shown in **Fig. 5.9**. This could potentially offer some inter-mediate scale applications such as signal coding/decoding and security bar for hidden code scanning/reading.

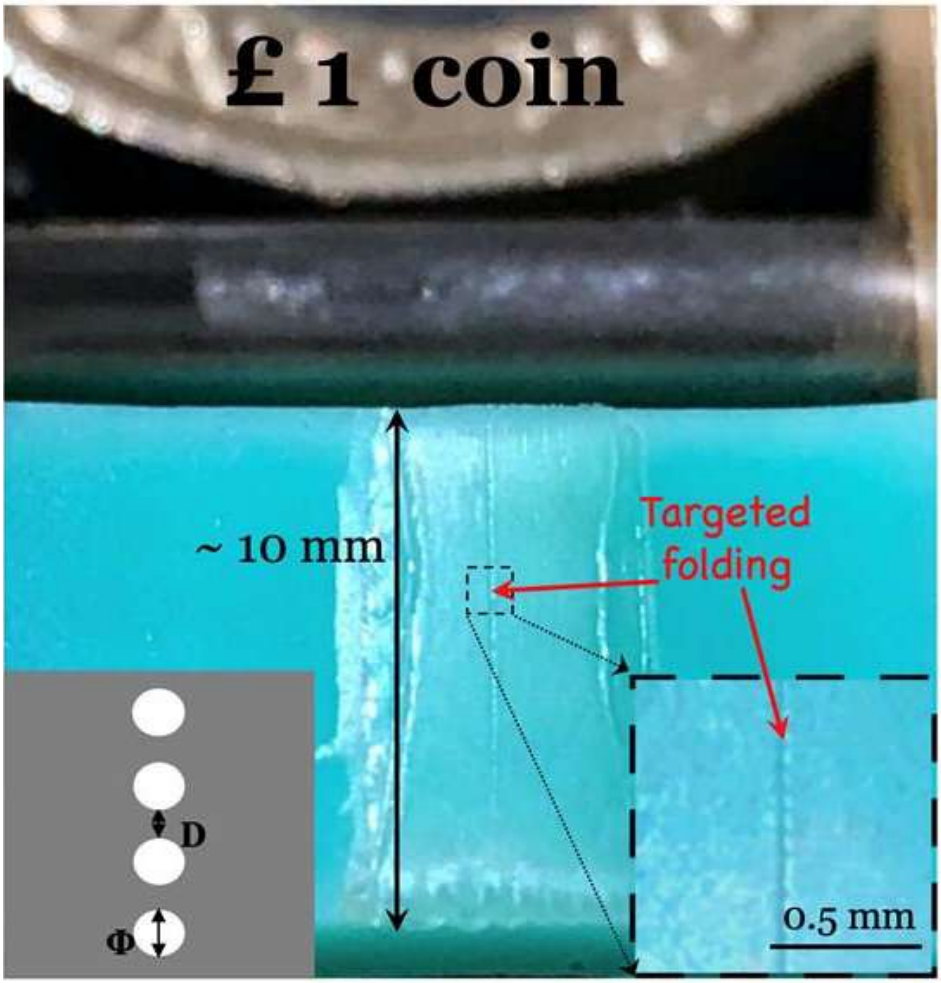

Figure 5.9 The observation of actuated fold for the surface with a single micro-hole array (Φ = 40 μm, D/Φ=2, h=12 μm) at macroscopic level under reflective light.

5.3.4 2D micro-arrays demonstration

Based on the understanding gained from studying the 1D microstructure patterned hole array, the more complex 2D micro arrays for the guided formation of surface morphologies have also been characterized. The surface design was extended to the square lattice patterns (such as arrays of circle and hexagon) shown in **Fig. 5.10a**, which obtained by Bruker® GTK. W is defined as distance between neighbouring lines (width distance). In order to

quantitative characterized the threshold strains of 2D hole array and study how W affects the ε_{th}, various W/Φ has been measured with the fixed D/Φ value. **Fig. 5.10b** shows that the wider gap between each line array (greater W/Φ ratio), the lower threshold strain ε_{th} was required. This can be predicted as PDMS elastomer is non-compressible [255], the greater number of large creases over the same length of compressing surface (smaller W), the less surface will be folded into each crease. Therefore, a demonstration figure has been displayed in **Fig. 5.10c,** the results suggest that varied ε_{th} at high strain range can be achieved by designing D/Φ, W/Φ of the lattice pattern, together with more capabilities on 2D designs.

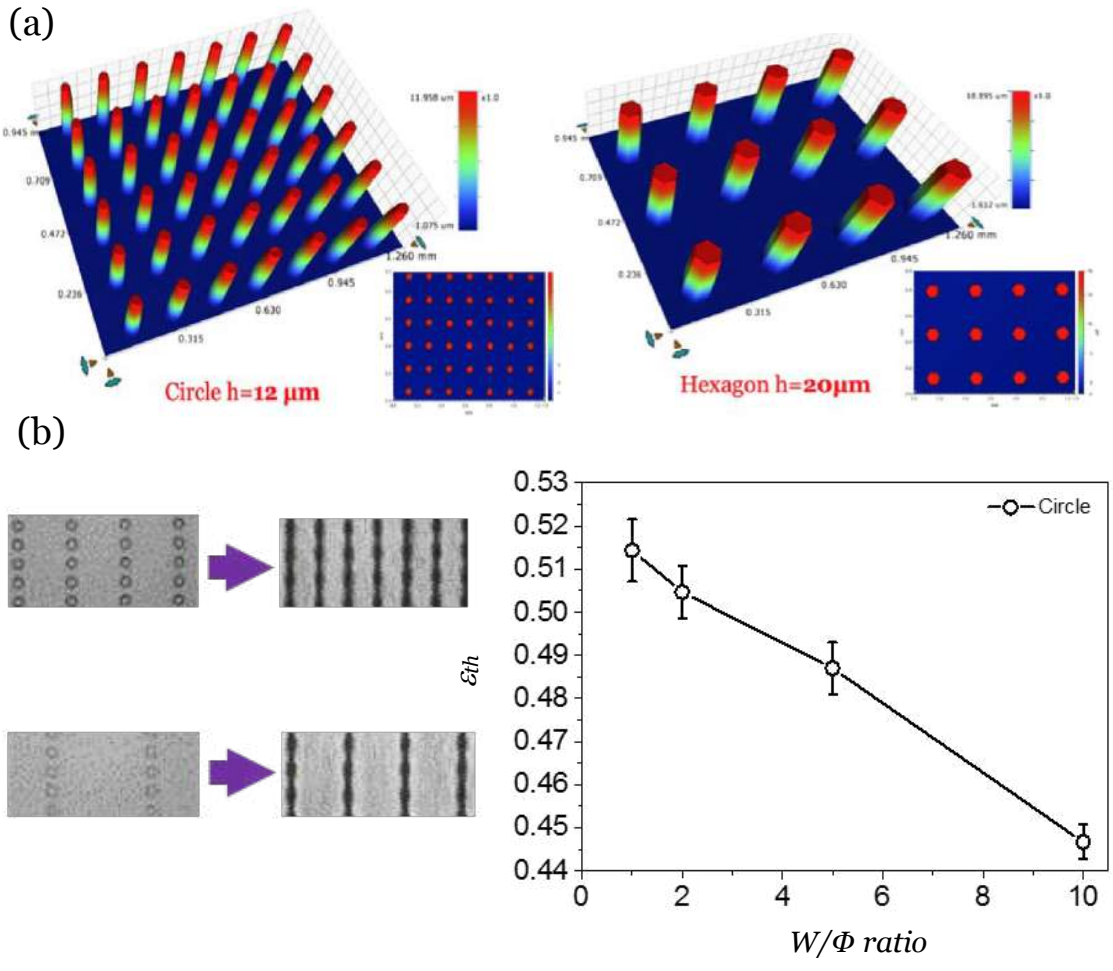

(c)

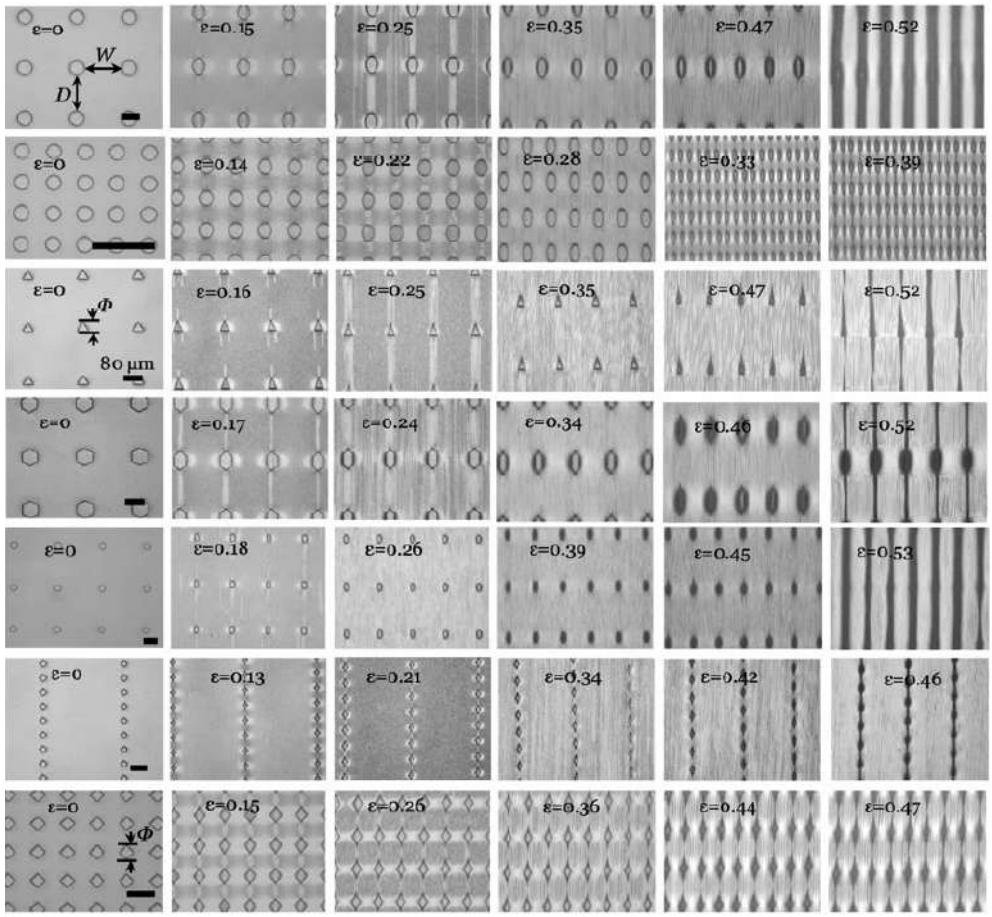

Figure 5.10 (a) Bruker® GTK shows the profiling of the fabricated SU-8 pillar array templates of circle (left) and hexagon (right) (b) large folding generation threshold strain vs. W/Φ for 2D hole array (c) the formation of folding guided by the square lattice pattern with different pattern shapes, W/Φ, and D/Φ ratios under Nikon optical microscope.

5.3.5 Realization of Topo-optical sensing (FoA)

The concept of translating surface topology into optical signal (Topo-optical sensing) is initially facilitated through casting and drying a drop of optical indicator solution containing 1.3 mM fluorescein o-acrylate (FoA) on the plasma treated elastic surface in **Fig. 5.11a** and **Fig. 5.11b**, to fulfil the

photo-luminescence function. The coated thin optical indicator layer is measured under laser scanning confocal microscope (LSCM) with a thickness of ~600 nm in **Fig. 5.11c**. The illustration in **Fig. 5.11d** indicates that, after coating with a thin optical indicator layer, fluorophore concentration effect can be observed after surface creases generated by uniaxial compression.

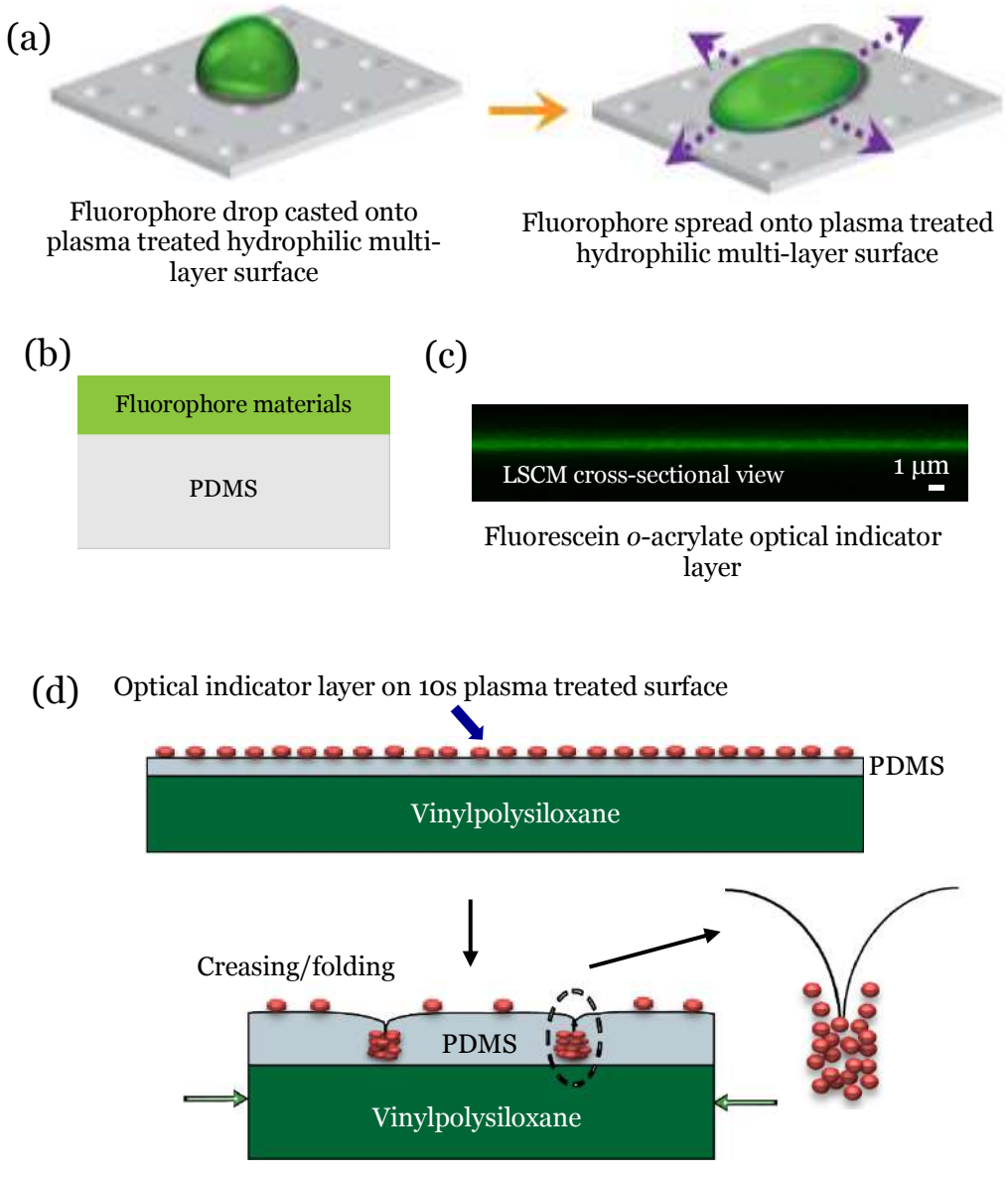

Figure 5.11 Schematic images illustrating the droplet casting process with (a) Fluorophore drop casted on the multi-layer surface (left) and spread to cover the

surface to generate the optical indicator layer (right) with (b) Cross-sectional view (c) LSCM cross-sectional view of formed optical Fluorescein O-acrylate (FOA) indicator layer with thickness of ~600nm before compression (d) Cross-section view of the multi-layer structure coated with fluorophore (dots). Fluorophore concentration effect can be observed after surface creases generated by uniaxial compression.

Without casting the optical indicator layer, the creasing/folding patterns can only be recognized under reflective light, such as example shown in **Fig. 5.9**. While when coating with fluorophore optical layer at the occurrence of creases/folds, the in-plane length (L) locally develops into a self-contact out-plane depth (H_c), lead to an optical signal from the top view because of the volumetric accumulation of intensity.

By assessing the optical properties for the morphologies at $\varepsilon = 0.52$ for both plain and micro-patterned surfaces under Laser Scanning Confocal Microscopy (LSCM, Nikon A1R) in **Fig. 5.12a** and **5.12b**, a single line optical signal is clearly shown on the location defined by the pre-placed micro-pattern with an enhanced intensity (side view). It has also been used to characterize the 3D (cross-plane) surface deformation, and to understand its relationship to the photo-luminescent signal characteristics. In **Fig. 5.12a**, when compressing plain surfaces beyond a certain strain (e.g. $\varepsilon \approx 0.52$), brighter luminescent lines were observed when deep creases were generated at random locations shown. With the single micro-hole array shown in **Fig. 5.12b**, a guided regular green luminescent line pattern formed between two adjacent holes where the largest crease with greatest self-contact depth H_c

was generated, surrounded by smaller winkles with weaker green luminescence, at various substrate strains.

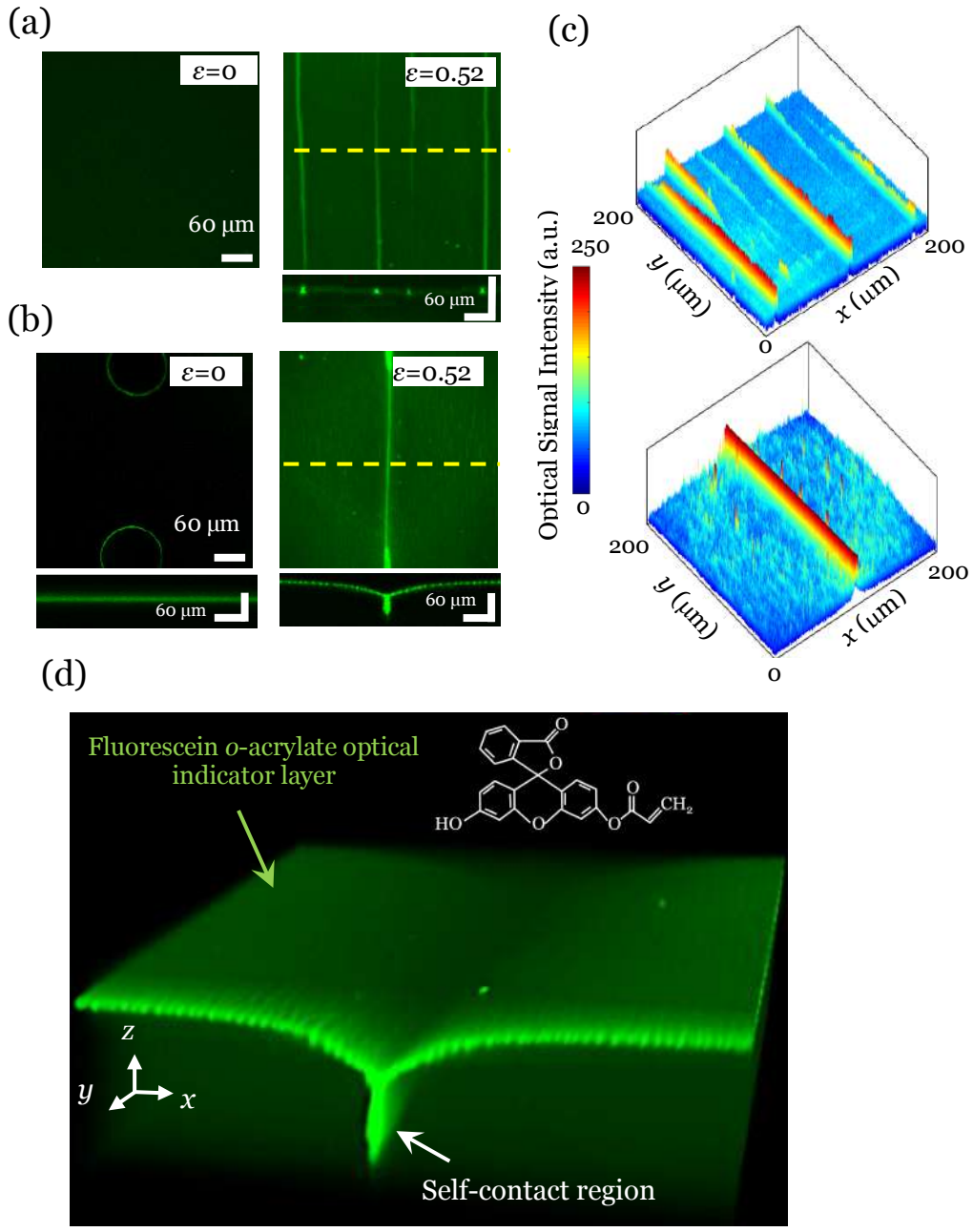

Figure 5.12 The generation of targeted surface folding on an elastic multi-layer system and translation of topological change on surface into optical sensing signal with an indicator layer: Laser Scanning Confocal Microscopy (LSCM) images showing top and cross-sectional (for the dashed lines in top view) views of optical

signals induced by (a) random folding on the plain surface, and (b) targeted folding on a micro-patterned surface, with the digital analysed results for top view optical signals in (c). (d) A green 'opened book' from 3D LSCM reconstruction to show the surface signal with targeted folding.

5.3.6 Luminescence-optical pattern characterization (FoA)

A signal-to-noise ratio, defined as $SNR = \frac{\text{peak intensity}}{noise}$, to quantitatively analyse the optical signal, where the peak intensity is collected from the signal of folded line and the "noise" represent the average luminescence signals originated by background surface (exclude the folding line). In **Fig. 5.12c**, a higher SNR is obtained for the patterned surface than that of plain surface. With the patterned hole array, surface energy can be guided to form a single fold with a deeper self-contact as shown in **Fig. 5.12b**, rather than a distractive energy localization with multiple folds/creases occurring on the plain surface. From the LSCM 3D reconstruction image (green 'opened book') in **Fig. 5.12d** for the FOA patterned surface, it can be seen that the signal noise on background remains considerably high, due to the discontinuous fluorescein aggregations caused by the small creases/folds.

Since the folding depth H_c is related to strain energy localization, further LSCM based studies of surface deformation were performed to further understand the relationship between the substrate strain and H_c distribution along the line patterns as shown in **Fig. 5.13**. The top-view luminescent images in **Fig. 5.13a** have clearly shown the in-plane 2D luminescent pattern development over increased substrate strains (from 0 to 0.55) identical to the

creasing/folding pattern observed by Nikon microscope and AFM in **Fig. 5.3**. From top view, when the strain reached 50%, the large creases almost connected in the midway. At 52% compressive strain, the large crease completely connected hole patterns and form a lateral strip pattern. The FoA samples' cross-sectional view (A-A1) in **Fig. 5.13b** visualized the cross-plane surface deformation, showing the hole-guided single large crease (middle point deep folding grew to 18.6 μm at 55% compressive strain) pattern, which was perpendicular to the compression direction, surrounded by smaller creases. It shows that FoA had more luminescent aggregation at larger compression strains related to deeper folding depths. The side cross-section view of **Fig. 5.13c** (B-B1) shows the middle area of crease growth (2.3 μm, 10.8 μm and 18.6 μm at strain of 0.50, 0.52 and 0.55) when increasing the compression strain, which to study the depth distribution along the deep crease/fold.

Beside the large crease/fold, smaller creases in parallel were also observed, with average folding depth values below or around 1 μm when strain < 50%. This gradually increased to around 2.5 μm as shown the inset of **Fig. 5.13b**, when strain reach to 55%. Based on this mechanism, the optical patterns can also be achieved with different organizations as displayed in **Fig. 5.13d** and **5.13e**.

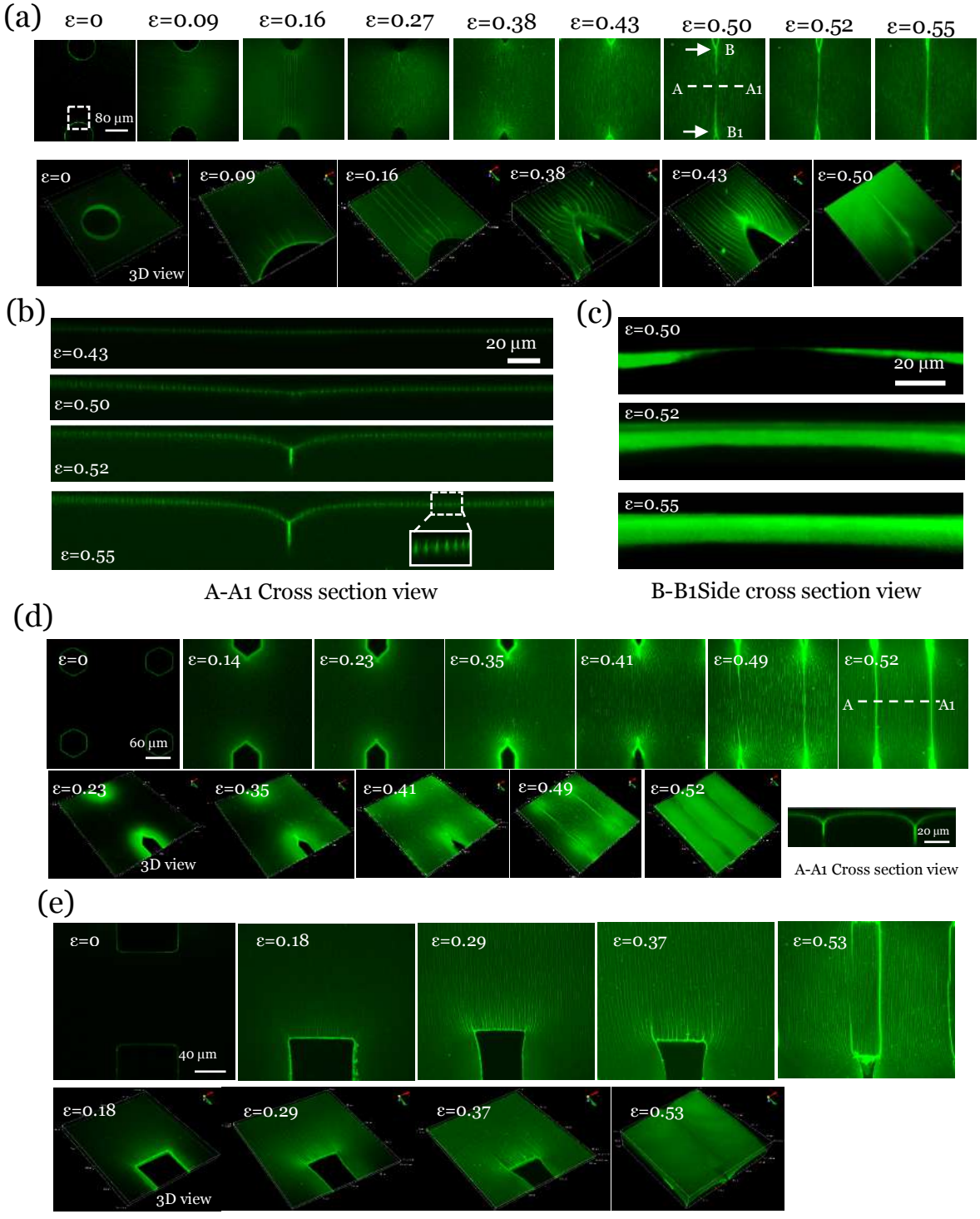

Figure 5.13 Laser Scanning Confocal Microscopy images showing top and cross-sectional views of (a) the in-plane 2D luminescent pattern development over increased substrate strains (from 0 to 0.55) with the 3D view of selective strains (b) A-A1 cross section view of strains at 0.43, 0.50, 0.52, 0.55 with folding depth of 1.6

μm, 2.3 μm, 10.8 μm and 18.6 μm, with (c) the corresponding B-B1 side cross section view at strain of 0.50, 0.52, 0.55 (d) fluorescent optical patterns generation by the surface creasing/folding with hexagon organization under uniaxial compression at different strain values with (e) square organization.

5.3.7 Potential applications (FoA)

Such employed mechanical responsive elastomer multilayer system which to generate creases by the folded surfaces, where the photoluminescent occur. This has brought potential applications such as super-flexible wireless strain sensing. The ON/OFF (or 0/1 output) switching strain has been defined to be the value at fluorescent line pattern forming. **Fig. 5.14a** shows the proposed optical switch strain sensing mechanism, which the detected signal is processed with the outputting ON/OFF status. **Fig. 5.14b** displays a programmable "two-step" switching mechanism which encoded in this design, where a reversible line pattern could be logically switched at two switching strains of ε=0.44 and ε=0.52 integrated in the same substrate, which should be feasible for applications such as secret codes for anticounterfeiting and product identification. This concept can be further developed by re-configurate it into dynamic 2D 'spy' barcode products with hidden information only appearing under a dedicated strain as displayed in **Fig. 5.14c**.

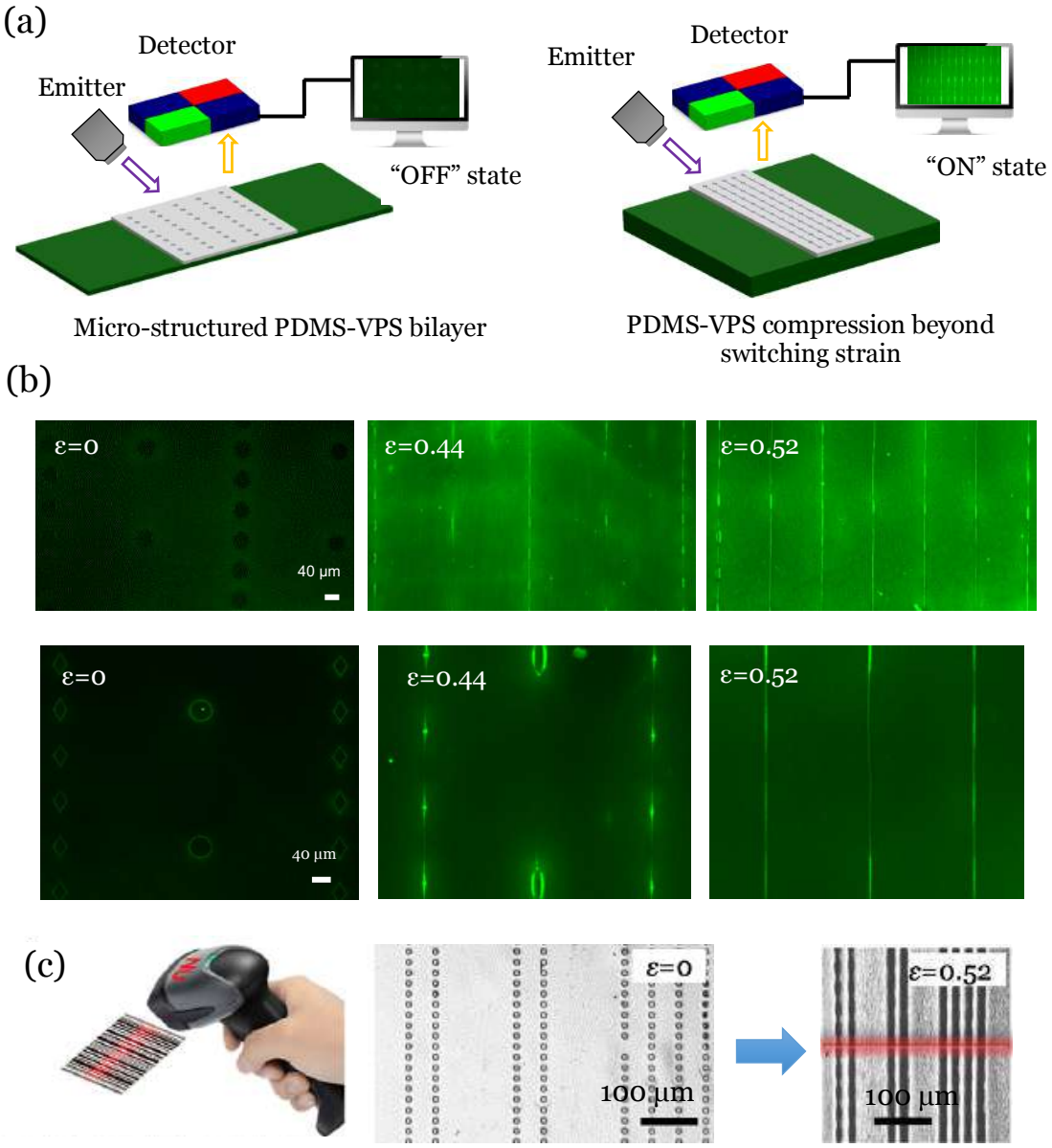

Figure 5.14 (a) The proposed sensing mechanism: optical signal generated by fluorophore-PDMS-VPS is detected by the rigid part of the sensor system giving ON/OFF digital outputs (b) A programmable two stepwise binary code at two different switching strains which integrated in the same substrate (c) A 2D 'spy' barcode design with a state of 'OFF' at ε=0 and an 'ON' state at ε=0.52.

Since the self-contact depth H_c was normally in the range from a few micron metres to tens micro metres. Given by casting a thin optical indicator layer in nanometres on the top, the signal has been identified with the assistant from

instrument such like quantified by microscope. This brings the potential opportunity to be integrability into micro-electronics device, the described indirect mechanism also inspired an idea of spy coding of hidden information which requires a conditional reader/kit to translate the message as shown in **Fig. 5.14c**, which potentially used as the security bar for hidden code scanning/reading.

Coupled by fluorescent light, the deforming super-flexible elastomer part of the sensing system is physically separated from the fixed rigid detector and signal processing part during operation. Since there is no metal interconnect on the deforming substrate, this development has shown an alternative solution to the challenges faced by stretchable/super-flexible sensor packaging, where creating electrical connection is challenged by the metal fracture and delamination. Providing a rich set of attracting features such as high strain sensing, wireless feature, embedding logical function, direct visualisation, high integrability and good adaptivity to local curvature, from which it will enable new opportunity for designing future flexible/wearable and lab on chip devices.

5.3.8 Selectively Oxygen-quenching induced ultra-high contrast (Ir-III)

The fabrication method is similar to what's described in section 5.3.5. Whilst in this case, instead of coating with FoA, a nanometre thin phosphorescent Iridium-III complex was employed as the optical indicator layer to develop a

dynamic, high contrast topo-optical pattern generation. The aim is to utilize the topological hypoxia zone created by targeted folding, to preserve the optical signal on the self-contact region for the Ir-III coating layer. **Fig. 5.15** shows the molecular and the spectrum of Iridium-III complex.

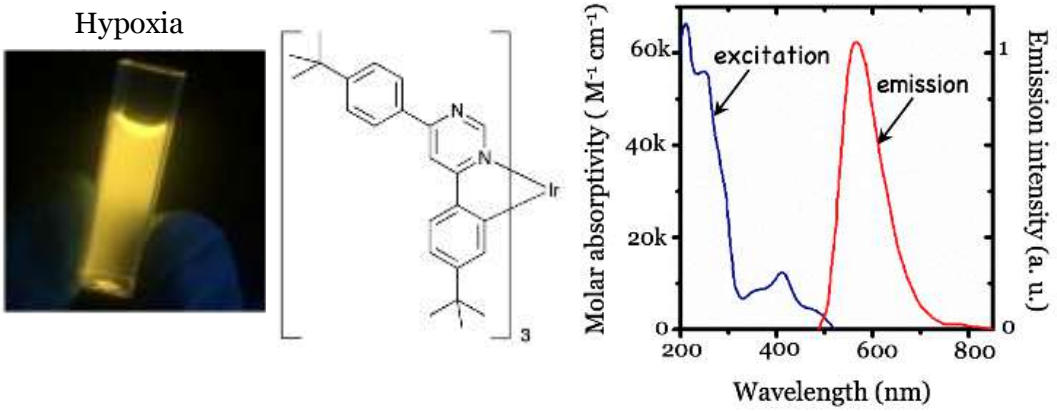

Figure 5.15 The Ir-III complex and its excitation and emission spectrum.

The optical indicator layer was created by coating the Iridium-III solution (Ir-III, fac-Ir(ppy)3, solvent mixture, 1.3 mM solution diluted in chloroform and ethanol). The self-contacting of elastic surface will create a localized hypoxia zone by automatically exclude the air. Therefore, photo-luminescent preserves only along the deep fold area as shown in **Fig. 5.16a**. It was observed from **Fig. 5.16b** (top and cross-sectional views) that, by employing this Ir-III optical indicator layer, strong photo-luminescent only occurred along the deep creasing line, where the self-contact region created localized hypoxia zone. Compared to FoA coated devices, the levels of luminescence noises from small creases and other surfaces exposed to the oxygen in open air were significantly supressed. While the photoluminescence outside of the

folding area is mostly eliminated by the oxygen quenching effect, leading to a topo-optical signal with ultra-high contrast. The 3D-view LSCM images in **Fig. 5.16c** (red micro-"blade" pattern) clearly show the difference between luminescent signals generated from large and small creases with FoA and Ir-III optical indicator layers.

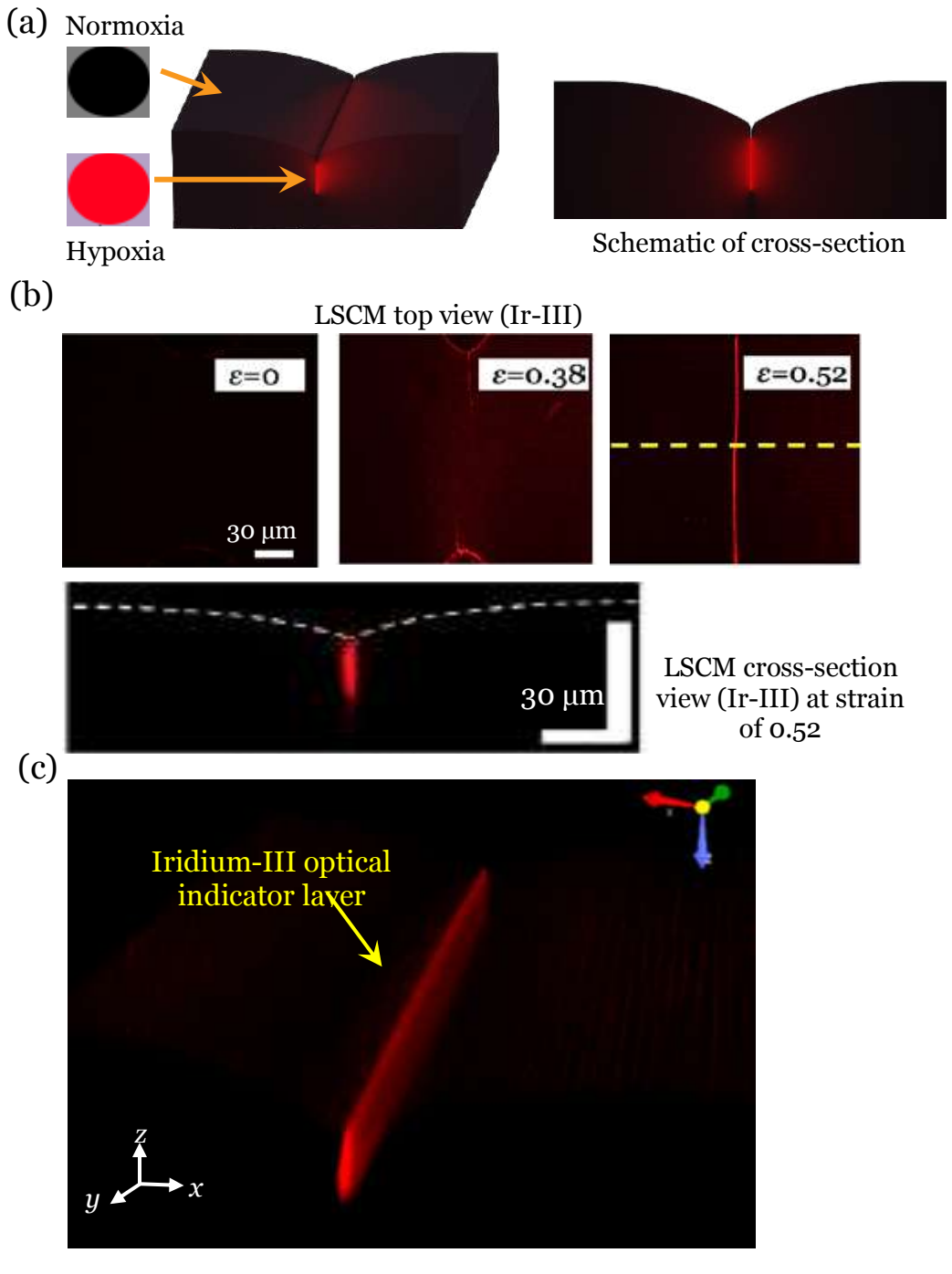

Figure 5.16 The generation of topo-optical sensing signal with ultra-high contrast (a) schematic illustration of surface folding generating the optical signal with two status of hypoxia and normxia (left) with cross-section view (right) (b) Top and cross-section views of the self-contact induced fluorescent line patterns generated from Ir-III indicator layer (c) A red 'blade' type super high-contrast singal from 3D LSCM reconstruction to show the optimised signal with minimal surface noise.

5.3.9 Ultra-high contrast optical pattern characterization (Ir-III)

The intrinsic optimisation by selectively oxygen-quenching lead to a topo-optical signal with ultra-high contrast by supressing most "noises" coming from non-contacted surface, as shown in **Fig. 5.17a**. The background luminescent signals generated by small texture were mostly quenched in comparison with FoA coated sample. Therefore, strain responsive, reversible, spatially defined, oxygen quenching photoluminescent pattern generation has been achieved.

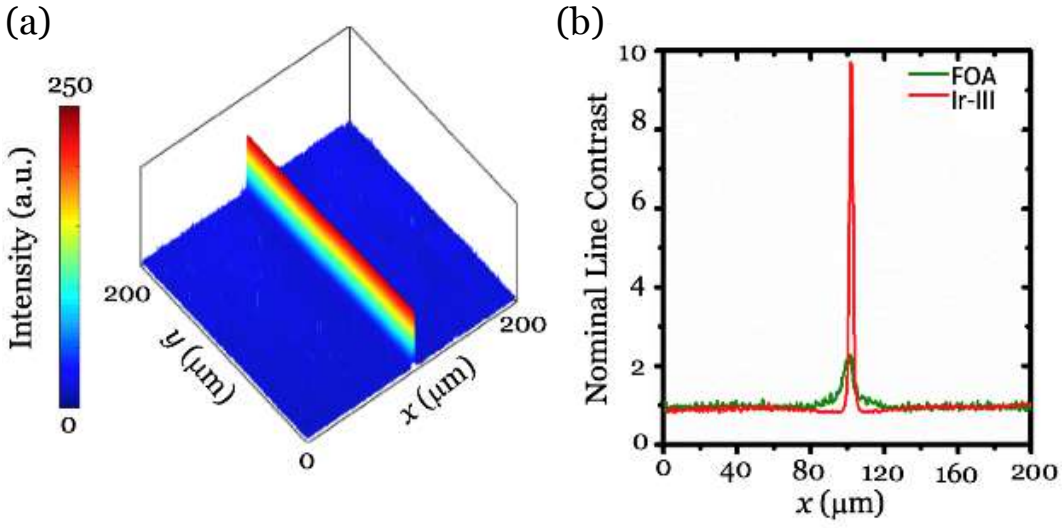

Figure 5.17 Optimisation of Topo-optical luminescence characteristics: (a) The analysed results for the top view signal in the selected image in Fig. 5.16b (b)

Comparison of the nominal line contrast (NLC) for the selected area in Fig. 5.16b and Fig. 5.12b.

A nominal line contrast (*NLC*) is defined as $NLC = \frac{\text{Peak intensity}}{\text{Mean average of the line intensity}}$, to describe the optical signal distribution for the selected area. **Fig. 5.17b** shows that after analysing the *NLC* data for the selected lines in **Fig. 5.16b** and **Fig. 5.12b**, an *NLC* value of 10 is achieved for the Ir-III coated surface, which is 5 folds of the *NLC* (~2) for FoA coated surface.

This topo-optical relationship has been then scaled (*SNR Versus Hc*) to understand the geometrical influence on the quality of signal. As shown in **Fig. 5.18a**, small *SNRs* between 0.47±0.04 are captured when the fold first occurs at ε_{th} with an onsite $H_c \approx 1.1$ μm, for both Ir-III and FoA coated surfaces. When H_c grows higher than 1.6 μm, a stable *SNR* plateau (*SNR* ≥ 2) is emerging for FoA coated surface which indicate that the physical accumulation along the folding depth reaches a threshold of intensity to enable a quality optical feedback. This development of self-contact depth, around 500 nm in distance, is very rapid within a strain window of ~ 0.037±0.017. Given by a nominal strain speed of 0.02 s^{-1}, the sensing signal can be instantly captured in microscope within 1 second, which shows how fast the fluorescent signal can be response to the mechanical force. On the contrary, an increasing trend is obtained for Ir-III coated surface at the same threshold when H_c increases, due to the oxygen quenching effect on the surface at the open air. When the H_c reaches 13.8 μm, the *SNR* on Ir-III coated surface increase significantly to 12.5, which is 6 folds of that from FoA

coated surface. By preserving the peak intensity at self-contact area, the Ir-III coated surface achieves higher *SNRs* when H_c is larger than 1.6 μm.

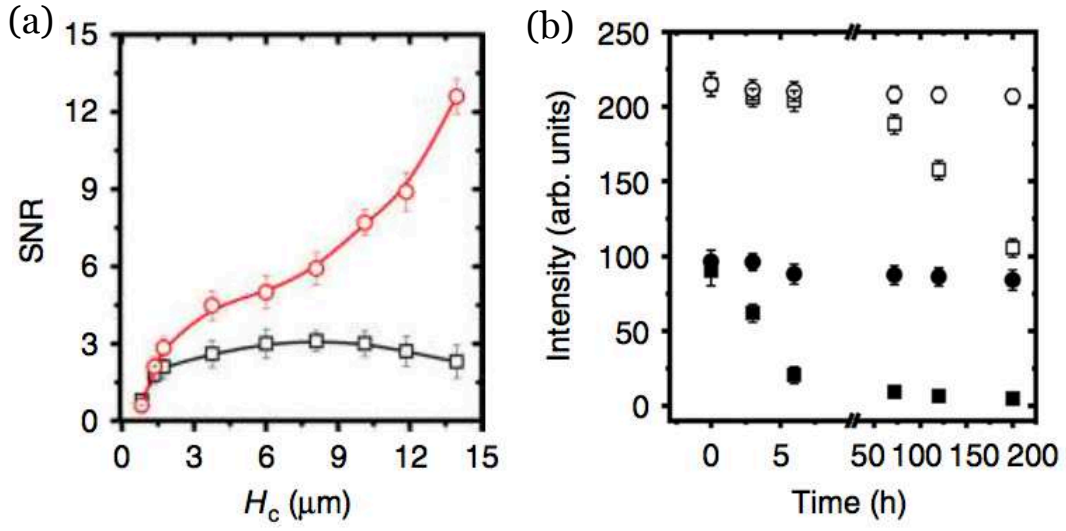

Figure 5.18 (a) The scaling relationships of *SNR versus* self-contact depth H_c, for different optical indicator layers (b) A time lapsing tracking of signal intensities in Fig. 5.16b and Fig. 5.12b at ε_{comp} = 0.52.

The time dependent degradation of photoluminescent signal is assessed by tracking the peak and background signals at ε_{comp} =0.55 (H_c ~ 13.8 μm) for up to 200 hours. The results displayed in **Fig. 5.18b** for FoA coated surface show a retainment of signal intensity after 200 hours with less than 8% decay for both peak and background signals. For Ir-III coated surface, a rapid decrease of around 92% intensity is discovered in first 6 hours for the background signal, whilst the peak signal maintains stable for the first 70 hours, then start to fade and finally reach a decrease of 54% in 200 hours.

The quenching kinetics analysis is analysed in **Fig. 5.19**, for the Ir-III films on PDMS surfaces with varied thicknesses in the open air, where the optical

signals for all layers are quenched in about 5 hours without compression. Under compression, the topology enabled hysteresis results into a high optical contrast for about 65 hours, then the peak intensity eventually reduces due to the diffusion of oxygen into the elastic solids. The kinetics of diffusing oxygen into the self-contact region of PDMS surface is complicated as it corresponds to the factors such as temperature, local oxygen concentration, humidity, surface porosity, chemical composition, etc.

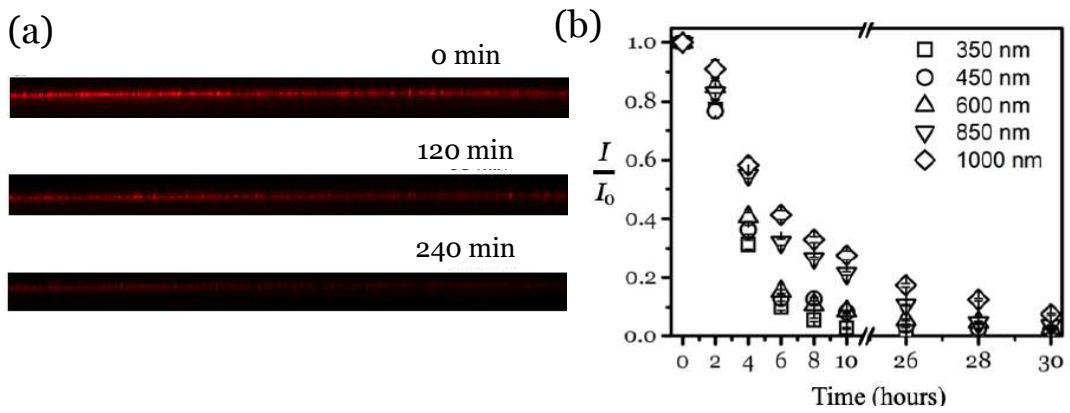

Figure 5.19 (a) The quenching observation for an Ir-III film of 450 nm (b) Quenching kinetics analysis Ir-III films coated on PDMS surface with different thickness in the open air.

Similar to section 5.3.6, the surface morphology change between two adjacent micro-holes on 1D hole array samples has been observed from different angles (cross-section, side cross-section) and analysed in details. The 3D morphology information of the surface at different compressive strains and photoluminescence signal of Ir-III complex was analysed by LSCM and comparatively studied with FoA. Studying the same area (surface between 2 holes in 1D hole array $\Phi = 80\,\mu m, r = D/\Phi = 2, h = 12\,\mu m$). **Fig. 5.20a**

shows LSCM imaged top views of different nominal strains. **Fig. 5.20b** and **5.20c** show the cross-sectional and side cross-sectional views at nominal strains of 50%, 52% and 55%. Clearly luminescence on non-folding surfaces was largely quenched by air ambient, with folded surfaces especially the large crease connecting two holes exhibit high luminescence intensity indicating localized hypoxia. This means while the photoluminescent light intensity large crease increases along with its depth, the signal from small creases were largely quenched despite still presented.

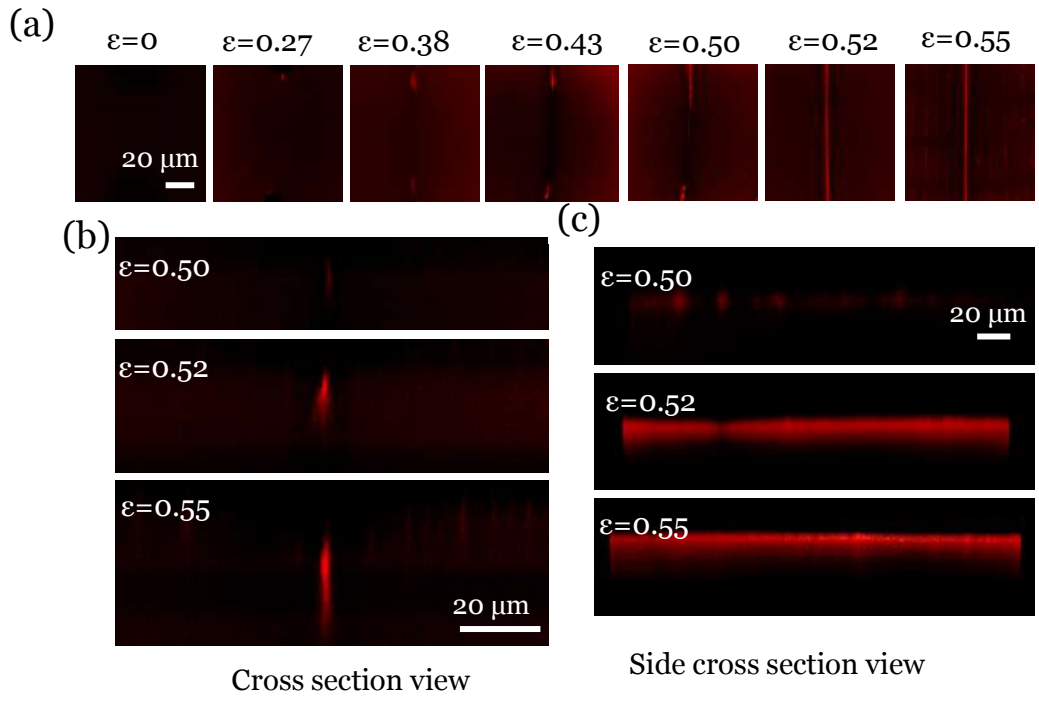

Figure 5.20 Laser Scanning Confocal Microscopy images showing top and cross-sectional views of (a) the in-plane 2D luminescent pattern development over increased substrate strains (from 0 to 0.55) with the 3D view of selective strains (b) A-A1 cross section view of strains at 0.50, 0.52, 0.55 with (c) the corresponding B-B1 side cross section view at strain of 0.50, 0.52, 0.55.

5.3.10 Demonstration of potential applications (Ir-III)

To demonstrate the potential of developing this topo-optical sensing mechanism into device applications, several conceptual designs (i.e. in-plane strain sensor, 2D 'spy' barcode, adaptive topo-optical grid, flexible bending sensor) have been successfully demonstrated. **Fig. 5.21a** presented an in-plane topo-optical sensor to detect large surface strains, by simply configuring the pattern parameters (shape, D/Φ, etc) for the pre-placed lattice. Similar with **Fig. 5.14b**, such programmable "two-step" switching code could be logically switched between '0,0,0' at ε=0, '1,0,1' at ε=0.44 and '1,1,1' at ε=0.52, with corresponding optical signals can be visualised by reflective optical microscopy and fluorescence microscopy at the same time. **Fig. 5.21b** shows an adaptative topo-optical luminescence grid, which contains a tuneable feature on the size of grid under equi-biaxial compression to track the cell behaviour *in situ*. The potential application for adaptive topo-optical grid could be promising for some biological applications (minutes to days), where the oxygen concentration can be controlled at relatively low level in bio-media (i.e. aqueous solutions).

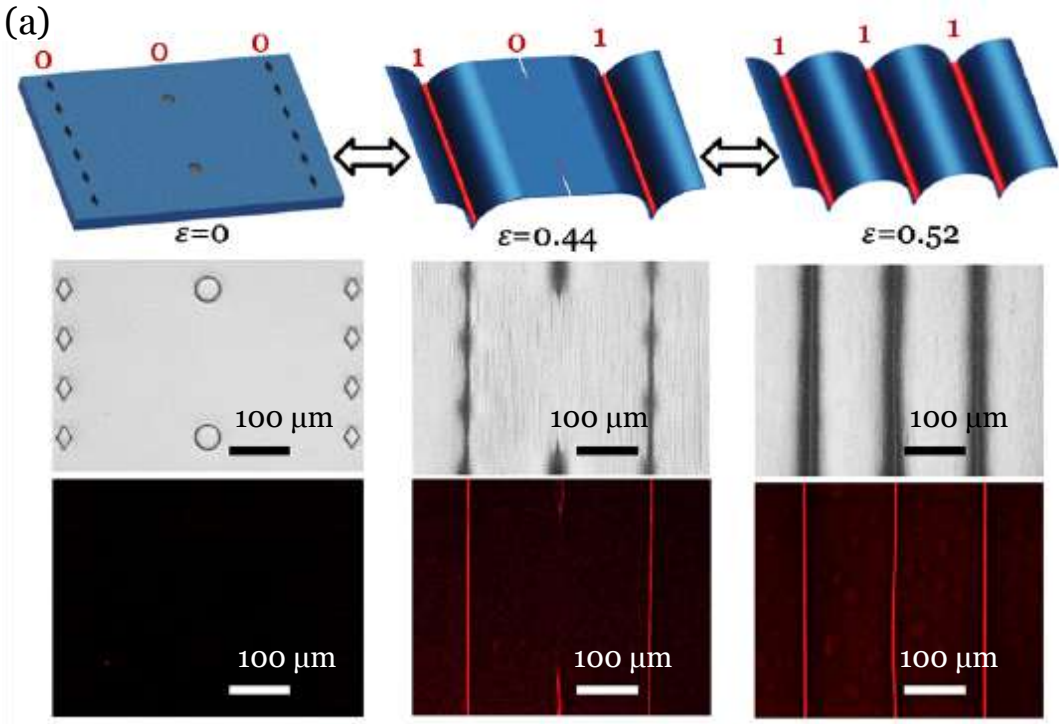
(a)
0
0
0
1
0
1
1
1
1
ε=0
ε=0.44
ε=0.52
100 μm
100 μm
100 μm
100 μm
100 μm
100 μm

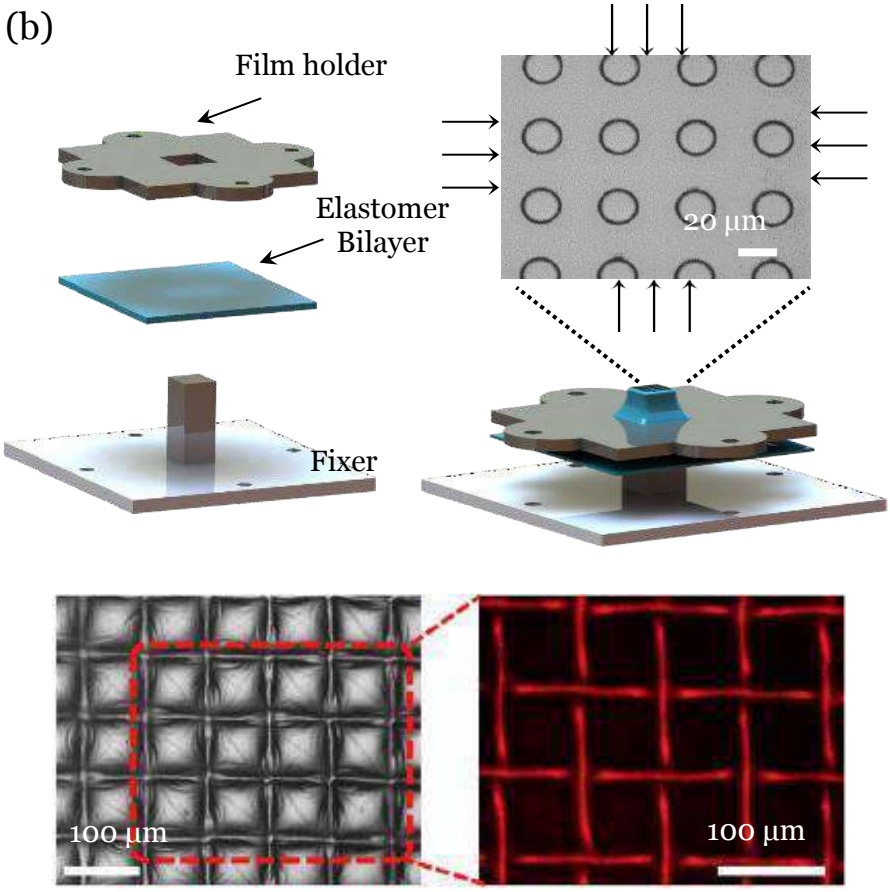
(b)
Film holder
Elastomer
Bilayer
Fixer
20 μm
100 μm
100 μm

Figure 5.21 Demonstration of conceptual applications based on Topo-optical sensing function: (a) An in plane strain sensor for large deformation with logic sensing (b) An adaptive topo-optical grid under equi-biaxial compression for bio-applications.

Based on this topo-optical sensing strategy, **Fig. 5.22** shows a flexible bending sensor developed by combining in-plane pre-compression $\varepsilon_{\text{pre-c}}$ to detect out-of-the-plane bending degree. After releasing pre-stretching strain of substrate (stage I), I deploy the device (combined thickness of ~3.1 mm) on the area to detect the bending level. By observing under microscopy, the device firstly experiences a selective fold on the lattice patterned surface at low degree bending (stage II), then all lattice patterns are folded at high degree bending (stage III). A brief phase diagram is created to distinguish the two-stage bending sensing for the patterned surface (Φ=80 μm, h=12 μm, D/Φ =1 (black line) and 5 (red line), W/Φ=5), where a clear map is obtained to determine localized curvature (K_c) with the provided $\varepsilon_{pre\text{-}c}$ when the optical signal occurs.

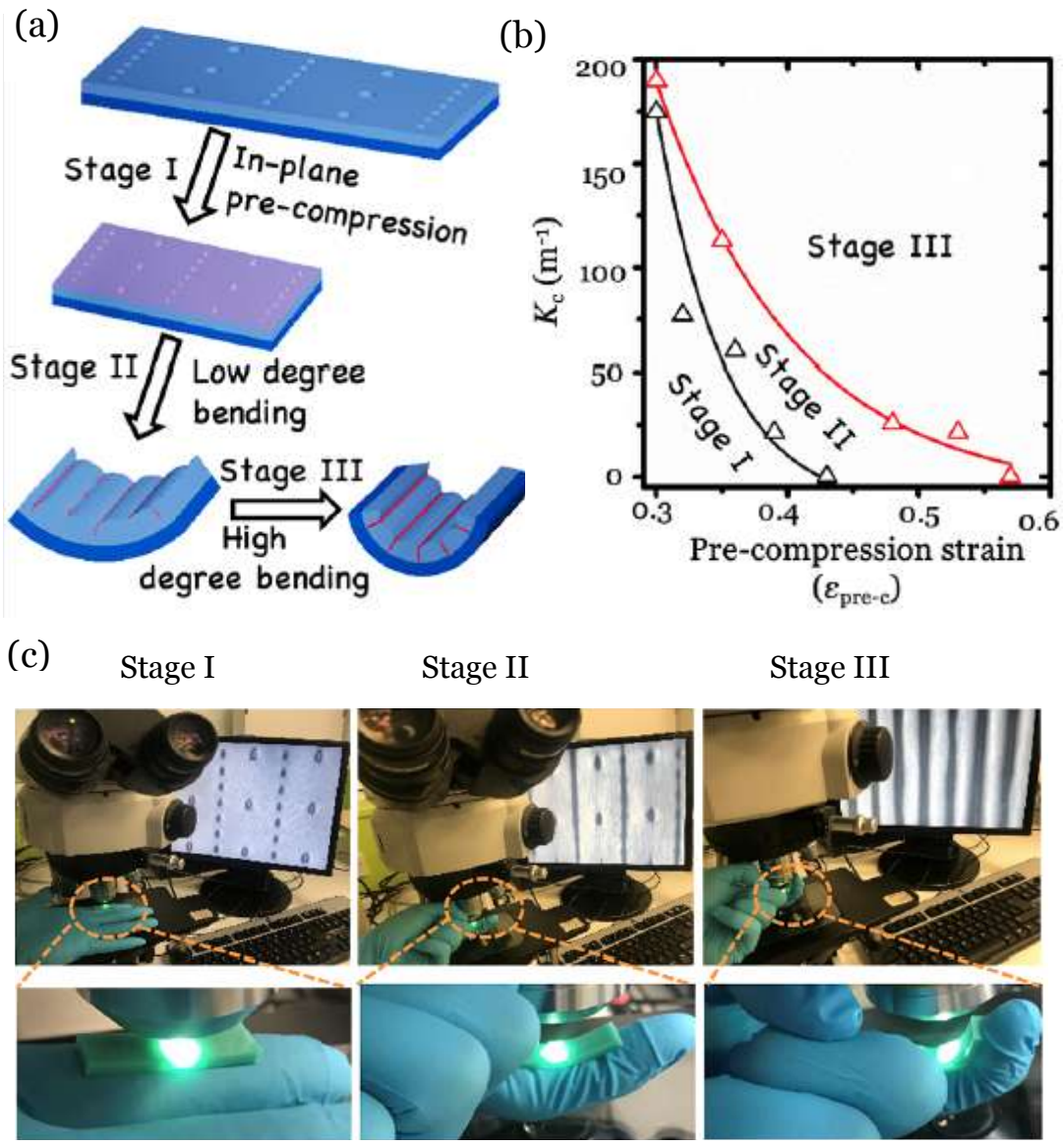

Figure 5.22 A flexible bending sensor to detect the bending degree (curvature) of joint with (a) schematic illustration of sensing principle (b) phase diagram of sensing (c) *in situ* sensing with generating signal from direct observation under reflective microscopy.

5.4 Chapter Summary

In this chapter, a topo-optical sensing strategy has been proposed by constructing an elastomeric multi-layer substrate coated with a nanometre thin optical indicator layer, which presents an innovate way of generating the optical sensing mechanism. The controllable formation of folding patterns has been studied with various geometrical inputs of lattice patterns and the results are in good agreement with the predictions from finite element analysis. Moreover, an inherited automatic optimisation on optical contrast is introduced by oxygen quenching the coated Ir-III based optical indicator layer, which lead to an ultra-high contract by significantly reducing the background noise. I anticipate this high-contrast topo-optical sensing strategy and the demonstrations of conceptual devices will open new windows for future applications as flexible/wearable electronics, tunable optics and bio-devices.

Chapter 6

Advanced 3D Morphing Transducers By Smart Hydrogel Patterning

Inspired by the reconfigurable shape-morphing devices by selectively swelling hydrogel in section 2.3.3, this chapter describes some initial research into functional hydrogel fabrication and patterning techniques. This work established a unique way of heterogeneous layered structures of soft functional materials that has configurable swelling behaviour for advanced transducer applications.

Hydrogel droplets with different composites mixtures were deposited and patterned into the same thin layer by a "two-parallel plate" configuration used in microfluidics applications. Resulted heterogeneous layered structures of hydrogel were created, generating reconfigurable 3D (3-dimensional) deformation responding to discrete levels of stimulation inputs, which brings the great potential of next generation reconfigurable, stimuli-responsive, morphing soft transducers.

6.1 Introduction

Biological systems in nature, such as octopus and cuttlefish, can respond to the environment change without the help from external devices, due to their complex heterogeneous structures [193]-[195], [198], [209]. Inspired by nature,

functional devices involving heterogeneous material thin layers can be achieved by deposit and pattern hydrogel solutions using the microfluidic hydrophobic/hydrophilic surface pattern, combined with two parallel plates with millimeter to sub-millimeter gap in-between [12], [15]. Researchers have found that in-plane heterogeneities could result in modulated internal stresses and three-dimensional (3D) deformations [12], [13], [15]. Moreover, the cooperative deformations of 2D periodically patterned shapes morphing material sheets could deform into 3D configurations [13]. This will greatly expand the areas such as the actuators, robots and shape morphing functional patterned soft devices [12]-[15].

Among the shape morphing materials, hydrogels are three-dimensional (3D) networks formed by hydrophilic polymer chains that embedded in a water-rich environment. It enables to swell or de-swell (shrink) through applying the external stimuli (e.g. pH, chemicals, temperature, electrical, light, etc.). Hydrogels have the abilities to change their volumes sizably and reversibly, can be synthesized into transparent, elastic solid, stretchable, ionic conductive and shape-morphing soft materials, which are promising in various applications such as soft robotics, tissue engineering, and biosensors [196], [208]-[210].

6.2 Research development

Morphing soft materials responding to external stimulation (e.g. electrical, mechanical and chemical) have promising applications in various fields, such

as flexible electronics, biomedical transducers and soft robotics [194]-[196]. As discussed in section 2.3.3, one of the desirable developments is to make the self-shaping process controllable and programmable, at least for specific configurations. Compared to the method used by Wang and co-workers [12], where hard masks were used to selectively swell hydrogel either towards top or bottom. They have demonstrated the "pre-designed" complex deformations through the periodically patterned hydrogel blocks that made from multi-step lithographically. Whilst patterned homogenous-layered structures can provide "pre-designed" 3D shapes, the post-swelling configurations are fixed. For reconfigurable morphing structures that dynamically change shapes responding to stimulation, heterogeneous structures are desired. Therefore, in this work, a desirable approach would be that the deformation configuration could be controlled in a "mask-less" way.

The state of the arts of this research are demonstrated from the following two aspects:

- Heterogeneous hydrogel blocks patterned and layered by controlled surface wetting at hydrophobic and hydrophilic boundaries as shown in **Fig. 6.1**. The layer thickness and uniformity are ensured and controlled by droplet volume and the gap between the two parallel plates.
- Reconfigurable 3D morphing response to the stimulation inputs such as changing ionic concentration and temperature of the solution this hydrogel structure is immersed in.

6.3 Experimental methods

6.3.1 Fabrication of heterogeneous hydrogel structure

To structure and shape the hydrogel, hydrophobic/hydrophilic patterns were created [14]. **Fig. 6.1** shows patterned Parylene-CTM hydrophobic area and hydrophilic silicon dioxide (SiO_2) patterns, both on smooth silicon substrate. Functional (swell-able) hydrogel droplets/blocks were deposited on this Parylene-SiO_2 surface, shape-controlled by hydrophobic/philic boundaries, and squeezed into "button" shape by non-functional soft substrate (e.g. non-swelling gel) before cross-linked to form the desired heterogeneous structure.

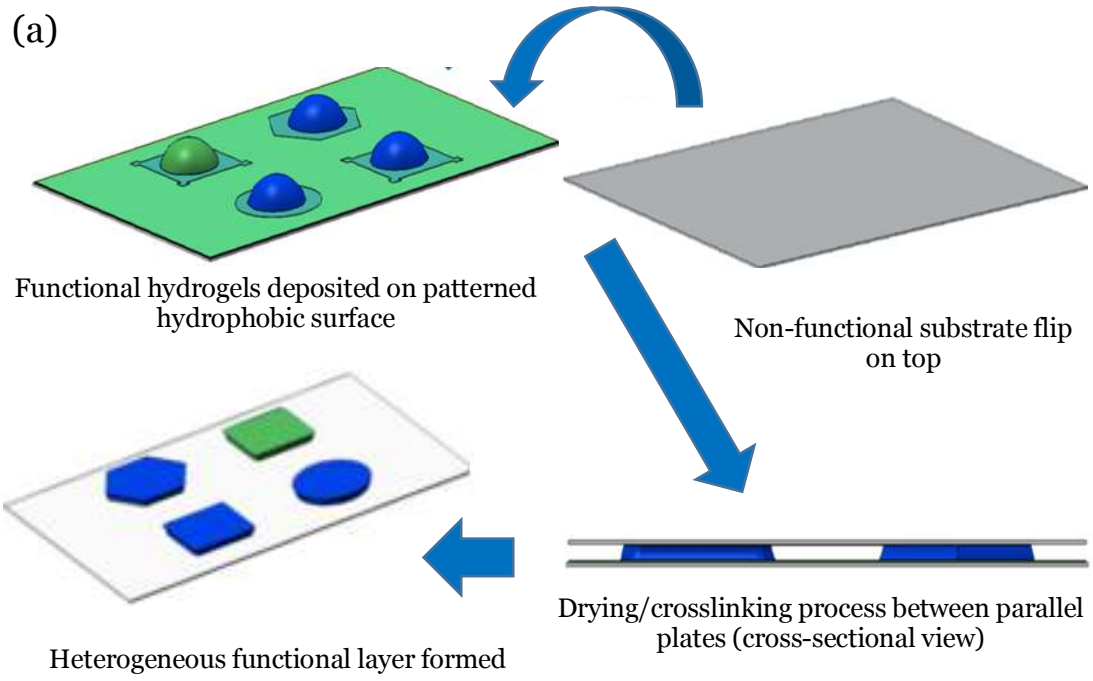

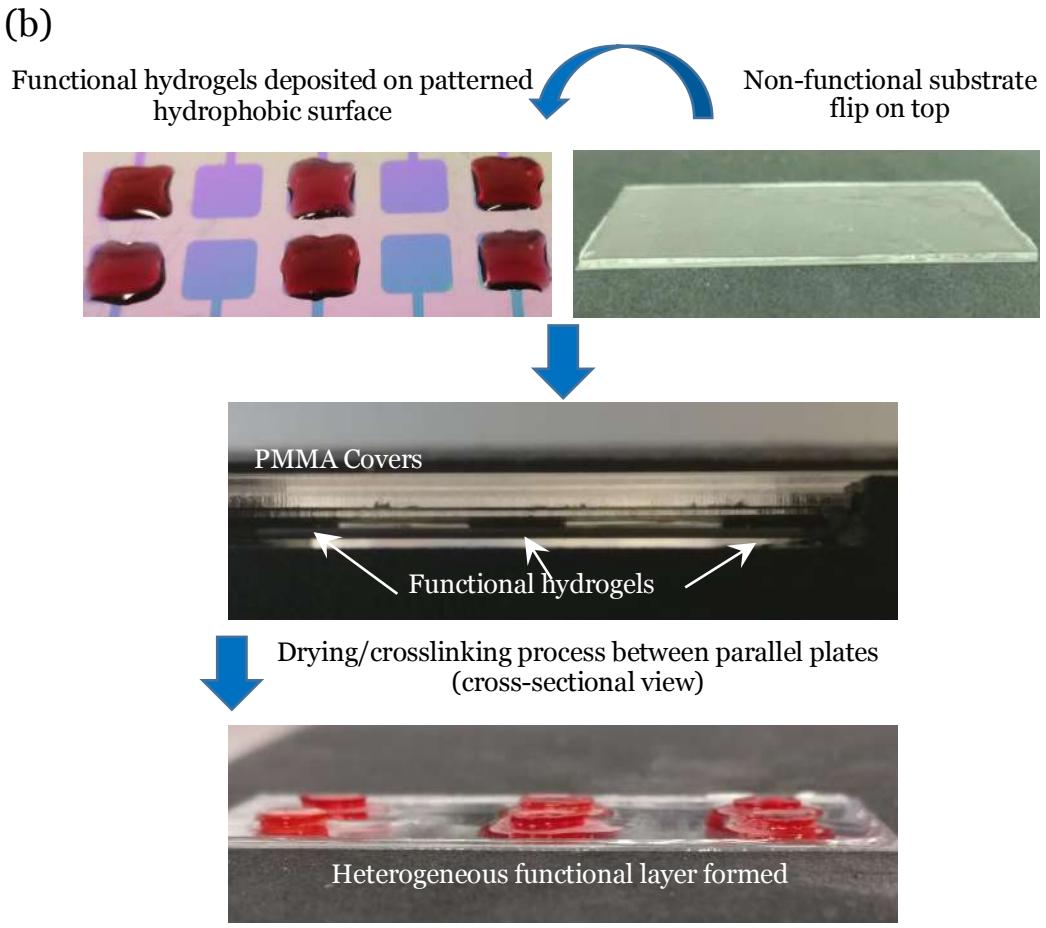

Figure 6.1 (a) Schematic view of the heterogeneous hydrogel structure patterned by hydrophobic/philic surface (b) photos show the fabrication process of the heterogeneous hydrogel structure patterned by hydrophobic/philic surface.

To prepare the nonofunctional soft substrate, Acrylamide powders were dissolved in DI water with the amount of acrylamide 14.0 wt%. N,N'-Methylenebisacrylamide (BisAA or MBAA) was used as a cross linker, with N,N,N′,N′-Tetramethylethylenediamine (TEMED) used as accelerator and Ammonium Persulfate (APS) as thermoinitiator, the molar ratios are 0.028, 0.031 and 0.152 mol%, respectively (relative to acrylamide monomer). Therefore, I have added 0.00085g BisAA, 0.00139g APS and 1.13ul TEMED into the 14.0 wt% acrylamide.

The functional hydrogel used are Poly(Acrylamide-Sodium Acrylate), created from poly-acrylamide (PAAm) network with Sodium Acrylate (SA) which contains free positive sodium ions. The crosslinking agent N,N'-Methylenebisacrylamide (BisAA or MBAA), with N,N,N′,N′-Tetramethylethylenediamine (TEMED) and Ammonium Persulfate (APS) used as initiators for the polymerization process. In order to prepare the different ionic concentration of the gels for different swelling/de-swelling behaviour, the amount of Sodium Acrylate (SA) has been modified, details shown on **Table 6.1**.

Table 6.1 The detailed concentration for different composites of two hydrogel blocks

Functional hydrogel patterns	**Pattern I**	**Pattern II**
Acrylamide (ul)	94.08	94.08
Sodium Acrylate (ul)	26.88	80.64
BisAA (ul)	17.47	17.47
Food dye (ul)	192.5	138.5
N,N,N′,N′-Tetramethylethylenediamine (TEMED, ul)	0.84	0.84
Ammonium Persulfate (APS, ul)	8.4	8.4

6.4 Results and discussion

6.4.1 Swelling and de-swelling

The gel swelling and de-swelling can happen when immersed in different concentrations of PBS (phosphate buffered saline) solution and DI water depending on ionic concentration of the gel and the solution. **Fig. 6.2a-c** demonstrate how the swelling and de-swelling behaviour is recorded, by showing a dried cylinder-shaped gel swelling for 35 minutes in different concentrations of PBS solution and DI water. The height of the swelling hydrogel was controlled by a cover slip, and the diameters were experimentally measured for swelling ratio calculation, given by swelling ratio=d_m/d_o, where d_o is the original diameter for the gel pattern before immersing in different solutions. d_m is the measured diameter for the gel pattern after swelling or de-swelling behavior. From the experiment results, it can be seen that when immersed in DI water, both of the hydrogel pattern have swelled, when immersed in 0.1M PBS, the higher concentration of hydrogel pattern (pattern I) swell while the lower concentration of hydrogel pattern (pattern II) de-swelling, when immersed in 0.5M PBS, due that the concentrations of both pattern I and II are lower than 0.5M PBS, in this case, all patterns behave de-swell which as expected.

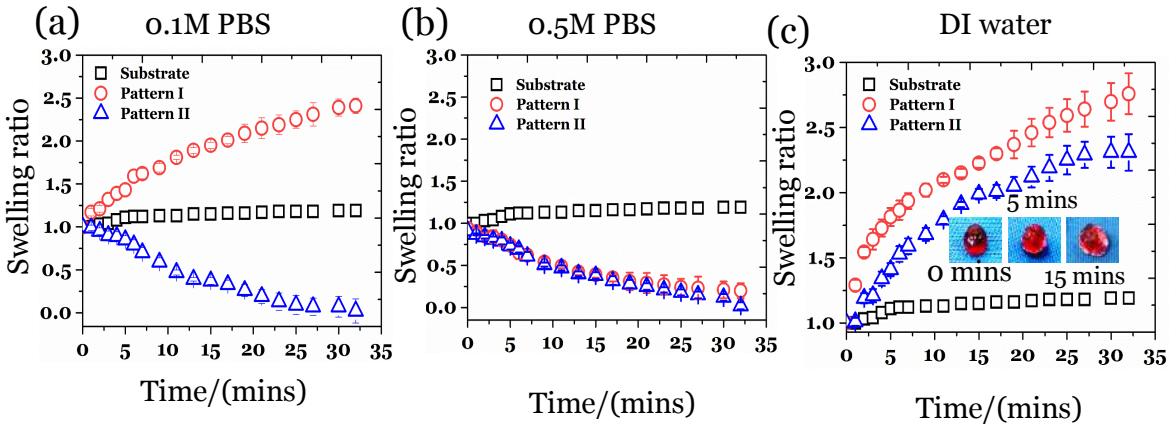

Figure 6.2 Swelling ratio behaviour at (a) 0.1M PBS (b) 0.5M PBS and (c) DI water for different composites of pattern I and pattern II.

6.4.2 Single configuration demonstration

Single configuration 3D surface shape control has been demonstrated by selectively swell and de-swell the heterogeneous functional hydrogel blocks with different composites/stimuli-responsive properties which are assembled on the same substrate as shown previously in **Fig. 6.1**. In this experiment, the pink coloured hydrogel block in **Fig. 6.3** swelled in the 0.1M PBS solution, causing localized surface raising. The red coloured hydrogel block de-swelled in the same solution, causing localized surface concaving. When the substrate was detached from the bottom of the solution container, a complex surface with raised (pink area) and concaved (red area) surface was achieved as shown in **Fig. 6.3**.

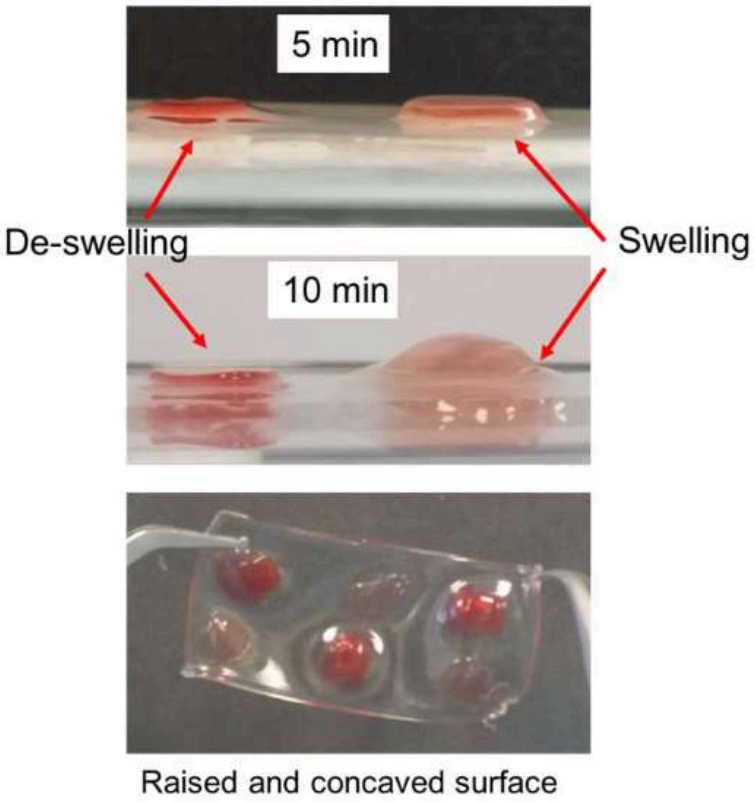

Figure 6.3 Photos showing hydrogel blocks with different composites swelling and de-swelling over time in 0.1M PBS, causing localized surface raising and concaving deformations.

6.4.3 Re-configuration characterization

Due to the heterogeneous nature of the functional hydrogel layer, the swelling vs. de-swelling spatial configuration can change responding to the external stimulation. By changing the ion concentration of the PBS solution, initial reconfigurable gel deformations were achieved (flat shape – "S" shape – "C" shape and "W" shape). This responsive shape morphing demonstration was shown in **Fig. 6.4**. When immersed in DI water, the gel started bending to "C" shape. When immersed inside the PBS concentrations with 0.1M and 0.5M,

the hydrogel structure shaped to “S” shape and “W” shape respectively. This is a combined result from:

- Hydrogel block-B (pink coloured) changes from deswelling to swelling state, responding to the PBS concentration decrease.
- Hydrogel block-A (red coloured) maintains high ratio swelling.

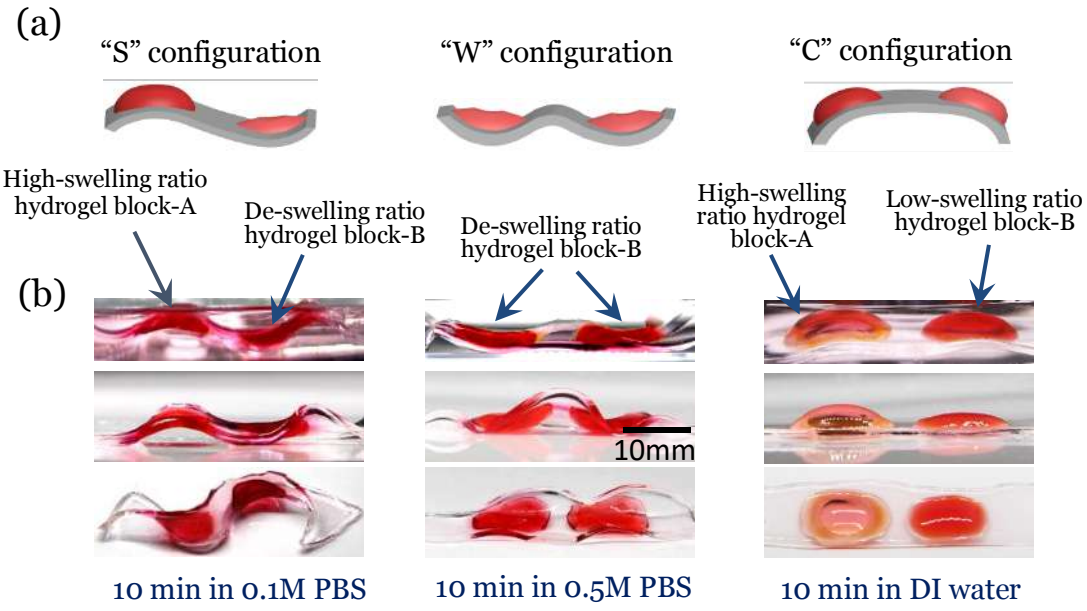

Figure 6.4 (a) Schematic illustration showing hydrogel structure shape reconfiguration with different shapes of “S”, “W” and “C” with (b) corresponding of photos view.

Such reconfigurable response shaping hydrogel shed a light on the great potential of sensing and actuation applications with complex 3D morphing materials. While this research currently focuses on ionic concentration related response to achieve 3D morphing patterns, other stimulations such as temperature, electrical and physical constrains could all affect the swelling

behaviour. Meanwhile, hydrogel is the soft material and can be tuned even more elastic and conductive by adding the nanoparticles into it, to achieve an integrated multilayer device with electro-luminescent responsive behaviour. It is foreseeable, that more advanced functions can be achieved with additional hydrogel functional blocks, which enabling next-generation flexible electronics with heterogeneous layered structures.

6.5 Chapter Summary

In summary, the design, fabrication and characterization of well-defined controllable morphing technology by patterning and controlling the variform of hydrogel droplets onto hydrophobically patterned surface, which to achieve the advanced and complex 3D morphing structures. The investigation considers deposited different composites of functional hydrogel droplets (with swelling ratio mismatch) onto patterned hydrophobic surface (a “two-parallel plate” configuration, shape-controlled by hydrophobic boundaries) to generate the heterogeneous layer. This unique way of generating 3D morphing structures could have potential applications in ionic concentration sensing, PH sensing and soft robotics.

Chapter 7

Conclusion and Future Possibilities

7.1 Conclusion

In general, this thesis discussed the research in developing elastic instabilities induced Strain-Gated logic sensing, Topo-Optical sensing and advanced 3D morphing actuation system. The engineering approach was mainly based on theories and technologies relevant to soft materials and associated micro-fabrication methods.

The elastic instabilities growth within the multi- layer elastomer systems has been discussed. It was observed that when a super-flexible multi-layer substrate with modulus mismatch was compressed under large strain, the surface would deform, and the elastic instabilities would evolve. By designing the mechanical properties and film thickness, different types of instabilities (e.g. wrinkles, creases, folds) have been observed and characterized on both plain and patterned surface. Patterned Au thin hard film layer has been designed to achieve the controllable formation of surface creasing and patterned micro-hole arrays thin hard film layer for controlling the local energy concentration and spatial location of the required deep creasing patterns.

Chapter 4 discussed the development of test structures for the realization of super-flexible strain-gated logic transducers with a high strain sensing range (up to 60%) by allowing intimate, mechanically conformable integration with soft materials. Such sensors with the ability to detect multiple strain values have been designed and fabricated through dual self-assembly monolayer (SAM) based method. The arrayed and interconnected “multiple finger” Au electrode structures with different gap value L_g are demonstrated to generate the stepwise electro-resistance sensing signals. Under mechanical in-plane compression, the surface instabilities of creases can be generated in between the finger electrodes that will bring the initially separated finger electrodes into contact sequentially due to their different L_g, the resistance displays a drop before and after the contact of each finger electrodes to generate the stepwise sensing signal. The designed devices have been developed to explore the geometry design effect on the electrode-elastomer “stiff film on soft elastomer” surface deformation. The enabled stepwise strain-electrical resistance switching is suitable for future interconnected sensor array type of super-compressible devices.

In the work discussed by chapter 5, a flexible topo-optical sensing technology was successfully achieved by employing functional luminescence composites in multi-layer elastomer structures (casting and drying a drop of optical indicator solution on the plasma treated PDMS surface), to translate surface topography into optical signal by inducing photo-luminescence function. This has been realized by the controllable formation of creasing/folding patterns

at threshold substrate strains. By designing the structural patterned templates with various geometrical inputs of lattice patterns, the threshold strains can be tuned. Apart from the threshold strains, folding-in depth distribution, results repeatability, and signal noise ratio (SNR) optical pattern contrast have also been studied.

In order to improve the SNR and contrast, a coated thin optical Iridium-III indicator layer has been introduced with which the photoluminescence can be largely quenched by the presence of oxygen. When the surface is functionalized with Iridium-III under mechanical compression, the self-folded creasing surface could create a hypoxia condition that emitted strong red luminescent light, while surfaces exposed to ambient air remain dark due to oxygen quenching effect. Thus the noise background has been removed and the SNR contrast is improved when compared with FOA. For such ultra-high contrast topo-optical sensing approach that coupled by fluorescent light, the deforming super-flexible elastomer part of the sensing system is physically separated from the fixed rigid detector and signal processing part during operation. Since there is no metal interconnects on the deforming substrate, this development has shown an alternative solution to the challenges faced by stretchable/super-flexible sensor packaging, providing opportunities for future applications in tuneable optics and stretchable electronics.

This thesis also discussed the initial study into the advanced 3D morphing actuation technology, where an innovative way of printing and patterning soft

functional hydrogel morphing structure has been focused to develop the heterogeneous layered structures of hydrogel to generate reconfigurable 3D morphing device. In chapter 6, a prototype of controllable 3D morphing transducers by functional different composites of hydrogel has been achieved. The functional hydrogels were deposited onto the patterned hydrophobic surface, after that, such functional hydrogels were covered with non-swelling substrate to transfer the hydrogels from mask to such soft substrate. Then, the transferred soft functional material was immersed inside the different solutions (e.g. PBS, DI water) to achieve the controllable shape patterns generation. Currently some initial configurations are achieved such as S, W and C shape due to the different swelling and de-swelling ratios. Such complex 3D soft structures can be potential used such as flexible electronics, soft robotics, and microfluidics.

7.2 Future Possibilities

Further to the work discussed in this thesis, some research challenges remain and more works are required for further structure optimization.

As described in session 4.3.4, the Au interconnects along the tension of y direction were increasingly likely to break due to the Possion effect, thus only the two-step electrical sensing was achieved. To address the challenge, future work will focus on optimizing the interconnect designs for better protection and improving stepwise electrical signal.

In chapter 5, a hardening skin layer was created by uniform plasma treatment of PDMS surface. A different approach would be to selectively treat the PDMS surface, which means some parts of the PDMS surface been treated with oxygen plasma to create the hardening thin layer while others are not. Therefore, due to the modulus mismatch on surface and cross different layers, much more complex micro patterns could be generated such as “N”, “U”, “T” or even LETTERS, which can be potentially used as bio-medical substrates for bio-marking or bio-tracing.

Currently, the time lapsing of the signal intensity start to drop at 75 h for the Ir-III at $\varepsilon = 0.52$, due to the oxygen sensitivity nature of Ir-III. Therefore, the potential application for adaptive topo-optical grid could be promising for some biological applications (minutes to days), where the oxygen concentration can be controlled at relatively low level in bio-media (i.e. aqueous solutions). However, for a long period of sensing time (such as for several weeks), the development of long lasting/permanent high contrast topo-optical sensing mechanism is of great importance, which could be specialized in luminescent materials in the future so that the high contrast window would be likely to be extended to weeks or even longer.

Most optical performances demonstrated in this thesis were quantified by microscope. When under the mechanical stimuli, the created microscopic folds are usually difficult to be observed by the naked eye. The future plan is to make it scalable which enable to apply this high contrast topo-optical sensing system for wider application field, such as under the macro-scale

(like center-meter scale) and can be captured by the eyeball directly and clearly. Therefore, the idea of macroscopic topo-optical sensing is interesting for its convenient implementation/integration in scaling-up applications, which could be as part of the future work.

In chapter 6, initial experimental works are presented to achieve the functional hydrogel based 3D morphing structures. For further understanding of the swelling and de-swelling performance, numerical analysis (e.g. ABAQUS FEA with hyper-elastic material model) can be used to perform the behaviour of substrate and hydrogel patterns. In order to understand how the convex and concave configuration can be generated, the simulation analysis enables to explain whether a tensile stress (σ) or a compressive stress (σ) can be induced on the top surface of the substrate, which causes either the clockwise or counter-clockwise bending moment (M). Furthermore, currently the research focuses on ionic concentration related response, other stimuli (e.g. temperature, electrical and physical constrains) could all affect the swelling behaviour that could be as part of the future work.

Bibliography

[1] Kim, D. H., Lu, N., Ma, R., Kim, Y. S., Kim, R. H., & Wang, S. & Rogers, JA (2011). *Epidermal electronics. Science*, *333*(6044), 838-843.

[2] Wu, W., Wen, X., & Wang, Z. L. (2013). Taxel-addressable matrix of vertical-nanowire piezotronic transistors for active and adaptive tactile imaging. *Science*, *340*(6135), 952-957.

[3] Gao, W., Emaminejad, S., Nyein, H. Y. Y., Challa, S., Chen, K., Peck, A., et al. & Lien, D. H. (2016). Fully integrated wearable sensor arrays for multiplexed in situ perspiration analysis. *Nature*, *529*(7587), 509-514.

[4] Madhvapathy, S. R., Ma, Y., Patel, M., Krishnan, S., Wei, C., Li, Y., et al. & Rogers, J. A. (2018). Epidermal electronic systems for measuring the thermal properties of human skin at depths of up to several millimeters. *Advanced Functional Materials*, *28*(34), 1802083.

[5] Xu, B., Chen, D., & Hayward, R. C. (2014). Mechanically gated electrical switches by creasing of patterned metal/elastomer bilayer films. *Advanced Materials*, *26*(25), 4381-4385.

[6] Khang, D. Y., Rogers, J. A., & Lee, H. H. (2009). Mechanical buckling: mechanics, metrology, and stretchable electronics. *Advanced Functional Materials*, *19*(10), 1526-1536.

[7] Pan, T., Pharr, M., Ma, Y., Ning, R., Yan, Z., Xu, R., et al. & Rogers, J. A. (2017). Experimental and theoretical studies of serpentine interconnects on ultrathin elastomers for stretchable electronics. *Advanced Functional Materials*, *27*(37), 1702589.

[8] Chu, Y., Wu, X., Lu, J., Liu, D., Du, J., Zhang, G., & Huang, J. (2016). Photosensitive and flexible organic field-effect transistors based on interface trapping effect and their application in 2D imaging array. Advanced Science, 3(8), 1500435.

[9] Wang, C., Wang, C., Huang, Z., & Xu, S. (2018). Materials and structures toward soft electronics. Advanced Materials, 30(50), 1801368.

[10] Guo, C. F., Liu, Q., Wang, G., Wang, Y., Shi, Z., Suo, Z., et al. & Ren, Z. (2015). Fatigue-free, superstretchable, transparent, and biocompatible metal electrodes. Proceedings of the National Academy of Sciences, 112(40), 12332-12337.

[11] Yang, C. H., Chen, B., Zhou, J., Chen, Y. M., & Suo, Z. (2016). Electroluminescence of giant stretchability. *Advanced Materials*, *28*(22), 4480-4484.

[12] Wang, Z. J., Hong, W., Wu, Z. L., & Zheng, Q. (2017). Site-Specific Pre-Swelling-Directed Morphing Structures of Patterned Hydrogels. Angewandte Chemie International Edition, 56(50), 15974-15978.

[13] Wang, Z. J., Zhu, C. N., Hong, W., Wu, Z. L., & Zheng, Q. (2017). Cooperative deformations of periodically patterned hydrogels. Science advances, 3(9), e1700348.

[14] Li, Y., McKenna, E. O., Parkes, W., Pitt, A. R., & Walton, A. J. (2011). The application of fixed hydrophobic patterns for confinement of aqueous solutions in proteomic microarrays. Applied Physics Letters, 99(7), 073703.

[15] Chiang, M. Y., Hsu, Y. W., Hsieh, H. Y., Chen, S. Y., & Fan, S. K. (2016). Constructing 3D heterogeneous hydrogels from electrically manipulated prepolymer droplets and crosslinked microgels. Science advances, 2(10), e1600964.

[16] Ji, X., Wu, R. T., Long, L., Ke, X. S., Guo, C., Ghang, Y. J., et al. & Sessler, J. L. (2018). Encoding, Reading, and Transforming Information Using Multifluorescent Supramolecular Polymeric Hydrogels. Advanced Materials, 30(11), 1705480.

[17] Jin, L., Chen, D., Hayward, R. C. & Suo, Z. (2014). Creases on the interface between two soft materials. *Soft Matter*, *10*,303-311.

[18] Tallinen, T., Biggins, J. S., & Mahadevan, L. (2013). Surface Sulci in Squeezed Soft Solids. *Physical Review Letters*, *110*(2), 024302.

[19] Wang, T., Yang, Y., Fu, C., Liu, F., Wang, K., & Xu, F. (2020). Wrinkling and smoothing of a soft shell. *Journal of the Mechanics and Physics of Solids*, *134*, 103738.

[20] Kim, D. H., Ahn, J. H., Choi, W. M., Kim, H. S., Kim, T. H., Song, J., et al. & Rogers, J. A. (2008). Stretchable and foldable silicon integrated circuits. *Science*, *320*(5875), 507-511.

[21] Su, Y., Ping, X., Yu, K. J., Lee, J. W., Fan, J. A., Wang, B., et al. & Yu, C. (2017). In-plane deformation mechanics for highly stretchable electronics. *Advanced materials*, *29*(8), 1604989.

[22] Cai, S., Bertoldi, K., Wang, H., & Suo, Z. (2010). Osmotic collapse of a void in an elastomer: breathing, buckling and creasing. *Soft Matter*, *6*(22), 5770-5777.

[23] Kim, D. H., & Rogers, J. A. (2008). Stretchable electronics: materials strategies and devices. *Advanced Materials*, *20*(24), 4887-4892.

[24] Rogers, J. A., Someya, T., & Huang, Y. (2010). Materials and mechanics for stretchable electronics. *science*, *327*(5973), 1603-1607.

[25] Son, D., Lee, J., Qiao, S., Ghaffari, R., Kim, J., Lee, J. E., et al. & Yang, S. (2014). Multifunctional wearable devices for diagnosis and therapy of movement disorders. *Nature Nanotechnology*, *9*(5), 397-404.

[26] Tee, B. C. K., Chortos, A., Berndt, A., Nguyen, A. K., Tom, A., McGuire, A., et al. & Mei, P. (2015). A skin-inspired organic digital mechanoreceptor. *Science*, *350*(6258), 313-316.

[27] Minev, I. R., Musienko, P., Hirsch, A., Barraud, Q., Wenger, N., Moraud, E. M., et al. & Torres, R. F. (2015). Electronic dura mater for long-term multimodal neural interfaces. *Science*, *347*(6218), 159-163.

[28] Khodagholy, D., Doublet, T., Quilichini, P., Gurfinkel, M., Leleux, P., Ghestem, A., et al. & Malliaras, G. G. (2013). In vivo recordings of brain activity using organic transistors. *Nature communications*, *4*, 1575.

[29] Kang, S. K., Murphy, R. K., Hwang, S. W., Lee, S. M., Harburg, D. V., Krueger, N. A., et al. & Liu, Z. (2016). Bioresorbable silicon electronic sensors for the brain. *Nature*, *530*(7588), 71-76.

[30] Gong, S., Schwalb, W., Wang, Y., Chen, Y., Tang, Y., Si, J., et al. & Cheng, W. (2014). A wearable and highly sensitive pressure sensor with ultrathin gold nanowires. *Nature communications*, *5*, 3132.

[31] Rus, D., & Tolley, M. T. (2015). Design, fabrication and control of soft robots. *Nature*, *521*(7553), 467-475.

[32] Khare, K., Zhou, J., & Yang, S. (2009). Tunable open-channel microfluidics on soft poly (dimethylsiloxane)(PDMS) substrates with sinusoidal grooves. *Langmuir*, *25*(21), 12794-12799.

[33] Khang, D. Y., Jiang, H., Huang, Y., & Rogers, J. A. (2006). A stretchable form of single-crystal silicon for high-performance electronics on rubber substrates. *Science*, *311*(5758), 208-212.

[34] Chen, D., Yoon, J., Chandra, D., Crosby, A. J., & Hayward, R. C. (2014). Stimuli responsive buckling mechanics of polymer films. *Journal of Polymer Science Part B: Polymer Physics*, *52*(22), 1441-1461.

[35] White, M. S., Kaltenbrunner, M., Głowacki, E. D., Gutnichenko, K., Kettlgruber, G., Graz, I., et al. & Major, Z. (2013). Ultrathin, highly flexible and stretchable PLEDs. *Nature Photonics*, *7*(10), 811-816.

[36] Grzybowski, B., Qin, D., Haag, R., & Whitesides, G. M. (2000). Elastomeric optical elements with deformable surface topographies: applications to force measurements, tunable light transmission and light focusing. *Sensors and Actuators A: Physical*, *86*(1-2), 81-85.

[37] Wilbur, J. L., Jackman, R. J., Whitesides, G. M., Cheung, E. L., Lee, L. K., & Prentiss, M. G. (1996). Elastomeric optics. *Chemistry of materials*, *8*(7), 1380-1385.

[38] Soboyejo, W (2002). Mechanical properties of engineered materials. *CRC press*, 152.

[39] Ashby, M.F., Jones, D. R. H. (2012). Engineering Materials: An Introduction to Properties, Applications and Design. *Elsevier*, 496.

[40] Rogers, J. A., Schueller, O. J., Marzolin, C., & Whitesides, G. M. (1997). Wave-front engineering by use of transparent elastomeric optical elements. *Applied optics*, *36*(23), 5792-5795.

[41] Wise, K. D., & Najafi, K. (1991). Microfabrication techniques for integrated sensors and microsystems. *Science*, *254*(5036), 1335-1342.

[42] Xia, Y., Kim, E., Zhao, X. M., Rogers, J. A., Prentiss, M., & Whitesides, G. M. (1996). Complex optical surfaces formed by replica molding against elastomeric masters. *Science*, *273*(5273), 347-349.

[43] Kim, E., Xia, Y., & Whitesides, G. M. (1995). Polymer microstructures formed by moulding in capillaries. *Nature*, *376*(6541), 581-584.

[44] Gerdle, B., Karlsson, S., Day, S., & Djupsjöbacka, M. (1999). Acquisition, processing and analysis of the surface electromyogram. In *Modern techniques in neuroscience research* (pp. 705-755). Springer, Berlin, Heidelberg.

[45] Ives, J. R., Mirsattari, S. M., & Jones, D. (2007). Miniaturized, on-head, invasive electrode connector integrated EEG data acquisition system. *Clinical neurophysiology*, *118*(7), 1633-1638.

[46] Kaltenbrunner, M., Sekitani, T., Reeder, J., Yokota, T., Kuribara, K., Tokuhara, T., et al. & Bauer, S. (2013). An ultra-lightweight design for imperceptible plastic electronics. *Nature*, *499*(7459), 458-463.

[47] Xu, S., Zhang, Y., Jia, L., Mathewson, K. E., Jang, K. I., Kim, J., et al. & Bhole, S. (2014). Soft microfluidic assemblies of sensors, circuits, and radios for the skin. *Science*, *344*(6179), 70-74.

[48] Lipomi, D. J., Vosgueritchian, M., Tee, B. C., Hellstrom, S. L., Lee, J. A., Fox, C. H., & Bao, Z. (2011). Skin-like pressure and strain sensors based on transparent elastic films of carbon nanotubes. *Nature Nanotechnology*, *6*(12), 788-792.

[49] Kim, D. H., Ghaffari, R., Lu, N., & Rogers, J. A. (2012). Flexible and stretchable electronics for biointegrated devices. *Annual review of biomedical engineering*, *14*, 113-128.

[50] Li, S., Zhao, H., & Shepherd, R. F. (2017). Flexible and stretchable sensors for fluidic elastomer actuated soft robots. *MRS Bulletin*, *42*(2), 138-142.

[51] Cerda, E., & Mahadevan, L. (2003). Geometry and physics of wrinkling. *Physical review letters*, *90*(7), 074302.

[52] Lacour, S. P., Wagner, S., Huang, Z., & Suo, Z. (2003). Stretchable gold conductors on elastomeric substrates. *Applied physics letters*, *82*(15), 2404-2406.

[53] Xu, F., Wang, X., Zhu, Y., & Zhu, Y. (2012). Wavy ribbons of carbon nanotubes for stretchable conductors. *Advanced Functional Materials*, *22*(6), 1279-1283.

[54] Robinson, A., Aziz, A., Liu, Q., Suo, Z., & Lacour, S. P. (2014). Hybrid stretchable circuits on silicone substrate. *Journal of Applied Physics*, *115*(14), 143511.

[55] Kim, D. H., Lu, N., Huang, Y., & Rogers, J. A. (2012). Materials for stretchable electronics in bioinspired and biointegrated devices. *MRS bulletin*, *37*(3), 226-235.

[56] Kim, T. A., Kim, H. S., Lee, S. S., & Park, M. (2012). Single-walled carbon nanotube/silicone rubber composites for compliant electrodes. *Carbon*, *50*(2), 444-449.

[57] Puig-Lleixà, C., Jiménez, C., Alonso, J., & Bartrolí, J. (1999). Polyurethane–acrylate photocurable polymeric membrane for ion-sensitive field-effect transistor based urea biosensors. *Analytica chimica acta*, *389*(1-3), 179-188.

[58] Kokkinis, D., Schaffner, M., & Studart, A. R. (2015). Multimaterial magnetically assisted 3D printing of composite materials. *Nature communications*, *6*, 8643.

[59] Dickey, M. D., Chiechi, R. C., Larsen, R. J., Weiss, E. A., Weitz, D. A., & Whitesides, G. M. (2008). Eutectic gallium-indium (EGaIn): a liquid metal alloy for the formation of stable structures in microchannels at room temperature. *Advanced Functional Materials*, *18*(7), 1097-1104.

[60] Liu, T., Sen, P., & Kim, C. J. (2011). Characterization of nontoxic liquid-metal alloy galinstan for applications in microdevices. *Journal of Microelectromechanical Systems*, *21*(2), 443-450.

[61] Mazlouman, S. J., Jiang, X. J., Mahanfar, A. N., Menon, C., & Vaughan, R. G. (2011). A reconfigurable patch antenna using liquid metal embedded in a silicone substrate. *IEEE Transactions on Antennas and Propagation*, *59*(12), 4406-4412.

[62] Vosgueritchian, M., Lipomi, D. J., & Bao, Z. (2012). Highly conductive and transparent PEDOT: PSS films with a fluorosurfactant for stretchable and flexible transparent electrodes. *Advanced functional materials*, *22*(2), 421-428.

[63] Hyun, D. C., Park, M., Park, C., Kim, B., Xia, Y., Hur, J. H., et al. & Jeong, U. (2011). Ordered zigzag stripes of polymer gel/metal nanoparticle composites for highly stretchable conductive electrodes. *Advanced Materials*, *23*(26), 2946-2950.

[64] Shang, S., Zeng, W., & Tao, X. M. (2011). High stretchable MWNTs/polyurethane conductive nanocomposites. *Journal of Materials Chemistry*, *21*(20), 7274-7280.

[65] Xu, F., Lu, W., & Zhu, Y. (2010). Controlled 3D buckling of silicon nanowires for stretchable electronics. *Acs Nano*, *5*(1), 672-678.

[66] Akinwande, D., Petrone, N., & Hone, J. (2014). Two-dimensional flexible nanoelectronics. *Nature communications*, *5*, 5678.

[67] Jariwala, D., Sangwan, V. K., Lauhon, L. J., Marks, T. J., & Hersam, M. C. (2014). Emerging device applications for semiconducting two-dimensional transition metal dichalcogenides. *ACS nano*, *8*(2), 1102-1120.

[68] Sagara, Y., & Kato, T. (2009). Mechanically induced luminescence changes in molecular assemblies. *Nature Chemistry*, *1*(8), 605.

[69] Jeong, S. M., Song, S., Lee, S. K., & Ha, N. Y. (2013). Colour manipulation of mechanoluminescence from stress-activated composite films. *Advanced Materials*, *25*(43), 6194-6200.

[70] Xu, S., Zhang, Y., Cho, J., Lee, J., Huang, X., Jia, L., et al. & Cheng, H. (2013). Stretchable batteries with self-similar serpentine interconnects and integrated wireless recharging systems. *Nature communications*, *4*, 1543.

[71] Kim, D. H., Song, J., Choi, W. M., Kim, H. S., Kim, R. H., Liu, Z., et al. & Rogers, J. A. (2008). Materials and noncoplanar mesh designs for integrated circuits with linear elastic responses to extreme mechanical deformations. *Proceedings of the National Academy of Sciences*, *105*(48), 18675-18680.

[72] Kim, D. H., Liu, Z., Kim, Y. S., Wu, J., Song, J., Kim, H. S., et al. & Rogers, J. A. (2009). Optimized structural designs for stretchable silicon integrated circuits. *Small*, *5*(24), 2841-2847.

[73] Suzuki, H. (2006). Stimulus-responsive gels: Promising materials for the construction of micro actuators and sensors. *Journal of intelligent material systems and structures*, *17*(12), 1091-1097.

[74] Ahn, S. K., Kasi, R. M., Kim, S. C., Sharma, N., & Zhou, Y. (2008). Stimuli-responsive polymer gels. *Soft Matter*, *4*(6), 1151-1157.

[75] Wang, D., Cheewaruangroj, N., Li, Y., McHale, G., Jiang, Y., Wood, D., et al. & Xu, B. B. (2018). Spatially configuring wrinkle pattern and multiscale surface evolution with structural confinement. *Advanced Functional Materials*, *28*(1), 1704228.

[76] Ouchi, T., Yang, J., Suo, Z., & Hayward, R. C. (2018). Effects of stiff film pattern geometry on surface buckling instabilities of elastic bilayers. *ACS applied materials & interfaces*, *10*(27), 23406-23413.

[77] Zhang, Y., Wang, S., Li, X., Fan, J. A., Xu, S., Song, Y. M., et al. & Lu, B. (2014). Experimental and theoretical studies of serpentine microstructures bonded to prestrained elastomers for stretchable electronics. *Advanced Functional Materials*, *24*(14), 2028-2037.

[78] Wang, C., Xu, B. B., Terry, J. G., Smith, S., Walton, A. J., Wang, S., et al. & Li, Y. (2019). Flexible, strain gated logic transducer arrays enabled by initializing surface instability on elastic bilayers. *APL Materials*, *7*(3), 031509.

[79] Zeng, S., Zhang, D., Huang, W., Wang, Z., Freire, S. G., Yu, X., et al. & Sun, L. (2016). Bio-inspired sensitive and reversible mechanochromisms via strain-dependent cracks and folds. *Nature communications*, *7*, 11802.

[80] Lee, E., Zhang, M., Cho, Y., Cui, Y., Van der Spiegel, J., Engheta, N., & Yang, S. (2014). Tilted pillars on wrinkled elastomers as a reversibly tunable optical window. *Advanced Materials*, *26*(24), 4127-4133.

[81] Kim, J., Yoon, J., & Hayward, R. C. (2009). Dynamic display of biomolecular patterns through an elastic creasing instability of stimuli-responsive hydrogels. *Nature materials*, *9*(2), 159-164.

[82] Yoon, J., Bian, P., Kim, J., McCarthy, T. J., & Hayward, R. C. (2012). Local switching of chemical patterns through light-triggered unfolding of creased hydrogel surfaces. *Angewandte Chemie International Edition*, *51*(29), 7146-7149.

[83] Li, B., Cao, Y. P., Feng, X. Q., & Gao, H. (2012). Mechanics of morphological instabilities and surface wrinkling in soft materials: a review. *Soft Matter*, *8*(21), 5728-5745.

[84] Vandeparre, H., Piñeirua, M., Brau, F., Roman, B., Bico, J., Gay, C., et al. & Damman, P. (2011). Wrinkling hierarchy in constrained thin sheets from suspended graphene to curtains. *Physical Review Letters*, *106*(22), 224301.

[85] Sharon, E., Marder, M., & Swinney, H. L. (2004). Leaves, flowers and garbage bags: Making waves. *American Scientist*, *92*(3), 254-261.

[86] Stafford, C. M., Harrison, C., Beers, K. L., Karim, A., Amis, E. J., VanLandingham, M. R., et al. & Simonyi, E. E. (2004). A buckling-based metrology for measuring the elastic moduli of polymeric thin films. *Nature materials*, *3*(8), 545.

[87] Sun, J. Y., Xia, S., Moon, M. W., Oh, K. H., & Kim, K. S. (2011). Folding wrinkles of a thin stiff layer on a soft substrate. *Proceedings of the Royal Society A: Mathematical, Physical and Engineering Sciences*, *468*(2140), 932-953.

[88] Cao, Y., & Hutchinson, J. W. (2012). Wrinkling phenomena in neo-Hookean film/substrate bilayers. *Journal of applied mechanics*, *79*(3), 031019.

[89] Zang, J., Zhao, X., Cao, Y., & Hutchinson, J. W. (2012). Localized ridge wrinkling of stiff films on compliant substrates. *Journal of the Mechanics and Physics of Solids*, *60*(7), 1265-1279.

[90] Diab, M., Zhang, T., Zhao, R., Gao, H., & Kim, K. S. (2013). Ruga mechanics of creasing: from instantaneous to setback creases. *Proceedings of the Royal Society A: Mathematical, Physical and Engineering Sciences*, *469*(2157), 20120753.

[91] Hutchinson, J. W. (2013). The role of nonlinear substrate elasticity in the wrinkling of thin films. *Philosophical Transactions of the Royal Society A:* Mathematical, Physical and Engineering Sciences, 371(1993), 20120422.

[92] Chater, E., & Hutchinson, J. W. (1984). On the propagation of bulges and buckles. Journal of Applied Mechanics-Transactions of the ASME, 51(2): 269-277.

[93] Krylov, S., Ilic, B. R., Schreiber, D., Seretensky, S., & Craighead, H. (2008). The pull-in behavior of electrostatically actuated bistable microstructures. *Journal of Micromechanics and Microengineering*, *18*(5), 055026.

[94] Hu, Y., Hiltner, A., & Baer, E. (2004). Buckling in elastomer/plastic/elastomer 3-layer films. *Polymer composites*, *25*(6), 653-661.

[95] Genzer, J., & Groenewold, J. (2006). Soft matter with hard skin: From skin wrinkles to templating and material characterization. *Soft Matter*, *2*(4), 310-323.

[96] Shivapooja, P., Wang, Q., Orihuela, B., Rittschof, D., López, G. P., & Zhao, X. (2013). Bioinspired surfaces with dynamic topography for active control of biofouling. *Advanced Materials*, *25*(10), 1430-1434.

[97] Basan, M., Joanny, J. F., Prost, J., & Risler, T. (2011). Undulation instability of epithelial tissues. *Physical Review Letters*, *106*(15), 158101.

[98] Jin, L., Cai, S., & Suo, Z. (2011). Creases in soft tissues generated by growth. *EPL (Europhysics Letters)*, *95*(6), 64002.

[99] Mei, Y., Thurmer, D. J., Cavallo, F., Kiravittaya, S., & Schmidt, O. G. (2007). Semiconductor Sub-Micro-/Nanochannel Networks by Deterministic Layer Wrinkling. *Advanced Materials*, *19*(16), 2124-2128.

[100] Lee, S., Kim, S., Kim, T. T., Kim, Y., Choi, M., Lee, S. H., et al. & Min, B. (2012). Reversibly stretchable and tunable terahertz metamaterials with wrinkled layouts. *Advanced Materials*, *24*(26), 3491-3497.

[101] Kim, J. B., Kim, P., Pégard, N. C., Oh, S. J., Kagan, C. R., Fleischer, J. W., et al. & Loo, Y. L. (2012). Wrinkles and deep folds as photonic structures in photovoltaics. *Nature Photonics*, *6*(5), 327.

[102] Chung, J. Y., Nolte, A. J., & Stafford, C. M. (2011). Surface wrinkling: a versatile platform for measuring thin-film properties. *Advanced Materials*, *23*(3), 349-368.

[103] Wilder, E. A., Guo, S., Lin-Gibson, S., Fasolka, M. J., & Stafford, C. M. (2006). Measuring the modulus of soft polymer networks via a buckling-based metrology. *Macromolecules*, *39*(12), 4138-4143.

[104] Howarter, J. A., & Stafford, C. M. (2010). Instabilities as a measurement tool for soft materials. *Soft Matter*, *6*(22), 5661-5666.

[105] Lee, H., Xia, C., & Fang, N. X. (2010). First jump of microgel; actuation speed enhancement by elastic instability. *Soft Matter*, *6*(18), 4342-4345.

[106] Lin, P. C., & Yang, S. (2009). Mechanically switchable wetting on wrinkled elastomers with dual-scale roughness. *Soft Matter*, *5*(5), 1011-1018.

[107] Xia, D., Johnson, L. M., & López, G. P. (2012). Anisotropic wetting surfaces with one-dimesional and directional structures: fabrication approaches, wetting properties and potential applications. *Advanced Materials*, *24*(10), 1287-1302.

[108] Lee, S. G., Lee, D. Y., Lim, H. S., Lee, D. H., Lee, S., & Cho, K. (2010). Switchable transparency and wetting of elastomeric smart windows. *Advanced materials*, *22*(44), 5013-5017.

[109] Kim, P., Hu, Y., Alvarenga, J., Kolle, M., Suo, Z., & Aizenberg, J. (2013). Rational Design of Mechano-Responsive Optical Materials by Fine Tuning the

Evolution of Strain-Dependent Wrinkling Patterns. *Advanced Optical Materials*, *1*(5), 381-388.

[110] Kolaric, B., Vandeparre, H., Desprez, S., Vallée, R. A., & Damman, P. (2010). In situ tuning the optical properties of a cavity by wrinkling. *Applied Physics Letters*, *96*(4), 043119.

[111] Mei, H., Huang, R., Chung, J. Y., Stafford, C. M., & Yu, H. H. (2007). Buckling modes of elastic thin films on elastic substrates. *Applied Physics Letters*, *90*(15), 151902.

[112] Cai, S., Breid, D., Crosby, A. J., Suo, Z., & Hutchinson, J. W. (2011). Periodic patterns and energy states of buckled films on compliant substrates. *Journal of the Mechanics and Physics of Solids*, *59*(5), 1094-1114.

[113] Cowin, S. C. (2004). Tissue growth and remodeling. *Annu. Rev. Biomed. Eng.*, *6*, 77-107.

[114] Tokarev, I., & Minko, S. (2009). Stimuli-responsive hydrogel thin films. *Soft Matter*, *5*(3), 511-524.

[115] Chan, E. P., Smith, E. J., Hayward, R. C., & Crosby, A. J. (2008). Surface wrinkles for smart adhesion. *Advanced Materials*, *20*(4), 711-716.

[116] Guvendiren, M., Burdick, J. A., & Yang, S. (2010). Solvent induced transition from wrinkles to creases in thin film gels with depth-wise crosslinking gradients. *Soft Matter*, *6*(22), 5795-5801.

[117] Tanaka, T., Sun, S. T., Hirokawa, Y., Katayama, S., Kucera, J., Hirose, Y., & Amiya, T. (1987). Mechanical instability of gels at the phase transition. *Nature*, *325*(6107), 796.

[118] Wang, Q., Zhang, L., & Zhao, X. (2011). Creasing to cratering instability in polymers under ultrahigh electric fields. *Physical review letters*, *106*(11), 118301.

[119] Wang, Q., Tahir, M., Zhang, L., & Zhao, X. (2011). Electro-creasing instability in deformed polymers: experiment and theory. *Soft Matter*, *7*(14), 6583-6589.

[120] Cai, S., Chen, D., Suo, Z., & Hayward, R. C. (2012). Creasing instability of elastomer films. *Soft Matter*, *8*(5), 1301-1304.

[121] Chen, D., Cai, S., Suo, Z., & Hayward, R. C. (2012). Surface energy as a barrier to creasing of elastomer films: An elastic analogy to classical nucleation. *Physical review letters*, *109*(3), 038001.

[122] Yang, S., Khare, K., & Lin, P. C. (2010). Harnessing surface wrinkle patterns in soft matter. *Advanced Functional Materials*, *20*(16), 2550-2564.

[123] Vella, D., Bico, J., Boudaoud, A., Roman, B., & Reis, P. M. (2009). The macroscopic delamination of thin films from elastic substrates. *Proceedings of the National Academy of Sciences*, *106*(27), 10901-10906.

[124] Breid, D., & Crosby, A. J. (2011). Effect of stress state on wrinkle morphology. *Soft Matter*, *7*(9), 4490-4496.

[125] Nowinski, J. L. (1969). Surface instability of a half-space under high two-dimensional compression. *Journal of The Franklin Institute*, *288*(5), 367-376.

[126] Biot, M. A. (1963). Surface instability of rubber in compression. *Applied Scientific Research, Section A*, *12*(2), 168-182.

[127] Biot, M. A. (1965). Mechanics of incremental deformations: theory of elasticity and viscoelasticity of initially stressed solids and fluids, including thermodynamic foundations and applications to finite strain, *Wiley*.

[128] Wang, Q., & Zhao, X. (2014). Phase diagrams of instabilities in compressed film-substrate systems. *Journal of applied mechanics*, *81*(5), 051004.

[129] Hohlfeld, E. B. (2008). *Creasing, point-bifurcations, and the spontaneous breakdown of scale-invariance*. Harvard University.

[130] Hohlfeld, E., & Mahadevan, L. (2011). Unfolding the sulcus. *Physical review letters*, *106*(10), 105702.

[131] Gent, A. N., & Cho, I. S. (1999). Surface instabilities in compressed or bent rubber blocks. *Rubber Chemistry and Technology*, *72*(2), 253-262.

[132] Saha, K., Kim, J., Irwin, E., Yoon, J., Momin, F., Trujillo, V., et al. & Hayward, R. C. (2010). Surface creasing instability of soft polyacrylamide cell culture substrates. *Biophysical journal*, *99*(12), L94-L96.

[133] Trujillo, V., Kim, J., & Hayward, R. C. (2008). Creasing instability of surface-attached hydrogels. *Soft Matter*, *4*(3), 564-569.

[134] Ghatak, A., & Das, A. L. (2007). Kink instability of a highly deformable elastic cylinder. *Physical review letters*, *99*(7), 076101.

[135] Reis, P. M., Corson, F., Boudaoud, A., & Roman, B. (2009). Localization through surface folding in solid foams under compression. *Physical review letters*, *103*(4), 045501.

[136] Caruso, M. M., Davis, D. A., Shen, Q., Odom, S. A., Sottos, N. R., White, S. R., & Moore, J. S. (2009). Mechanically-induced chemical changes in polymeric materials. *Chemical reviews*, *109*(11), 5755-5798.

[137] Ooyama, Y., & Harima, Y. (2011). Molecular design of mechanofluorochromic dyes and their solid-state fluorescence properties. *Journal of Materials Chemistry*, *21*(23), 8372-8380.

[138] Teng, M. J., Jia, X. R., Yang, S., Chen, X. F., & Wei, Y. (2012). Reversible Tuning Luminescent colour and Emission Intensity: A Dipeptide-Based Light-Emitting Material. *Advanced Materials*, *24*(9), 1255-1261.

[139] Sun, J., Chen, Y., & Liang, Z. (2016). Electroluminochromic materials and devices. *Advanced Functional Materials*, *26*(17), 2783-2799.

[140] Sagara, Y., Mutai, T., Yoshikawa, I., & Araki, K. (2007). Material design for piezochromic luminescence: hydrogen-bond-directed assemblies of a pyrene derivative. *Journal of the American Chemical Society*, *129*(6), 1520-1521.

[141] Mutai, T., Satou, H., & Araki, K. (2005). Reproducible on–off switching of solid-state luminescence by controlling molecular packing through heat-mode interconversion. *Nature materials*, *4*(9), 685.

[142] Yamane, S., Tanabe, K., Sagara, Y., & Kato, T. (2011). Stimuli-responsive photoluminescent liquid crystals. In *Liquid Crystals* (pp. 395-405). Springer, Berlin, Heidelberg.

[143] Jin, M., Seki, T., & Ito, H. (2017). Mechano-responsive luminescence via crystal-to-crystal phase transitions between chiral and non-chiral space groups. *Journal of the American Chemical Society*, *139*(22), 7452-7455.

[144] Ito, H., Muromoto, M., Kurenuma, S., Ishizaka, S., Kitamura, N., Sato, H., & Seki, T. (2013). Mechanical stimulation and solid seeding trigger single-crystal-to-single-crystal molecular domino transformations. *Nature communications*, *4*, 2009.

[145] Kato, T., Mizoshita, N., & Kishimoto, K. (2006). Functional liquid-crystalline assemblies: self-organized soft materials. *Angewandte Chemie International Edition*, *45*(1), 38-68.

[146] Kato, T., Yasuda, T., Kamikawa, Y., & Yoshio, M. (2009). Self-assembly of functional columnar liquid crystals. *Chemical Communications*, (7), 729-739.

[147] Tschierske, C. (2007). Liquid crystal engineering–new complex mesophase structures and their relations to polymer morphologies, nanoscale patterning and crystal engineering. *Chemical Society Reviews*, *36*(12), 1930-1970.

[148] Ha, N. Y., Jeong, S. M., Nishimura, S., Suzaki, G., Ishikawa, K., & Takezoe, H. (2008). Simultaneous Red, Green, and Blue Lasing Emissions in a Single-Pitched Cholesteric Liquid-Crystal System. *Advanced Materials*, *20*(13), 2503-2507.

[149] Tan, H., Lyu, Q., Xie, Z., Li, M., Wang, K., Wang, K., et al. & Zhu, J. (2019). Metallosupramolecular Photonic Elastomers with Self-Healing Capability and Angle-Independent colour. *Advanced Materials*, 31(6), 1805496.

[150] Brau, F., Damman, P., Diamant, H., & Witten, T. A. (2013). Wrinkle to fold transition: influence of the substrate response. *Soft Matter*, *9*(34), 8177-8186.

[151] Ebata, Y., Croll, A. B., & Crosby, A. J. (2012). Wrinkling and strain localizations in polymer thin films. *Soft Matter*, *8*(35), 9086-9091.

[152] Pocivavsek, L., Dellsy, R., Kern, A., Johnson, S., Lin, B., Lee, K. Y. C., & Cerda, E. (2008). Stress and fold localization in thin elastic membranes. *Science*, 320(5878), 912-916.

[153] Dervaux, J., & Amar, M. B. (2008). Morphogenesis of growing soft tissues. *Physical review letters*, 101(6), 068101.

[154] McKee, C. T., Last, J. A., Russell, P., & Murphy, C. J. (2011). Indentation versus tensile measurements of Young's modulus for soft biological tissues. *Tissue Engineering Part B: Reviews*, 17(3), 155-164.

[155] Yin, J., Chen, X., & Sheinman, I. (2009). Anisotropic buckling patterns in spheroidal film/substrate systems and their implications in some natural and

biological systems. *Journal of the Mechanics and Physics of Solids*, 57(9), 1470-1484.

[156] Jin, L., Auguste, A., Hayward, R. C., & Suo, Z. (2015). Bifurcation diagrams for the formation of wrinkles or creases in soft bilayers. *Journal of Applied Mechanics*, 82(6), 061008.

[157] Tallinen, T., & Biggins, J. S. (2015). The mechanics of invagination and folding: a soft layer growing on a soft substrate (No. arXiv: 1503.03843).

[158] Zhao, R., Zhang, T., Diab, M., Gao, H., & Kim, K. S. (2015). The primary bilayer ruga-phase diagram I: Localizations in ruga evolution. *Extreme Mechanics Letters*, 4, 76-82.

[159] Wang, Q., & Zhao, X. (2015). A three-dimensional phase diagram of growth-induced surface instabilities. *Scientific reports*, 5, 8887.

[160] Tallinen, T., & Biggins, J. S. (2015). Mechanics of invagination and folding: Hybridized instabilities when one soft tissue grows on another. *Physical Review E*, *92*(2), 022720.

[161] Zhang, J. C., Zhao, L. Z., Long, Y. Z., Zhang, H. D., Sun, B., Han, W. P., et al. & Wang, X. (2015). Colour manipulation of intense multiluminescence from CaZnOS: Mn2+ by Mn2+ concentration effect. *Chemistry of Materials*, *27*(21), 7481-7489.

[162] Brau, F., Vandeparre, H., Sabbah, A., Poulard, C., Boudaoud, A., & Damman, P. (2010). Multiple-length-scale elastic instability mimics parametric resonance of nonlinear oscillators. *Nature Physics*, *7*(1), 56-60.

[163] Auguste, A., Jin, L., Suo, Z., & Hayward, R. C. (2017). Post-wrinkle bifurcations in elastic bilayers with modest contrast in modulus. *Extreme Mechanics Letters*, *11*, 30-36.

[164] Bae, H., J., Bae, S., Park, C., Han, S., Kim, J., Kim, L., N., Kim, K., S, S., H., Park, W., & Kwon, S. (2015). Biomimetic Microfingerprints for Anti-Counterfeiting Strategies. *Advanced Materials*, 27, 2083-2089.

[165] Jones, J., Lacour, S. P., Wagner, S., & Suo, Z. (2004). Stretchable wavy metal interconnects. *Journal of Vacuum Science & Technology A: Vacuum, Surfaces, and Films*, *22*(4), 1723-1725.

[166] Sagara, Y., & Kato, T. (2008). Stimuli responsive luminescent liquid crystals: change of photoluminescent colours triggered by a shear induced phase transition. *Angewandte Chemie International Edition*, *47*(28), 5175-5178.

[167] Gonzalez, M., Axisa, F., Bulcke, M. V., Brosteaux, D., Vandevelde, B., & Vanfleteren, J. (2008). Design of metal interconnects for stretchable electronic circuits. *Microelectronics Reliability*, *48*(6), 825-832.

[168] Van Der Sluis, O., Hsu, Y. Y., Timmermans, P. H. M., Gonzalez, M., & Hoefnagels, J. P. M. (2010). Stretching-induced interconnect delamination in stretchable electronic circuits. *Journal of Physics D: Applied Physics*, *44*(3), 034008.

[169] Zhang, Y., Xu, S., Fu, H., Lee, J., Su, J., Hwang, K. C., et al. & Huang, Y. (2013). Buckling in serpentine microstructures and applications in elastomer-supported ultra-stretchable electronics with high areal coverage. *Soft Matter*, *9*(33), 8062-8070.

[170] Rhee, D., Lee, W. K., & Odom, T. W. (2017). Crack-Free, Soft Wrinkles Enable Switchable Anisotropic Wetting. *Angewandte Chemie International Edition*, *56*(23), 6523-6527.

[171] Sagara, Y., Yamane, S., Mitani, M., Weder, C., & Kato, T. (2016). Mechanoresponsive luminescent molecular assemblies: an emerging class of materials. *Advanced Materials*, *28*(6), 1073-1095.

[172] Jeong, S. M., Song, S., Kim, H., Joo, K. I., & Takezoe, H. (2016). Mechanoluminescence colour Conversion by Spontaneous Fluorescent-Dye-Diffusion in Elastomeric Zinc Sulfide Composite. *Advanced Functional Materials*, *26*(27), 4848-4858.

[173] Wang, Q., & Zhao, X. (2016). Beyond wrinkles: Multimodal surface instabilities for multifunctional patterning. *Mrs Bulletin*, *41*(2), 115-122.

[174] Keplinger, C., Sun, J. Y., Foo, C. C., Rothemund, P., Whitesides, G. M., & Suo, Z. (2013). Stretchable, transparent, ionic conductors. *Science*, *341*(6149), 984-987.

[175] Groenewold, J. (2001). Wrinkling of plates coupled with soft elastic media. *Physica A: Statistical Mechanics and its Applications*, *298*(1-2), 32-45.

[176] Bai, Y., Jiang, Y., Chen, B., Chiang Foo, C., Zhou, Y., Xiang, F., et al. & Suo, Z. (2014). Cyclic performance of viscoelastic dielectric elastomers with solid hydrogel electrodes. *Applied Physics Letters*, *104*(6), 062902.

[177] Chen, B., Bai, Y., Xiang, F., Sun, J. Y., Mei Chen, Y., Wang, H., et al. & Suo, Z. (2014). Stretchable and transparent hydrogels as soft conductors for dielectric elastomer actuators. *Journal of Polymer Science Part B: Polymer Physics*, *52*(16), 1055-1060.

[178] Li, T., Li, G., Liang, Y., Cheng, T., Dai, J., Yang, X., et al. & Xie, T. (2017). Fast-moving soft electronic fish. *Science advances*, *3*(4), e1602045.

[179] Zhang, C., Sun, W., Chen, H., Liu, L., Li, B., & Li, D. (2016). Electromechanical deformation of conical dielectric elastomer actuator with hydrogel electrodes. *Journal of Applied Physics*, *119*(9), 094108.

[180] Xu, C., Li, B., Xu, C., & Zheng, J. (2015). A novel dielectric elastomer actuator based on compliant polyvinyl alcohol hydrogel electrodes. *Journal of Materials Science: Materials in Electronics*, *26*(11), 9213-9218.

[181] Byun, I., Coleman, A. W., & Kim, B. (2013). Transfer of thin Au films to polydimethylsiloxane (PDMS) with reliable bonding using (3-mercaptopropyl) trimethoxysilane (MPTMS) as a molecular adhesive. *Journal of Micromechanics and Microengineering*, *23*(8), 085016.

[182] Larson, C., Peele, B., Li, S., Robinson, S., Totaro, M., Beccai, L., et al. & Shepherd, R. (2016). Highly stretchable electroluminescent skin for optical signaling and tactile sensing. *Science*, *351*(6277), 1071-1074.

[183] Lim, K. S., Chang, W. J., Koo, Y. M., & Bashir, R. (2006). Reliable fabrication method of transferable micron scale metal pattern for poly (dimethylsiloxane) metallization. *Lab on a Chip*, *6*(4), 578-580.

[184] Gothe, P. K., Gaur, D., & Achanta, V. G. (2018). Mptms self-assembled monolayer deposition for ultra-thin gold films for plasmonics. *Journal of Physics Communications*, *2*(3), 035005.

[185] Sun, J. Y., Keplinger, C., Whitesides, G. M., & Suo, Z. (2014). Ionic skin. *Advanced Materials*, *26*(45), 7608-7614.

[186] Lee, K. J., Fosser, K. A., & Nuzzo, R. G. (2005). Fabrication of stable metallic patterns embedded in poly (dimethylsiloxane) and model applications in non-planar electronic and lab-on-a-chip device patterning. *Advanced Functional Materials*, *15*(4), 557-566.

[187] Singh, J., & Whitten, J. E. (2008). Adsorption of 3-mercaptopropyltrimethoxysilane on silicon oxide surfaces and adsorbate interaction with thermally deposited gold. *The Journal of Physical Chemistry C*, *112*(48), 19088-19096.

[188] Lei, Z., Wang, Q., & Wu, P. (2017). A multifunctional skin-like sensor based on a 3D printed thermo-responsive hydrogel. *Materials Horizons*, *4*(4), 694-700.

[189] Byun, I., Ueno, R., & Kim, B. (2014). Micro-heaters embedded in PDMS fabricated using dry peel-off process. *Microelectronic Engineering*, *121*, 1-4.

[190] Yang, C. H., Chen, B., Lu, J. J., Yang, J. H., Zhou, J., Chen, Y. M., & Suo, Z. (2015). Ionic cable. *Extreme Mechanics Letters*, *3*, 59-65.

[191] Kitai, A. (Ed.). (2008). *Luminescent materials and applications* (Vol. 25). John Wiley & Sons.

[192] Qiu, Y., & Park, K. (2001). Environment-sensitive hydrogels for drug delivery. *Advanced drug delivery reviews*, *53*(3), 321-339.

[193] Drury, J. L., & Mooney, D. J. (2003). Hydrogels for tissue engineering: scaffold design variables and applications. *Biomaterials*, *24*(24), 4337-4351.

[194] Randall, C. L., Gultepe, E., & Gracias, D. H. (2012). Self-folding devices and materials for biomedical applications. *Trends in biotechnology*, *30*(3), 138-146.

[195] Kempaiah, R., & Nie, Z. (2014). From nature to synthetic systems: shape transformation in soft materials. *Journal of Materials Chemistry B*, *2*(17), 2357-2368.

[196] Ionov, L. (2014). Polymeric actuators. *Langmuir*, *31*(18), 5015-5024.

[197] Hu, Z., Zhang, X., & Li, Y. (1995). Synthesis and application of modulated polymer gels. *Science*, *269*(5223), 525-527.

[198] Jamal, M., Kadam, S. S., Xiao, R., Jivan, F., Onn, T. M., Fernandes, R., et al. & Gracias, D. H. (2013). Bio-origami hydrogel scaffolds composed of photocrosslinked PEG bilayers. *Advanced healthcare materials*, *2*(8), 1142-1150.

[199] Shim, T. S., Kim, S. H., Heo, C. J., Jeon, H. C., & Yang, S. M. (2012). Controlled origami folding of hydrogel bilayers with sustained reversibility for robust microcarriers. *Angewandte Chemie International Edition*, *51*(6), 1420-1423.

[200] Palleau, E., Morales, D., Dickey, M. D., & Velev, O. D. (2013). Reversible patterning and actuation of hydrogels by electrically assisted ionoprinting. *Nature communications*, *4*, 2257.

[201] Na, J. H., Evans, A. A., Bae, J., Chiappelli, M. C., Santangelo, C. D., Lang, R. J., et al. & Hayward, R. C. (2015). Programming reversibly self-folding origami with micropatterned photo-crosslinkable polymer trilayers. *Advanced Materials*, *27*(1), 79-85.

[202] Silverberg, J. L., Na, J. H., Evans, A. A., Liu, B., Hull, T. C., Santangelo, C. D., et al. & Cohen, I. (2015). Origami structures with a critical transition to bistability arising from hidden degrees of freedom. *Nature materials*, *14*(4), 389.

[203] Raisch, M., Genovese, D., Zaccheroni, N., Schmidt, S. B., Focarete, M. L., Sommer, M., & Gualandi, C. (2018). Highly Sensitive, Anisotropic, and Reversible Stress/Strain-Sensors from Mechanochromic Nanofiber Composites. *Advanced Materials*, 30(39), 1802813.

[204] Fratzl, P., & Barth, F. G. (2009). Biomaterial systems for mechanosensing and actuation. *Nature*, *462*(7272), 442.

[205] Armon, S., Efrati, E., Kupferman, R., & Sharon, E. (2011). Geometry and mechanics in the opening of chiral seed pods. *Science*, *333*(6050), 1726-1730.

[206] Liu, Y., Genzer, J., & Dickey, M. D. (2016). “2D or not 2D”: Shape-programming polymer sheets. *Progress in Polymer Science*, 52, 79-106.

[207] Ionov, L. (2013). Biomimetic hydrogel-based actuating systems. *Advanced Functional Materials*, 23(36), 4555-4570.

[208] Studart, A. R. (2015). Biologically inspired dynamic material systems. *Angewandte Chemie International Edition*, 54(11), 3400-3416.

[209] Studart, A. R. (2015). Biologisch inspirierte dynamische Materialsysteme. *Angewandte Chemie*, 127(11), 3463-3479.

[210] Barbarino, S., Bilgen, O., Ajaj, R. M., Friswell, M. I., & Inman, D. J. (2011). A review of morphing aircraft. *Journal of intelligent material systems and structures*, 22(9), 823-877.

[211] Xu, B., & Hayward, R. C. (2013). Low-voltage switching of crease patterns on hydrogel surfaces. *Advanced Materials*, 25(39), 5555-5559.

[212] Xu, B. B., Liu, Q., Suo, Z., & Hayward, R. C. (2016). Reversible electrochemically triggered delamination blistering of hydrogel films on micropatterned electrodes. *Advanced Functional Materials*, 26(19), 3218-3225.

[213] Xu, R., Lee, J. W., Pan, T., Ma, S., Wang, J., Han, J. H., et al. & Huang, Y. (2017). Designing thin, ultrastretchable electronics with stacked circuits and elastomeric encapsulation materials. *Advanced functional materials*, 27(4), 1604545.

[214] Nan, K., Luan, H., Yan, Z., Ning, X., Wang, Y., Wang, A., et al. & Zhang, Y. (2017). Engineered elastomer substrates for guided assembly of complex 3D mesostructures by spatially nonuniform compressive buckling. *Advanced functional materials*, 27(1), 1604281.

[215] Crawford, K. E., Ma, Y., Krishnan, S., Wei, C., Capua, D., Xue, Y., et al. & Webb, C. (2018). Advanced approaches for quantitative characterization of thermal transport properties in soft materials using thin, conformable resistive sensors. *Extreme Mechanics Letters*, 22, 27-35.

[216] Chen, D., Jin, L., Suo, Z., & Hayward, R. C. (2014). Controlled formation and disappearance of creases. *Materials Horizons*, 1(2), 207-213.

[217] Chen, Y. C., & Crosby, A. J. (2014). High aspect ratio wrinkles via substrate prestretch. *Advanced Materials*, 26(32), 5626-5631.

[218] Lee, G., Lee, T., Choi, Y. W., Pikhitsa, P. V., Park, S. J., Kim, S. M., et al. & Choi, M. (2017). Metal–elastomer bilayered switches by utilizing the superexponential behavior of crack widening. *Journal of Materials Chemistry C*, 5(42), 10920-10925.

[219] Li, Y., Terry, J. G., Smith, S., Walton, A. J., McHale, G., & Xu, B. (2015, March). Elastic instabilities induced large surface strain sensing structures (EILS). *In Proceedings of the 2015 International Conference on Microelectronic Test Structures* (pp. 94-99). IEEE.

[220] Pan, C., Dong, L., Zhu, G., Niu, S., Yu, R., Yang, Q., et al. & Wang, Z. L. (2013). High-resolution electroluminescent imaging of pressure distribution using a piezoelectric nanowire LED array. *Nature Photonics*, 7(9), 752.

[221] Wang, X., Que, M., Chen, M., Han, X., Li, X., Pan, C., & Wang, Z. L. (2017). Full Dynamic-Range Pressure Sensor Matrix Based on Optical and Electrical Dual-Mode Sensing. *Advanced Materials*, 29(15), 1605817.

[222] Wang, J., Yan, C., Cai, G., Cui, M., Lee-Sie Eh, A., & See Lee, P. (2016). Extremely stretchable electroluminescent devices with ionic conductors. *Advanced Materials*, 28(22), 4490-4496.

[223] Li, Y. F., Chou, S. Y., Huang, P., Xiao, C., Liu, X., Xie, Y., et al. & Sun, H. B. (2019). Stretchable Organometal-Halide-Perovskite Quantum-Dot Light-Emitting Diodes. *Advanced Materials*, 1807516.

[224] Song, S., Song, B., Cho, C. H., Lim, S. K., & Jeong, S. M. (2019). Textile-fiber-embedded multiluminescent devices: A new approach to soft display systems. *Materials Today*.

[225] Guo, Q., Huang, B., Lu, C., Zhou, T., Su, G., Jia, L., & Zhang, X. (2019). A cephalopod-inspired mechanoluminescence material with skin-like self-healing and sensing properties. *Materials Horizons*, 6(5), 996-1004.

[226] Leung, E. M., Escobar, M. C., Stiubianu, G. T., Jim, S. R., Vyatskikh, A. L., Feng, Z., et al. & Karshalev, E. (2019). A dynamic thermoregulatory material inspired by squid skin. *Nature communications*, 10(1), 1947.

[227] Cao, Y., Tan, Y. J., Li, S., Lee, W. W., Guo, H., Cai, Y., et al. & Tee, B. C. K. (2019). Self-healing electronic skins for aquatic environments. *Nature Electronics*, 2(2), 75.

[228] Li, F., Wang, X., Xia, Z., Pan, C., & Liu, Q. (2017). Photoluminescence Tuning in Stretchable PDMS film Grafted Doped Core/Multishell Quantum Dots for Anticounterfeiting. *Advanced functional materials*, *27*, 1700051.

[229] Sun, J., Pu, X., Liu, M., Yu, A., Du, C., Zhai, J., et al. & Wang, Z. L. (2018). Self-healable, stretchable, transparent triboelectric nanogenerators as soft power sources. *ACS nano*, 12(6), 6147-6155.

[230] Mukherjee, S., & Thilagar, P. (2019). Renaissance of Organic Triboluminescent Materials. *Angewandte Chemie International Edition*, 58(24), 7922-7932.

[231] Wang, X., Sun, J., Dong, L., Lv, C., Zhang, K., Shang, Y., et al. & Shan, C. X. (2019). Stretchable and transparent electroluminescent device driven by triboelectric nanogenerator. *Nano Energy*, 58, 410-418.

[232] Wong, M. C., Chen, L., Bai, G., Huang, L. B., & Hao, J. (2017). Temporal and remote tuning of piezophotonic-effect-induced luminescence and colour gamut via modulating magnetic field. *Advanced Materials*, 29(43), 1701945.

[233] Wang, Z. L. (2012). Introduction of Piezotronics and Piezo-Phototronics. In Piezotronics and Piezo-Phototronics (pp. 1-17). *Springer, Berlin, Heidelberg*.

[234] Yan, D., Lu, J., Ma, J., Qin, S., Wei, M., Evans, D. G., & Duan, X. (2011). Layered host–guest materials with reversible piezochromic luminescence. *Angewandte Chemie International Edition*, 50(31), 7037-7040.

[235] Zhao, H., Li, K., Han, M., Zhu, F., Vázquez-Guardado, A., Guo, P., et al. & Luan, H. (2019). Buckling and twisting of advanced materials into morphable 3D mesostructures. *Proceedings of the National Academy of Sciences*, 116, 13239–13248.

[236] Zhang, J. C., Wang, X., Marriott, G., & Xu, C. N. (2019). Trap-controlled mechanoluminescent materials. *Progress in Materials Science*.

[237] Zhao, W., He, Z., Peng, Q., Lam, J. W., Ma, H., Qiu, Z., et al. & Tang, B. Z. (2018). Highly sensitive switching of solid-state luminescence by controlling intersystem crossing. *Nature communications*, 9(1), 3044.

[238] Kim, H. N., Ge, D., Lee, E., & Yang, S. (2018). Multistate and On-Demand Smart Windows. *Advanced materials*, *30*, 1803847.

[239] Ge, D., Lee, E., Yang, L., Cho, Y., Li, M., Gianola, D. S., & Yang, S. (2015). A Robust Smart Window: Reversibly Switching from High Transparency to Angle-Independent Structural colour Display. *Advanced Materials*, 27(15), 2489-2495.

[240] Lee, E., Zhang, M., Cho, Y., Cui, Y., Spiegel, J. V. D., Engheta, N., & Yang, S. (2014). Tilted Pillars on Wrinkled Elastomers as a Reversibly Tunable Optical Window. *Advanced materials*, *26*, 4127-4133.

[241] Yang, J., Jin, L., Hutchinson, J. W., & Suo, Z. (2019). Plasticity retards the formation of creases. *Journal of the Mechanics and Physics of Solids*, 123, 305-314.

[242] Wang, D., & Tang, B. Z. (2019). Aggregation-Induced Emission Luminogens for Activity-Based Sensing. *Accounts of chemical research*, 52(9), 2559-2570.

[243] Bünau, G. (1970). JB Birks: Photophysics of Aromatic Molecules. Wiley-Interscience, London 1970. 704 Seiten. Preis: 210s. *Berichte der Bunsengesellschaft für physikalische Chemie*, 74(12), 1294-1295.

[244] Qiu, Z., Zhao, W., Cao, M., Wang, Y., Lam, J. W., Zhang, Z., et al. & Tang, B. Z. (2018). Dynamic visualization of stress/strain distribution and fatigue crack propagation by an organic mechanoresponsive AIE luminogen. *Advanced Materials*, 30(44), 1803924.

[245] Ji, X., Li, Z., Liu, X., Peng, H. Q., Song, F., Qi, J., et al. & Tang, B. Z. (2019). A Functioning Macroscopic "Rubik's Cube" Assembled via Controllable Dynamic Covalent Interactions. *Advanced Materials*.

[246] Liu, X., Li, M., Han, T., Cao, B., Qiu, Z., Li, Y., et al. & Hu, X. (2019). In-situ Generation of Azonia-containing Polyelectrolytes for Luminescent Photopatterning and Superbug Killing. *Journal of the American Chemical Society*.

[247] López Jiménez, F., Kumar, S., & Reis, P. M. (2016). Soft colour composites with tunable optical transmittance. *Advanced Optical Materials*, 4(4), 620-626.

[248] Silverberg, J. L., Evans, A. A., McLeod, L., Hayward, R. C., Hull, T., Santangelo, C. D., & Cohen, I. (2014). Using origami design principles to fold reprogrammable mechanical metamaterials. *Science*, 345(6197), 647-650.

[249] Turnbull, G., Williams, J. G., & Kozhevnikov, V. N. (2017). Rigidly linking cyclometallated Ir (III) and Pt (II) centres: an efficient approach to strongly absorbing and highly phosphorescent red emitters. *Chemical communications*, 53(18), 2729-2732.

[250] Xue, P., Ding, J., Wang, P., & Lu, R. (2016). Recent progress in the mechanochromism of phosphorescent organic molecules and metal complexes. *Journal of Materials Chemistry C*, 4(28), 6688-6706.

[251] Wang, L., Castro, C. E., & Boyce, M. C. (2011). Growth strain-induced wrinkled membrane morphology of white blood cells. *Soft Matter*, 7(24), 11319-11324.

[252] Ciarletta, P. (2013). Buckling instability in growing tumor spheroids. *Physical review letters*, 110(15), 158102.

[253] Trejo, M., Douarche, C., Bailleux, V., Poulard, C., Mariot, S., Regeard, C., & Raspaud, E. (2013). Elasticity and wrinkled morphology of Bacillus subtilis pellicles. *Proceedings of the National Academy of Sciences*, 110(6), 2011-2016.

[254] Tallinen, T., Biggins, J. S., & Mahadevan, L. (2013). Surface sulci in squeezed soft solids. *Physical review letters*, 110(2), 024302.

[255] Hong, W., Zhao, X., & Suo, Z. (2009). Formation of creases on the surfaces of elastomers and gels. *Applied Physics Letters*, 95(11), 111901.

[256] Shou, H., Jia, K., Zhou, X., Gao, L., He, X., Zhou, X., et al. & Liu, X. (2017). Large scale synthesis of an amorphous polyester elastomer with tunable mechanoluminescence and preliminary application in optical strain sensing. *Journal of Materials Chemistry C*, 5(17), 4134-4138.

[257] Calvino, C., Guha, A., Weder, C., & Schrettl, S. (2018). Self-Calibrating Mechanochromic Fluorescent Polymers Based on Encapsulated Excimer-Forming Dyes. *Advanced Materials*, 30(19), 1704603.

[258] Yang, C., & Suo, Z. (2018). Hydrogel ionotronics. *Nature Reviews Materials*, *3*(6), 125.

[259] Li, T., Suo, Z., Lacour, S. P., & Wagner, S. (2005). Compliant thin film patterns of stiff materials as platforms for stretchable electronics. *Journal of materials research*, *20*(12), 3274-3277.

[260] Chi, Z., Zhang, X., Xu, B., Zhou, X., Ma, C., Zhang, Y., et al. & Xu, J. (2012). Recent advances in organic mechanofluorochromic materials. *Chemical Society Reviews*, *41*(10), 3878-3896.

[261] Efimenko, K., RacK. Litis, M., Manias, E., Vaziri, A., Mahadevan, L., & Genzer, J. (2005). Nested self-similar wrinkling patterns in skins. *Nature materials*, *4*(4), 293-297.

[262] Bowden, N., Brittain, S., Evans, A. G., Hutchinson, J. W., & Whitesides, G. M. (1998). Spontaneous formation of ordered structures in thin films of metals supported on an elastomeric polymer. *Nature*, *393*(6681), 146.

[263] Yin, J., Yagüe, J. L., Eggenspieler, D., Gleason, K. K., & Boyce, M. C. (2012). Deterministic order in surface micro-topologies through sequential wrinkling. *Advanced materials*, *24*(40), 5441-5446.

[264] Atmaja, B., Frommer, J., & Scott, J. C. (2006). Atomically flat gold on elastomeric substrate. *Langmuir*, *22*(10), 4734-4740.

[265] Monclus, M. A., Young, T. J., & Maio, D. D. (2010). AFM indentation method used for elastic modulus characterization of interfaces and thin layers. *Journal of Materials Science*, *45*, 3190-3197.

[266] Enderling, S., Brown. C., L., M., Smith, S., Dicks, M., H., Stevenson, J., T., M., Mitkova, M., Kozicki, M., N., & Walton, A., J. (2006). Sheet Resistance Measurement of Non-Standard Cleanroom Materials Using Suspended Greek Cross Test Structures. *IEEE Transactions on semiconductor manufacturing*, *19*, 2-9.

[267] Lide, R. D. (1975). CRC Handbook of Chemistry and Physics. *56 ed. R. C. Weast, Ed., CRC Press*.

[268] Chopra, K. L., Bobb, L. C., & Francombe, M. H. (1963). Electrical resistivity of thin single-crystal gold films. *Journal of Applied Physics*, *34*, 1699-1702.

[269] Johnston, I. D., McCluskey, D. K., Tan, C. K. L., & Tracey, M. C. (2014). Mechanical characterization of bulk sylgard 184 for microfluidics and

microengineering. *Journal of Micromechanics and Microengineering*, *24*, 035017.

[270] Khanafer, K., Duprey, A., Schlicht, M., & Berguer, R. (2009). Effects of strain rate, mixing ratio, and stress–strain definition on the mechanical behavior of the polydimethylsiloxane (PDMS) material as related to its biological applications. *Biomed Microdevices, 11*, 503-508.

[271] Chou, N., Jeong, J., & Kim, S. (2013). Crack-free and reliable lithographical patterning methods on PDMS substrate. *Journal of Micromechanics and Microengineering*, *23*, 125035.

[272] Palchesko, R. N., Zhang, L., Sun, Y., & Feinberg, A. W. (2012). Development of Polydimethylsiloxane Substrates with Tunable Elastic Modulus to Study Cell Mechanobiology in Muscle and Nerve. *Plos One*, *7*, e51499.

[273] Voyiadjis, Z. G., & Kattan, P. I. (2013). On the Theory of Elastic Undamageable Materials. *Journal of Engineering Materials and Technology*, *135*, 021002.

Appendix 1

Run-sheet of PDMS bilayer creasing with Au micro-pattern embedded by SAM treatment.

Step	Description	Equipment	Recipe/Parameters	Comments
1.	Put Au wafer into a big glass petri-dish, then sock in the acetone	Glass petri-dish	Top up acetone when it to be evaporated	Lift off process
2.	Clean with IPA then dry with CDA		Carefully dry with CDA gun	
3.	Clean small glass petri-dish with IPA then dry with CDA	Isopropanol water and air gun	Clean with isopropanol water and dry with high pressure nitrogen air gun	
4.	Clean Silicon chips inside glass petri-dish with ethanol	Ethanol	Cut Au patterned silicon chips from Edinburgh wafer	Refresh ethanol wash bottle if necessary
5.	**20mM** MPTMS in glass petri-dish	Pipette and 5 ml syringe	**9.5ul** MPTMS with **2.5ml** ethanol	Carefully injected with syringe
6.	Soak silicon chips in MPTMS	Glass petri-dish	**3 hours**	
7.	Preparing De-gassed PDMS (30:1)	Petri-dish, Microbalance, Vacuum oven	Mix vigorously for **10 mins**, degassing for 30 mins	Max vacuum, no more bubbles present
8.	Rinse the silicon chips with ethanol then dry	Air gun	Rinsing for 10s	Uniform rinsing the silicon chips
9.	First spin coating PDMS	Spin coater in lab E109	**At 600rmp for 5s, 800rmp for 5s and 1000 rpm for 2 mins**	Protect the coater with cardboard. Spinning on silicon chips
10.	Curing at **70°C**	Vacuum oven	**1 hour**	During 1h waiting, prepare the mechanical vice
11.	Second spin coating PDMS	Spin coater in lab E109	**At 1000rmp for 5s, 2000rmp for 5s and 3000 rpm for 2 mins**	Protect the coater with cardboard. Spinning on silicon chips
12.	Spin coater cleaning	Isopropanol water	Wipe clean after use	
13.	Transfer onto pre-stretched layer	Tweezers	Transfer the adhesive coated PDMS layer to the pre-stretched substrate	Carefully transferred to avoid air bubble generation
14.	Baking at **70°C**	Vacuum oven	**8 hours**	Timing the oven for 8h
15.	Cut the chips/PDMS and peel off	Small knife	Thin film of PDMS layer with Au left on the pre stretched elastic substrate	Carefully cut (gently) and peel off, observe the Au transfer success rate
16.	Pre-stretched substrate released and observe the sample	Microscope		Compressive strain induced creasing instability between Au micro-patterns

Appendix 2

Run-sheet of PDMS bilayer creasing with Au embedded-SAM with MPTMS.

Step	Description	Equipment	Recipe/Parameters	Comments
1.	Cleaning preparation (glass/plastic chip)	Isopropanol water and air gun		Clean with isopropanol water and dry with high pressure nitrogen air gun
2.	Preparing De-gassed PDMS (30:1)	Petri-dish, Microbalance, Vacuum oven	Mix vigorously for **10 mins**, degassing for **30 mins**	Max vacuum, no more bubbles present
3.	First spin coating PDMS	Spin coater in lab E109	**At 600rmp for 5s, 800rmp for 5s and 1000 rpm for 2 mins**	Protect the coater with cardboard. Spinning on silicon chips
4.	Curing at 70°C	Vacuum oven	**1 hour**	During 1h waiting, prepare the mechanical vice
5.	Second spin coating PDMS	Spin coater in lab E109	**At 1000rmp for 5s, 2000rmp for 5s and 3000 rpm for 2 mins**	Protect the coater with cardboard. Spinning on silicon chips
6.	Spin coater cleaning	Isopropanol water		Wipe clean after use
7.	Transfer onto pre-stretched layer			Transfer the adhesive coated PDMS layer to the pre-stretched substrate
8.	Curing at 70°C	Lab vacuum oven	**8 hours**	
9.	Peel off from glass/silicon chip	Small knife	Thin film of PDMS layer left on the pre stretched elastic substrate	Carefully cut and peel off
10.	Oxygen plasma treatment	Fabricated vice	**10s**	
11.	Iridium III fluorescent solution casting		**1.5 mM**	Drop Iridium III fluorescent solution onto top of plasma treated surface
12.	Pre-stretched substrate released to original length and observe the sample	AFM/ LSCM/Bruker		Compressive strain induced creasing instability and micro-optical patterns generation

Appendix 3

Publications and award certification are presented in the following pages.

Step	Description	Equipment	Recipe/Parameters	Comments
1.	Prepare the solution of acrylamide, sodium acrylate and BisAA	Pipette and syringe		Diluted from the powders
2.	**Prepare the thin film substrate:** mixing the acrylamide, sodium acrylate, DI water and TEMED together, then finally add the Polyacrylamide (APS) inside the mixture	Pipette and Small glass container	Wait around 20mins to crosslink	The Polyacrylamide (APS) is for solidify, so add as quick as possible Drop the thin film onto the clean glass slide and then cover with acrylic Carefully injected with syringe
3.	**Prepare the hydrogel drop (before crosslinking):** Mixing the solution of acrylamide, sodium acrylate and BisAA together	Pipette and small tube	Pre-polymer preparation with the different concentrations	After preparation, keep inside the glass container
4.	**Crosslinking:** Adding the TEMED and Polyacrylamide (APS) inside the mixture	Pipette and small tube		Before adding APS, add 3ul of food dye, then add APS
5.	**Polymerization inside two-plates configuration:** Drop different concentrations of the hydrogels onto the designed mask	Pipette		
6.	Cover the patterns with pre-prepared thin film substrate		Leaving for ~1h	
7.	Peel off the acrylic slide, leave the solid hydrogel onto the glass slide			Carefully peeling off
8.	Attach the glass slide on the top of the designed mask		Leaving for ~20 mins	
9.	Peel off the glass slide, then put the samples inside different concentrations of PBS			Carefully peeling off Observe the samples shaping change

Appendix 4

Publications and award certification are presented in the following pages.

IEEE International Flexible Electronics Technology Conference
Aug. 7-9, 2018 Ottawa, Canada

Outstanding Student Paper Award

is presented to

Cong Wang

IEEE

For the paper coauthored by Ben Xu; Jonathan Terry; Stewart Smith; Anthony Walton; and Yifan Li entitled "Metal-Elastomer Surface Deformation Control on Super-Compressible Strain Transducer Arrays"

Ta-Ya Chu, Award Committee Chair

George Xiao, General Chair

Engineering and Physical Sciences Research Council

search

FUNDING | RESEARCH | INNOVATION | SKILLS | NEWS, EVENTS AND PUBLICATIONS | ABOUT US

NEWS 17 APR 2020

Researchers discover novel optical sensing technology

Researchers at Northumbria University have developed a new optical sensing technology which can light up areas of an object or material by creating microscopic wrinkles and folds within its surface.

Quick links

- EPSRC BLOG
- CALLS
- VISUALISING OUR PORTFOLIO
- GATEWAY TO RESEARCH (GTR)
- LENS ON RESEARCH AND

EPSRC Twitter Feed

@EPSRC - 1 day ago
RT @CRUKresearch: Reminder that our next innovation sandpit, in partnership with @PancreaticCanUK and @EPSRC, will now take place from 29 N...

@EPSRC - 2 days ago
Don't miss @stormlamp_edu's digital meeting to mark the end of the STORMLAMP #research project. #STORMLAMP is an E... twitter.com/i/web/status/1...

@EPSRC - 3 days ago
RT @MedTectales: The lives of thousands of people with #mobilityissues could be transformed thanks to ground-breaking research by scientist...

CALL: EXPRESSION OF INTEREST 08 APR 2020

Call for participants to attend a virtual workshop: 'Identifying challenges for a Sustainable Digital Society'

This is a call for expressions of interest to take part

NEWS: ANNOUNCEMENT 31 MAR 2020

Coronavirus updates

The latest guidance and information on the vital work of UKRI and our community in response to the crisis

CALL: INVITATION FOR PROPOSALS 31 MAR 2020

Circular Economy Network+ in Transportation Systems – Call for Feasibility Studies

The EPSRC funded Circular Economy Network+ in

Skip Nav | Accessibility | Disability tools | Media Enquiries

Engineering and Physical Sciences Research Council

search

FUNDING | RESEARCH | INNOVATION | SKILLS | NEWS, EVENTS AND PUBLICATIONS | ABOUT US

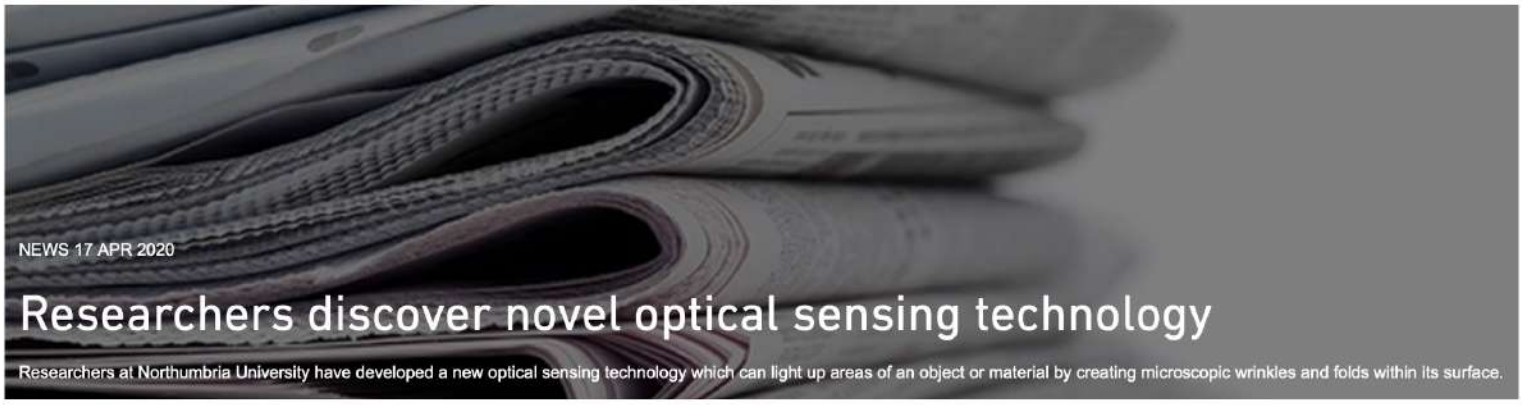

NEWS 17 APR 2020

Researchers discover novel optical sensing technology

Researchers at Northumbria University have developed a new optical sensing technology which can light up areas of an object or material by creating microscopic wrinkles and folds within its surface.

Researchers discover novel optical sensing technology

Issue date: 17 April 2020

Tag: News

Related theme: Healthcare technologies (http://www.epsrc.ac.uk/research/ourportfolio/themes/healthcaretechnologies)

Researchers at Northumbria University have developed a new optical sensing technology which can light up areas of an object or material by creating microscopic wrinkles and folds within its surface.

Inspired by the way the outer layer of plants and animals can change colour in nature, researchers have combined their expertise in physics and chemistry to create the new technology. It could have a variety of practical applications, including within flexible wearable devices, electronics, and in 3D printing. The research was carried out by Dr Ben Bin Xu, Dr Yifan Li and Dr Valery Kozhevnikov, from Northumbria University, supported by EPSRC and the Royal Society Kan Tong Po International Fellowship 2019.

There are two specific elements to the research. The first was the creation of a thin 'film' or material which, when stimulated with a mechanical or electronic signal, results in microscopic folds being created on its surface, usually too small to be seen with the naked eye. The second element was the creation of a chemical 'paint' which is applied to the material. When the folds are created in the surface, the resulting change in oxygen levels within the 'paint' leads to a chemical reaction. This creates a luminescent effect, making the surface of the material appear to 'light up' in the area where the fold has occurred.

Dr Xu, an associate professor in Mechanical Engineering who led the project said: "Wrinkles and folds are usually unwanted in engineering terms. Similarly, an oxygen quenching effect is not popular in fluorescence science. However, through micro-engineering, magic happened, and two unwanted phenomena were turned into a responsive and programmable 'fold to glitter' function."

When subjected to mechanical stimuli, elastomeric materials such as that created by the Northumbria University researchers can undergo surface changes, such as wrinkles and cracks. This can be used to create switchable optical features and structural colour with dynamic luminescent patterns. The phenomenon of elastic wrinkling and folding exists widely in nature and there has been much research by academics to understand the mathematical and physical science behind these changes and to explore how this could be used for innovative engineering solutions.

The research paper setting out the findings has been published in scientific journal Nature Communications and it is hoped this latest research will create new opportunities for designing the next generation of flexible/wearable devices.

Researchers discover novel optical sensing technology

17 April 2020

Credit: CC0 Public Domain

Researchers at Northumbria University have developed a new optical sensing technology which can light up areas of an object or material by creating microscopic wrinkles and folds within its surface.

Inspired by the way the outer layer of plants and animals can change color in nature, researchers have combined their expertise in physics and chemistry to create the new technology. It could have a variety of practical applications, including within flexible wearable devices, electronics, and in 3-D printing. The research was carried out by Dr. Ben Bin Xu, Dr. Yifan Li and Dr. Valery Kozhevnikov, from Northumbria University, supported by EPSRC and the Royal Society Kan Tong Po International Fellowship 2019.

There are two specific elements to the research. The first was the creation of a thin 'film' or material which, when stimulated with a mechanical or electronic signal, results in microscopic folds being created on its surface, usually too small to be seen with the naked eye. The second element was the creation of a chemical 'paint' which is applied to the material. When the folds are created in the surface, the resulting change in oxygen levels within the 'paint' leads to a chemical reaction. This creates a luminescent effect, making the surface of the material appear to 'light up' in the area where the fold has occurred.

Dr. Xu, an associate professor in Mechanical Engineering who led the project said: "Wrinkles and folds are usually unwanted in engineering terms. Similarly, an oxygen quenching effect is not popular in fluorescence science. However, through micro-engineering, magic happened, and two unwanted phenomena were turned into a responsive and programmable 'fold to glitter' function."

When subjected to mechanical stimuli, elastomeric materials such as that created by the Northumbria University researchers can undergo surface changes, such as wrinkles and cracks. This can be used to create switchable optical features and structural color with dynamic luminescent patterns. The phenomenon of elastic wrinkling and folding exists widely in nature and there has been much research by academics to understand the mathematical and physical science behind these changes and to explore how this could be used for innovative engineering solutions.

The research paper setting out the findings has been published in scientific journal *Nature Communications* and it is hoped this latest research will create new opportunities for designing the next generation of flexible/wearable devices.

More information: Cong Wang et al. A flexible topo-optical sensing technology with ultra-high contrast, *Nature Communications* (2020). DOI: 10.1038/s41467-020-15288-8

Provided by Engineering and Physical Sciences Research Council

APA citation: Researchers discover novel optical sensing technology (2020, April 17) retrieved 13 July 2020 from https://phys.org/news/2020-04-optical-technology.html

ELASTIC FOLDING ON SOFT MATTER SURFACES AIDS HIGH-CONTRAST OPTICAL SENSING.

Shardell Joseph
Materials World magazine, 3 Jun 2020

Creating folds on the surface of materials has led to a 'fold-to-glitter' optical technology.

With potential applications in flexible wearable, healthcare and or engineering devices, the technology proves, for the first time, that elastic folding on the surface of soft matter can enable high-contrast optical sensing.

Creating folds on the surface of materials has led to a 'fold-to-glitter' optical technology, with potential for application in flexible and wearable healthcare and engineering devices.

According to researchers from Northumbria University, UK, the technology proves, for the first time, that elastic folding on the surface of soft matter can enable high-contrast optical sensing.

The mechanics study of surface morphology has led to the discovery of the optical sensing technology. Credit: Northumbria University

'Wrinkles and folds are usually unwanted in engineering terms, as they represent structural failures,' says Ben Xu, Associate Professor in Mechanical Engineering at the University. 'In this research, we harness this reversible transition.'
The soft multi-layer of the elastomeric material is designed and micro-engineered, and then subjected to mechanical stimuli. The desired wrinkles and fold patterns are, in turn, realised on the surface in a controlled and targeted way, to create switchable optical features and structural colour with dynamic luminescent patterns.

'The actuated folds in the soft material can be easily observed from top view under fluorescence microscope with the assistance from an optical indicator layer,' says Xu. 'By further applying a thin layer, around 600nm, of functional phosphorescent cyclometallate on the surface, the targeted folding can lead to an ultra-high-contrast optical sensing.'

The research consists of two different elements – creating a thin film and a chemical paint. When stimulated with a mechanical or electronic signal, the thin film results in microscopic folds being created on its surface, usually too small to be seen with the naked eye.

This is followed by applying the chemical paint developed by the researchers to the material. When the folds are created in the surface, the resulting change in oxygen levels within the paint leads to a chemical reaction, creating a luminescent effect. This makes the surface appear to light up in the region where the fold exists.

According to Xu, some applications have already been demonstrated. These include an in-plane topo-optical sensor to detect large surface strains, a dynamic 2D spy barcode that can hide information, an adaptive topo-optical luminescence grid and a flexible bending sensor to detect out-of-the-plane bending degree. The team plans to integrate the technology in a wider range of applications.

2020
2019
2018
2017
2016
2015
2014
2013
2012
2011
2010
2009
2008
2007
2006
2005
2004
2001

'Due to the elastic nature of the multi-layer structure and the instability morphology, this technology can be developed into a wearable device with proper [integration of] other electronic units, or combined with signal reading/interpreting mechanism to increase the visibility of generated high-contrast optical signal,' Xu explains.

'We are aiming to develop one or two flexible devices for epidermal diagnosis or therapeutic application next, with proper funding support.'

FOLD TO GLITTER – RESEARCHERS DISCOVER NOVEL OPTICAL SENSING TECHNOLOGY

Posted by Dave Stopher | Apr 21, 2020 | Education | 0

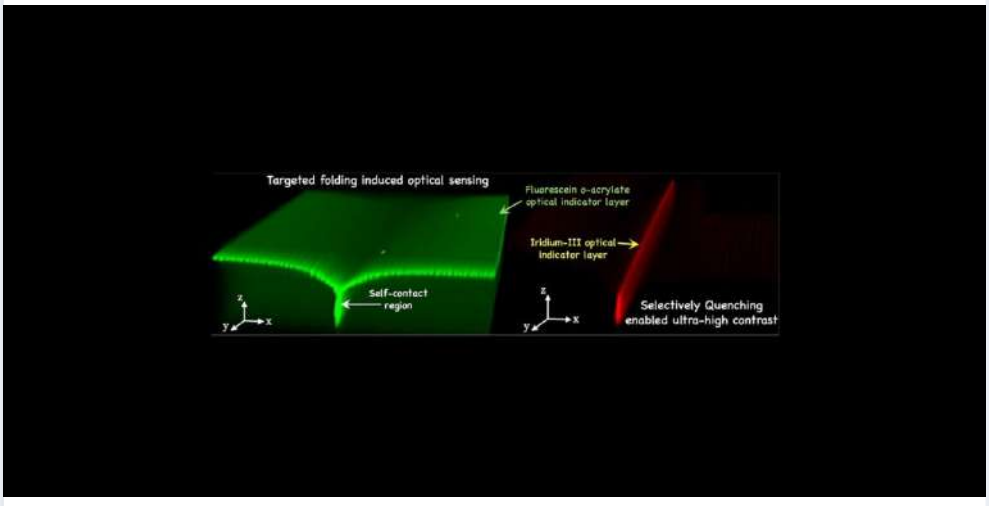

Scientists from Northumbria University have developed a new optical sensing technology which can light up areas of an object or material by creating microscopic wrinkles and folds within its surface.

Inspired by the way the outer layer of plants and animals can change colour in nature, the researchers have combined their expertise in physics and chemistry to create the new technology.

It could have a variety of practical applications, including within flexible wearable devices, electronics, and in 3D printing.

Their research paper setting out the findings, entitled A flexible topo-optical sensing technology with ultra-high contrast, has been published in the prestigious scientific journal *Nature Communications*.

There are two specific elements to the research. The first was the creation of a thin 'film' or material which, when stimulated with a mechanical or electronic signal, results in microscopic folds being created on its surface, usually too small to be seen with the naked eye.

The second element was the creation of a chemical 'paint' which is applied to the material. When the folds are created in the surface, the resulting change in oxygen levels within the 'paint' leads to a chemical reaction. This creates a luminescent effect,

making the surface of the material appear to 'light up' in the area where the fold has occurred (see diagram below).

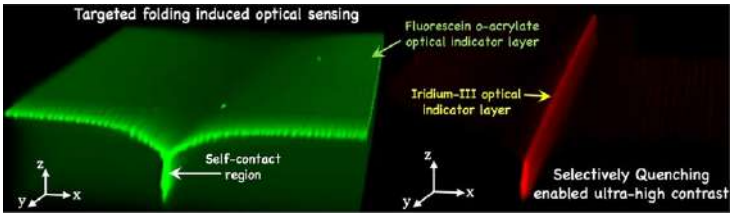

The research was carried out by Dr Ben Bin Xu and Dr Yifan Li, from Northumbria University's Department of Mechanical and Construction Engineering, and Dr Valery Kozhevnikov from Northumbria's Department of Applied Sciences.

Dr Xu, an associate professor in Mechanical Engineering, led the project and said: "Wrinkles and folds are usually unwanted in engineering terms. Similarly, an oxygen quenching effect is not popular in fluorescence science.

"However, through micro-engineering, magic happened, and two unwanted phenomena were turned into a responsive and programmable 'fold to glitter' function."

When subjected to mechanical stimuli, elastomeric materials such as that created by the Northumbria University researchers can undergo surface changes, such as wrinkles and cracks. This can be used to create switchable optical features and structural colour with dynamic luminescent patterns.

The phenomenon of elastic wrinkling and folding exists widely in nature and there has been much research by academics to understand the mathematical and physical science behind these changes and to explore how this could be used for

innovative engineering solutions.

It is hoped this latest research will create new opportunities for designing the next generation of flexible/wearable devices.

Professor John Woodward, Pro Vice-Chancellor of Northumbria University's Faculty of Engineering and Environment, said: "This is exciting new research with a number of emerging applications in flexible and wearable electronics and bio-devices."

The work at Northumbria is part of a wider international collaborative research programme which also involved Prof Jie Kong from Northwestern Polytechnical University in China and Prof Ben Zhong Tang from Hong Kong University of Science and Technology.

It has been supported by the Engineering and Physical Sciences Research Council (EPSRC) and the Royal Society Kan Tong Po International Fellowship 2019.

Professor Laurent Dala, head of Northumbria's Department of Mechanical and Construction Engineering, added: "The outcomes show promise for future international collaboration between Northumbria University, Northwestern Polytechnic University, China and Hong Kong University of Science and Technology and indicate the benefit of UKRI finding International research teams through fellowship grants."

Find out more about Northumbria University's Department of Mechanical and Construction Engineering and Engineering Materials and Mechanics Group (EM²G).

SHARE:

‹ PREVIOUS

ROCKLIFFE HALL DONATES TOILETRIES TO DARLINGTON MEMORIAL HOSPITAL

NEXT ›

ROCKLIFFE HALL PARTNERS WITH WINE SUPPLIER TO RAISE FUNDS FOR GNAAS

ABOUT THE AUTHOR

Dave Stopher

RELATED POSTS

Funding announced to research cybersecurity risks of digital hoarding

ScamFighter

Some Good Websites that Write Essays for You

24th January

Youth Sport Nutrition Hoping For Healthy Growth With Small Loan Fund Investment

Record exam results at fast-improving Academy 360

NASA-NOAA's Suomi NPP Satellite Analyzes Saharan Dust Aerosol Blanket

Jul 13, 2020 | Space

NASA, Partner Space Agencies to Release Global View of COVID-19 Impacts

Jul 13, 2020 | Space

Viewing the Red Planet

Jul 13, 2020 | Space

Northumbria University NEWCASTLE

Apr 15, 2020 13:44 BST

Fold to Glitter – researchers discover novel optical sensing technology

Scientists from Northumbria University have developed a new optical sensing technology which can light up areas of an object or material by creating microscopic wrinkles and folds within its surface.

Inspired by the way the outer layer of plants and animals can change colour in nature, the researchers have combined their expertise in physics and chemistry to create the new technology.

It could have a variety of practical applications, including within flexible wearable devices, electronics, and in 3D printing.

Their research paper setting out the findings, entitled A flexible topo-optical sensing technology with ultra-high contrast, has been published in the prestigious scientific journal *Nature Communications*.

There are two specific elements to the research. The first was the creation of a thin 'film' or material which, when stimulated with a mechanical or electronic signal, results in microscopic folds being created on its surface, usually too small to be seen with the naked eye.

The second element was the creation of a chemical 'paint' which is applied to the material. When the folds are created in the surface, the resulting change in oxygen levels within the 'paint' leads to a chemical reaction. This creates a luminescent effect, making the surface of the material appear to 'light up' in the area where the fold has occurred (see diagram below).

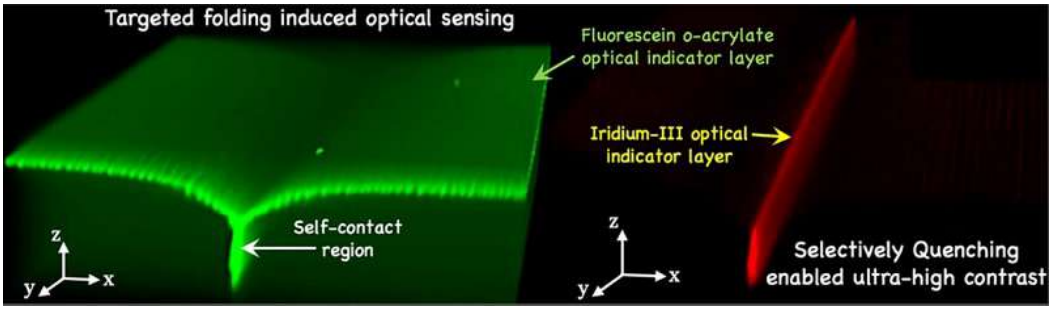

The research was carried out by Dr Ben Bin Xu and Dr Yifan Li, from Northumbria University's Department of Mechanical and Construction Engineering, and Dr Valery Kozhevnikov from Northumbria's Department of Applied Sciences.

Dr Xu, an associate professor in Mechanical Engineering, led the project and said: "Wrinkles and folds are usually unwanted in engineering terms. Similarly, an oxygen quenching effect is not popular in fluorescence science.

"However, through micro-engineering, magic happened, and two unwanted phenomena were turned into a responsive and programmable 'fold to glitter' function."

When subjected to mechanical stimuli, elastomeric materials such as that created by the Northumbria University researchers can undergo surface changes, such as wrinkles and cracks. This can be used to create switchable optical features and structural colour with dynamic luminescent patterns.

The phenomenon of elastic wrinkling and folding exists widely in nature and there has been much research by academics to understand the mathematical and physical science behind these changes and to explore how this could be used for innovative engineering solutions.

It is hoped this latest research will create new opportunities for designing the next generation of flexible/wearable devices.

Professor John Woodward, Pro Vice-Chancellor of Northumbria University's Faculty of Engineering and Environment, said: "This is exciting new research with a number of emerging applications in flexible and wearable electronics and bio-devices."

The work at Northumbria is part of a wider international collaborative research programme which also involved Prof Jie Kong from Northwestern Polytechnical University in China and Prof Ben Zhong Tang from Hong Kong University of Science and Technology.

It has been supported by the Engineering and Physical Sciences Research Council (EPSRC) and the Royal Society Kan Tong Po International Fellowship 2019.

Professor Laurent Dala, head of Northumbria's Department of Mechanical and Construction Engineering, added: "The outcomes show promise for future international collaboration between Northumbria University, Northwestern Polytechnic University, China and Hong Kong University of Science and Technology and indicate the benefit of UKRI finding International research teams through fellowship grants."

Find out more about Northumbria University's Department of Mechanical and Construction Engineering and Engineering Materials and Mechanics Group (EM²G).

Northumbria is a research-rich, business-focused, professional university with a global reputation for academic excellence. Find out more about us at www.northumbria.ac.uk

Please contact our Media and Communications team at media.communications@northumbria.ac.uk or call +44 (0)191 227 4604 with any media enquiries or interview requests.

Contacts

Rachel Lippe
Press Contact
Assistant Director (Corporate Communications and Reputation Management)
media.communications@northumbria.ac.uk
07805 086 449

Rik Kendall
Press Contact
PR and Media Manager
Business and Law
rik.kendall@northumbria.ac.uk
07923 382339

Andrea Slowey
Press Contact
PR and Media Manager
Engineering and Environment / Health and Life Sciences
andrea.slowey@northumbria.ac.uk
07708 509436

James Fox
Press Contact
Student Communications Manager
james2.fox@northumbria.ac.uk
07875 489974

Kelly Elliott
Press Contact
PR and Media Coordinator
Arts Design and Social Sciences / Engineering and Environment
kelly2.elliott@northumbria.ac.uk
07979 365018

Rachael Barwick
Press Contact
PR and Media Coordinator
Health and Life Sciences / Sport
rachael.barwick@northumbria.ac.uk
07377422415

Ruth Lognonne
Press Contact
PR and Media Coordinator
Health and Life Sciences / Sport
ruth.lognonne@northumbria.ac.uk
07971 274 523

Emily Morris
Press Contact
Corporate Communications Coordinator
emily.l.morris@northumbria.ac.uk
0770 8509437

nature COMMUNICATIONS

ARTICLE

https://doi.org/10.1038/s41467-020-15288-8 OPEN

A flexible topo-optical sensing technology with ultra-high contrast

Cong Wang[1], Ding Wang[1], Valery Kozhevnikov[2], Xingyi Dai[3], Graeme Turnbull[2], Xue Chen[1], Jie Kong[3]✉, Ben Zhong Tang[4]✉, Yifan Li[1]✉ & Ben Bin Xu[1]✉

Elastic folding, a phenomenon widely existing in nature, has attracted great interests to understand the math and physical science behind the topological transition on surface, thus can be used to create frontier engineering solutions. Here, we propose a topo-optical sensing strategy with ultra-high contrast by programming surface folds on targeted area with a thin optical indicator layer. A robust and precise signal generation can be achieved under mechanical compressive strains (>0.4). This approach bridges the gap in current mechano-responsive luminescence mechanism, by utilizing the unwanted oxygen quenching effect of Iridium-III (Ir-III) fluorophores to enable an ultra-high contrast signal. Moreover, this technology hosts a rich set of attractive features such as high strain sensing, encoded logic function, direct visualisation and good adaptivity to the local curvature, from which we hope it will enable new opportunities for designing next generation flexible/wearable devices.

[1] Department of Mechanical and Construction Engineering, Faculty of Engineering and Environment, Northumbria University, Newcastle upon Tyne NE1 8ST, UK. [2] Department of Applied Sciences, Faculty of Health and Life Science, Northumbria University, Newcastle upon Tyne NE1 8ST, UK. [3] MOE Key Laboratory of Material Physics and Chemistry under Extraordinary, Shaanxi Key Laboratory of Macromolecular Science and Technology, School of Chemistry and Chemical Engineering, Northwestern Polytechnical University, Xi'an 710072, China. [4] Department of Chemistry, The Hong Kong Branch of Chinese National Engineering Research Center for Tissue Restoration and Reconstruction and Institute for Advanced Study, The Hong Kong University of Science and Technology, Clear Water Bay, Kowloon, Hong Kong, China. ✉email: kongjie@nwpu.edu.cn; tangbenz@ust.hk; yifan.li@northumbria.ac.uk; ben.xu@northumbria.ac.uk

One of the latest trends in next generation micro-electronics technology is to develop flexible optical sensors and actuators, which holds promises in strain/pressure sensing[1–4], wearable devices[5–7], electronic skin[8–10], camouflaging[11], etc. By utilizing soft materials, recent efforts have explored the flexible optical technology with extra controllability and on-demand color changing such as triboelectric–photonic[12,13], piezo-electroluminescent[14], piezo-photonics[15–17], mechano-responsive luminescence (MRL) and mechanochromism[18]. Among those approaches, MRL, a tunable and switchable luminescence (or chromism) in response to mechanical stimulus[19,20], have attracted considerable interests for their potentials in sensing/micro-devices[21], data storage[22,23], flexible display[24,25], security pattern/inks[26], etc. However, the optical performance has been discounted by aggregation-caused quenching (ACQ)[27,28], thus limit the further applications for MRL materials. Whereas the current advances in Aggregation-induced emission (AIE) have achieved emergence characteristics at molecular level to overcome the drawbacks of ACQ[29–31], novel optical sensing mechanisms remain yet to be exploited to enable wider scale-up perspectives.

Inspired by epidermal color changing scheme from nature, researchers have been able to amplify signal by generating luminescent molecular dominos[19] thus realize multi-state optical switching by engineering micro/nano-structures on surface[18]. By far, all practiced strategies will easily result into a noisy and low-resolution signal, which poses challenges in triggering controllable signals for scalable applications. Subject to the mechanical stimuli, elastomeric materials can undergo surface morphological change (e.g. wrinkles and cracks) which has been used to create switchable optical features[25,32], and structural colour with dynamic luminescent patterns[33]. Zeng et al reported an interesting mechanochromic device by using cracks and folds[34] to trigger optical signals within a moderate stretching strain of 0.2. While the understandings on controllably generating elastic instability morphologies have been extended[35–38], even to form 3D structures[39–41], surface topology enabled optical sensing in response to large compressive strain (more than 0.4) has not been reported elsewhere.

In this work, we propose a topo-optical sensing strategy with ultra-high contrast by constructing a patterned elastic multilayer coated with a nanometer thin optical indicator layer. The keys to achieve such high contrast topo-sensing strategy include the targeted folding on elastic surface guided by the pre-defined lattice pattern and the autonomous optimization of contrast by selectively oxygen quenching of the coated Iridium-III complexes (Ir-III) fluorophore layer. The unique self-contact geometry of folding area preserves intensity by mechanically creating a hypoxia zone, whereas the intensity reduces significantly for the rest of surface due to the oxygen-quenching at the open air. Moreover, we successfully demonstrate several conceptual designs based on this topo-sensing approach such as an in-plane strain sensor, a 2D spy barcode, an adaptive topo-optical grid with potential for bio-applications and a flexible bending sensor, to shed the lights on the future applications in micro-devices and flexible/wearable electronics.

Results

Configuration of targeted folding on elastic multilayer. The multilayer system consists of a soft polydimethylsiloxane film (PDMS, shear modulus $G_{sub} \approx 0.15$ MPa, thickness of 125 μm) on a vinylpolysiloxane mounting substrate (VPS, shear modulus ≈ 0.35 MPa, thickness of 1.5 mm). Oxygen plasma was applied to create a hard skin layer (shear modulus $G_f \approx 1.8$ MPa, thickness of 100 nm) on the top of PDMS film. By applying a uniaxial compression (Fig. 1a), $\varepsilon_{comp} = \frac{L_0}{L} - 1$, an elastic morphological development is shown on the surface. A similar setting has been previously used to configure wrinkle pattern by pre-placing Bravais lattice holes on the surface at low compression[42], where an unexpected formation of wrinkle-to-crease/folding transition was discovered occasionally under a higher compression ($\varepsilon > 0.4$) but have not been studied further. The key in this work is to investigate the controllable formation of targeted crease/fold at higher compression and translate this topographical transition into a dedicated sensing signal in responding to a compressive strain.

We first compare the development of elastic morphologies with reflective optical microscopy between a plain (Fig. 1b) and a patterned surface with a single-line array of micro-holes as shown in Fig. 1c (diameter = 60 μm, distance $D = 120$ μm, hole depth $h = 12$ μm, Supplementary Movie 1). Wrinkle patterns are developed globally for both plain and centre lattice hole patterned surfaces at low compressive strains and evolved into visible textures when strain increases to $\varepsilon = 0.27$. A strain energy localization guided by the pre-placed pattern can be clearly identified along the micro-holes array. The surface presents a post-wrinkling development with mixed morphologies at middle compressive strains (i.e. $\varepsilon = 0.38$). According to Kim and co-workers, surface wrinkles will first undergo period doubling, followed by the formation of creases under a modulus ratio (G_f/G_{sub}) between 5.86 and 13.89[43,44]. A threshold strain (ε_{th}) is the compressive strain when the first fold occurs on surface, which is variable against the setting factors for multilayer. Here, a compressive strain of $\varepsilon = 0.52$, which is slightly higher than ε_{th}, is chosen to compare folding conditions at the same energy level. We find that a few random folds (pointed by red arrows in Fig. 1b) appear on the plain surface, while a single big fold locates at the area that is defined by the pre-placed holes on surface (dotted line in Fig. 1c). Single-line array with varied pattern shapes (circles, diamonds, squares, triangles and hexagons, Supplementary Fig. 1) and different D/Φ (Supplementary Fig. 2) are also attempted, where a range of ε_{th} from 0.42 to 0.58 can be achieved by designing the shape and D/Φ. However, the ε_{th} shows less sensitivity on the depth of lattice pattern (Supplementary Fig. 3), which agrees with the reported results on configuring the wrinkle patterns with Bravais lattice[45].

Realization of topo-optical sensing. The concept of translating surface topology into optical signal (Topo-optical sensing) is initially facilitated (Fig. 1a) through casting and drying a drop of solution containing 1.3 mM fluorescein o-acrylate (FoA) on the elastic surface, to fulfil the photo-luminescence function. When the fold occurs, the in-plane length (L) locally develops into a self-contact depth (H_c, Fig. 1a), lead to an optical signal from the top view because of the volumetric accumulation of intensity. By assessing the optical properties for the morphologies at ($\varepsilon = 0.52$) for both plain and micropatterned surfaces under laser scanning confocal microscopy (LSCM, Fig. 1d, e), a single-line optical signal is clearly shown on the location defined by the micro-pattern with an enhanced intensity (side view). We define a signal-to-noise ratio (SNR) as, $\mathrm{SNR} = \frac{\text{peak intensity}}{\text{noise}}$, to quantitatively analyse the optical signal, where the peak intensity is collected from the signal of folded line and the noise represent the average luminescence signals originated from the background surface (excluding the folding line). In Fig. 1f, a higher SNR value is obtained for the patterned surface than that of plain surface. With a hole array, surface energy can be guided to form a single fold with a deeper self-contact (Fig. 1e), rather than a distractive energy localization with multiple folds/creases on the plain surface. From the LSCM 3D reconstruction image (green opened book, Fig. 1g) for the FoA patterned surface, we note that the

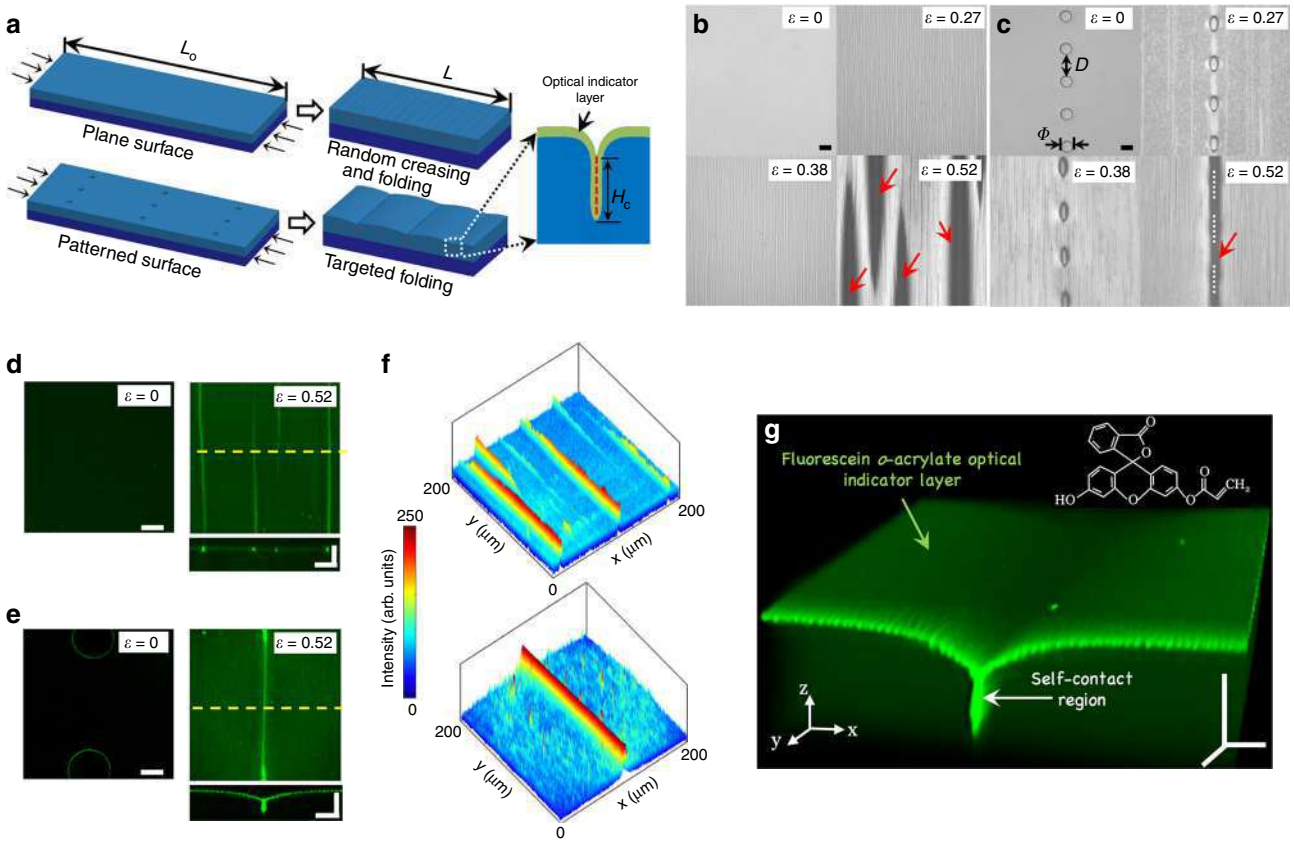

Fig. 1 The realization of topo-optical sensing. a Schematic illustrations and optical microscopic observations on the morphological changes on (**b**) plain surface and (**c**) surface patterned with single-line of micro-hole array ($\Phi = 60$ μm, $D = 120$ μm, $h = 12$ μm, dot lines showing the location of closed holes) under compression. Laser scanning confocal microscopy (LSCM) images showing top and cross-sectional (for the dash lines in top view images) views of signals induced by (**d**) random folding on the plain surface, and (**e**) targeted folding on a micropatterned surface, with the digital analysed results for top view optical signals in (**f**). **g** A signal image of green opened book from 3D LSCM reconstruction to show the surface signal with targeted folding. All scale bars are 30 μm.

signal noise on background remains considerably high, due to the discontinuous fluorescein aggregation caused by small creases/folds[45].

Selectively oxygen-quenching induced ultra-high contrast. The Iridium-III (Ir-III) complex is an oxygen-quenching phosphorescent material which usually emits orange-red coloured light ($\lambda_{emission} = 580$ nm, Fig. 2a) in hypoxia condition after being excited[45]. Our aim is to utilize the topological hypoxia zone, created by targeted folding, to preserve the optical signal on the self-contact region for the Ir-III coating layer (Fig. 2b). Exposed to the oxygen in open air, Ir-III complex luminescence outside of the folding area is mostly eliminated by the oxygen quenching effect, leading to a topo-optical signal with ultra-high contrast (see "blade" pattern in Fig. 2c and intensity analysis in Fig. 2d). A nominal line contrast (NLC) is defined as $\mathrm{NLC} = \frac{\text{peak intensity}}{\text{mean average of the line intensity}}$, to describe the optical signal distribution for the selected area. After analysing the NLC data (Fig. 2e) for the selected lines in Figs. 2b, 1e, an NLC value of 10 is achieved for the Ir-III coated surface, which is 5 folds of the NLC (~2) for FoA coated surface.

We next scale this topo-optical relationship (SNR versus H_c, Fig. 2f) to understand the geometrical influence on the quality of signal. Small SNRs of 0.47 ± 0.04 are captured when the fold first occurs at ε_{th} with an onsite $H_c \approx 1.1$ μm, for both Ir-III and FoA coated surfaces. When H_c grows higher than 1.6 μm, a stable SNR plateau (SNR ≥ 2) is emerging for FoA coated surface which indicate that the physical accumulation along the folding depth reaches a threshold of intensity to enable a quality optical feedback. This development of self-contact depth, around 500 nm in distance, is very rapid within a strain window of ~0.037 ± 0.017. Given by a nominal strain speed of 0.02 s^{-1}, the sensing signal can be instantly captured in microscope within 1 s. In contrast, an increasing trend is obtained for Ir-III coated surface at the same threshold when H_c increases, due to the oxygen quenching effect at the open air. When the H_c reaches 13.8 μm, the SNR on Ir-III coated surface increases significantly to 12.5 which is 6 folds of that from FoA coated surface. By preserving the peak intensity at self-contact area, the Ir-III coated surface achieve higher SNRs when H_c is larger than 1.6 μm.

The time-dependent degradation of photoluminescent signal is assessed by tracking the peak and background signals at $\varepsilon_{comp} = 0.55$ ($H_c \sim 13.8$ μm) for up to 200 h. The results for FoA coated surface (Fig. 2g) show a retainment of intensity after 200 h with less than 8% decay for both peak and background signals. For Ir-III coated surface, a rapid decrease of around 92% intensity is discovered in first 6 h for the background signal, whilst the peak signal remains stable for the first 70 h, then starts to fade and reaches a decrease of 54% in 200 h. The quenching kinetics is analysed for the Ir-III films on PDMS surfaces with varied thicknesses (Supplementary Fig. 4) in the open air, where the optical signals are quenched for about 5 h in all layers without compression. Under compression, the topology enabled hysteresis results (Fig. 2g) into a high optical contrast for about 65 h, then the peak intensity eventually reduces due to the diffusion of

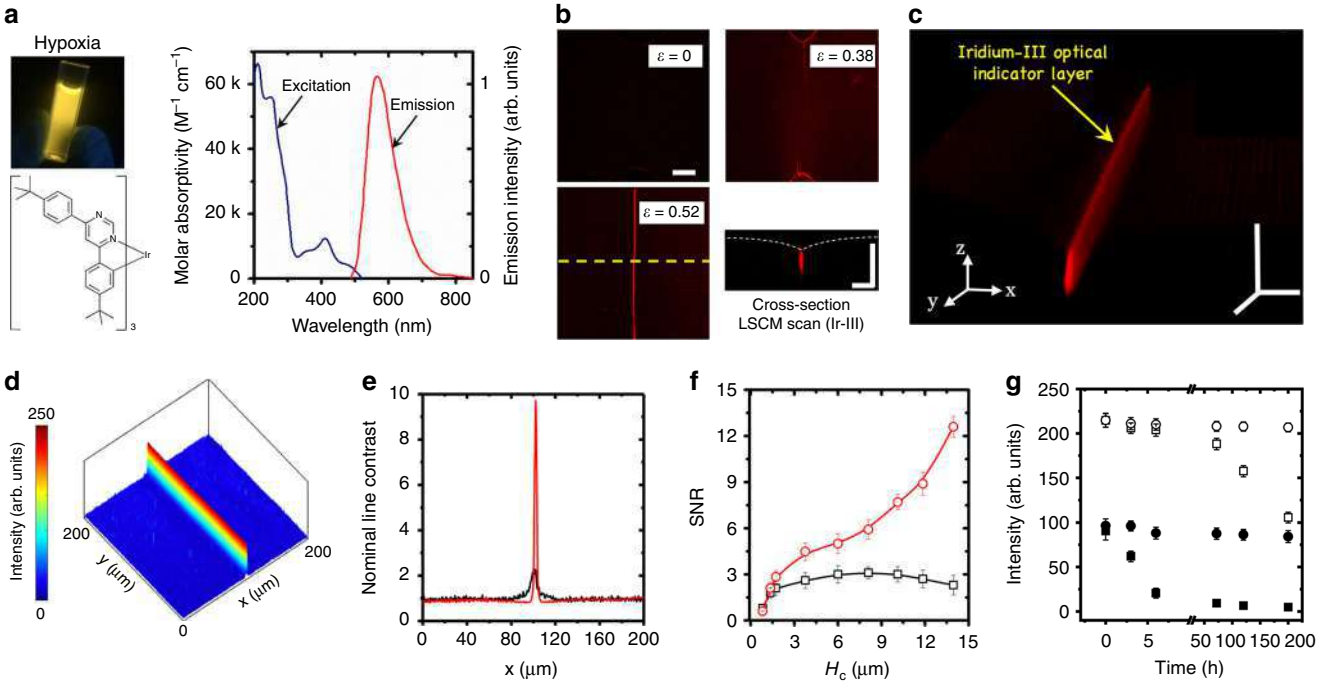

Fig. 2 The generation of ultra-high contrast signal. a Ir-III complex and its excitation and emission spectrum (**b**) Top and cross-sectional views of signal generated by an Ir-III indicator layer; (**c**) A signal image of red blade with ultra-high contrast signal from 3D LSCM reconstruction. **d** The analysed results for top view signal in the selected image in (**b**). **e** Comparison of the nominal line contrast (NLC) for the selected areas in (**b**) (red line) and Fig. 1e (green line). **f** The scaling of signal noise ratio (SNR) versus self-contact depth (H_c) for fluorescein o-acrylate (FoA, black symbol) and Iridium-III (IR-III, red symbol). **g** A time lapsing tracking of signal intensities in (**b**) and Fig. 1e at $\varepsilon_{comp} = 0.52$, circle for FoA, square for Ir-III, hollow for the peak signals, solid for the background signals. All scale bars are 30 μm.

oxygen into the elastic solids. The kinetics of diffusing oxygen into the self-contact region of PDMS surface is complicated as it corresponds to the factors such as temperature, local oxygen concentration, humidity, surface porosity, chemical composition, etc, we thus defer this understanding into future study.

Numerical analysis of self-contact depth guided by surface pattern. We next perform numerical analysis with a commercial finite element simulation software to understand the mechanism of generating targeted folding. The single array of holes with varied geometrical inputs are considered to simulate the in-plane (Supplementary Movie 2) and out of plane (cross-section, Supplementary Movie 3) strain energy localization. By comparing the results for $D/\Phi = 1$ (Fig. 3a) and $D/\Phi = 5$ (Fig. 3b), we find that the in-plane strain concentration for $D/\Phi = 1$ is stronger than that for $D/\Phi = 5$. The out-of-plane (cross-section) simulation results suggest a progressing deformation with the closure of hole (initiation of H_c), development of H_c as a folded contact with non-contact at the bottom (see Fig. 3b), then finally reaching a fully self-contact stage (creasing type, Fig. 3a).

As described above, the development of self-contact is rapid from an onsite H_c at ε_{th}, to the H_c that can provide enough contrast. We next numerically analysis the ε_{th} as a function of D/Φ ($\Phi = 40$ μm) to study the threshold of generating optical signal guided by hole pattern. After comparing with the experimental results (Fig. 3c), the experimental results seem larger than the simulation results for $\Phi = 40$ μm, but good agreements on the overall trend are obtained for the surface, even for those surfaces patterned with different D/Φ. It should be noted that we slightly over-compressed the surface to determine the closure stage for each hole under reflective optical microscope, due to the visco-elastic nature of materials. Thus, the experimental ε_{th} in this paper are a little larger than the simulated ones. The simulation for surface patterned with sharp corners (diamonds, squares, triangles and hexagons) are less successful at the moment as the current simulation programme does not allow the mesh process to progress over the sharp corner, we then separate the investigation in future work.

Following to the onsite of folding, further transient development of H_c is critical in determining the intensity of optical signal. We plot nominal self-contact depths (H_c/h) for different D/Φ ($\Phi = 40$ μm) as a function of compressive strain (Fig. 3d) to understand this geometrical development. Excellent alignments are found between the numerical outcomes and experimental results for $D/\Phi = 1$ and $D/\Phi = 5$, meanwhile a slight mismatch is presented for $D/\Phi = 2$. A region (grey zone) with H_c/h values between 0.15 and 1.2 located on a strain range of 0.39–0.59 is outlined by analysing the experimental results where we can expect the ideal optical signals. The results from cyclic testing (Fig. 3e) indicate a good resilience on generating target folding with a desired self-contact H_c (H_c of 10 μm for $\Phi = 40$ μm and a H_c of 18 μm for $\Phi = 80$ μm, $D/\Phi = 2$), to create enough intensity of optical signal, after a short saturation period of 1–2 cycles. The marathon cyclic assessment reveals a reliable reproducibility of H_c even after 100 cycles (Supplementary Fig. 5), due to the elastic nature of multilayer. Further study on the relaxation of folding was performed by tracing H_c over a longer time duration, to compare with the simulation results (Supplementary Fig. 6a) at a nominal compressive strain (ε_{comp}) of 0.5. The result indicates a limited relaxation in H_c, which is in the same trend with the theoretical approximation. Low hysteresis is observed during the compression/recovery cycle (Supplementary Fig. 6b). The reason could be the elastic nature of multilayer system and low surface tension[45,46] after being coated by Ir-III compound. We then extend the surface design to the square lattice patterns

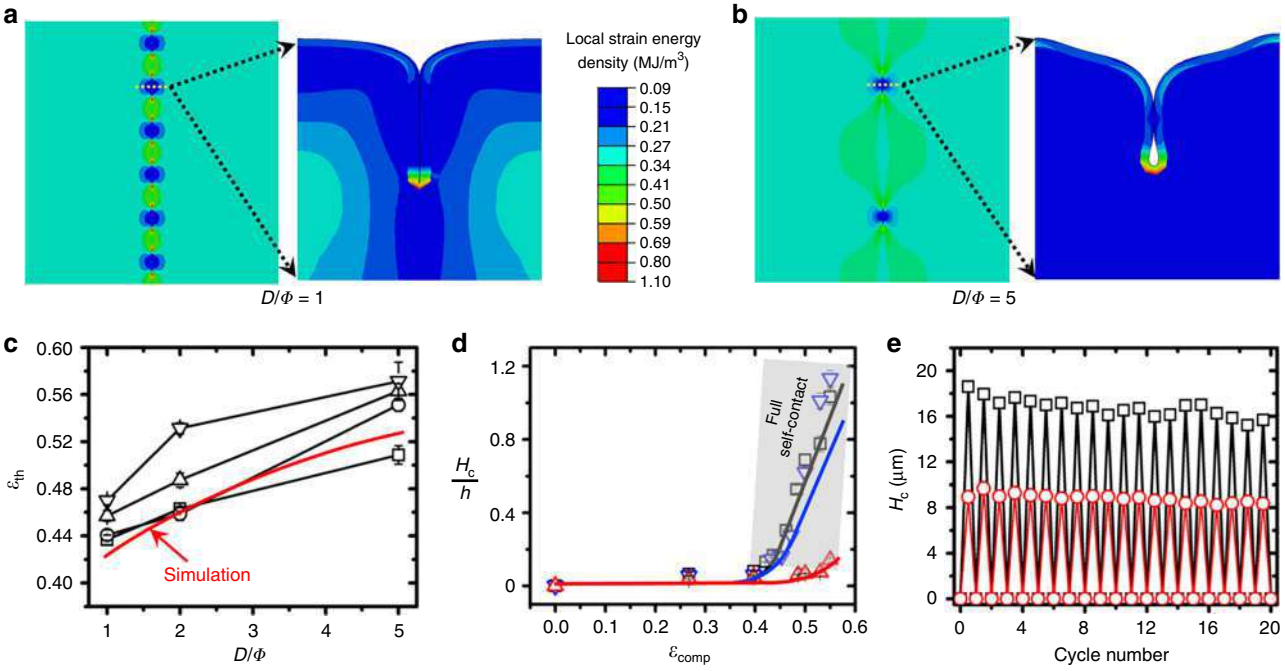

Fig. 3 Numerical analysis and reproducibility assessment. In-plane and out-of-plane strain energy analyses for the surfaces with a single micro-hole array ($\Phi = 40$ μm) of (**a**) $D/\Phi = 1$ and (**b**) $D/\Phi = 5$, at $\varepsilon_{comp} = 0.5$. **c** Comparison of the simulated ε_{th} (threshold strain of hole closure) with experimental ones at different D/Φ for the surface with hole array (□ for $\Phi = 20$ μm, O for $\Phi = 40$ μm, Δ for $\Phi = 60$ μm, ∇ for $\Phi = 80$ μm). **d** Comparison the simulation (line) and experimental (symbol) results for nominal self-contact depth (H_c/h) under a progressive ε_{comp} for the surface with a single micro-hole array ($\Phi = 40$ μm; black for $D/\Phi = 1$, blue for $D/\Phi = 2$, red for $D/\Phi = 5$). **e** The cyclic testing results with $\Phi = 80$ μm (□) and $\Phi = 40$ μm (O), at $D/\Phi = 2$.

(Supplementary Movie 4), where W is defined as the distance between neighbouring lines (Supplementary Fig. 7). The results suggest that varied ε_{th} at high strain can be achieved by designing D/Φ, W/D of the lattice pattern, together with more capabilities on 2D designs.

Demonstration of potential applications. To demonstrate the potential of developing this topo-optical sensing mechanism into device applications, an in-plane topo-optical sensor (Fig. 4a) is presented to detect large surface strains, by simply configuring the pattern parameters (shape, D/Φ, etc) for the pre-placed lattice (Supplementary Movie 5). A programmable stepwise switching mechanism is encoded in this design, where a reversible line pattern could be logically switched between '0,0,0' at $\varepsilon = 0$, '1,0,1' at $\varepsilon = 0.44$ and '1,1,1' at $\varepsilon = 0.52$, with corresponding optical signals can be visualized by reflective optical microscopy and fluorescence microscopy at the same time. This concept can be further developed into dynamic 2D spy barcode products with hidden information only appearing under a dedicated stain (Fig. 4b) and an adaptive topo-optical luminescence grid (Fig. 4c), which contains a tuneable feature on the size of grid under equi-biaxial compression to track the cell behaviour.

Based on this topo-optical sensing strategy, a flexible bending sensor can be developed by combining the in-plane pre-compression ($\varepsilon_{pre\text{-}c}$, Fig. 4d) to detect out-of-the-plane bending degree. After releasing pre-stretching strain of substrate (stage I), we deploy the device on the area to detect the bending level. By observing under microscopy, the device first experiences a selective fold on the lattice patterned surface at low degree bending (stage II), then all lattice patterns are folded at high degree bending (stage III). A brief phase diagram is created to distinguish the two-stage bending sensing for the patterned surface ($\Phi = 80$ μm, $h = 12$ μm, $D/\Phi = 1$ (black line) and 5 (red line), $W/\Phi = 5$), where a clear map is obtained to determine localized curvature with the provided $\varepsilon_{pre\text{-}c}$ when the optical signal occurs.

Discussion

We have described a topo-optical sensing strategy by targeted generating folds on a micropatterned surface, with a coated optical indicator layer. The elastic multilayer shows a robust and precise optical signal by activating folds at the pre-patterned area under certain strain values. The formation of folding patterns has been studied with various geometrical inputs of the lattice patterns and the results are in a good agreement with the predictions from numerical analysis. An inherited automatic optimization on optical contrast is also introduced by oxygen quenching the Ir-III based optical indicator layer, which lead to an ultra-high contrast by significantly reducing the background noise. We anticipate this high-contrast topo-optical sensing strategy with the demonstrated conceptual devices will open new windows for future applications such as flexible/wearable electronics and bio-devices.

Methods

Fabrication of patterned multilayer elastomeric substrate. The lattice patterns were prepared through SU-8 pillar array templates photo-lithographically patterned on silicon wafer (Supplementary Fig. 8) and followed by a stamp transfer (Supplementary Fig. 9). Single-line and square (multi-line) lattice arrays of SU-8 pillars were lithographically patterned on silicon substrates to create the stamp template. Firstly, 1, 1, 1, 3, 3, 3-hexamethylsilazane (ACROS ORGANICS) was spin-coated (30 s, 1000 rpm) onto the silicon wafer to promote adhesion. A thin layer of SU-8 (2025, Micro Chem) was then spin-coated, followed by soft baking at 95 °C for 5 min, before being exposed to UV light under a mask aligner (EVG 620). Post-exposure-bake was then performed (65 °C for 1 min, then ramped to 95 °C for 5 min). After being developed in an EC (ethylene lactate based) solution for 5 min, the patterned SU-8 templates were cleaned by isopropyl alcohol and DI (de-ionized) water. It was baked for another 15 min at 200 °C before stamp transfer.

The mounting substrates were made from vinylpolysiloxane elastomer (VPS, Elite Double 22, Zhermack) and cut into rectangular strip (9 mm wide, 30 mm long and 1.5 mm thick). The VPS strips were then mounted on mechanical vices (Supplementary Fig. 9), before being pre-stretched uniaxially to 600% strain. A thin layer (~125 μm) of polydimethylsiloxane (PDMS, Sylgard 184, base-to-crosslinker weight ratio = 30:1) was spin-coated on the fabricated SU-8 pillars, followed by 60 min soft bake at 70 °C. An adhesion PDMS layer was then spin-coated (30:1) onto the soft-baked PDMS to bond it to the mounting VPS layer. The multilayer structures were cured at 70 °C for 8 h. An air plasma treatment (100 w, Henniker

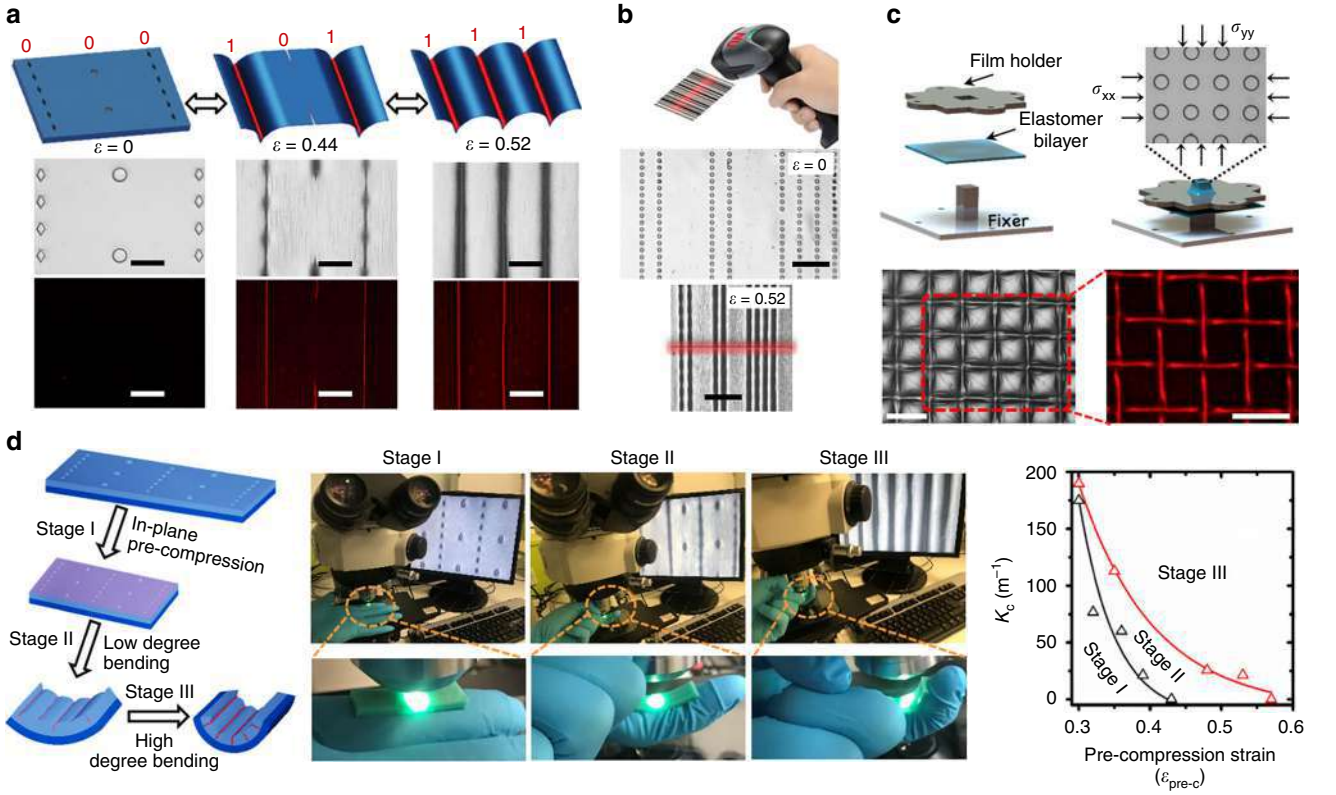

Fig. 4 Demonstration of application concepts. a An in-plane logic strain sensor with stepwise responses for large deformation sensing. **b** A 2D spy barcode design with a state of 'OFF' at $\varepsilon = 0$ and an 'ON' state at $\varepsilon = 0.52$. **c** An adaptive topo-optical grid under equi-biaxial compression. **d** A flexible tactile sensor to detect the change on local curvature with (left) schematic illustration of sensing principle, (middle) observation of conformal sensing under reflective microscopy, (right) phase diagram of the conformal tactile sensing. All scale bars are 100 μm.

HPT-100) of 10 s was applied to create a thin hard skin layer on the lattice patterned PDMS surface.

Solution casting of optical indicator layer. After the air plasma treatment, optical indicator solutions (1.5 mM) were prepared by dissolving the dye into the absolute ethanol and chloroform. A droplet of solution containing either fluorescein O-acrylate (Sigma-Aldrich) or Iridium-III complex (synthesized in house following the published route[47]) was then casted on the surface of multilayer. The solution droplet then spread and dried at room temperature to form an optical indicator layer with a measured thickness of ~600 nm.

Characterizations. Upon releasing the pre-stretched VPS mounting substrates, the PDMS thin layer experienced uniaxial compression. Incremental deformation in a unit nominal strain of ≈0.004 was applied to the sample during the compression (progressing) or tension (withdrawing/recovery) by a fixed amount at regular intervals in room temperature. A reflective optical microscope (Nikon LV-100) was used for observation under white light. 3D and 2D fluorescence imaging was performed using Nikon A1R LSCM system (LSCM). For all observations/tests, multiple measurements were performed on 7–15 selected samples (areas) to minimize the system error. For the fluorescein O-acrylate images, the scanner selection was set to be Galvano, with laser excitation wavelength of 488 nm and emission wavelength of 540 nm. For the Iridium-III images, the scanner selection was set to be Galvano, with laser excitation wavelength of 406.6 nm and emission wavelength of 595 nm. The captured fluorophore images were subsequently analysed by the MATLAB to get its light intensity data and image (surf, shading interp). Standard deviations (error bars in the figures) were calculated based on the mean averaging of a group of data from 7 to 9 independent measurements on different samples.

Numerical simulation. We used the commercial simulation package—ABAQUS, to simulate surface folding on the multilayer under uniaxial compression. The incompressible neo-Hookean material model was used for all elastic materials in this analysis. Structural symmetry was assumed when the fold is simulated. The pseudo-dynamic method incorporated in ABAQUS was adopted. The geometrical inputs have been magnified by 1000 times due to the limitation of mesh size in ABAQUS. An element type CAX8H was used for mesh.

Data availability

The data that support the findings of this study are available via Northumbria Research Data Management scheme and per request from the corresponding author (B.X.).

Code availability

The numerical code developed in this work is available upon request from Dr. Xue Chen (sherry.chen@northumbria.ac.uk).

Received: 4 October 2019; Accepted: 25 February 2020;
Published online: 19 March 2020

References

1. Wu, W., Wen, X. & Wang, Z. L. Taxel-addressable matrix of vertical-nanowire piezotronic transistors for active and adaptive tactile imaging. *Science* **340**, 952–957 (2013).
2. Pan, C. et al. High-resolution electroluminescent imaging of pressure distribution using a piezoelectric nanowire LED array. *Nat. Photonics* **7**, 752–758 (2013).
3. Wang, X. et al. Full dynamic-range pressure sensor matrix based on optical and electrical dual-mode sensing. *Adv. Mater.* **29**, 1605817 (2017).
4. Wang, J. et al. Extremely stretchable electroluminescent devices with ionic conductors. *Adv. Mater.* **28**, 4490–4496 (2016).
5. Yang, C. H., Chen, B., Zhou, J., Chen, Y. M. & Suo, Z. Electroluminescence of giant stretchability. *Adv. Mater.* **28**, 4480–4484 (2016).
6. Li, Y.-F. et al. Stretchable organometal-halide-perovskite quantum-dot light-emitting diodes. *Adv. Mater.* **31**, 1807516 (2019).
7. Song, S., Song, B., Cho, C.-H., Lim, S. K. & Jeong, S. M. Textile-fiber-embedded multiluminescent devices: a new approach to soft display systems. *Mater. Today* https://doi.org/10.1016/j.mattod.2019.08.004 (2019).
8. Guo, Q. et al. A cephalopod-inspired mechanoluminescence material with skin-like self-healing and sensing properties. *Mater. Horiz.* **6**, 996–1004 (2019).
9. Leung, E. M. et al. A dynamic thermoregulatory material inspired by squid skin. *Nat. Commun.* **10**, 1947 (2019).

10. Cao, Y. et al. Self-healing electronic skins for aquatic environments. *Nat. Electron.* **2**, 75–82 (2019).
11. Bu, T. et al. Stretchable triboelectric–photonic smart skin for tactile and gesture sensing. *Adv. Mater.* **30**, 1800066 (2018).
12. Sun, J. et al. Self-healable, stretchable, transparent triboelectric nanogenerators as soft power sources. *ACS Nano* **12**, 6147–6155 (2018).
13. Mukherjee, S. & Thilagar, P. Renaissance of organic triboluminescent. *Mater. Angew. Chem. Int. Ed.* **58**, 7922–7932 (2019).
14. Wang, X. et al. Stretchable and transparent electroluminescent device driven by triboelectric nanogenerator. *Nano Energy* **58**, 410–418 (2019).
15. Wong, M.-C., Chen, L., Bai, G., Huang, L.-B. & Hao, J. Temporal and remote tuning of piezophotonic-effect-induced luminescence and color gamut via modulating magnetic field. *Adv. Mater.* **29**, 1701945 (2017).
16. Wang, Z. in *Piezotronics and Piezo-Phototronics* 1–17 (Springer, Berlin, Heidelberg, 2012).
17. Yan, D. et al. Layered host–guest materials with reversible piezochromic luminescence. *Angew. Chem. Int. Ed.* **50**, 7037–7040 (2011).
18. Zhao, H. et al. Buckling and twisting of advanced materials into morphable 3D mesostructures. *Proc. Natl Acad. Sci.* **116**, 13239–13248 (2019).
19. Sagara, Y., Yamane, S., Mitani, M., Weder, C. & Kato, T. Mechanoresponsive luminescent molecular assemblies: an emerging class of materials. *Adv. Mater.* **28**, 1073–1095 (2016).
20. Zhang, J.-C., Wang, X., Marriott, G. & Xu, C.-N. Trap-controlled mechanoluminescent materials. *Prog. Mater. Sci.* **103**, 678–742 (2019).
21. Jeong, S. M., Song, S., Lee, S.-K. & Ha, N. Y. Color manipulation of mechanoluminescence from stress-activated composite films. *Adv. Mater.* **25**, 6194–6200 (2013).
22. Zhao, W. et al. Highly sensitive switching of solid-state luminescence by controlling intersystem crossing. *Nat. Commun.* **9**, 3044 (2018).
23. Bai, L. et al. Halogen-assisted piezochromic supramolecular assemblies for versatile haptic memory. *J. Am. Chem. Soc.* **139**, 436–441 (2017).
24. Jeong, S. M., Song, S., Kim, H., Joo, K.-I. & Takezoe, H. Mechanoluminescence color conversion by spontaneous fluorescent-dye-diffusion in elastomeric zinc sulfide composite. *Adv. Funct. Mater.* **26**, 4848–4858 (2016).
25. Ge, D. et al. A robust smart window: reversibly switching from high transparency to angle-independent structural color display. *Adv. Mater.* **27**, 2489–2495 (2015).
26. Zhu, Q., Van Vliet, K., Holten-Andersen, N. & Miserez, A. A double-layer mechanochromic hydrogel with multidirectional force sensing and encryption capability. *Adv. Funct. Mater.* **29**, 1808191 (2019).
27. Wang, D. & Tang, B. Z. Aggregation-induced emission luminogens for activity-based sensing. *Acc. Chem. Res.* **52**, 2559–2570 (2019).
28. v. Bünau, G. J. B. Birks: photophysics of aromatic molecules. Wiley-Interscience, London 1970. 704 Seiten. Preis: 210s. Berichte der Bunsengesellschaft für. *Phys. Chem.* **74**, 1294–1295 (1970).
29. Qiu, Z. et al. Dynamic visualization of stress/strain distribution and fatigue crack propagation by an organic mechanoresponsive AIE luminogen. *Adv. Mater.* **30**, 1803924 (2018).
30. Ji, X. et al. A functioning macroscopic "Rubik's Cube" assembled via controllable dynamic covalent interactions. *Adv. Mater.* **31**, 1902365 (2019).
31. Liu, X. et al. In situ generation of azonia-containing polyelectrolytes for luminescent photopatterning and superbug killing. *J. Am. Chem. Soc.* **141**, 11259–11268 (2019).
32. Lee, E. et al. Tilted pillars on wrinkled elastomers as a reversibly tunable optical window. *Adv. Mater.* **26**, 4127–4133 (2014).
33. López Jiménez, F., Kumar, S. & Reis, P. M. Soft color composites with tunable optical transmittance. *Adv. Opt. Mater.* **4**, 620–626 (2016).
34. Zeng, S. et al. Bio-inspired sensitive and reversible mechanochromisms via strain-dependent cracks and folds. *Nat. Commun.* **7**, 11802 (2016).
35. Brau, F. et al. Multiple-length-scale elastic instability mimics parametric resonance of nonlinear oscillators. *Nat. Phys.* **7**, 56–60 (2010).
36. Xu, B., Chen, D. & Hayward, R. C. Mechanically gated electrical switches by creasing of patterned metal/elastomer bilayer films. *Adv. Mater.* **26**, 4381–4385 (2014).
37. Xu, B., Liu, Q., Suo, Z. & Hayward, R. C. Reversible electrochemically triggered delamination blistering of hydrogel films on micropatterned electrodes. *Adv. Funct. Mater.* **26**, 3218–3225 (2016).
38. De Jong, E., Wang, Y., Den Toonder, J. M. J. & Onck, P. R. Climbing droplets driven by mechanowetting on transverse waves. *Sci. Adv.* **5**, eaaw0914 (2019).
39. Kang, J.-H., Kim, H., Santangelo, C. D. & Hayward, R. C. Enabling robust self-folding origami by pre-biasing vertex buckling direction. *Adv. Mater.* **31**, 193006 (2019).
40. Silverberg, J. L. et al. Origami structures with a critical transition to bistability arising from hidden degrees of freedom. *Nat. Mater.* **14**, 389–393 (2015).
41. Silverberg, J. L. et al. Using origami design principles to fold reprogrammable mechanical metamaterials. *Science* **345**, 647–650 (2014).
42. Wang, D. et al. Spatially configuring wrinkle pattern and multiscale surface evolution with structural confinement. *Adv. Funct. Mater.* **28**, 1–9 (2018).
43. Auguste, A., Jin, L., Suo, Z. & Hayward, R. C. Post-wrinkle bifurcations in elastic bilayers with modest contrast in modulus. *Extrem. Mech. Lett.* **11**, 30–36 (2017).
44. Zhao, R., Zhang, T., Diab, M., Gao, H. & Kim, K.-S. The primary bilayer ruga-phase diagram I: localizations in ruga evolution. *Extrem. Mech. Lett.* **4**, 76–82 (2015).
45. Chen, D., Cai, S. Q., Suo, Z. & Hayward, R. C. Surface energy as a barrier to creasing of elastomer films: an elastic analogy to classical nucleation. *Phys. Rev. Lett.* **109**, 038001 (2012).
46. Yang, J., Jin, L., Hutchinson, J. & Suo, Z. Plasticity retards the formation of creases. *J. Mech. Phys. Solids* **123**, 305–314 (2019).
47. Turnbull, G., Williams, J. A. G. & Kozhevnikov, V. N. Rigidly linking cyclometallated Ir(iii) and Pt(ii) centres: an efficient approach to strongly absorbing and highly phosphorescent red emitters. *Chem. Commun.* **53**, 2729–2732 (2017).

Acknowledgements

The work was supported by the Engineering and Physical Sciences Research Council (EPSRC) grant-EP/N007921/1 and EP/S01280X/1, and Royal Society Kan Tong Po International Fellowship 2019-KTP\R1\191012. Dr Ben Xu and Dr Ding Wang would thank Reece Innovation for the studentship support. Professor Jie Kong thanks the financial support from Natural Science Basic Research Plan in Shaanxi Province (2018JC-008, Distinguished Young Scholar).

Author contributions

The idea was initially generated between B.X., Y.L. and V.K. B.X. and Y.L. directed the research programme and designed the experiments with C.W. C.W. carried out the major part of experiments with D.W.'s assistances on multilayer fabrication and pattern transformation. The micro-pattern template was engineered by D.W. V.K. and G.T. synthesis and characterized the Ir-III complex and diluted it into the mixed solvent for casting. B.X., X.C. and X.D. developed the analytical simulations. B.X., Y.L. J.K. V.K. and B.Z.T analyzed and interpreted the data. B.X., Y.L. J.K. and B.Z.T defined the scope together and wrote the paper with contributions from all authors.

Competing interests

The authors declare no competing interests.

Additional information

Supplementary information is available for this paper at https://doi.org/10.1038/s41467-020-15288-8.

Correspondence and requests for materials should be addressed to J.K., B.Z.T., Y.L. or B.B.X.

Peer review information *Nature Communications* thanks Kin Liao and the other, anonymous, reviewer(s) for their contribution to the peer review of this work. Peer reviewer reports are available.

Reprints and permission information is available at http://www.nature.com/reprints

Publisher's note Springer Nature remains neutral with regard to jurisdictional claims in published maps and institutional affiliations.

Supplementary Information

A Flexible Topo-optical Sensing Technology with Ultra-high Contrast

Wang et al.

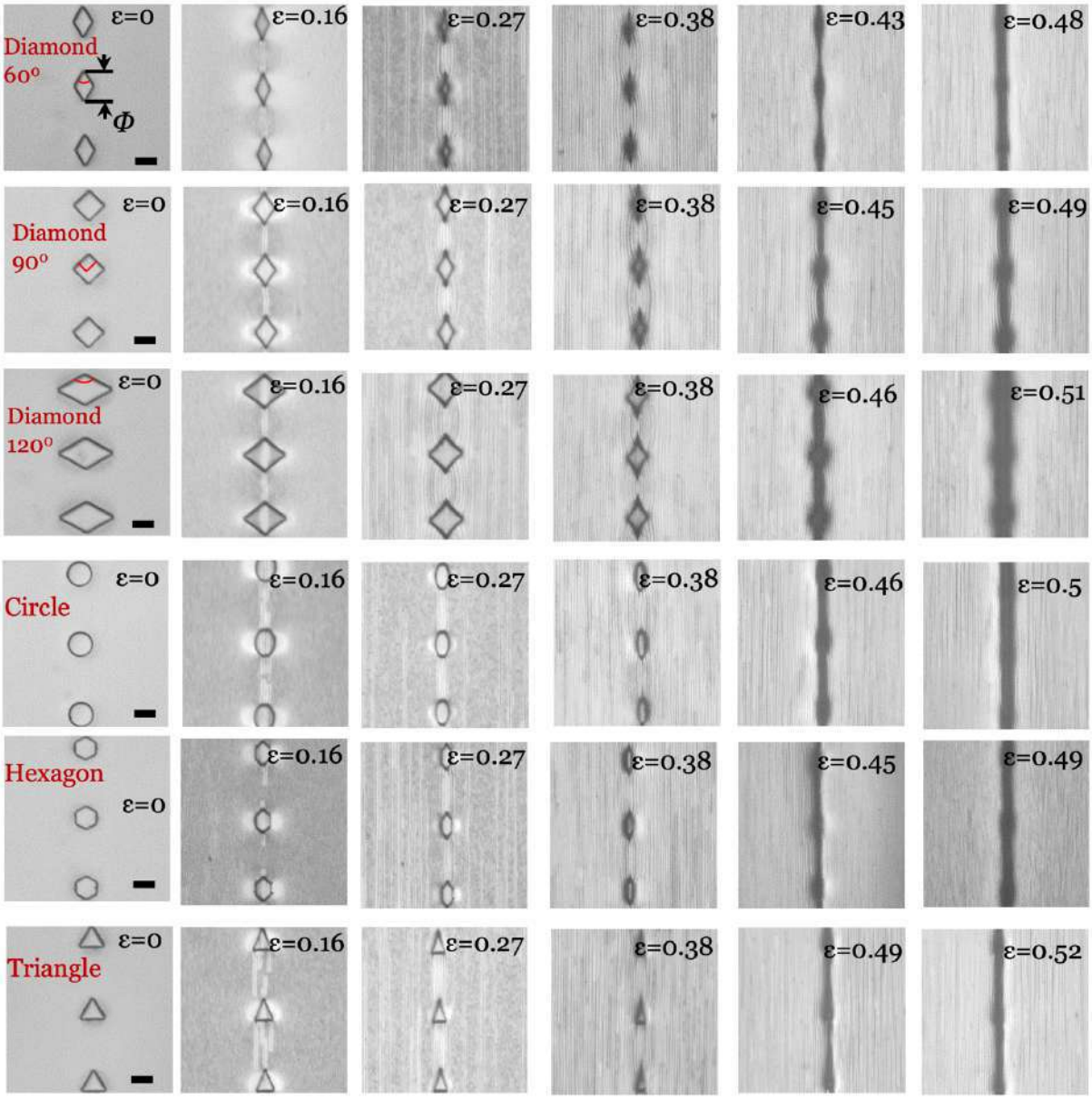

Supplementary Figure 1. The formation of folding guided by the single line lattice pattern with different pattern shape, scale bar = 40 μm.

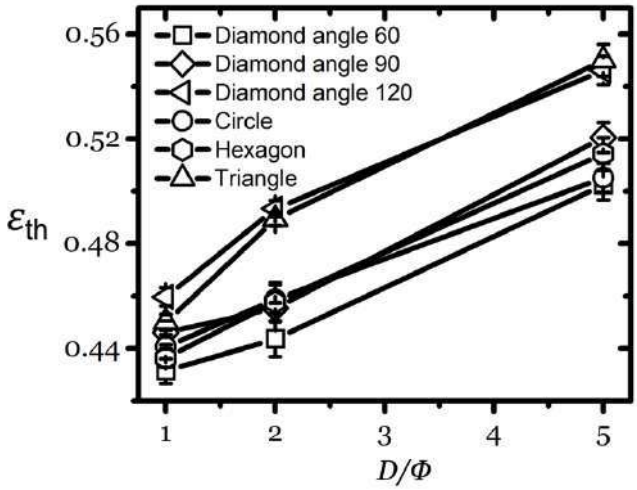

Supplementary Figure 2. Summary of threshold strains to achieve targeted folding on the surface patterned with different shape.

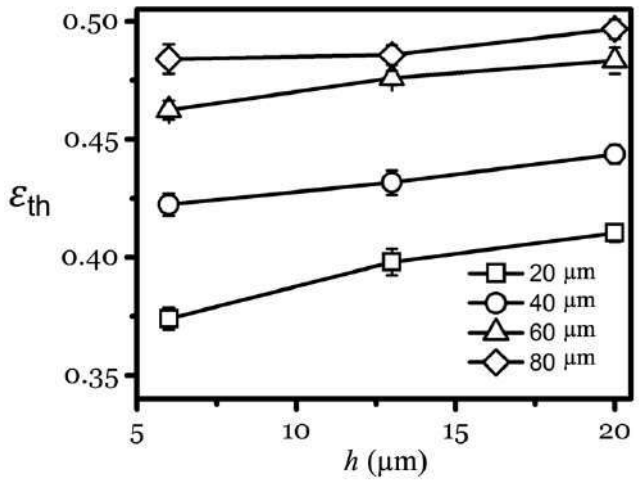

Supplementary Figure 3. Summary of threshold strains to achieve targeted folding with dependence on the hole depth.

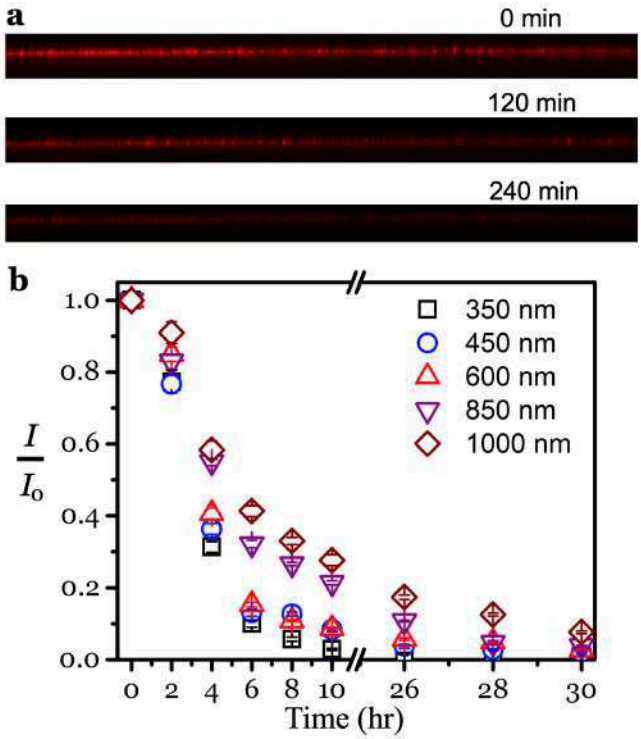

Supplementary Figure 4 (a). The quenching observation for an Ir-III film of 450 nm; (b) Quenching kinetics analysis Ir-III films coated on PDMS surface with different thickness in the open air.

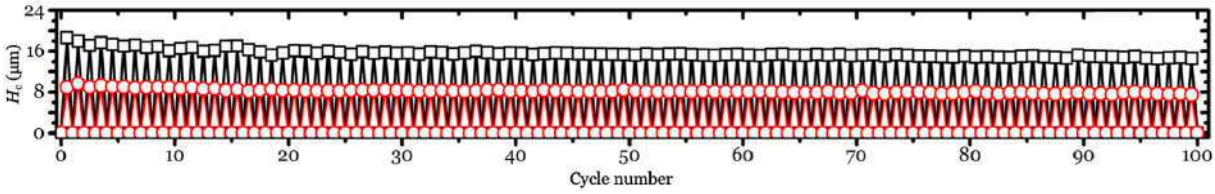

Supplementary Figure 5 The cyclic testing results (up to 100 cycles) for samples with Φ = 80 μm (□) and Φ = 40 μm (○), at D/Φ =2.

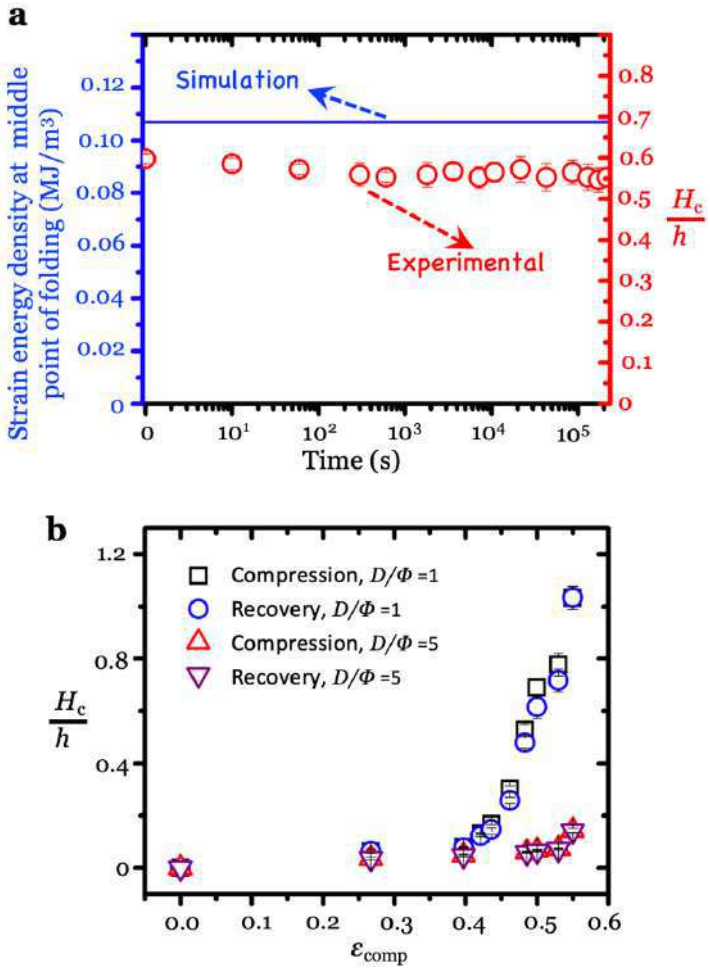

Supplementary Figure 6 (a). Comparison the simulation and experimental results for relaxation behaviour under a progressive ε_{comp} =0.5 for the surface with a single micro-hole array (Φ = 40 μm, D/Φ=5). (b) The hysteresis results for targeted folding depth on the surface with a single micro-hole array (Φ = 40 μm, D/Φ=1 and D/Φ=5).

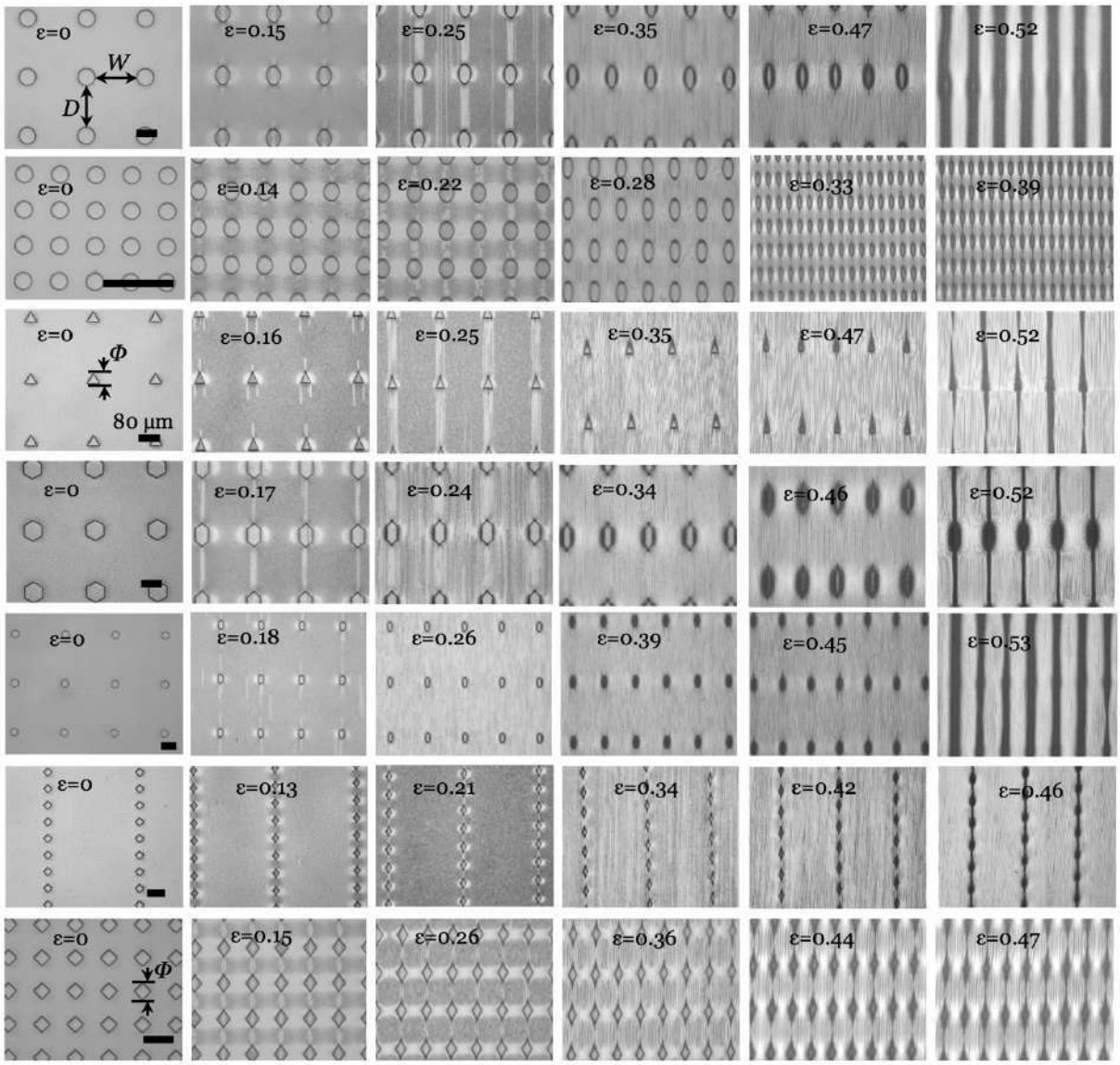

Supplementary Figure 7 The formation of folding guided by the square lattice pattern with different pattern shape, W/D, and D/Φ.

.

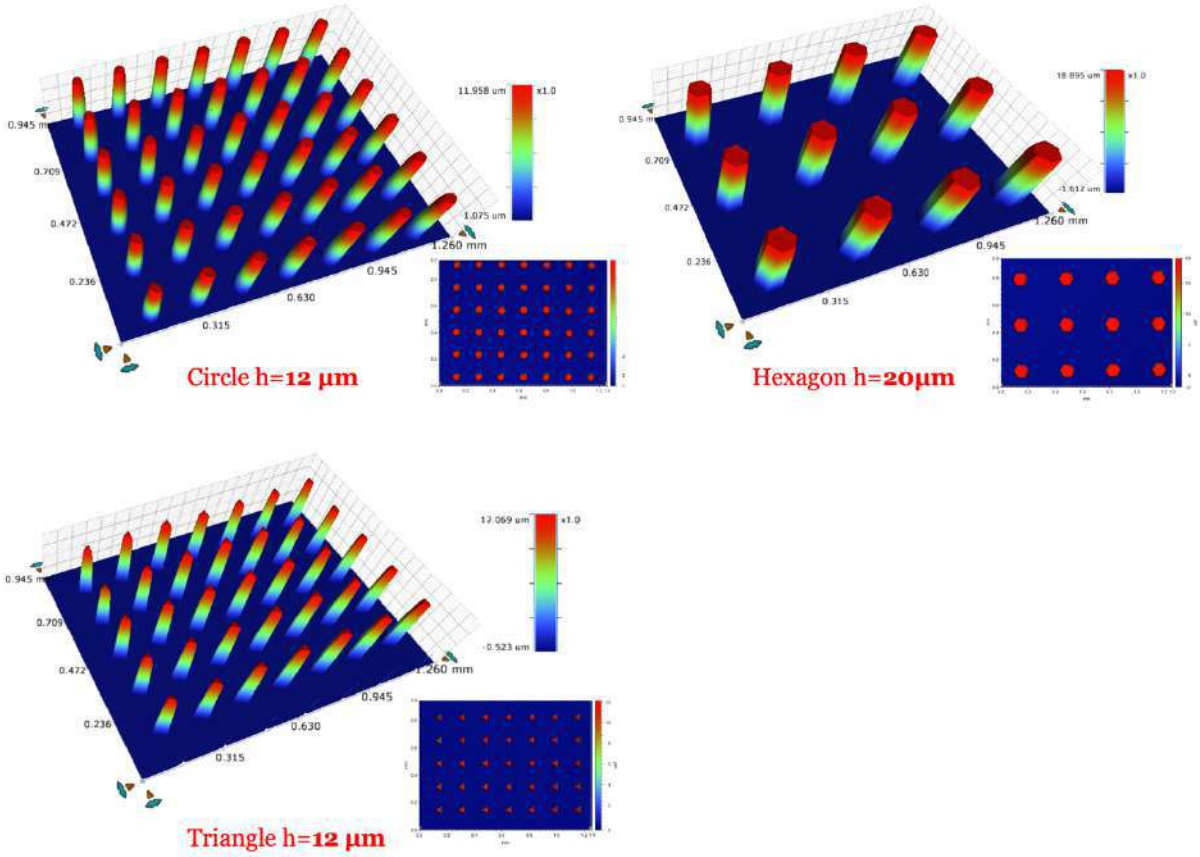

Supplementary Figure 8 Profiling of the fabricated SU-8 array templates with different geometrical factors.

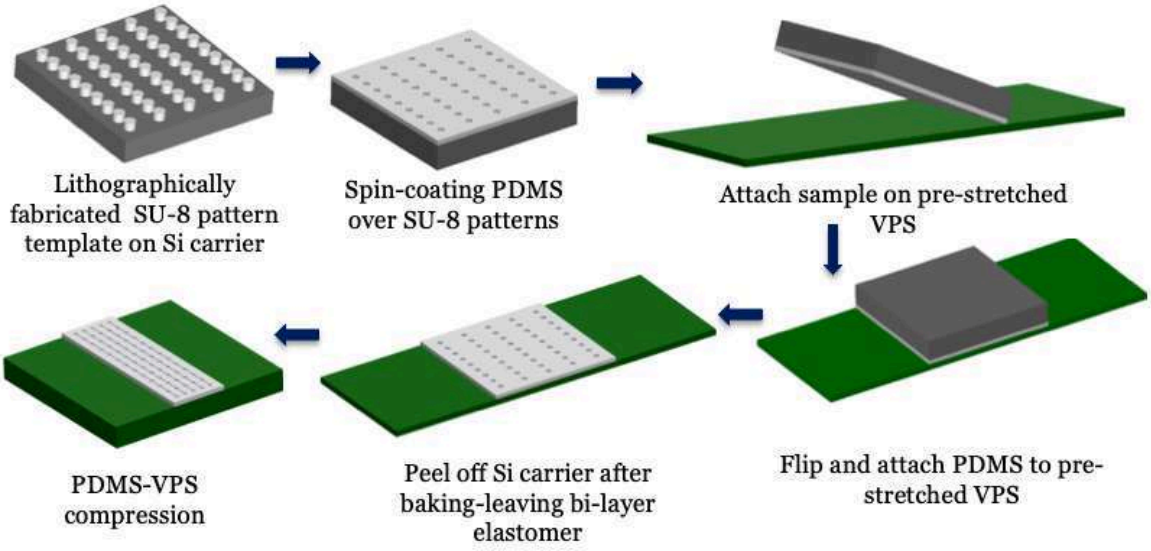

Supplementary Figure 9 The schematic illustration of fabrication process of structural surface by spin-coating a thin PDMS precursor layer on a lithographically made template.

APL Materials

Flexible, strain gated logic transducer arrays enabled by initializing surface instability on elastic bilayers

Cite as: APL Mater. **7**, 031509 (2019); https://doi.org/10.1063/1.5079403
Submitted: 30 October 2018 . Accepted: 13 March 2019 . Published Online: 28 March 2019

Cong Wang, Ben Bin Xu, Jonathan G. Terry, Stewart Smith, Anthony J. Walton, Steven Wang, Haibao Lv, and Yifan Li

Flexible, strain gated logic transducer arrays enabled by initializing surface instability on elastic bilayers

Cite as: APL Mater. 7, 031509 (2019); doi: 10.1063/1.5079403
Submitted: 30 October 2018 • Accepted: 13 March 2019 •
Published Online: 28 March 2019

Cong Wang,[1] Ben Bin Xu,[1,a)] Jonathan G. Terry,[2] Stewart Smith,[2] Anthony J. Walton,[2] Steven Wang,[3] Haibao Lv,[4] and Yifan Li[1,a)]

AFFILIATIONS

[1]Department of Mechanical and Construction Engineering, Faculty of Engineering and Environment, Northumbria University, Newcastle upon Tyne NE1 8ST, United Kingdom
[2]SMC, Institute for Integrated Micro and Nano Systems, School of Engineering, The University of Edinburgh, Edinburgh EH9 3JF, United Kingdom
[3]School of Chemical Engineering and Advanced Materials, Newcastle University, Newcastle upon Tyne NE1 7RU, United Kingdom
[4]Science and Technology on Advanced Composites in Special Environments Laboratory, Harbin Institute of Technology, Harbin 150080, China

[a)]**Authors to whom correspondence should be addressed:** yifan.li@northumbria.ac.uk and ben.xu@northumbria.ac.uk

ABSTRACT

Developing flexible sensors with a high strain sensing range could enable widespread downstream applications, by allowing intimate, mechanically conformable integration with soft biological tissues. By characterizing interconnected metal electrode arrays on super-flexible substrates, we have established a surface deformation control strategy of an array of strain transducers. The strain gated switches are capable of measuring various compressive strains (up to 60%) by bringing metal electrodes into self-contact via creasing elastic instability beyond a threshold substrate strain. The designed devices have been developed to explore the geometry design effect on the electrode-elastomer "stiff film on soft elastomer" surface deformation. The enabled transducer array yielded a stepwise strain-electrical resistance switching mechanism which opens up the potential of future interconnected sensor array type of super-compressible devices.

Flexible electronics and transducers where devices are subject to stretching, bending, and twisting forces have grown into one of the more interesting technologies for next generation applications such as bio-medical electronics, smart skin, wearable sensors, epidermal electronics, and sensors and actuators.[1–10,12,16] Recent research on elastic substrates complying with local features such as metal interconnects and integrated transducers has shown great potential to withstand high strain deformation during bending, compressing, and stretching.[7,12–14] Such structured elastic surfaces under compression and stretching can undergo various deformations such as wrinkling, creasing, folding, and buckling, which generates interest in engineering applications in sensing and actuation.[11,15–25] Among them, recently developed metal-elastomer strain gated transducers have utilized mechanically gated super-flexible electrical switches to provide sensing mechanisms for wearable electronics.[5,8,9,23]

Controllably and reversibly generating creasing and other instability patterns on the surfaces of soft materials by electrical,[26] temperature,[27] mechanical,[28] and electrochemical[29] stimulations have attracted considerable interest in developing them into sensing and actuation applications. One of the latest super-compressible (up to 60%) strain-gated electrical switching sensing mechanisms utilizes surface instabilities such as wrinkles and creases on soft elastomer substrates under compression with stiff film patterns on top (e.g., metal electrodes).[5] Such devices with single-pair of metal "finger" electrodes relying on the controllable formation of surface

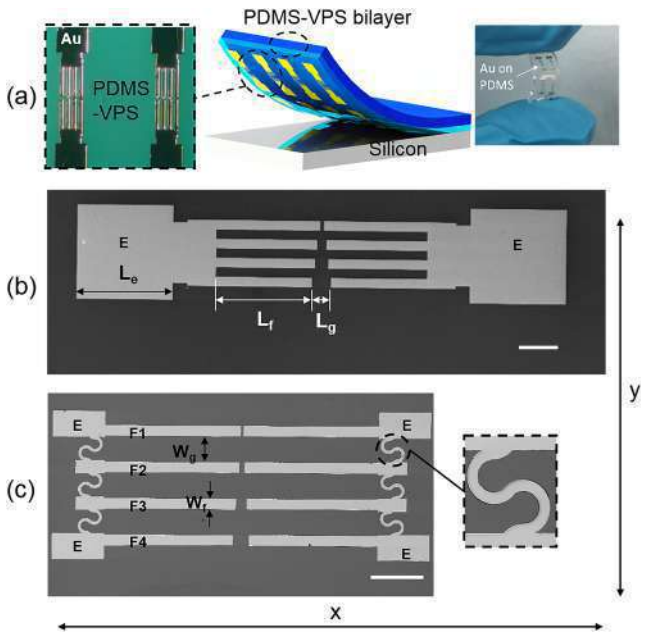

FIG. 1. (a) Schematic (middle) and microscopic image (left) of patterned multi-switching Au strain transducer array, with Au patterns transferred from silicon to the PDMS-VPS substrate by a dual-SAM (self-assembly monolayer) assisted metal transfer process. SEM top-view images showing two different interconnect configurations: (b) 4 pairs of finger transducers "F" interconnected with two bulk contact electrodes "E"; (c) 4 pairs of finger transducers interconnected with contact electrodes by serpentine structures (scale bars = 200 μm).

creases to bring initially disconnected regions of the metal electrode into self-contact were previously reported.[5] When compressed (x-direction in Fig. 1), the stiff Au film (Young's modulus 50–70 GPa) wrinkles due to its near inextensibility. The much softer (Young's modulus 0.4–4 MPa) substrate areas in the gap between Au electrodes can have greater deformation due to the local amplification of strain by the stiff films nearby. At higher compression, a crease forms in this gap between electrodes, generating the desired electrodes' self-contact switching mode.[5] The measured resistance displayed a significant step change from ~10^{13} Ω to ~10^{2} Ω after the self-contact of the electrodes after the substrate compression strain surpasses threshold values.[5] The switching threshold strains can be controlled by geometry design (e.g., Au electrode width W_f, length L_f, and gap width L_g) as well as material and structural properties,[5] and recent research in surface instabilities has shown that the deformation mode can also be controlled via such designs.[21] Moreover, the latest study into surface instabilities on such heterogeneous surfaces with patterned regions of different materials (e.g., stiff metal electrodes and soft elastomers) opens the possibilities for research into advanced surface morphing and more complex application devices.[21]

For future development of transducer arrays applied to a larger area under compression, it is important to develop electrode interconnect technologies which should ultimately enable row-column addressing. This paper discusses a multi-finger switching mechanism with the controllable competing elastic instability growth on super-flexible surfaces, by design and micro-engineering interconnect more complex Au on polydimethylsiloxane-vinylpolysiloxane (PDMS-VPS) bilayer structures. Such a structure was fabricated by a dual-SAM (self-assembly monolayer) assisted metal transfer process which transfers photolithographically patterned Au electrodes (thickness = 74 nm) from silicon to the PDMS-VPS substrates [Fig. 1(a)] with details given in the supplementary material, providing a stepwise resistance-strain response sensing mechanism which could shed light on the future applications in widespread downstream applications, tunable and stretchable electronics.[24–28] This work also experimentally studied instabilities (patterned stiff and soft regions) on heterogeneous surfaces under large compression strains (up to 60%) which could help the development in related theoretical studies, such as that initiated in Ref. 21.

The designed and fabricated transducer arrays and interconnects are shown in Fig. 1. Each of the paired Au finger electrodes based on the previous design[5] with key dimensions (e.g., finger electrode width W_f, length L_f, and gap width L_g) was interconnected by two different configurations. Figure 1(b) shows the SEM image (Tescan® Mira3) of the bulk interconnect configuration linking 4 pairs of finger electrode transducers (labeled F1 to F4) with 2 contact electrodes (labeled E). Figure 1(c) shows the serpentine interconnect configuration which helped protecting the Au electrodes from damage caused by perpendicular direction stretching due to Poisson effect (see details in the supplementary material). This research focuses on the relationship between the geometry design parameters such as W_f, L_f, and L_g and 2D (top-view) deformation for the Au electrodes and gaps in-between at different substrate compression strains ε_{sub}. Other parameters such as the contact electrode length L_e and the adjacent serpentine interconnect spacing W_g [Fig. 1(c)] were also considered.

The uniaxial (x-direction) substrate compression was provided by releasing the pre-stretched PDMS-VPS mounting layer from L_0 to L. Wrinkles on Au finger electrodes started to develop at low strain, and eventually both wrinkles on Au and creases on PDMS after substrate strain $\varepsilon_{sub} = (L_0 - L)/L_0$ went beyond threshold as illustrated in Fig. 2(a). Figures 2(a) and 2(b) show that the reversible wrinkling process on Au has reduced the finger length from L_{f0} to L_f, resulting in a local strain change $\varepsilon_{Au\text{-}x} = (L_{f0} - L_f)/L_{f0}$. Meanwhile as discussed, the gap area in-between (softer PDMS surface) will have its local strain amplified due to surrounding stiffer film patterns with $\varepsilon_{Gap\text{-}x} = (L_{g0} - L_g)/L_{g0}$.

Figure 2(c) shows the Au wrinkling 3D profiles obtained by Atomic Force Microscopy (AFM Bruker™ 3100) scan with which they progressively grew under different substrate strains. Based on the critical wrinkling strain of $\varepsilon_w = 0.25(\frac{3\bar{E}s}{\bar{E}f})^{2/3}$, the expected theoretical $\varepsilon_w = 6.7 \times 10^{-4}$ calculated based on the elastic plane-strain moduli of $E_f = 7 \times 10^{10}$ Pa and 74 nm gold film of $E_s = 4 \times 10^5$ Pa. In reality, the wrinkles started to form at a substrate strain $\varepsilon_{sub} = 9 \times 10^{-3}$. This indicates and confirms that the local strains on stiff Au electrodes significantly lagged behind those of the substrate and soft PDMS gap areas, which is considered as a helpful technique to protect metal films under large compression strains. The wrinkles on Au continuously grew under further x-direction compression, covering the majority of the Au electrodes at the substrate strain of 0.12. The wrinkle wavelength at substrate strain $\varepsilon_{sub} = 0.12$ was calculated to be 17 μm according to $\lambda_0 = (2\pi h_f)(\frac{\bar{E}f}{3\bar{E}s})^{1/3}$, which closely agreed with

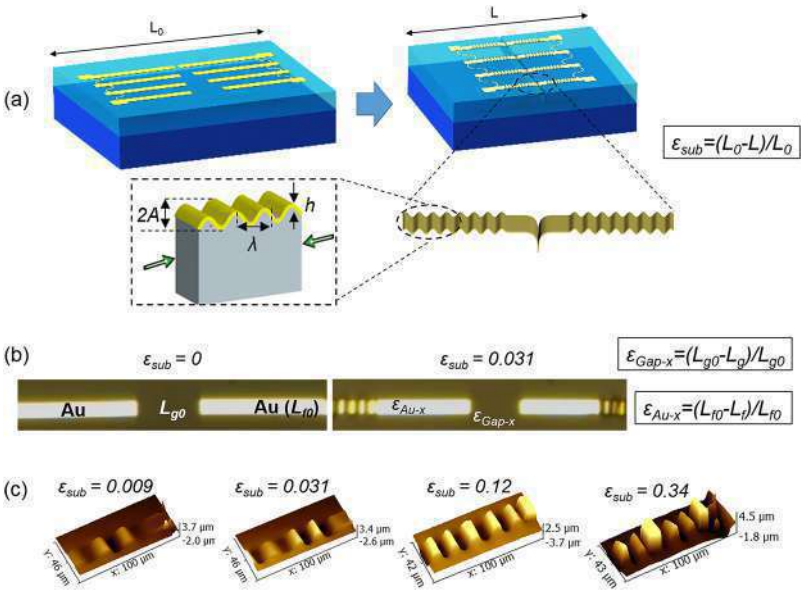

FIG. 2. (a) 3D Schematics showing the Au wrinkling—PDMS creasing 3D deformation process under uniaxial substrate compression—pair of finger electrodes into self-contact due to PDMS creasing, and wrinkling on Au finger electrodes. (b) Top view optical microscopic image showing local strain changes on Au due to wrinkling, and PDMS gap area due to creasing. (c) AFM scan 3D surface profile view of the wrinkle development on the Au electrode at various substrate strains for a device with W_f = 25 μm, L_g = 50 μm, and L_f = 225 μm.

the actual measured value of 18 μm (shown in the supplementary material).

To further understand this local strain difference between Au and PDMS areas against the substrate strain, characterization experiments were designed and conducted using a Nikon® LV-100 optical microscope. We focused on local strains of each Au finger electrodes $\varepsilon_{Au\text{-}x} = (L_{f0} - L_f)/L_{f0}$, as well as PDMS gap area $\varepsilon_{Gap\text{-}x} = (L_{g0} - L_g)/L_{g0}$ between the paired finger electrodes. The length data L_{f0}, L_f and L_{g0}, L_g were all measured by the Nikon system from top view. The relationships between $\varepsilon_{Au\text{-}x}$, $\varepsilon_{Gap\text{-}x}$, and ε_{sub} were comparatively studied against other key geometry design parameters of the Au electrodes such as L_f, L_g, finger width W_f, and locations in the transducer array (E, F1 to F4).

Figure 3(a) shows the relationship between the Au local strains against the substrate strains. The $\varepsilon_{Au\text{-}x}$ always lagged behind the ε_{sub} which is indicated by the dashed line. The strain gap was observed to be constantly ~0.03, until ε_{sub} = 0.45 where this gap increased to around 0.05 when large creases started to appear on PDMS surfaces which absorbed more strain energy. This has confirmed the previous assumption that the local strains on stiff Au electrodes significantly lagged behind those of the substrate. Together with the reversible wrinkling mechanism, most Au electrodes remain

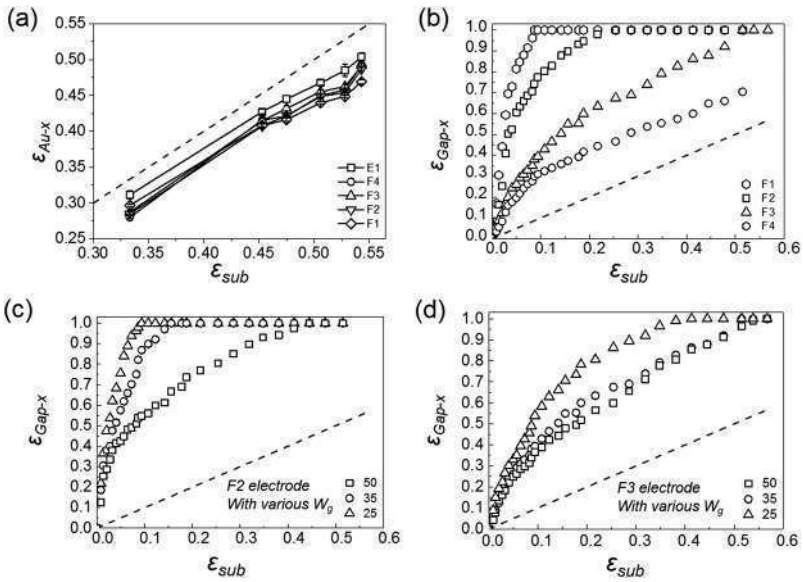

FIG. 3. Local strain change comparisons: (a) Au electrodes strain vs. substrate strain comparing F1 to F4, and contact pads E1. (b) The PDMS gap strain vs. substrate strain comparing between electrodes with varied L_{g0} and L_{f0}. [(c) and (d)] Finger electrode width W_f effect on the PDMS gap strain vs. substrate strain for F2 and F3 electrodes; all dashed lines indicate substrate strain value as a reference.

intact after >10 cycles of repeated compression. For determining the switching strain values that bring Au finger pair electrodes into self-contact, Figs. 3(b)–3(d) show detailed comparative results of the PDMS gap strain $\varepsilon_{Gap\text{-}x}$ versus the substrate strain ε_{sub}. When $\varepsilon_{Gap\text{-}x} = 1$ at $L_g = 0$, it was an indication that the PDMS area in the gap was completely folded into the crease from the top view, as illustrated in Fig. 2(a). The corresponding value of ε_{sub} at this point is close to the switching strain.

Figure 3(b) shows the comparison of results between different finger electrodes (F1 to F4) on the same transducer array where $W_f = 35\ \mu$m, initial L_{f0} ranges from 225 μm to 250 μm, and L_{g0} from 10 μm to 55 μm, respectively. All $\varepsilon_{Gap\text{-}x}$ are far greater than the ε_{sub} (indicated by a dashed line) due to the expected strain amplification effect. It can be observed that for a pair of electrodes F1 with smallest L_{g0}, the self-contact strain is around $\varepsilon_{sub} = 0.08$, which is significantly lower than typical creasing strains of around 50% on plain PDMS surfaces.[5,20] As L_g gradually increased, it required much higher substrate strains to bring F2 and F3 pair electrodes into self-contact, at $\varepsilon_{sub} = 0.2$ and $\varepsilon_{sub} = 0.5$, respectively. For F4 electrodes, it is understandable that the large L_{g0} made it impossible for the pair of electrodes to reach each other before the 0.6 substrate strain limit [Fig. 3(b)], due to insufficient self-contact depth (estimated to be around 19 μm) before reaching the limit. Since the natural wavelength of the crease is ~3.5 times of substrate thickness H ($H = 110\ \mu$m in this case), multiple creases may occur at larger distances, which prevents the electrodes from achieving contacts even at higher strains.

We also compared finger electrode width W_f (25 μm, 35 μm, and 50 μm) effect on gap strain $\varepsilon_{Gap\text{-}x}$, as shown in Figs. 3(c) and 3(d). The initial gap distance L_{g0} for F2 electrodes [Fig. 3(c)] was kept at 15 μm while L_{g0} for F3 [Fig. 3(d)] was kept at 25 μm. The electrode lengths L_{f0} are 250 μm and 245 μm, respectively. It was clearly observed in both cases that electrodes with narrow W_f (25 μm) had much lower ε_{sub} of 0.1 and 0.4, respectively, when the electrode pair made self-contact. This suggests that a wider Au electrode may require more energy to be pulled into the creasing created in the PDMS gap area, since the electrode prefers small wrinkling.

Based on the above deformation study, we demonstrated multi-step or "stepwise" electrical resistance change corresponding to different levels of ε_{sub}. The Everbeing EB8 manual probe station (with EB-05 probes) which connected to a Keithley® 4200 analyzer (I-V mode, −1 V to +1 V sweep, with 0.2 V/step) was used to characterize the resistance value change. As shown in Fig. 4, the step-wise strain-resistance sensing has been achieved by surface elastic instability induced multi-finger electrodes with different distances between the electrodes. For the designed L_g values ($L_f = 510\ \mu$m and 520 μm, respectively), the estimated finger electrode resistance would be in the region of 50 Ω. When the first pair of electrodes was in contact, the calculated resistance would be ~100 Ω, assuming that the contact resistance is zero. This will be reduced to 50 Ω when the second switching was achieved. Figure 4(b) shows greater details of the two-step switching resistance-strain relationship. Between 0.45 and 0.52, the first step switching stage was achieved, with a resistance of ~120 Ω. Under further compression, the second step switching stage occurred at the substrate strain range of $0.54 < \varepsilon_{sub} < 0.58$ by measuring the resistance to be ~50 Ω. Note that the error bars indicate multiple measurements at different current

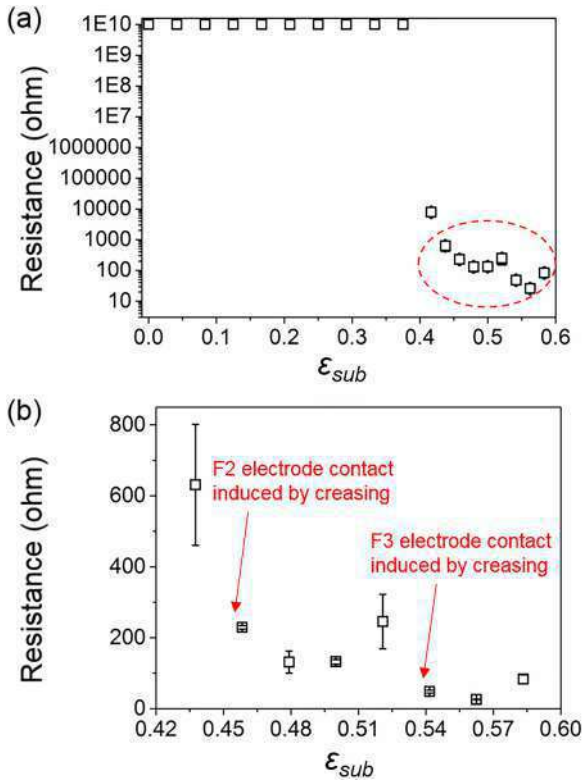

FIG. 4. (a) Resistance of the test structure as a function of strain. The resistance change during the two-stage switching is highlighted in a red ring and detailed in (b). Two-stage resistance switching strain sensing: Resistance of the transducer array as a function of strain during the two-stage switching period ($0.45 < \varepsilon < 0.52$ and $0.54 < \varepsilon < 0.6$) (b).

levels that in most cases indicate that Joule heating is not influencing the measurement. The probe-Au electrode contact resistance was characterized to be ~7.9 Ω with a standard deviation of 1.17. The variation of the experimental resistance values may be mainly caused by the contact resistance between the touching Au finger electrodes. The corresponding substrate strains at switching were also in good agreement with the electrode deformation observations.

In conclusion, a new strategy has been established to detect the multiple strain values on a soft elastic substrate to study the metal-elastomer deformation behavior of a super-compressible strain transducer array. We have characterized the relationship between electrode geometries and compression strain ratios, together with the growth and co-existence of wrinkles and creases on multi-switching electrodes. Multi-steps of electrical resistances were generated at different switching strains on an individual device. This has been demonstrated by using the multiple finger electrode soft electronics with different distances between the electrodes, which has potential for future stretchable/epidermal electronics, flexible sensors, health monitoring, and wearable device applications.

This supplementary material contains the experimental and fabrication method, as well as the additional results to support the results and claims in the main context.

This work was supported by EPSRC (Grant Nos. EP/N007921/1 and EP/L026899/1) and the Royal Society (Grant No. RG150662). The authors would like to thank Everbeing who donated the probing system used in this work, and MEMSstar, Ltd., for providing the SAM coating facility. Data associated with this paper are available via Northumbria Research Data Management scheme.

REFERENCES

[1]D.-H. Kim, N. Lu, R. Ma, Y.-S. Kim, R.-H. Kim, S. Wang, J. Wu, S. M. Won, H. Tao, A. Islam, K. J. Yu, T.-I. Kim, R. Chowdhury, M. Ying, L. Xu, M. Li, H.-J. Chung, H. Keum, M. McCormick, P. Liu, Y.-W. Zhang, F. G. Omenetto, Y. Huang, T. Coleman, and J. A. Rogers, Science **333**, 838–843 (2011).
[2]W. Wu, X. Wen, and Z. L. Wang, Science **340**, 952 (2013).
[3]W. Gao, S. Emaminejad, H. Y. Nyein, S. Challa, K. Chen, A. Peck, H. M. Fahad, H. Ota, H. Shiraki, D. Kiriya, D.-H. Lien, G. A. Brooks, R. W. Davis, and A. Javey, Nature **529**, 509 (2016).
[4]S. R. Madhvapathy, Y. Ma, M. Patel, S. Krishnan, C. Wei, Y. Li, S. Xu, X. Feng, Y. Huang, and J. A. Rogers, Adv. Funct. Mater. **28**, 1802083 (2018).
[5]B. Xu, D. Chen, and R. C. Hayward, Adv. Mater. **26**, 4381–4385 (2014).
[6]D.-Y. Khang, J. A. Rogers, and H. H. Lee, Adv. Funct. Mater. **18**, 1526–1536 (2008).
[7]T. Pan, M. Pharr, Y. Ma, R. Ning, Z. Yan, R. Xu, X. Feng, Y. Huang, and J. A. Rogers, Adv. Funct. Mater. **27**, 1702589 (2017).
[8]C. Wang, B. B. Xu, J. G. Terry, S. Smith, A. J. Walton, and Y. Li, in *Proceedings of the 30th International Conference on Microelectronic Test Structures, Grenoble, France* (IEEE, 2017), pp. 150–155.
[9]C. Wang, B. B. Xu, J. G. Terry, S. Smith, A. J. Walton, and Y. Li, in *1st IEEE International Flexible Electronics Technology Conference, Ottawa, Canada* (IEEE, 2018).
[10]Y. Chu, X. Wu, J. Lu, D. Liu, J. Du, G. Zhang, and J. Huang, Adv. Sci. **3**, 1500435 (2016).
[11]D. Chen, L. Jin, Z. Suo, and R. C. Hayward, Mater. Horiz. **1**, 207 (2014).
[12]C. Wang, C. Wang, Z. Huang, and S. Xu, Adv. Mater. **30**, 1801368 (2018).
[13]X. Xue, S. Wang, C. Zeng, L. Li, and C. Li, Surf. Interface Anal. **50**, 180–187 (2018).
[14]K. E. Crawford, Y. Ma, S. Krishnan, C. Wei, D. Capua, Y. Xue, S. Xu, Z. Xie, S. M. Won, L. Tian, C. Webb, Y. Li, X. Feng, Y. Huang, and J. A. Rogers, Extreme Mech. Lett. **22**, 27–35 (2018).
[15]Y.-C. Chen and A. J. Crosby, Adv. Mater. **26**, 5626–5631 (2014).
[16]C. F. Guo, Q. Liu, G. Wang, Y. Wang, Z. Shi, Z. Suo, C.-W. Chu, and Z. Ren, Proc. Natl. Acad. Sci. U. S. A. **112**, 12332 (2015).
[17]X. Guo, X. Wang, D. Ou, J. Ye, W. Pang, Y. Hung, J. A. Rogers, and Y. Zhang, npj Flexible Electron. **14**, 14 (2018).
[18]A. Auguste, L. Jin, Z. Suo, and R. C. Hayward, Extreme Mech. Lett. **11**, 30–36 (2017).
[19]D. Wang, N. Cheewaruangroj, Y. Li, G. Mchale, Y. Jiang, D. Wood, J. S. Biggins, and B. B. Xu, Adv. Funct. Mater. **28**, 1704228 (2018).
[20]D. Chen, S. Cai, Z. Suo, and R. C. Hayward, Phys. Rev. Lett. **109**, 038001 (2012).
[21]T. Ouchi, J. Yang, Z. Suo, and R. C. Hayward, ACS Appl. Mater. Interfaces **10**, 23406–23413 (2018).
[22]K. Nan, H. Luan, Z. Yan, X. Ning, Y. Wang, A. Wang, J. Wang, M. Han, M. Chang, K. Li, Y. Zhang, W. Huang, Y. Xue, Y. Huang, Y. Zhang, and J. A. Rogers, Adv. Funct. Mater. **27**, 1604281 (2017).
[23]G. Lee, T. Lee, Y. W. Choi, P. V. Pikhitsa, S. J. Park, S. M. Kim, D. Kang, and M. Choi, J. Mater. Chem. C **5**, 10920 (2017).
[24]D. Rhee, W.-K. Lee, and T. Odom, Angew. Chem., Int. Ed. **56**, 6523 (2017).
[25]H. Lu, Y. Liu, B. Xu, D. Hui, and Y. Fu, Composites, Part B **122**, 9 (2017).
[26]B. Xu and R. Hayward, Adv. Mater. **25**, 5555 (2013).
[27]J. Kim, J. Yoon, and R. Hayward, Nat. Mater. **9**, 159 (2010).
[28]S. Cai, D. Chen, Z. Suo, and R. Hayward, Soft Matter **8**, 1301 (2012).
[29]B. Xu, Q. Liu, Z. Suo, and R. Hayward, Adv. Funct. Mater. **26**, 3218 (2016).

SUPPLEMENTARY MATERIAL

Fabrication process – dual-SAMS assisted metal transfer process from silicon to PDMS-VPS:

Dual SAMS preparation of patterned Au on silicon: The gold layer was patterned with a lift-off process on the silicon substrates. Firstly, MEGAPOSIT™ SPR™ 220-7 positive photoresist was spin coated on silicon wafers. The photoresist then patterned through photolithography process (Karl-Suss™ MA8 mark aligner). An anti-stiction SAM layer Perfluoro-decyl-trichloro- silane (FDTS) was then deposited using a MemsStar AURIX™ system. Au layers with thicknesses ranging between ~16nm and ~100nm were then deposited on top of FDTS treated patterned photoresist via sputtering. The lift-off process was performed by soaking the sample in acetone solvent before cleaning with isopropyl alcohol (IPA) and absolute ethanol. The patterned Au electrodes on FDTS-silicon were then treated with MPTMS (3-Mercaptopropyl-trimethoxysilane) as an SAM adhesive, by soaking in 25mM MPTMS in absolute ethanol solution for 3 hours. The sample was then washed in absolute ethanol before N2 drying and ready for Au transfer process (Fig. S1a).

Pre-stretched PDMS-VPS bilayer fabrication: The PDMS-VPS bi-layer elastomer, consists of a strip of thick and stiff mounting layer (3 mm thick, 9 mm wide and 30 mm long) made of Vinylpolysiloxane (VPS) (mixing ratio base with catalyst of 1:1), which was prefabricated before being fixed in a mechanical vice and pre-stretched from 5mm to 30mm length, a softer unstressed thin PDMS film layer (Sylgard™ 184, ~110 μm thick, 30:1 for elastomer base and cross-linker, Young's Modulus of 0.12 ± 0.02 MPa) was attached on the VPS stiff layer under tensile stress (due to its pre-stretching).

Au transfer and substrate compression: The Au-on-Silicon sample with MPTMS-SAM adhesive was then flipped and pressed against PDMS surface of the pre-stretched PDMS-VPS substrate for 10 minutes, before being peeled off to complete the Au PDMS-VPS transducer device fabrication (Fig. 1a and S1b). The completed device was then compressed in a controlled manner via releasing the pre-stretched VPS mounting layer by slowly turning the screw thread (pitch = ~ 1.25mm/turn) of the mechanical vice.

Poisson effect caused damage and improved interconnects design:

During the substrate compression process from 0 to 0.6 strain, it is inevitable that tensile transverse strains (y-direction in Fig. 1) perpendicular to the compression direction with $G=E/2(1+v)$ are generated by the uniaxial compressive strain change due to the Poisson's effect (where G is shear modulus, E represents Young's modulus and v is the Poisson's ratio). This non-uniform strain distribution causes the unwanted damage to some interconnection part of the transducers when substrate strain went above 0.25, as shown in Fig. S2a. In order to prevent such damage, serpentine shaped Au interconnects have been designed

to "bridge" connect finger electrodes "islands" across the serpentine spacing W_g in some devices (Fig. 1). Fig S2b shows the effect of y stretching onto the gap serpentine as substrate strain increases. It successfully prevented cracking damage for substrate strains up until 0.35 (Fig. S2b). The interconnecting areas of finger electrodes F1 and F4 started to sustain certain degrees of damage beyond 0.35, while F2 and F3 remained intact upto 0.6 substrate strain. Future work will focus on optimizing the interconnect designs for better protection.

AFM profile of Au wrinkling at various substrate strains:

Figure S3a has shown the cross-section wrinkling profile of the Au finger electrodes sustaining various substrate strains. The cross-section line was taken from the 3D profile shown in Fig 2c and S3b. At a substrate strain of 0.12, the wrinkling wavelength can be calculated as 18 μm, agreeing with the theoretical calculation described in the main paper.

Magnified Images showing before and after the Au contact caused by creasing:

Figure S4 shows sequential microscopic images showing the Au finger electrodes (bright area) and the PDMS gap, before and after the contact caused by creasing. The substrate strains change from 0.38 (Fig. S4 - image 1) to 0.52 (contact point, image 5), 0.55 (image 6).

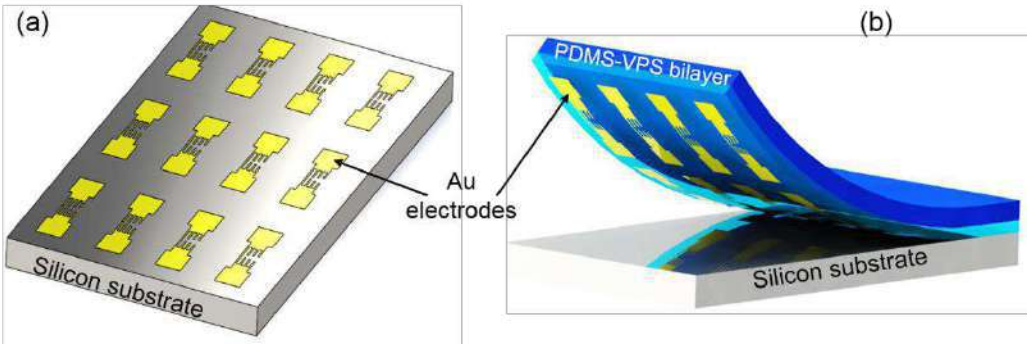

FIG. S1. Schematic images illustrating the dual SAM Au transfer process: (a) Lift-off + lithographically patterned multi-switching Au strain transducer array on silicon substrate ready for transfer. (b) Au patterns transferred from silicon to PDMS-VPS substrate by dual-SAM (self-assembly monolayer) assisted metal transfer process.

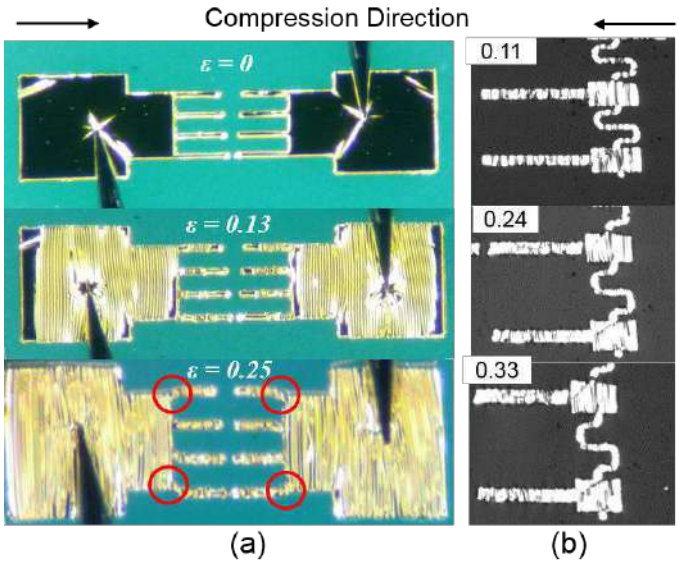

FIG. S2. (a) Consecutive microscopic images at various substrate strains on bulk interconnect electrode devices with probing needles (dark colored) in the view. Circled areas started showing interconnecting areas of F1 and F4 finger electrodes being stretched due to Poisson effect; (b) Consecutive microscopic images showing serpentine shaped structure significantly reduced interconnects stretching from Poisson effect upto 35% substrate compression. (Scale bars = 200 μm)

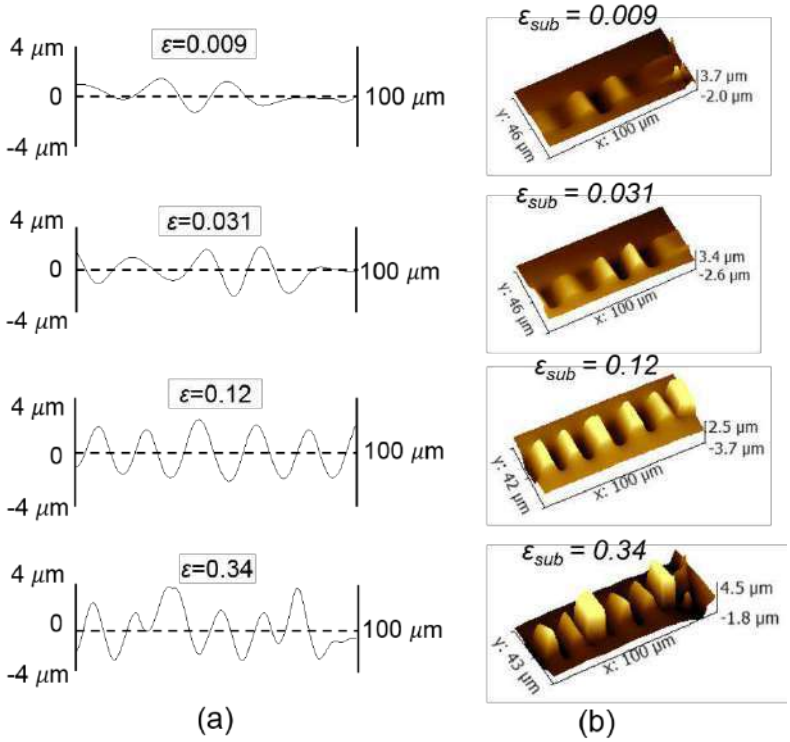

FIG. S3. (a) Cross-section wrinkling profiles for the Au finger electrodes sustaining various substrate strains. These cross-section line was taken from (b) the 3D profile measured by the Bruker™ AFM system.

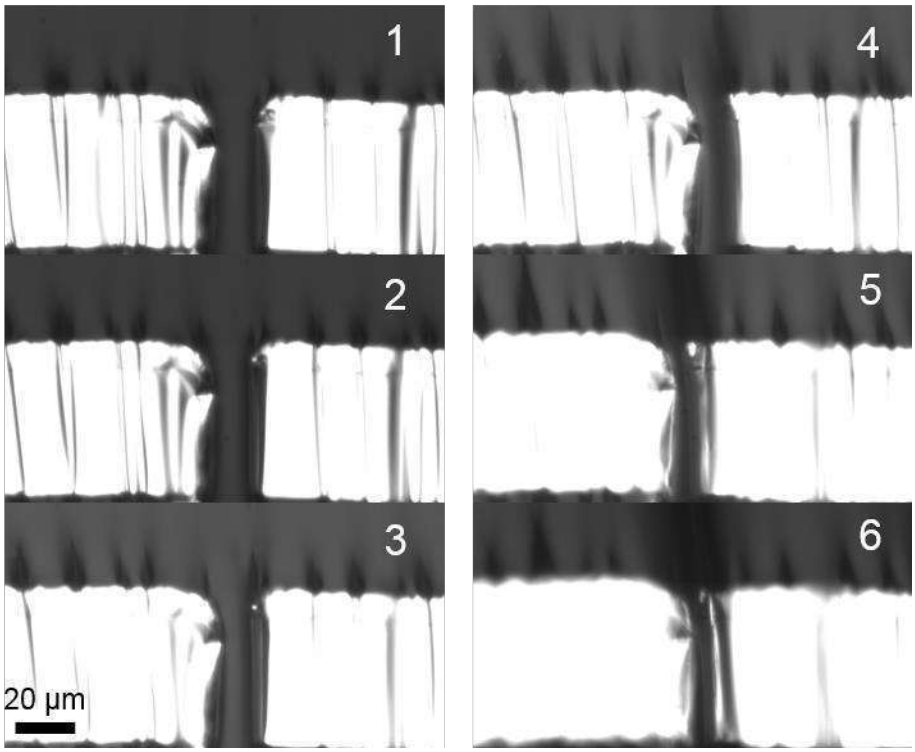

FIG. S4. Sequential microscopic images showing the Au finger electrodes (bright area) and the PDMS gap, before and after the contact caused by creasing. The substrate strains change from 0.38 (image 1) to 0.52 (contact point, image 5), 0.55 (image 6).

ADVANCED 3D MORPHING TRANSDUCERS BY SMART HYDROGEL PATTERNING

Cong Wang[1], Sreepathy Sridhar[1], Jonathan G. Terry[2], Ansu Sun[1], Zhenghong Li[3], Haibao Lv[3], Ben B. Xu[1] and Yifan Li[1]

[1]Mechanical and Construction Engineering, Faculty of Engineering and Environment, Northumbria University, Newcastle upon Tyne, NE1 8ST, UK

[2]SMC, Institute for Integrated Micro and Nano Systems, School of Engineering, University of Edinburgh, Edinburgh, EH9 3JF, UK

[3]Science and Technology on Advanced Composites in Special Environments Laboratory, Harbin Institute of Technology, Harbin, 150080, P.R. CHINA

ABSTRACT

This paper demonstrates a unique way of creating heterogeneous layered structures of soft functional materials for advanced transducer applications. Hydrogel droplets with different composites were patterned by a "two-parallel plate" configuration used in microfluidics applications. Resulted heterogeneous layered structures of hydrogel were created, generating reconfigurable 3D (3-dimensional) deformation responding to discrete levels of stimulation inputs.

KEYWORDS

Heterogeneous hydrogel, droplet microfluidics, responsive swelling, flexible sensors, surface wettability

INTRODUCTION

Morphing soft materials responding to external stimulation (e.g. electrical, mechanical and chemical) have promising applications in various fields, such as flexible electronics, biomedical transducers and soft robotics. One of the desirable developments is to make the self-shaping process controllable and programmable, at least for specific configurations.

Wang et al. [1] has demonstrated 3D shape control through planar (flat) patterned, homogeneous swell-able hydrogels. "Pre-designed" complex deformations were demonstrated by the periodically patterned hydrogel blocks made from multi-step lithographically. The shape morphing was then generated due to elastic mismatch between non-swelling substrate and swelling gel blocks [1, 2]. Holed "swelling masks" were employed to control the swelling directions, in order to re-configure the deformation patterns [1].

Whilst patterned homogenous layered structures can provide "pre-designed" 3D shapes, the post-swelling configurations are fixed in [1, 2]. For reconfigurable morphing structures which dynamically change shapes responding to stimulation, heterogenous structures are desired.

Uniform heterogenous bio-content deposition was achieved previously by droplet microfluidics utilizing surface wettability (hydrophobic/philic patterns) [3]. More recently, using droplet microfluidics to control the formation of encoded multifunctional, and heterogeneous hydrogel building blocks have been exploited to form complex hydrogel architectures, inspired by natural bio-structures [4, 5].

In such cases [1, 4], two parallel plates with millimeter to sub-millimeter gap in-between (similar to a Hele-Shaw Cell) were introduced to help achieve a uniformly thin deposited layer.

Combining the latest development in smart hydrogel patterning, and the hydrogel-based 3D morphing technology brings the great potential of next generation re-configurable, stimuli-responsive, morphing soft transducers.

METHODOLOGY

The state of the art of this work are demonstrated from the following two aspects:

• Heterogeneous hydrogel blocks patterned and layered by controlled surface wetting at hydrophobic and hydrophilic boundaries (figure 1). The layer thickness and uniformity are ensured and controlled by droplet volume and the gap between the two parallel plates shown in figure 1.

• Reconfigurable 3D morphing response to the stimulation inputs such as changing ionic concentration and temperature of the solution this hydrogel structure is immersed in.

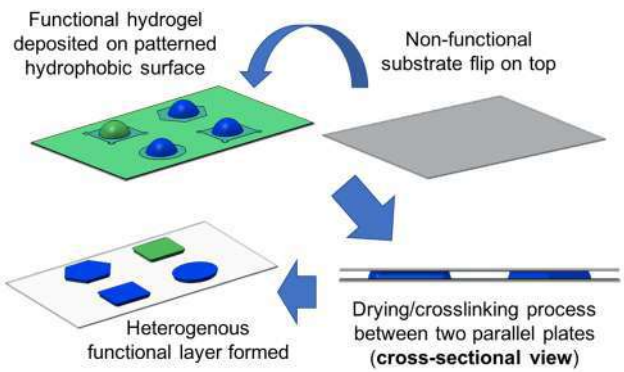

Figure 1: Schematic view of the heterogenous hydrogel structure patterned by hydrophobic/philic surface.

The hydrogel used are Poly(Acrylamide-Sodium Acrylate), created from poly-acrylamide (PAAm) network with Sodium Acrylate (SA) which contains free positive sodium ions. N,N'-Methylenebisacrylamide (BisAA or MBAA) was used as a cross linker, with N,N,N′,N′-Tetramethylethylenediamine (TEMED) and Ammonium Persulfate (APS) used as initiators for the polymerization process.

The gel swelling will happen when immersed in PBS (phosphate buffered saline) solution depending on ionic concentration of the gel and the solution. Other stimulation such as temperature, electrical potential and physical constrains will all affect the swelling behaviour.

To structure and shape the hydrogel, hydrophobic/hydrophilic patterns were created. Fig. 2 (top left) shows patterned Parylene-C^{TM} hydrophobic area (light green color) and hydrophilic silicon dioxide (SiO_2) patterns (dark green colored & square shaped), both on smooth silicon substrate.

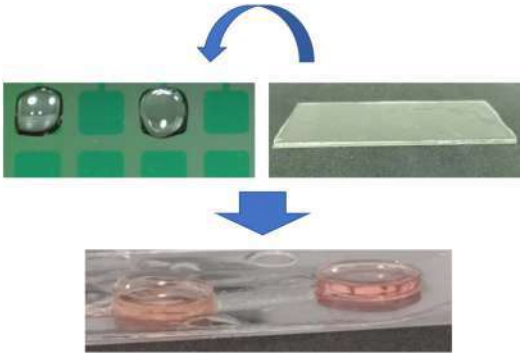

Figure 2: Photos showing two hydrogel blocks with different swelling behavior (different composites) assembled to non-swelling gel substrate.

Functional (swell-able) hydrogel droplets/blocks were deposited on this Parylene-SiO_2 surface, shape-controlled by hydrophobic/philic boundaries, and squeezed into "button" shape by non-functional soft substrate (e.g. non-swelling gel) before cross-linked to form the desired heterogeneous structure (illustrated in Fig. 1 and pictured in Fig. 2).

EXPERIMENTAL RESULTS

Swelling and de-swelling demonstration

The swelling ratio and de-swelling ratio dynamically responding to PBS concentration and SA composition were obtained. Figure 3a to 3h demonstrate how the swelling kinetics is recorded, by showing a dried cylinder-shaped gel swelling for 10 minutes in 0.01M PBS solution. The height of the swelling hydrogel was controlled by a cover slip, and the diameter was measured for swelling and de-swelling ratio calculation. This work currently focuses on ionic concentration related response, however near future work will also investigate temperature response (illustrated in figure 3i).

Single configuration demonstration

Single configuration 3D surface shape control has been demonstrated by selectively swell and de-swell the heterogenous functional hydrogel blocks with different composites/stimuli-responsive properties which are assembled on the same substrate as shown previously in figure 2.

In this experiment, the pink colored hydrogel block (figure 4) swelled in the 0.1M PBS solution, causing localized surface raising. The red colored hydrogel block de-swelled in the same solution, causing localized surface concaving. When the substrate was detached from the bottom of the solution container, a complex surface with raised (pink area) and concaved (red area) surface was achieved (shown in figure 4).

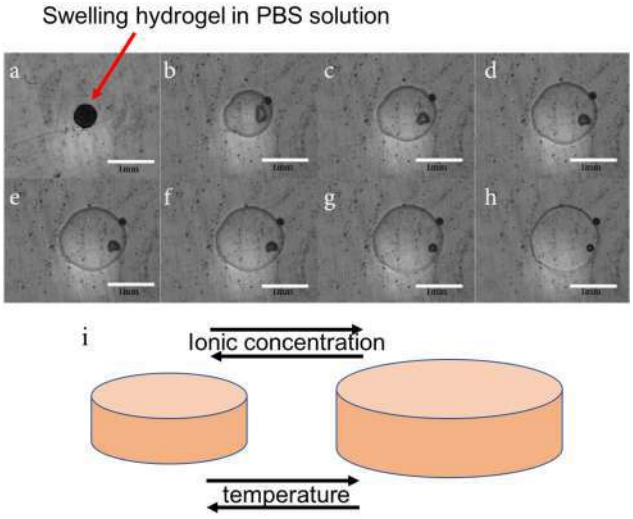

Figure 3: Microscopic photo shows PAAm-SA hydrogel swelling from (a) 0 min to (h) 10 minutes in 0.01M PBS solution. (i) The swelling hydrogel responds to ionic concentration variation and other stimulation such as temperature. Scale bar indicates 1mm.

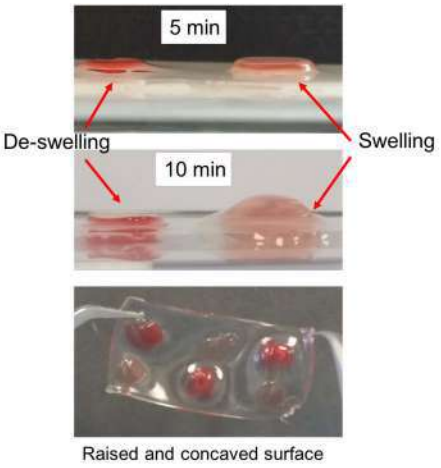

Figure 4: Photos showing hydrogel blocks with different composites swelling and deswelling over time in 0.1M PBS, causing localized surface raising and concaving deformations.

Re-configuration demonstration

Due to the heterogenous nature of the functional hydrogel layer, the swelling vs. de-swelling spatial configuration can change responding to the external stimulation. By changing the ion concentration of the PBS solution, initial reconfigurable gel deformation was achieved (flat shape – "S" shape – "C" shape).

This responsive shape morphing demonstration was shown in Fig. 5. When immersed in 0.1M PBS solution, the gel started bending. When the PBS concentrations changed

(0.1M to 0.01M), the hydrogel structure reshaped from "S" shape to "C" shape. This is a combined result from:

• Hydrogel block-B (pink colored) changes from de-swelling to swelling state, responding to the PBS concentration decrease;

• Hydrogel block-A (red colored) maintains high ratio swelling.

Such reconfigurable response shed a light on the great potential of sensing and actuation applications with complex 3D morphing materials [6 - 8]. It is foreseeable, that more advanced functions can be achieved with additional hydrogel functional blocks – to be carried out during our on-going research work.

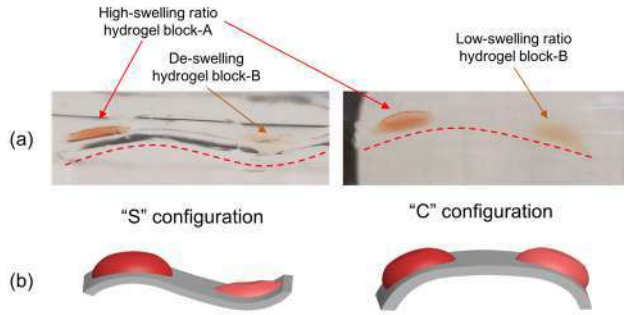

Figure 5: (a) microscopic photos; and (b) schematic illustration showing hydrogel structure shape reconfiguration from "S" shape to "C" shape.

ACKNOWLEDGEMENTS

This work was supported by EPSRC UK Fluid Network (Grant No. EP/N032861/1, https://fluids.ac.uk/). The authors would also like to acknowledge other support from the EPSRC (Grant Nos. EP/N007921/1 and EP/L026899/1) and the Royal Society (Grant No. RG150662). Data associated with this paper are available via Northumbria Research Data Management scheme.

REFERENCES

[1] Z. Wang et al., "Site-Specific Pre-Swelling Directed Morphing Structures of Patterned Hydrogels", *Angew. Chem. Int. Ed.*, vol. 56, pp. 15974 – 15978, 2017.

[2] Z. Wang et al., "Cooperative deformations of periodically patterned hydrogels", *Science Advances*, vol. 3, e1700348, 2017.

[3] Y. Li et al., "The application of fixed hydrophobic patterns for confinement of aqueous solutions in proteomic microarrays", *Appl. Phys. Lett.,* vol. 99, pp. 073703, 2011

[4] M-Y. Chiang et al., "Constructing 3D heterogeneous hydrogels from electrically manipulated prepolymer droplets and crosslinked microgels", *Science Advances,* vol. 2, e1600964, 2016

[5] X. Ji et al., "Encoding, reading, and transforming information using multi-fluorescent supramolecular polymeric hydrogels", *Advanced Materials,* vol. 30, 1705480, 2018

[6] X. Du et al., "Inside-Out 3D Reversible Ion-Triggered Shape-Morphing Hydrogels", *AAAS Research,* vol. 2019, Article ID 6398296, 2019

[7] S. Y. Zheng et al., "Programmed Deformations of 3D□Printed Tough Physical Hydrogels with High Response Speed and Large Output Force", *Advanced Functional Materials,* vol. 28, 1803366, 2018

[8] X. Zhou et al., "Shape morphing of anisotropy-encoded tough hydrogels enabled by asymmetrically-induced swelling and site-specific mechanical strengthening", *Journal of Materials Chemistry B,* vol. 6, pp. 4731-4737, 2018

CONTACT

*Dr. Yifan Li, Tel: +44-191-349-5936; yifan.li@northumbria.ac.uk

Metal-Elastomer Surface Deformation Control on Super-Compressible Strain Transducer Arrays

Cong Wang
Faculty of Eng. Environ.
Northumbria University
Newcastle upon Tyne, UK
cong.wang@northumbria.ac.uk

Ben Bin Xu
Faculty of Eng. Environ.
Northumbria University
Newcastle upon Tyne, UK
ben.xu@northumbria.ac.uk

Jonathan G. Terry
School of Engineering
The University of Edinburgh
Edinburgh, UK
jon.terry@ed.ac.uk

Stewart Smith
School of Engineering
The University of Edinburgh
Edinburgh, UK
stewart.smith@ed.ac.uk

Anthony J. Walton
School of Engineering
The University of Edinburgh
Edinburgh, UK
anthony.walton@ed.ac.uk

Yifan Li
Faculty of Eng. Environ
Northumbria University
Newcastle upon Tyne, UK
yifan.li@northumbria.ac.uk

***Abstract*— This paper reports the metal-elastomer surface deformation control strategy of a strain transducer array capable of measuring compressive strains up to 60%. Pairs of multi-finger electrodes separated by different inter-digit gap distances are forced into contact by induced surface creasing deformation at different strains. Test structures have been developed to explore and optimize the electrode-elastomer hybrid surface deformation. The deformation is due to large compressive strains in the "x-direction" but stretching caused by the Poisson effect can also take place in the "y-direction".**

Keywords—elastomer, elastic instability, wrinkle, crease, strain sensing, test structure, stretchable electronics

I. Introduction and Methodology

A. Introduction

In the growing field of flexible electronics, devices are subjected to stretching, bending and twisting forces [1-7]. Elastomer substrates can also be compressed, during which surface elastic instabilities will occur, such as wrinkles and creases, which provide potential opportunities in engineering applications [3,7-10].

Initial studies on super-compressible strain gated switches and their applications, have reported a surface creasing induced resistance change in response to mechanical inputs of up to 60% strain [3, 7]. The energy absorbing elastic instabilities (wrinkles and creases) on metal-elastomer surfaces helped to prevent metal electrode damage while providing the sensing mechanism. However, due to the large Poisson's ratio of the elastomer substrates (close to 50%), the electrodes are also stretched along the y-direction (Fig. 1a), causing unwanted damage.

To understand how to design the metal finger electrode array and interconnects, such that they can survive both large compression as well as stretching caused by Possion's effect, requires investigation to determine how Au-PDMS (polydimethyl-silosane) surfaces deform.

B. Methodology

In situations where Au electrodes cover an area of the PDMS, an "island-bridge" type of flexible device results. The much stiffer Au (Young's Modulus 50-70 GPa) tends to deform less than the underlying PDMS (0.4 - 4 MPa) when both are subjected to the same substrate compression strain. This has caused creases to be generated on some PDMS surfaces "squeezed" between Au electrodes at a substrate strain < 10%, which is significantly lower than typical creasing strains of around 50% on a plain PDMS surface.

To investigate, Au finger electrode test structures (Fig. 1a) with different thicknesses (16nm - 100nm) were fabricated by patterning electrodes on a silicon carrier wafer, and subsequently transferring them onto PDMS surfaces, supported on pre-stretched VPS (Vinyl-polysiloxane) elastomer substrates (Fig. 1b). Transfer was achieved using a self-assembly thiol based dry-peel-off soft lithography method optimised after [3, 7].

Figure 1c shows the schematics of Au-PDMS surface deformation process under substrate compression. The creasing on PDMS elastomer surface results in Au finger electrode tips coming into contact (resistance step change [3, 7]), with wrinkles on the Au helping to absorb the deformation energy. The 2D geometry deformation (measured while viewing from above) can be measured as a change in either:

- Au finger electrode length L_f and width W_f (fig. 1a)
- or, PDMS surface length between opposite Au finger electrode tips L_g, and the adjacent finger spacing, W_g (fig. 1a)

To investigate the parameter space, a range of finger electrode array devices were fabricated and tested in parallel. Finger length was varied from the longest at 525 µm (F4 in figure 1a) to the shortest at 240 µm (F1), with L_g ranging between 5 and 100 µm, and W_g from 100 to 200 µm.

978-1-5386-3357-1/18/$31.00 ©2018 IEEE

In an attempt to prevent Poisson's effect related damage, serpentine shaped Au interconnects have been designed to "bridge" connect finger electrodes "islands" across the PDMS spacing W_g in some devices, as shown in Fig 1c inset.

II. Experiments and Results Summary

A. Au-PDMS 2D geometry change under compression

By applying substrate compression through releasing pre-stretched VPS mounting layer [7], differences have been observed in the deformation strain of both the Au finger electrode and PDMS along x ($\varepsilon_{Au\text{-}x}$, $\varepsilon_{PDMS\text{-}x}$), and y-direction ($\varepsilon_{Au\text{-}y}$, $\varepsilon_{PDMS\text{-}y}$), where:

$$\varepsilon_{Au\text{-}x}=(L_{f0} - L_f)/L_{f0} \quad (1)\ ;\ \varepsilon_{Au\text{-}y}=(W_{f0} - W_f)/W_{f0} \quad (2);$$

$$\varepsilon_{PDMS\text{-}x}=(L_{g0} - L_g)/L_{g0} \quad (3);\ \varepsilon_{PDMS\text{-}y}=(W_{g0} - W_g)/W_{g0} \quad (4);$$

The 2D geometry dimension changes have been observed and measured by both Nikon LV100 optical system and Atomic Force Microscope (Fig. 2) at different substrate strains. Fig. 3 shows selected results of PDMS deformation in the gap (L_g) between two finger electrodes $\varepsilon_{PDMS\text{-}x}$, which are consistently >> substrate strain (dashed line). The electrode gap strain of 1.0 in these plots indicates the contact of two Au finger tips brought by the formation of surface creases.

B. 3D geometry deformation under compression

The 3D profile of the electrode deformation was primarily measured by AFM (Fig. 2 and 4, Bruker™ 3100). Fig. 4 shows the 3D geometry of the progressive wrinkling of an Au electrode characterised from substrate strain. The wrinkling instability is seen to begin at a substrate strain of 0.009, whereas the theoretical value for Au on PDMS is calculated to be 6.7×10^{-4}. This discrepancy is not a surprise, as 2D geometry observations confirm that Au deformation lags significantly behind that of the substrate.

C. Poisson's Effect and Result Summary

Figure 5 shows the y-direction stretching which affects the Au electrodes, serpentine interconnects and PDMS areas as a result of the Poisson's effect. The y-direction stretching strain of Au and PDMS are measured to be $\varepsilon_{Au\text{-}y} = 8.7\%$ *and* $\varepsilon_{PDMS\text{-}y} = 37.1\%$, under a substrate compression of *33%* and a Poisson's ratio of *42%* (strain dependant).

III. Conclusions

Test structures have been developed to characterize the metal-elastomer deformation behaviour of a super-compressible strain transducer array under compression up to 60%. This initial study has been focused on the relationship between electrode geometries and compression strain ratios, with the growth and co-existence of wrinkles and creases on multi-switching electrodes being characterised for the first time. Future work will focus on fully characterising the mechano-responsive electrical switching mechanism of the designed sensors.

References

[1] D.-H. Kim, et al., *Science*, 333, pp. 838, 2011.

[2] W. Wu , X. Wen , and Z. L. Wang , *Science*, 340, pp. 9 52, 2013.

[3] B. Xu , et al., *Adv. Materials*, 26, pp. 4381, 2014.

[4] T. Pan, et al., *Adv. Funct. Mater.*, 27, 1702589, 2017.

[5] D. Y. Khang, et al., *Adv. Func. Mater.*, 19, pp. 1526, 2009.

[6] M. S. White, et al., *Nature Photonics*, 7, pp. 811, 2013.

[7] C. Wang, et al., *Proc. IEEE ICMTS*, Grenoble, France, pp 1-5, 2017.

[8] D. Chen, et al., *Phys. Rev. Lett.*, 109, 038001, 2012.

[9] A. Auguste, et al., *Ext. Mech. Lett.*, 11, pp 30-36, 2017.

[10] G. Lee, et al., *J. Mater. Chem. C*, 5, pp.10920-10925, 2017.

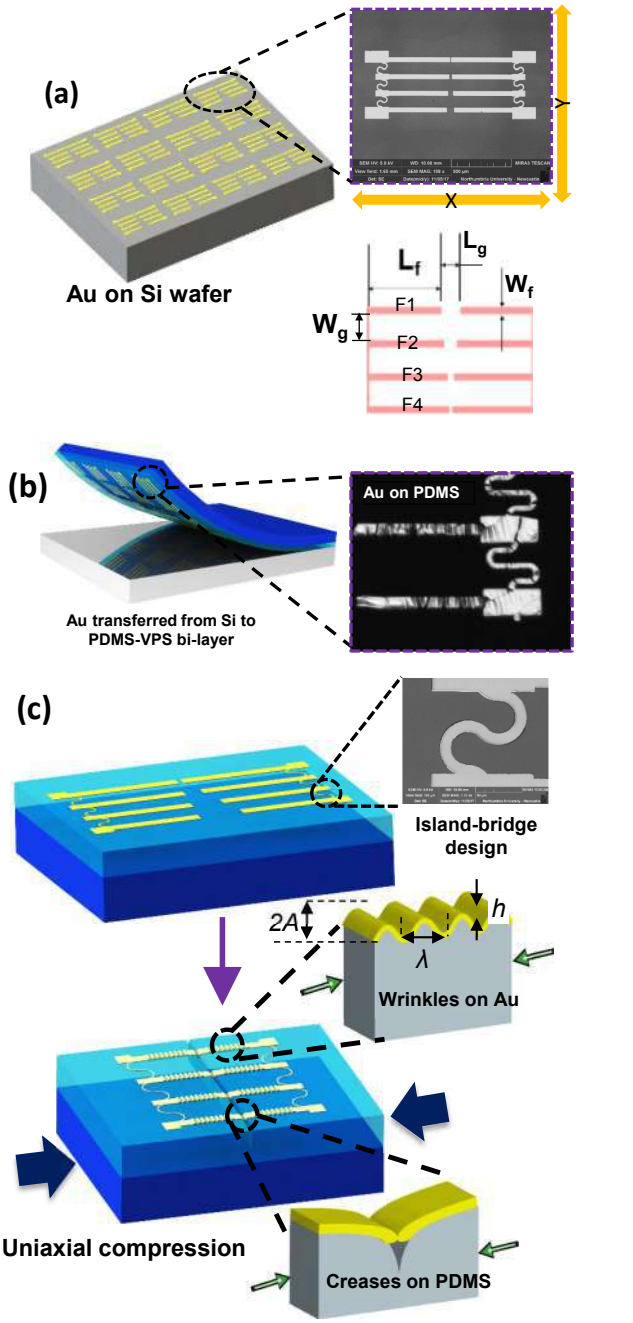

Figure 1. (a) Patterned Au strain transducer test structures on a silicon wafer with a top SEM view and the finger electrode design dimensions (top view); (b) Au transferred to PDMS-VPS bi-layer (inset photo by Nikon microscope) (c) Schematic view of the Au-PDMS 3D deformation process under uniaxial substrate compression.

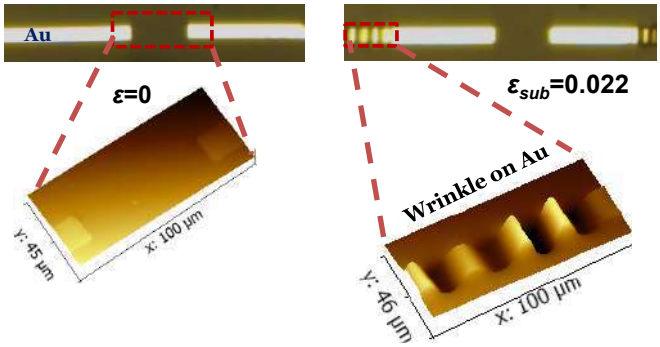

Figure 2. AFM image showing Au 3D deformation initialization under uniaxial substrate compression (0% and 2.2% strains).

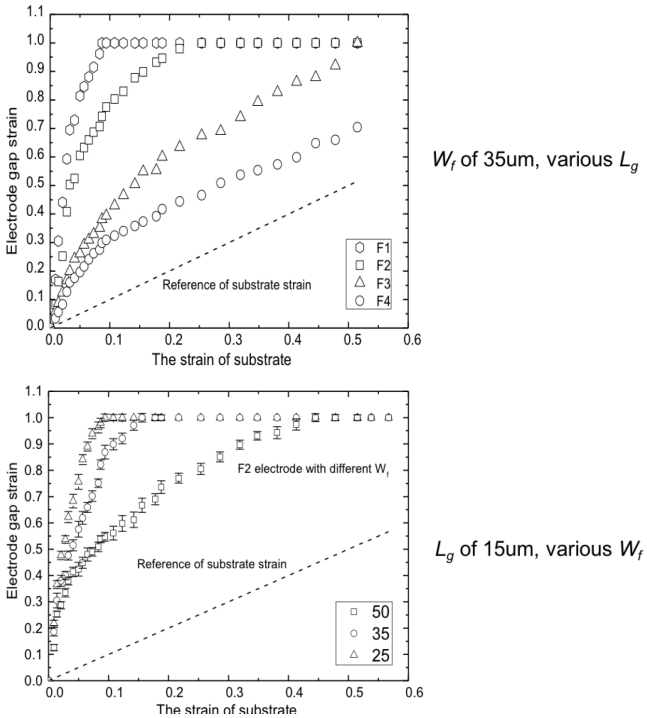

Figure 3. Electrode gap PDMS strain $\varepsilon_{PDMS\text{-}x}$ vs. applied substrate strain (from 0 to 60%) with different Au electrode geometry designs

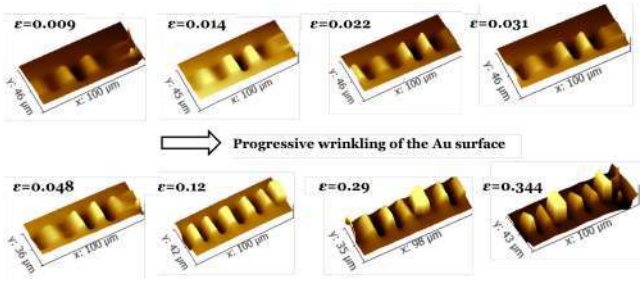

Figure 4. AFM profile of wrinkle development on Au electrode at various substrate strains

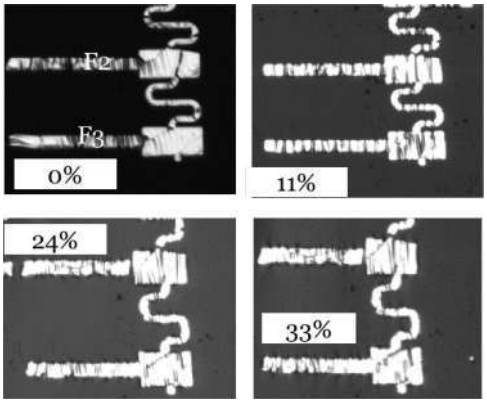

Figure 5. Y-direction stretching (Poisson's Effect) of PDMS and Au under various x-direction compression strains

Elastic Instability Induced Mechano-Responsive Luminescence for Super-Flexible Strain Sensing

Cong Wang, Ding Wang, Valery Kozhevnikov, Ben Bin Xu‡ and Yifan Li*
Smart Materials and Surfaces Lab, Faculty of Engineering and Environment
Northumbria University, Newcastle upon Tyne, UK
* yifan.li@northumbria.ac.uk
‡ ben.xu@northumbria.ac.uk

***Abstract*—This paper reports a novel sensing strategy by employing elastic instability as a key mechanism to achieve super flexible (up to 60%) strain sensing. Inspired by Mechano-Responsive Luminescence (MRL) phenomenon, we have demonstrated this optical strain sensing strategy by employing PDMS based functional luminescence composites multi-thin-layer structure, where fluorescent pattern signal was generated at designed strain values. Line-shaped fluorescent patterns were switched ON and OFF by elastic instabilities (e.g. wrinkling, creasing) on micro-structural soft surfaces during compressive deformation. This has extended the current understanding of large strain sensing where creating electrical connection is challenged by the metal fracture and delamination. The control of switching strain values by micro-structural geometry design has been demonstrated and discussed.**

Keywords — mechano-responsive luminescence, elastic instability, crease, strain sensing, stretchable

I. INTRODUCTION

Bendable and stretchable sensor and actuator technologies based on soft functional materials have become ever popular with emerging applications such as epidermal electronics, artificial skins, and soft robotics [1-4]. Conventional flexible electronics are bendable devices where the substrate has a reduced thicknesses, laminated with metal interconnects to reduce the strain change due to bending. For the emerging stretchable/super-flexible devices [1-4], substrate deformation strain could be much higher than the fracture strains of rigid materials during compressing and stretching. To avoid compromising local features such as metal interconnects and integrated transducers, different strategies have been developed, such as island-bridge and serpentine shaped interconnects [1, 5] and competing growth of elastic instabilities [4, 6].

This paper presents a concept in which large mechanical strain change (up to ~60% or 0.6) is transduced to optical signals switching by elastomeric substrates with micro-engineered materials and structural characteristics. Coupled by fluorescent light, the deforming super-flexible elastomer part of the sensing system is physically separated (Fig. 1) from the fixed rigid detector and signal processing part during operation.

For example, the rigid detection part (Fig. 1) could be integrated to a "close to body" device (e.g. wrist band), while the flexible Mechano-Responsive Luminescence (MRL) part could be mounted to deforming surfaces e.g. a skin patch. Since there is no metal interconnects on the deforming substrate, this development has shown an alternative solution to the challenges faced by stretchable/super-flexible sensor packaging, providing opportunities for future applications in tunable optics and stretchable electronics.

This work is supported by EPSRC (EP/N007921/1, EP/L026899/1), and the royal society (RG150662).

II. BACKGROUND

Optical strain sensors have long been developed, mainly in the form of fibre optics [7], although with a relatively low strain span (typically < 0.004 or 0.4%).

This paper presents an elastomer based super-flexible (up to 0.6) optical-strain signal transformation mechanism, utilizing Mechano-Responsive Luminescence (MRL).

A. Mechano-Responsive Luminescence

The term of MRL is getting more researched in recent years, and used to describe a reversible change in photophysical properties such as luminescence color, intensity, pattern or lifetime by mechanical stimulation e.g. expansion, compression and twisting [8, 9].

Examples can be found, such as using the mechanical force to change the arrangement of luminescent molecular which can lead to the optical switching response [8, 9]. Such properties could potentially be facilitated for sensing applications integrated with optical detection systems, such as photo-diodes, fluorescence microscopes (e.g. laser scanning confocal microscope (LSCM), fluorescence lifetime imaging (FLIM)), fluorescence scanners and devices with image sensors (e.g. mobile phones, sports smart wristbands).

B. Elastic Instability Growth on Bi-layer Elastomers

Elastic instabilities such as surface creases play a crucial role in many natural and engineering systems [4, 10]. Recently, super-flexible strain sensing with step-wise electrical signals has been achieved by utilizing elastic instabilities generated on micro-engineered elastomer bi-layers [4, 6].

Such configuration usually consists of multi-layers of elastomer thin films with different Young's Modulus, e.g. a softer Polydimethylsiloxane (PDMS) layer on top of a spre-stretched Vinylpolysiloxane (VPS) layer with higher modulus [4, 6]. By relaxing the pre-stretched VPS layer from a length of L_0 to a reduced lenghth L, the PDMS top layer is compressed controllably [4, 6]. Hence, the elastic instabilities e.g. surface creases would be created subject to the uniaxial compression strain, given by:

$$\varepsilon = (L_0-L)/L_0 \qquad (1)$$

978-1-5090-1012-7/17/$31.00 ©2017 IEEE

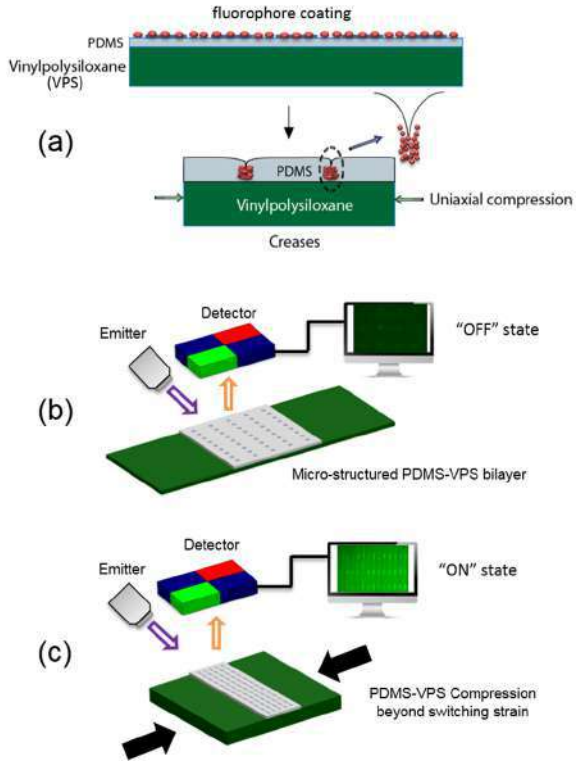

Fig. 1. (a) Cross-section view of the PDMS-VPS bi-layer structure coated with fluorophore (dots). Fluorophore concentration effect can be seen after surface creases generated by uniaxial compression. (b) and (c) The proposed sensing mechanism: optical signal generated by fluorophore-PDMS-VPS is detected by the rigid part of the sensor system giving ON/OFF digital outputs.

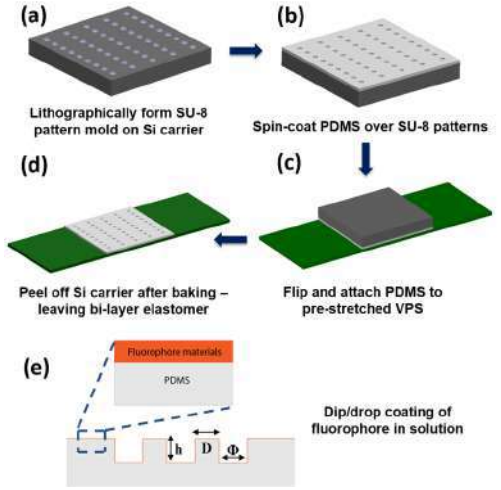

Fig. 2. 3D (a to d) and cross-sectional (e) views of the device fabrication process: (a) lithographically patterned SU-8 on silicon carrier wafer; (b) PDMS spin-coating over SU-8 patterns; (c) flip the silicon carrier and attach PDMS to pre-streched VPS; (d) Peel off silicon/SU-8 after baking, leaving patterned PDMS on VPS; (e) dip/drop coating of fluorophore (fluorescein o-acrylate) on top of plasma treated PDMS surface.

III. Methodology

A. *Surface Creasing Induced MRL for Strain Sensing:*

Fig. 1a shows the set-up of PDMS on pre-stretched VPS bi-layer described in previous section. The fluorophore coating on PDMS surface will be physically concentrated and show high-contrast fluorescence pattern when surface creases generated by uniaxial compression (fig. 1a). And we propose to utilize this surface instability induced MRL effect for strain sensing applications. Fig. 1b and 1c show the proposed optical switch strain sensing mechanism based on MRL:

- **Fabrication:** Micro-structured elastomer bilayer MRL device monitored by fluorescence detector.
- **Surface creasing pattern generation:** Uniaxial compressive generates surface creasing at the surface micro structures (an array of holes in this case)
- **Fluorescent pattern generation:** Surface creasing pattern creates line-shaped fluorescent patterns
- **Signal processing:** The detected signal is then processed, outputting "ON/OFF" status.

B. *Fabrication of Patterned Elastomer Bi-layer*

Fig. 2 shows the fabrication process of patterned elastomer bi-layer by using SU-8/Si dry peel-off soft lithography technology. Different thicknesses of SU-8 photoresist was spin-coated and lithographically patterned on silicon carrier wafer (fig. 2a). PDMS (Sylgard 184™ kit) mixture with 30:1 base to curing agent ratio was then spin-coated over SU-8 patterns (fig. 2b). The PDMS coated silicon carrier was then flipped and attach to pre-streched VPS to form a VPS-PDMS bond (fig. 2c). After baking at 70°C for 8 hours, the silicon/SU-8 carrier mold was peeled off, leaving patterned PDMS on VPS (fig. 2d). After a 30 sec oxygen plasma treatment, the PDMS surface was then coated with fluorescein o-acrylate (Sigma Aldrich®) (fig. 2e).

The patterned PDMS surfaces consist of arrays of circular holes with different diameters Φ, pitches $r = D/\Phi$ and depths h (fig. 2e), by designing SU-8 mold dimensions and thicknesses.

IV. Results and Discussion

A. *Surface Creasing Pattern Generation*

The arrays of circular holes on PDMS surface control surface creasing patterns during uniaxial compression, by concentrating the local energy. Thus, surface creases are expected to form along the column of holes perpendicular to the compression axis.

Fig. 3 shows the surface instability growth on hole patterned PDMS surface, during the uniaxial compression of the pre-stretched VPS. When substrate strain $\varepsilon=0$ (fig. 3a), there is only hole array geometry on the PDMS surface. When the uniaxial compression (fig. 3b, horizontal direction) initiates (e.g., a small $\varepsilon=0.13$), the surface instabilities start to grow at or near the hole patterns. After the compression strain goes beyond a critical point (in this case $\varepsilon=0.515$ *or* 51.5%), large creases perpendicular to the compression axial start to form along the column of holes (fig. 3c).

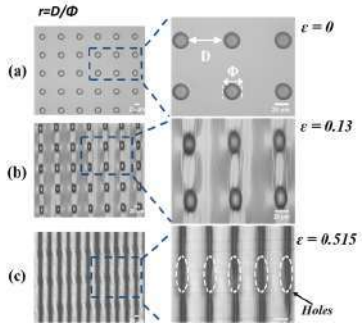

Fig. 3. Microscopic view of hole-patterned PDMS surface during uniaxial compression (horizontal direction), with D=20μm, r=3 and h=13μm at different strains: (a) ε=0; (b) ε=0.13; (c) ε=0.515.

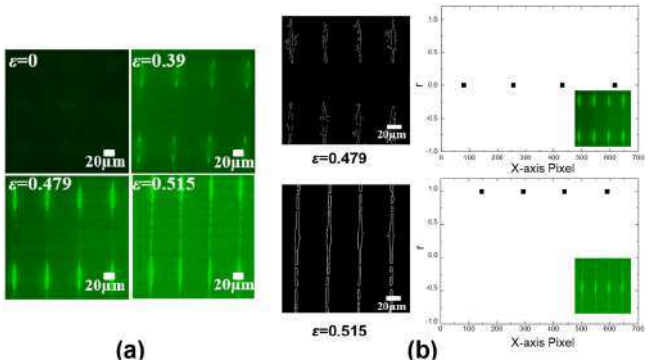

Fig. 4. (a) Fluorescent patterns on patterned PDMS surface under uniaxial compression at different strain values. (b) Fluoresecence image signal processing to determine whether line pattern is formed: (left) Canny edge detection; (right) Hough conversion.

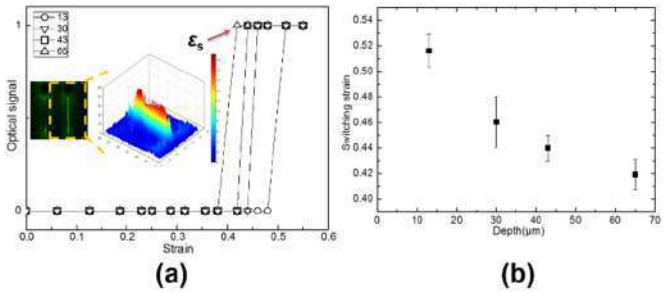

Fig. 5. Relationship between (a) strain ε and output signal switches from 0 to 1, (b) switching strain ε and hole depth h, representing the formation of fluorescence line pattern.

B. Fluorescent Pattern Generation

To observe the fluorescence signals, a Leica® DMR fluorescence microscope has been used initially. Fig. 4a shows the fluorescent patterns generated by the surface creases during uni-axial (horizontal direction) substrate compression at different strain values. The line patterns along the holes start to form after a compression strain of 0.515 (51.5%).

C. Signal Processing

The ON/OFF (or 0/1 output) switching strain has been defined to be the value at fluorescent line pattern forming. To automatically determine whether fluorescent line patterns have been formed (logic "1"), we: (1) used the Canny edge detection (2) Mapping of edge points to the Hough space in an accumulator (r, theta), followed by infinite line conversion to finite lines (min. length set to 200 pixels). Hence a detected line longer than 200 px. will return a logic "1" as in Fig. 4b.

D. Hole Depth vs. Switching Strain

Fig. 5 shows the relationship between hole depth h and switching strain ε_s. For different hole geometries, the output signal changes from 0 to 1 when substrate strain increases beyond the switching strain ε_s (Fig. 5a). Fig. 5b indicates a trend of increased switching strain ε_s.

Fig. 5b shows that the switching strain ε_s value increases from 0.410 to 0.515, with reduced hole depth from 65 μm to 13 μm respectively. This suggests the switching strain value could be controlled by micro-structure geometry design, giving the opportunity to develop future MRL strain sensors with multiple switching strain values.

ACKNOWLEDGMENT

Data associated with this paper is available via Northumbria Research Data Management scheme.

REFERENCES

[1] D.-H. Kim, et al., "Epidermal Electronics", Science, Vol. 333, pp. 838-843, 2011.

[2] W. Wu , X. Wen , and Z. L. Wang , "Taxel-Addressable Matrix of Vertical-Nanowire Piezotronic Transistors for Active and Adaptive Tactile Imaging", Science, Vol. 340 , pp. 952-957, 2013.

[3] Y. Su, et al., "In-Plane Deformation Mechanics for Highly Stretchable Electronics", Advanced Materials, Vol. 29, pp. 1604989, 2017.

[4] B.B. Xu , D. Chen , and R. C. Hayward, "Mechanically Gated Electrical Switches by Creasing of Patterned Metal/Elastomer Bilayer Films", Advanced Materials, Vol. 26, pp. 4381-4385, 2014.

[5] Y. Zhang, et al., "Buckling in serpentine microstructures and applications in elastomer-supported ultra-stretchable electronics with high areal coverage", Soft Matter., Vol. 33, pp. 8062-8070, 2013.

[6] C. Wang, B. Xu, J. G. Terry, S. Smith, A. J. Walton and Y. Li, "Test Structures for Stepwise Deformation Sensing on Super-flexible Strain Sensors", IEEE ICMTS, Grenoble, France, pp. 150-155, 2017.

[7] R. Maaskant, T. Alavie, R. M. Measures, G. Tadros, S. H. Rizkalla, A. Guaha-Thakurta, "Fiber-optic Bragg grating sensors for bridge monitoring", Cement and Concrete Composites, Vol. 19, pp. 21-33, 1997.

[8] Y. Sagara, S. Yamane, M. Mitani , C. Weder, and T. Kato, "Mechanoresponsive Luminescent Molecular Assemblies: An Emerging Class of Materials", Adv. Mater., Vol. 28, pp. 1073–1095, 2016.

[9] S. M. Jeong, S. K. Song, H. Kim, K. I. Joo, and H. Takezoe, "Mechanoluminescence Color Conversion by Spontaneous Fluorescent-Dye-Diffusion in Elastomeric Zinc Sulfide Composite", Adv. Funct. Mater. Vol. 26, pp. 4848-4858, 2016.

[10] A. Auguste, L. Jin, Z. Suo and R. C. Hayward, "Post-wrinkle bifurcations in elastic bilayers with modest contrast in modulus", Extreme Mechanics Letters, Vol. 11, pp. 30-36, 2017.

Test Structures for Stepwise Deformation Sensing on Super-flexible Strain Sensors

C. Wang [1], B. B. Xu [1], J.G. Terry [2], S. Smith [2], A.J. Walton [2], Y. Li [1]
[1]Smart Materials and Surfaces Lab, Faculty of Engineering and Environment,
Northumbria University, Newcastle upon Tyne, NE1 8ST, UK
Email: yifan.li@northumbria.ac.uk
ben.xu@northumbria.ac.uk
[2]SMC, Institute for Integrated Micro and Nano Systems
School of Engineering, the University of Edinburgh, Edinburgh, EH9 3JF, UK

***Abstract* — Developing MEMS sensors with a high strain sensing range (up to 0.6) and a stepwise sensing mechanism could enable widespread downstream applications, by allowing intimate, mechanically conformable integration with soft biological tissues. Most approaches to date focus on challenges to associate the sensing mechanism with high peak strains under large deformation.**

By designing and characterizing test structures with multi-switching electrodes on super-flexible substrates, this research has established a strategy for stepwise strain-sensing mechanism based on elastic instabilities. The growing and co-existence of wrinkles and creases on multiple electrodes with different dimensions are observed under lateral strains ranging between 0.3 and 0.6. Initial electrical measurements of the multi-switching mechanism has been demonstrated with a two stage resistance value change observed under changing compressive strain. Further investigation will focus on the device optimization and mechano-electrical signal processing.

I. Background

Flexible electronic and MEMS devices have become one of the more interesting technologies for next generation applications such as bio-medical electronics, flexible circuits, sensors and actuators [1-4]. Recent development has shown that elastic substrates have great potential to withstand high strain deformation during bending, compressing and stretching, when complying with local features such as metal interconnects and integrated transducers [5-8].

Among recently developed flexible MEMS applications, a versatile set of approaches exploits the sensing and actuation of planar compression strain achieved by triggering the elastic instabilities with placing pre-strain in an elastomer mounting substrate [9-11]. This paper presents a concept in which elastomeric substrates with engineered distributions of a set of materials and structural characteristics yield stepwise strain sensing of in-plane deformations. The related technologies and newly developed sensing mechanism could shed a light on the future applications in tunable optics and stretchable electronics.

II. Methodology

Test structures with a single switching mechanism to sense super-flexible strain have been reported [4, 8]. These devices operate by a pair of finger electrodes contacting as a result of surface creasing generated in the gap at the critical strain. At this point the measured resistance of these device switches from open (~10^{13} Ω) to closed (~10^{2} Ω). The critical strain values are of course related to the dimensions of the designed gap between the finger electrodes along the compression axis [8].

Such mechano-electrical response (strain - resistance) test structures can be employed for super-flexible substrate strain sensing. However, each device performs as a digital sensor with "ON/OFF" logic, therefore only measuring a single critical strain value [8].

In order to increase the number of critical strain values the test structures can deliver without increasing the pad count, this paper focuses on studying the deformation behaviour of a test structure with multi-switching electrodes on super-flexible substrates. The ultimate target is to enable a multi-switching mechanism where the strain value can be determined by measuring the resistance of the test structures. The following characterisation will be focused on electrode geometry design related to the surface deformation (optical measurement), and electrical signal (resistance) as a function of strain change.

A. Test Structure Design

Figure 1 shows the test structures used, with the deformation study focusing using two different layouts:

- A two-terminal structure with four pairs of "finger" electrodes labelled F1 (longest) to F4 (shortest) making up the multi-switching strain sensing gate
- A four-terminal structure with a similar finger arrangement to that in design I

The original lengths of finger electrodes ($L_f = L_{f0}$ in figure 1) range from 225 to 265µm and 500µm to 525µm, with electrode widths either 20µm or 50µm. The gap between the finger electrodes L_g ranged between 5 and 95µm. The probe pads were all 500 µm x 500 µm (original length $L_e = L_{e0}$ = 500 µm) in size.

978-1-5090-3615-8/17 $31.00

These test structures are designed to enable both 2-point and 4-point Kelvin measurement of device resistance. The test structures are fabricated on stretched substrates and as the tension is reduces, the finger electrodes F1 to F4 will be brought into contact sequentially due to their different L_g values [4, 8]. The finger resistance values and any contact resistance can then be measured.

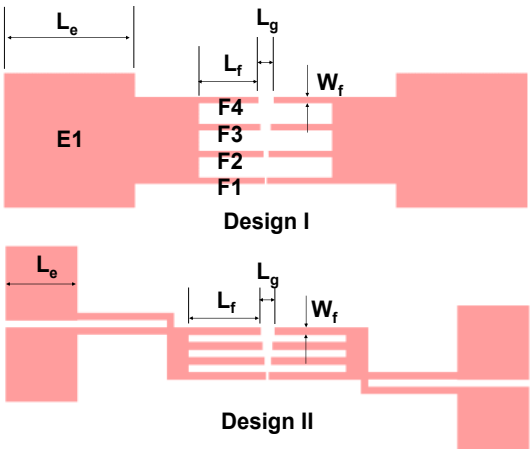

Fig. 1. Design layouts of the multi-switching high-strain sensing test structures.

B. *Fabrication Process*

The fabrication process involves the patterning of a gold layer on a silicon substrate and then transferring the pattern onto a pre-tensioned flexible substrate. The gold layer was patterned with a lift-off process using MEGAPOSIT™ SPR™ 220-7 positive photoresist. This involved depositing Au layers (with thickness ranging between ~16nm and ~100nm) on a silicon wafer with an anti-stiction SAM layer Perfluoro-decyl-trichloro-silane (FDTS, deposited using a MemsStar AURIX™ system). Alternatively, a thin C_4F_8 passivation layer deposited by Plasmatherm® Inductively Coupled Plasma (ICP) system could also be employed as an anti-stiction layer.

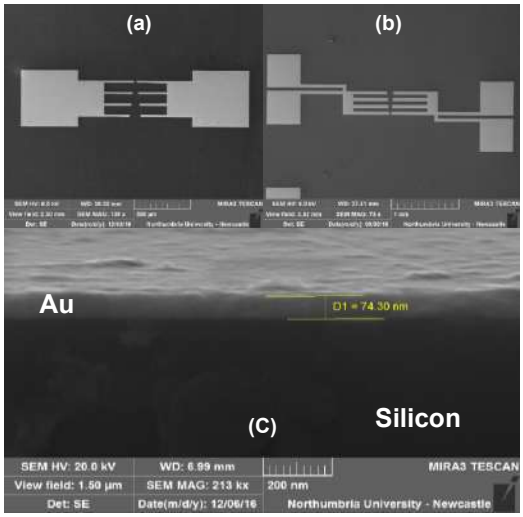

Fig. 2. SEM images showing (a) and (b) top view of the Au multi-switching test structures on silicon substrate, and (c) cross-sectional view showing Au thickness.

Fig. 2(a) and (b) shows SEM images (Tescan® Mira3) of the multi-switching electrode designs on silicon, with Fig2(c) showing a cross-section of the gold layer with a thickness of 74nm. With the test structure geometric designs reported above, the resistance of the fingers would be expected to vary between ~25 to 175 Ω for the reported gold film thicknesses.

With the gold now patterned the next stage is to transfer it onto the PDMS bi-layer. This bi-layer elastomer, consists of a thick and stiff mounting layer (3 mm thick, 9 mm width and 30 mm length) made of Vinylpolysiloxane, which was prefabricated and placed in a mechanical vice and pre-stretched from 5mm to 30mm length, before a softer unstressed thin PDMS bilayer (~110.13 µm thick) was attached.

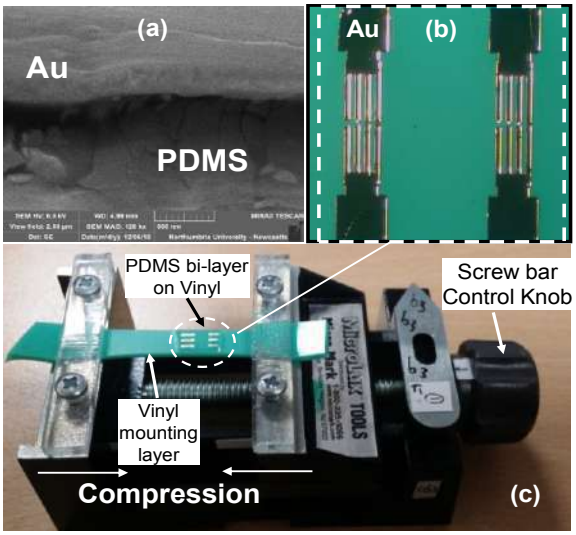

Fig. 3. (a) SEM images showing transferred Au sitting on PDMS bilayer (~110 µm thick), (b) microscopic top view of the transferred Au test structures on PDMS, and (c) photo of the entire device tensioned in the mechanical vice.

To transfer the Au electrodes they were treated with MPTMS (3-Mercaptopropyl-trimethoxysilane) as an SAM adhesive, by soaking in 25mM MPTMS in absolute ethanol solution for 3 hours. The electrodes were then transferred to the bi-layer elastomer flexible substrate (shown in Fig. 3) from the silicon carrier wafer using the dual SAMs stamping method reported in [4, 8].

C. *Strain testing set-up*

Figure 3(c) shows the completed devices in their jig with the Au - PDMS test structures, mounted on the Vinylpolysiloxane (green coloured) stiff layer under tensile stress (mechanically pre-stretched). The PDMS bilayer with the Au test structures (figure 3b) was then compressed by relaxing the pre-stretched Vinylpolysiloxane mounting layer controlled by turning the screw thread (pitch = ~ 1.25mm/turn) of the mechanical vice.

By relaxing the pre-stretched Vinylpolysiloxane mounting layer from L_0 to L, the PDMS bi-layer is compressed. Hence, the PDMS surface instabilities would be expected to change (Wrinkles-Creases) depending on the strain under uniaxial compression, which is given by:

$$\varepsilon = (L_0-L)/L_0 \qquad (1)$$

III. Measurements and Results

A. Optical measurement of Electrode Deformation

To quantitatively study the electrode deformation, compression strains were calculated before and during the formation of crease in the gap between electrodes by measuring the "L_{f0} and L_f" of the 4 finger electrodes, and "L_{e0} and L_e" of the contact electrodes. These results can then be compared with the mounting layer or substrate strain ε given by Eq. 1 which acts as a reference.

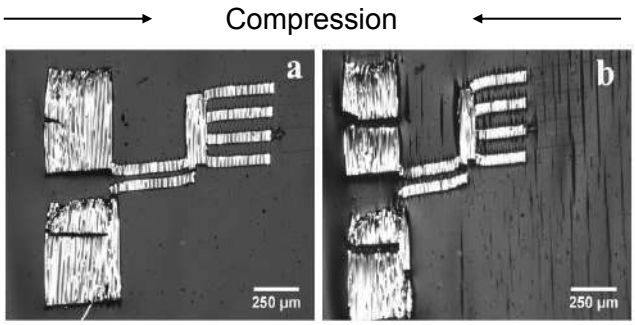

Fig. 4. Time sequential microscopic images showing the compression process generating creases (b) on PDMS and wrinkles on Au electrodes

As a result of the surface instability growth, Au electrodes on the PDMS surface may endure a different strain change to the PDMS bi-layer and the Vinylpolysiloxane mounting layers. Hence, 2-D measurements of the electrode deformation were undertaken using ImageJ software on photos taken using a Nikon® Eclipse LV100 microscope. The lengths were measured to determine the compression strain on Au electrodes of the multi-switching test structures during the compression process (fig. 4).

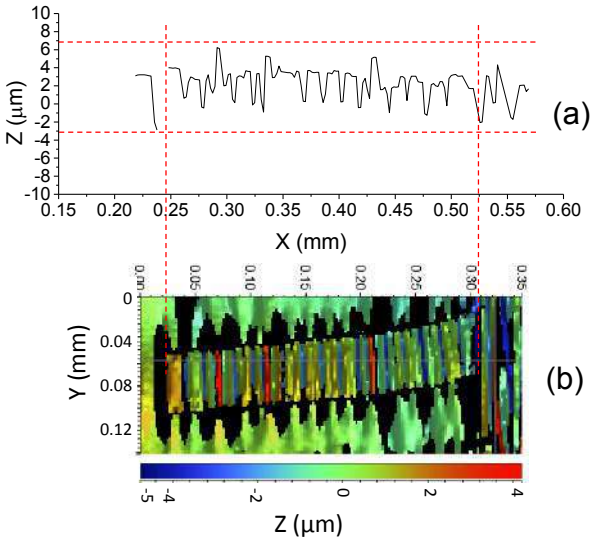

Fig, 5. Bruker GTK surface scan providing surface profile of F2 electrode shows both wrinkles on Au and creases on PDMS as (a) cross-section view, and (b) 2D contour top view

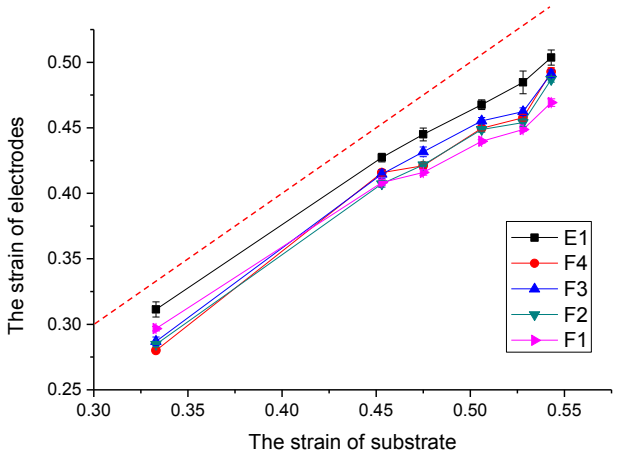

Fig. 6. Strain change comparison on multi-switching Au electrodes – finger electrodes F1 to F4, and contact pads E1. Red dotted line indicates the substrate strain change as a reference.

Figure 5 shows a surface deformation profile of the Au electrode test structures measured using a Bruker® GTK interferometry surface profiler. In addition to the length information, the amplitude of wrinkles (figure 5(a)) can also be observed during the process.

While Au wrinkling was observed at lower strain levels in a similar manner to previous reported single-switching test structures, the multi-switching structures have shown some interesting behaviour.

Details recorded in Fig. 4 and 5 show that, when creases start to form at strains $\varepsilon > 0.45$ on the PDMS surfaces, the compression ratios $(L_{f0} - L_f) / L_f$ start to lag behind the substrate strain change as shown in Fig. 6. This is more obvious on the finger electrodes (F1 to F4) than the probe pad (E1).

As a result, the multi-switching structures (especially the finger electrodes) are largely undamaged along the uniaxial compression direction, which makes electrical measurement of the multi-switching mechanism promising.

B. Electrical measurement of the Multi-switching mechanism

When there is a large strain change of up to 0.6 or 60%, it is inevitable that tensile transverse strains are generated by the uniaxial compressive strain change. Such tensile strain is usually perpendicular to the compression direction, and has been observed to cause damage to some parts of the test structure.

Figure 7(a) shows that the tensile strain changes on finger electrodes F1 to F4 are considerably larger than on the probe pads E1. This non-uniform strain distribution causes undesirable shear force to be generated on interconnects between the contact pads (E1) and (F1 and F4) in both design I and II. Figure 7(b) shows that on design II, right-angled interconnects also suffered damage due to similar shear forces.

This damage has resulted in the following compromises during the electrical testing:

1. Only 2-point resistance measurements were conducted at this stage.

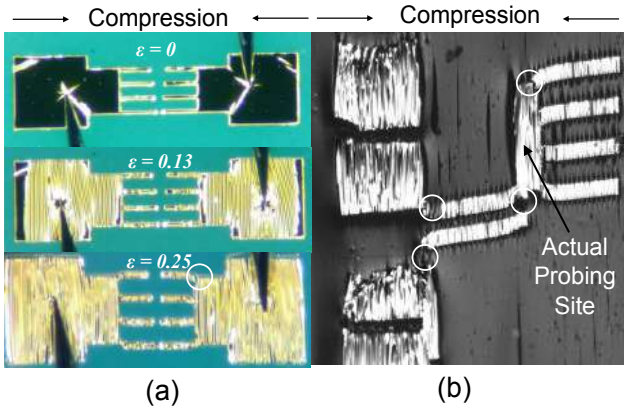

Fig. 7. Tensile strain perpendicular to the compression direction generated during strain increase on both (a) design I (probe tips present) and (b) design II. The damaged interconnects are highlighted by white circles.

2. The actual probing site of design II is as indicated in figure 7(b).
3. Only finger electrodes F2 and F3 were successfully involved in the multi-switching strain sensing.

However, despite the above issues, multi-switching with a large strain sensing mechanism has been achieved. Figure 8 shows the resistance measurements performed using an Everbeing EB8 manual probe station (with EB-05 probes) connected to a Keithley® 4200 analyzer (-1V to +1V sweep, with 0.2V/step). It should be noted that probing these devices is complicated by the wrinkling and creasing of the gold as well as the flexible and soft nature of the substrate membrane.

Figure 9 shows the resistance values of the test structure as a function of strain for design II shown in Figure 1. Each point is measured for a range of current level by sweeping between -1V and +1V, with 0.2V/steps. For this structure the designed L_g values for F2 and F3 finger electrodes were 12 µm and 21 µm respectively, with L_f = 509 µm and 518 µm, and W_f = 50 µm. Given the Au thickness in this case was around 70 nm, then the estimated finger electrode resistance would be in the region of 50 Ω. Therefore when the F2 electrodes are in contact, the calculated resistance of the test structure will be 100 Ω, assuming the contact resistance is zero. This will be reduced to

Fig. 8. Photo shows resistance measurements performed using an Everbeing EB8 manual probe station

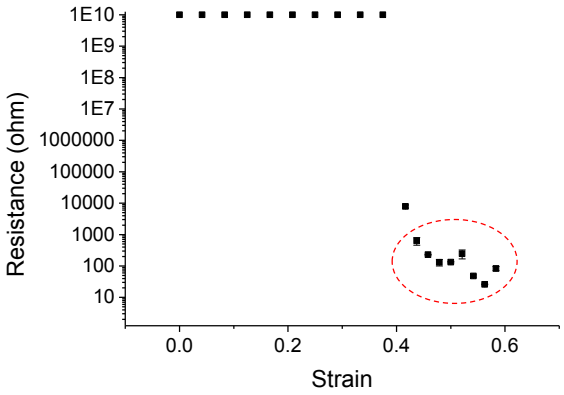

Fig. 9. Resistance of the test structure (design II, L_g) as a function of strain. The resistance change during the two-stage switching are highlighted in a red ring and detailed in figure 10.

50 Ω when F3 electrodes are also connected due to a higher strain.

From figure 10, it can be observed that the first switching stage happens at ε_s = 0.45, strain range 0.45 < ε < 0.52 with a resistance of ~120 Ω. The second switching stage occurs at ε_s = 0.54, strain range 0.54 < ε < 0.58 with the measured resistance being ~ 50 Ω. Note the error bars indicate multiple measurements at different current levels that in most cases indicate that Joule heating is not influencing the measurement. It is thought that the large variability in just the two data points is related to the contact resistance just before a good contact is achieved.

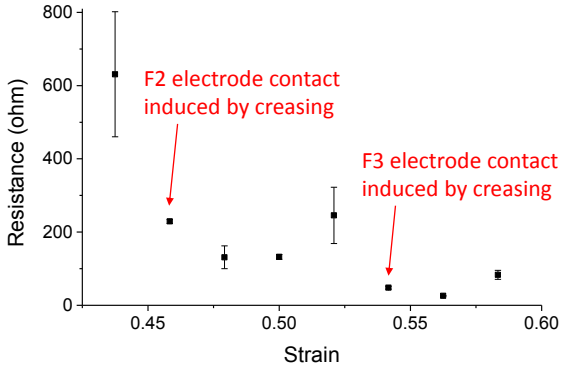

Fig. 10. Two-stage resistance switching strain sensing: Resistance of the test structure (design II, Lg) as a function of strain during the two-stage switching period (0.45< ε <0.52, and 0.54< ε <0.6).

The "switch on" strain ε_s results from the multi-switching test structure seem different to the previous reported values of single switching test structures with L_g = 12 µm and 21 µm reported in [8], which are 0.22 and 0.42 respectively and further investigation is required.

IV. Conclusions and Discussions

Test structures with the ability to detect multiple strain values on a super-flexible substrate have been designed, fabricated and

characterised, both optically and electrically. In contrast to the previously reported single switching test structures, multiple resistance values were generated at different switching strains on an individual device. This has been demonstrated using the multiple finger electrode test structure with different distances between the electrodes (the gaps are aligned along the compression axis).

During characterization, issues related to unwanted tensile strain perpendicular to the compression axis have been observed, which resulted in unexpected damage to the test structure interconnects. Future work will have to address minimizing such damage by layout modifications. The switching strain values of the multi-switching test structures related to the gap distances were observed to be different than values reported for the single switching devices and further investigation is required to compare the performance of the two structures.

ACKNOWLEDGMENT

This work is supported by EPSRC (EP/N007921/1, EP/L026899/1), and the royal society (RG150662). The authors would like to thank Everbeing who donated the probing system used in this work, and memsstar for providing the SAM coating facility. Data associated with this paper is available via Northumbria Research Data Management scheme: https://www.northumbria.ac.uk/research/research-data-management/

REFERENCES

[1] D.-H. Kim, et al., "Epidermal Electronics", Science, Vol. 333, pp. 838-843, 2011.

[2] W. Wu , X. Wen , and Z. L. Wang , "Taxel-Addressable Matrix of Vertical-Nanowire Piezotronic Transistors for Active and Adaptive Tactile Imaging", Science, Vol. 340 , pp. 952-957, 2013.

[3] D.-H. Kim , et al., "Stretchable and Foldable Silicon Integrated Circuits", Science, Vol. 320, pp. 507-511, 2008 .

[4] B.B. Xu , D. Chen , and R. C. Hayward, "Mechanically Gated Electrical Switches by Creasing of Patterned Metal/Elastomer Bilayer Films", Advanced Materials, Vol. 26, pp. 4381-4385, 2014.

[5] D. Y. Khang, H. Q. Jiang, Y. Huang, and J. A. Rogers, "A Stretchable Form of Single-Crystal Silicon for High-Performance Electronics on Rubber Substrates", Science, Vol. 311, pp. 208-212, 2006.

[6] D. Y. Khang, J. A. Rogers, and H. H. Lee, "Mechanical Buckling: Mechanics, Metrology, and Stretchable Electronics", Advanced Functional Materials, Vol. 19, pp. 1526-1536, 2009.

[7] M. S. White, et al., "Ultrathin, highly flexible and stretchable PLEDs", Nature Photonics, Vol. 7, pp. 811-816, 2013.

[8] Y. Li, J.G. Terry, S.Smith, A.J. Walton, G. McHale and B.B. Xu, "Elastic Instabilities Induced Large Surface Strain Sensing Structures (ElLS)", IEEE ICMTS, Tempe, AZ, USA, pp. 94-99, 2015.

[9] B.B. Xu, Q. Liu, Z. Suo, and R.C. Hayward, "Reversible Electrochemically Triggered Delamination Blistering of Hydrogel Films on Micropatterned Electrodes", Advanced Functional Materials, Vol. 26, pp. 3218-3225, 2016

[10] R. Xu et al., "Designing Thin, Ultrastretchable Electronics with Stacked Circuits and Elastomeric Encapsulation Materials", Advanced Functional Materials, published online, doi: 10.1002/adfm.201604545, 2017

[11] K. Nan et al., "Engineered Elastomer Substrates for Guided Assembly of Complex 3D Mesostructures by Spatially Nonuniform Compressive Buckling", Advanced Functional Materials, Vol. 27, p. 1604281, 2017